Ultrafast laser plasma doping of rare earth ions for optical waveguiding applications

Suraya Binti Ahmad Kamil

Submitted in accordance with the requirements for the degree of
Doctor of Philosophy

The University of Leeds

School of Chemical and Process Engineering

February, 2018

The candidate confirms that the work submitted is her own, except where work, which has formed part of jointly authored publications, has been included. The contribution of the candidate and the other authors to this work has been explicitly indicated below. The candidate confirms that appropriate credit has been given within the thesis where references has been made to the work of others.

Conference journals and paper

Chapter 4

S. A. Kamil, J. Chandrappan, M. Murray, P. Steenson, T. F. Krauss, and G. Jose. Ultrafast laser plasma doping of Er^{3+} ions in silica-on-silicon for optical waveguiding applications. *Optics Letters.* 2016, **41** (20), pp. 4684-4687.

S. A. Kamil, J. Chandrappan, M. Murray, P. Steenson, T. F. Krauss, and G. Jose. Novel technique for doping rare earth ions in silica-on-silicon for photonic integrated circuits. In: *PHOTON16, 5-8 September 2016, Leeds.* Institute of Physics (IOP).

M. Murray, S.A. Kamil, S. Mickelthwaite, T. Nunney, J. Treacy, and G. Jose. Implantation of erbium doped TeO_2-ZnO-Na_2O glass into silicon for gain media in silicon photonics. In: *Glass Reflections, 7-9 September 2015, Cambridge.* Society of Glass Technology.

G. Jose, J. Chandrappan, S. A. Kamil, M. Murray, Z. Zolnai, E. Agocs, P. Petrik, P. Steenson and T. Krauss. Ultrafast laser plasma assisted rare-earth doping for silicon photonics. In: *Conference on Lasers and Electro-Optics (CLEO), 5-10 June 2016, San Jose, California.* IEEE.

M. Murray, J. Chandrappan, S. A. Kamil, T. Kakkar, P. Petrik, E. Agocs, Z. Zolnai, R. Hogg, D. Childs, T. Krauss, I. White, R. Penty, P. Steenson, A. Jha and G. Jose. Platform manufacturing technique for next generation integrated photonic components. In: *17th International Conference on Transparent Optical Networks (ICTON), 5-9 July 2015, Budapest, IEEE.*

Most of the results that shown in the papers were obtained by the author of the thesis, and the results that obtained from other people has been stated in the thesis.

ACKNOWLEDGEMENTS

ABSTRACT

The work presented here is to introduce and investigate a novel material and a fabrication technique for an Er^{3+} ion doped waveguide amplifier (EDWA) on a silicon platform. EDWA performance strongly depends on the erbium concentration and the nature of the host material. There are two materials studied for this work. For the first material, TeO_2-ZnO-Na_2O-Er_2O_3 (Er-TZN) is doped into the silica-on-silicon (SOS) substrate surface, and for the second material, Er-TZN is doped into the surface of Si_3N_4-on-silicon. For the first material, the mixing of Er-TZN with SiO_2 produces a homogeneous layer which has the potential to be used for EDWA applications. The fabrication is carried out using a novel technique which is named ultrafast laser plasma doping (ULPD). In this technique, the Er-TZN target is bombarded using a femtosecond laser and the interfacial reaction between a high energy plasma plume and heated silica-on-silicon substrate results in a highly dense erbium doped silicate that is referred to as erbium-doped tellurite modified silica (EDTS). The success of this EDTS resulted in this work being extended to produce two types of a channel waveguide, i.e. diffused and ridge waveguide. However, for the diffused waveguide, the attempt to fabricate this type of waveguide failed to produce satisfactory results because it is believed that the metal mask moved during the fabrication process. For ridge waveguide, etching results still do not show satisfactory output. Therefore, further optimisation is needed to accomplish a practical optical waveguide. On the other hand, the doping of Er-TZN into Si_3N_4 which is also prepared using the ULPD technique is less successful compared to SiO_2 because the doped layer exhibits inhomogeneous material distribution although various process parameters have been tried. Failure to obtain a layer like EDTS is probably due to the limitation of the current instruments and also the rigid structural network of Si_3N_4.

TABLE OF CONTENTS

LIST OF TABLES

LIST OF FIGURES

LIST OF ABBREVIATIONS

ADF	Annular dark field
AMP	Amplifying loop section
BE	Binding energy
BF	Bright field
BO	Bridging oxygen
BSE	Backscattered electron
CMOS	Complementary metal-oxide-semiconductor
CVD	Chemical vapour deposition
DC	Direct current
DF	Dark field
EDFA	Erbium doped fiber amplifiers
EDTS	Erbium-doped tellurite modified silica
EDWA	Erbium-doped waveguide amplifier
EDX	Energy dispersive x-ray
EELS	Electron energy loss spectroscopy
Er-TZN	$TeO_2\text{-}ZnO\text{-}Na_2O\text{-}Er_2O_3$
ESA	Excited state absorption
FEG	Field emission gun
FHD	Flame hydrolysis deposition
FIB	Focused ion beam
Fs-laser	Femtosecond laser
Fs-PLD	Femtosecond pulse laser deposition
FWHM	Full half width maximum
HAADF	High field annular dark field
HRTEM	High-resolution TEM
IB	Inverse Bremsstrahlung
ICT	Information and communication technology
LIMS	Liquid metal ions source
NBO	Non-bridging oxygen
OFA	Optical fiber amplifier
PECVD	Plasma-enhanced chemical vapour deposition
PLD	Pulsed laser deposition
PIC	Photonic integrated circuit
PL	Photoluminescence
RF	Radio frequency
SE	Secondary electron
SAED	Selected area electron diffraction
SEM	Scanning electron microscope
SOA	Semiconductor optical amplifier
SOI	Silicon-on-insulator
SOS	Silica-on-silicon
SPL	Signal splitter

STEM	Scanning transmission electron microscope
TE	Transverse electric
TEM	Transmission electron microscope
TM	Transverse magnetic
UHV	Ultra-high vacuum
ULPD	Ultrafast laser plasma doping
WDM	Wavelength multiplexes
XPS	X-ray photoelectron spectroscopy
XRD	X-ray diffraction

LIST OF SYMBOLS

at.	Atomic percent
c	Speed of light
D	Plasma density
D_0	Initial plasma density at the target
d	Thin film thickness
e	Electron charge
E_g	Energy band gap
h	Planck constant
k_0	Free space propagation constant
k_B	Boltzmann constant
l	Laser intensity
m	Order of reflection
n	Refractive index
n_{eff}	Effective index
n_a	Refractive index of air
n_f	Refractive index for thin film
n_p	Refractive index for prism
n_s	Refractive index for substrate
m_e^*	Effective electron mass
m_h^*	Effective hole mass
p	Number of modes
P	Gas pressure
r	Radius
rpm	Rotation per minute
t	Distance plasma from target
T	Temperature
T_g	Glass transition temperature
x	Collisional cross section
α	Coupling angle
ω	Laser frequency
θ	Angle
$\mathcal{E}$	Angle of the prism
$\mathcal{E}_0$	Permittivity of free space
$\mathcal{E}_s$	Relative permittivity of the solid
λ	Wavelength
λ_m	Mean free path
υ	Frequency
Φ	Work function
σ	Total cross section for plasma-to-ambient gas collisions

CHAPTER 1
INTRODUCTION

1.1 Overview

The world has seen a surge in demand for information and communication technology (ICT) applications. This rapid development has coaxed the world of ICT to turn their attention towards photonic integrated circuits (PICs) to meet these wavelength spectral bandwidth-hungry applications that require a faster internet and computing powers. PICs are versatile as they are laden with functional photonic components such as an optical filter, laser, waveguide arrays, splitters, modulator, and photodetector [1]. However, as the number of PIC components increases, the associated inherent loss due to propagation and interconnects also increases. An integrated optical amplifier can boost the signal to mitigate such losses associated with dense integrations. Due to the high demands for greater bandwidth and to go with the ever-increasing need for speed in all aspects of society, industry and business, this, in turn, requires smaller and more efficient integrated optical amplifiers.

Generally, optical amplifiers can be classified into two main types which are optical fibre amplifier (OFA) and semiconductor optical amplifier (SOA) [2]. Erbium-doped fibre amplifiers (EDFAs) are an example of an OFA that has the capability to become gain media for the broadband amplifier and laser for a standard telecommunication wavelength of around 1550 nm. The ability of EDFAs to amplify signals in the long-haul network without reducing the quality of signal significantly due to noise, cross-talk between adjacent channels and polarisation dependence is highly impressive [3,4]. For this reason, EDFA is a vital component of the global fibre optic communication infrastructure. A typical EDFA consists of silica glass-based optical fibre with its core doped with erbium, and it is a few metres long. SOAs, on the other hand, have become competitive amplifiers for the long and short haul network and are able to amplify the incident light signal by using electrical pumping. Compared with EDFA, SOA is smaller and less expensive. SOAs can also be integrated with other devices such as semiconductor lasers and modulators. Nevertheless, performance wise, SOAs still lag behind EDFAs because of higher noise, lower gain, polarisation dependence and high cross-talk level [4,5].

EDFA has proved to be an effective optical amplifier and has been widely used within the long-haul and short-haul telecommunication system. However, EDFA integration with other optical and electronic components on a compact integrated platform is

difficult due to its bulky structure which makes the packaging expensive and is a hindrance for a miniature device. To overcome this, the concept of erbium-doped waveguide amplifier (EDWA) was introduced, and its operation principle is similar to an EDFA but as a miniaturised planar version to meet the emerging demands. EDWA inherits EDFA's magnificent performance but with a smaller size and it can be fabricated on silicon platforms compatible with complementary metal-oxide-semiconductor (CMOS) processing.

The selection of the material host for an EDWA is very important as it affects the gain per unit length which is closely related to solubility of the dopant, erbium and its photoluminescence lifetime [6]. Silica-based waveguides have the potential to provide the best characteristics of a host to erbium in EDWAs due to its refractive index matching with silica optical fibre thus minimising coupling loss. However, silica has a serious issue whereby it has limited solubility for erbium. Er^{3+} ions tend to cluster in silica even at moderate concentration of 0.7×10^{18} cm^{-3} [7]. This low solubility problem is due to the continuous tetrahedral structural units $(SiO_4)^{4-}$ in the silica glass network which, in turn, fails to accommodate Er^{3+} ions effectively [8]. When clustering occurs, energy transfer between excited Er^{3+} ions can occur, and this can cause luminescence quenching through the non-radiative relaxation. As a result, luminescence lifetime of the metastable state will also be reduced [9]. Generally, in order to obtain a reasonable gain over a length of a few centimetres, the erbium concentration in the host material should be in the range of 10^{20}–10^{21} Er^{3+} ions/cm^3 without reducing the metastable lifetime and having concentration quenching [10].

A possible way to avoid the clustering issue and increase the amount of Er^{3+} ion in the silica glass network is by introducing a co-dopant agent into the matrix such as Al_2O_3 [11–13], P_2O_5 [11,14,15] and HfO_2 in silica [8,16]. However, at high doping concentration, the competition among Er^{3+} ions to bond with the oxygen atom becomes greater, and this still leads to a clustering problem. On the other hand, tellurite (TeO_2) based glass has been reported to have a high solubility of Er^{3+} ions, and it had been doped into many tellurite host glass such as TeO_2-WO_3-Na_2O [17], TeO_2-Nb_2O_5-Na_2O [18] and TeO_2-GeO_2-Na_2O-ZnO [19]. Nevertheless, tellurite have a severe problem in that it has low thermal stability which hinders it from being used for many practical applications [20].

The advantages of tellurite offer the potential solution to solve the limitation of Er^{3+} ions solubility and clustering in silica by forming a multicomponent glass combining

them. Furthermore, the addition of TeO_2 into the silica glass will increase the refractive index of the glass and make it more advantageous for EDWA applications. However, to the best of our knowledge, glass that has the combination of SiO_2 and TeO_2 is very scarce been reported. This mixture may be due to phase separation that occurred in a ternary or quaternary glass as reported in the glass systems TeO_2-B_2O_3-SiO_2 [21], Li_2O-TeO_2-SiO_2 [22] and TeO_2-SiO_2-ZnO-K_2O [23] which, in turn, made it less enticing to be studied. Due to this complication, the emerging technique called ultrafast laser plasma doping (ULPD) is introduced which allows SiO_2 and TeO_2 based glass to mix together without phase separation [24–26]. The resultant doped glass layer achieved with the composition SiO_2-TeO_2-ZnO-Na_2O-Er_2O_3 has been named as erbium doped tellurite modified silica (EDTS).

Apart from silica, silicon nitride (Si_3N_4) is also seen to be a potential host material for EDWA applications. Si_3N_4 is an attractive candidate due to its higher refractive index (1.99), and also the fact that it is a Si-based material like SiO_2 that is compatible with CMOS processing.

1.2 Research aim and objectives

This research aims to explore the properties of a new EDWA host material on a silicon platform and explore its prospects as a component in silicon-based photonic integrated circuits. In particular, the objectives of this research are to:

a) form a layer of a mixture of erbium-doped tellurite glass and SiO_2 on silica-on-silicon (SOS) substrate and investigate the influence of process parameters on the properties of the obtained EDTS layer.

b) form a layered mixture of erbium-doped tellurite glass and silicon nitride in Si_3N_4-on-silicon substrate and investigate the influence of process parameters on the characteristics of the obtained layer.

c) design, fabricate and investigate the characteristics of an optical channel waveguide formed with an EDTS on SOS.

1.3 Thesis outline

The content of this thesis is organised as follows:

Chapter 1 provides the overview of this research. The research aim and objective are also included in this chapter. Chapter 2 covers a literature review of the theory related to erbium-doped waveguide amplifiers (EDWAs). A review of the literature regarding host materials for erbium for EDWA applications is also discussed and some of the

common techniques for fabricating an EDWA are presented. This chapter also includes an introduction and discussion of the ultrafast laser plasma doping (ULPD) technique which is the main technique used to fabricate the samples in this research. Chapter 3 provides a detailed review of the equipment involved and also the methodology used in this research. The principles and theories underlying the operation of the instruments are briefly presented in this chapter. Chapters 4 and 5 include the results and discussion on EDTS fabrication and its optical, structural and chemical properties in relation to the process parameters used. Chapter 6 details the ULPD attempted on the Si_3N_4-on-silicon substrate and an analysis of the results obtained. Chapter 7 describes the design, fabrication and characterisation of the channel waveguide. Chapter 8 provides a conclusion for the thesis and suggestions for future work.

CHAPTER 2
LITERATURE REVIEW

Erbium-doped waveguide amplifiers (EDWAs) are seen to be a potential solution for signal loss in a photonic integrated circuit. AN EDWA's operation principle with its related matters such as luminescence lifetime and limiting factors are explained in this chapter. Some of the reported host materials for erbium and common techniques for fabricating an EDWA are presented after that. This chapter also provides the fundamental discussion of the ultrafast laser plasma doping (ULPD) technique.

2.1 Erbium-doped waveguide amplifiers (EDWA) on silicon

An EDWA which inherits an EDFA's optical signal amplification properties but with a much smaller size enables it to be integrated with other PIC components in the same chip on silicon (Figure 2.1). Such EDWA integration on a planar waveguide form also contributes to fabrication cost reduction. Unlike EDFA which is in the form of a long fibre, an EDWA is in a planar form that is a few cm long or less and can be fabricated on a silicon substrate with a cladding material in between them.
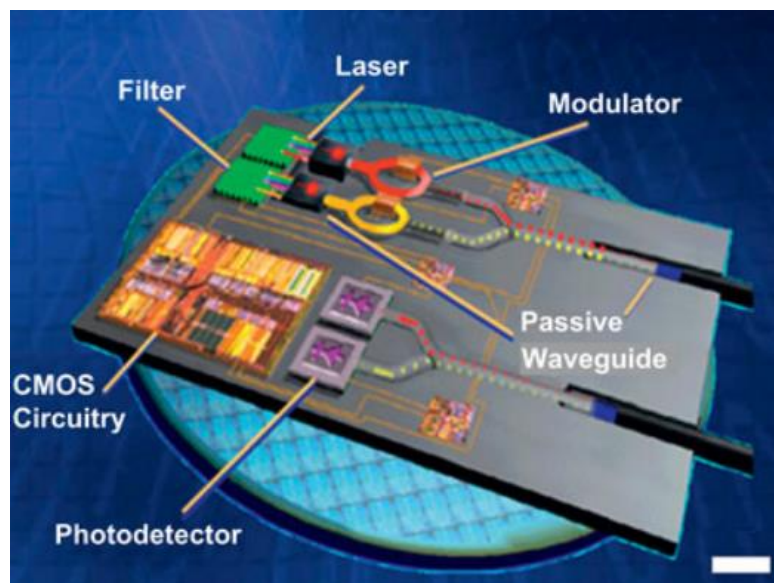
Figure 2.1: An example of PIC that consists of a filter, laser, modulator, photodetector, CMOS circuitry, and passive waveguide (optical amplifier) [27,28].

The material for the cladding should have a lower refractive index from the waveguide core in order to prevent or minimise the leakage of the signal to the substrate. Higher contrast between cladding and waveguide cores allows strong confinement of the optical mode that leads to high intensity in the waveguide. For optimum performance, an EDWA is normally fabricated in the form of a channel waveguide. There are a few

channel waveguide structures that have been reported such as buried, strip-loaded, rib, diffused and ridge waveguide [29,30] as shown in Figure 2.2.

(a)   (b)   (c)

(d)   (e)
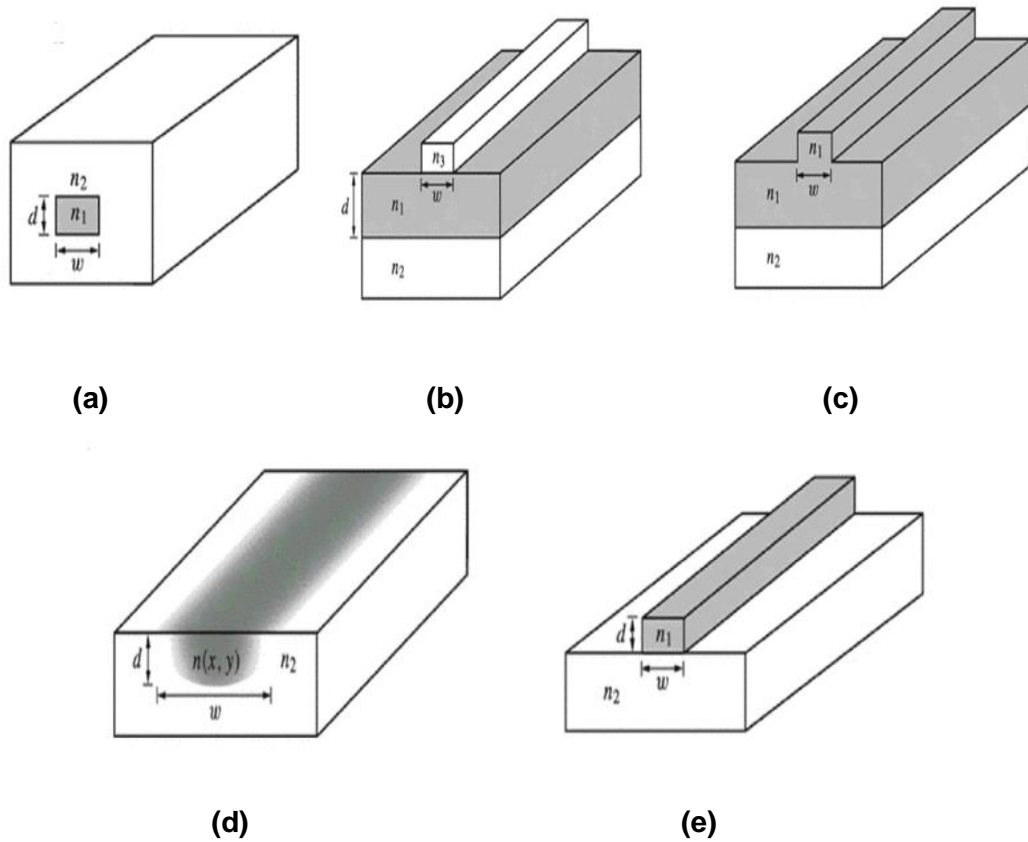
Figure 2.2: Channel waveguides can be fabricated into a few structures [30] which are (a) buried, (b) strip-loaded, (c) rib, (d) diffused, and (e) ridge. The core of the waveguides is indicated with dark shade and n_x, (x=1, 2, 3) is the refractive index of different regions.

2.1.1 Principle of operation

In EDFAs and EDWAs, erbium is incorporated in the waveguide core. Pure erbium is metal with an electronic configuration of [Xe] $4f^{12} 6s^2$. When it is incorporated as a dopant in the host material, erbium, usually in the form of a trivalent charge state with an electronic configuration of [Xe] $4f^{11}$ with electrons in the 4f-shell, is shielded by $5s^2$ and $5p^6$ closed shells. The 4f electrons undergo interaction of spin-spin and spin-orbit which causes the 4f energy level to be split into several different energy states [3,31] as shown in Figure 2.3. The splitting is also referred to as Stark splitting. Due to this shielding effect, the exact energy in 4f states is only slightly different based on the host materials used.
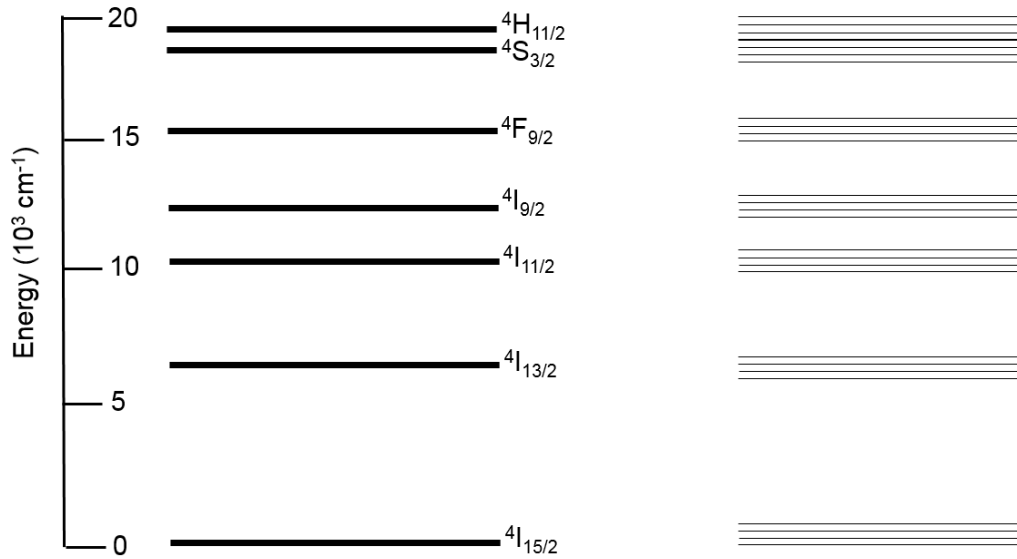
Figure 2.3: Energy levels of Er^{3+} ions with Stark splitting for each energy level (adapted from [31]).

The light amplification of an EDWA is based on stimulated emission from $^4I_{13/2}$ to $^4I_{15/2}$ energy levels. With external laser pumping of the waveguide, erbium ions are excited to a higher energy level based on the laser wavelength. Erbium ions are excited to their first excited state ($^4I_{13/2}$) when a laser with a wavelength of 1480 nm is used while, with 980 nm, they can be excited to a higher lying excited state ($^4I_{11/2}$) as shown in Figure 2.4. For the latter case, the erbium ions will then rapidly relax to the first excited state at $^4I_{13/2}$. This process is called non-radiative transition, and the corresponding energy is released to the host in the vibrational form (as phonons). After that, an erbium ion relaxes to the ground state $^4I_{15/2}$ by emitting photons with a peak emission wavelength of around 1535 nm with a certain emission bandwidth. This radiative transition is also called luminescence. This luminescence transition from the first excited state ($^4I_{13/2}$) to ground states ($^4I_{15/2}$) is exploited in an EDFA and EDWA for signal amplification typically in the C-band (1535-1565 nm) of optical communication.
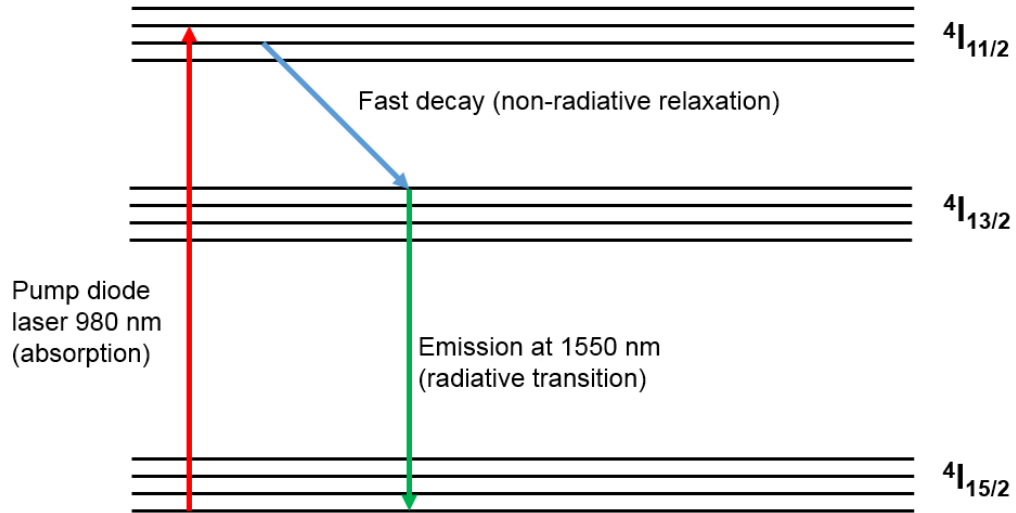
Figure 2.4: Schematic diagram of absorption and emission process of Er^{3+} ions upon 980 nm laser excitation (adapted from [32]).

2.1.2 Luminescence lifetime

Luminescence lifetime is a measure of the time an erbium ion specifically stays in the excited states before decaying to the ground state. Excited erbium ions undergo two main channels of decay, radiative and non-radiative, which can be used to define the lifetime:

$$\frac{1}{\tau} = \frac{1}{\tau_r} + \frac{1}{\tau_{nr}}$$

(2.1)

where τ is the total lifetime, τ_r is the radiative lifetime and τ_{nr} is a non-radiative lifetime. The radiative lifetime arises from the luminescence of erbium ions that relax from $^4I_{13/2}$ to $^4I_{15/2}$. Whilst, the non-radiative lifetime depends on the composition of host materials and the vibration coupling between erbium ions and host ions [33].

2.1.3 Limiting factors

The luminescence of erbium ion can be influence by several factors which are discussed in the following sections.

2.1.3.1 Solubility in host material

In most host materials, erbium ions tend to form precipitates beyond certain concentrations. These precipitates can form from either clustering between erbium ions or form compounds with components in the network of the host material [6]. As a result of the formation of these aggregates, it can cause interaction of ions between

erbium ions or group ions which may further induce luminescence quenching (this will be further explained in 2.1.3.3). In addition, this precipitation can also lead to the formation of non-optically active erbium compound. The precipitation issue is varied for the different host material. Therefore, the selection of host material is very crucial because it plays an essential role in determining a high-efficiency EDWA [6].

2.1.3.2 Phonon interactions

Phonon interaction is closely related to non-radiative transition occurring from various higher energy levels of Er^{3+} ions. Non-radiative relaxation is favoured when the host phonon energy is larger and less number of phonons are needed to bridge the energy band gap, E_g, between higher energy excited levels and lower/ground states [6]. Generally, if the phonon cut-off energies are greater than 25% of the energy gap, the luminescence will be almost completely quenched. For phonon cut-off energy in between 10-25% of E_g, the resulting quenching will be dependent on temperature and it causes luminescence lifetime as well as being dependent on temperature. For lower phonon cut-off energy, multi-phonon relaxation is negligible [34]. The phonon interaction is strongly dependent on the host material and type of rare-earth ions in the host. Therefore, the selection of low phonon energy hosts such as tellurite and fluoride can reduce the multi-phonon relaxation effect which, in turn, can increase radiative transition [6].

2.1.3.3 Ion-ion interactions

Rare earth ions incorporated in a host material such as glass tend to have ion-ion interactions. These interactions can be either between different types of rare earth ions or the same type of ions (e.g., Er^{3+}-Er^{3+}, for the case of clustering). Ion-ion interaction between different ions can be employed in novel pumping schemes whereby excitation is provided to one species and transferred to another. An example of such a mechanism is Er/Yb co-doping in a host material in order to increase the luminescence efficiency of the Er^{3+} ions by coupling to the absorption bands of the Yb co-dopant (Figure 2.5) [35]. The Yb^{3+} ions from $^2F_{5/2}$ transfer their energy to $^4I_{11/2}$ of Er^{3+} ions and increase the luminescence efficiency around 1550 nm. Introducing a second rare-earth dopant can also provide the bonus of hampering aggregation of the Er^{3+} ions through the generation of a solvation shell [6]. On the other hand, ion-ion interaction between the same types of rare earth ions constitutes a loss mechanism and increases non-radiative decay from unwanted transitions. For one type of rare earth species, a number of different methods of ion-ion interaction occur as outlined below.
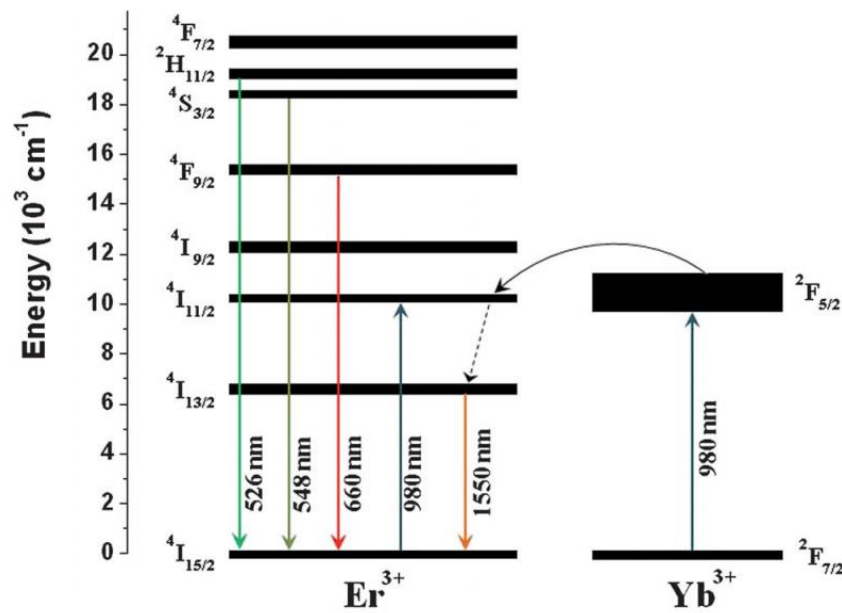
Figure 2.5: Energy level diagram of Er^{3+} and Yb^{3+} ions [35]. The Yb^{3+} ions from $^2F_{5/2}$ transfer their energy to $^4I_{11/2}$ of Er^{3+} ions, increasing the luminescence efficiency at 1550 nm.

Co-operative upconversion

Luminescence inefficiency in an EDWA is often associated with the co-operative upconversion process [36]. This process can occur when erbium ions are close to each other causing them to interact among them. Figure 2.6 (a) shows more clearly the interaction of two erbium ions when they are close to each other. The transition of ion A to the ground state from $^4I_{13/2}$ causes energy release which will then be transferred to ion B. After that, it is excited to a higher state ($^4I_{9/2}$), and the excited ion B then relaxes non-radiatively to $^4I_{13/2}$ and subsequently to ground state. For erbium doped in the oxide glasses, the relaxation is very fast and non-radiative, therefore the co-operative upconversion results in the release of heat to the host [6]. The extra heating can generate other effects such as further depletion of a lifetime because of thermal quenching [37].

Apart from that, the emission of green light may happen through the second order process of co-operative upconversion. It occurs when there is an interaction between two ions at the $^4I_{13/2}$ level where one ion will decay to the ground state and promote another ion to rise to the $^4I_{9/2}$ level. The ion will then relax at the $^4I_{11/2}$ level and again interact with another ion which is also at the $^4I_{11/2}$ level. Then, it will be excited to the $^2H_{11/2}$ or $^2S_{3/2}$ level. Green light emission (530-535 nm) is produced when the erbium ion relaxes from either the $^2H_{11/2}$ or $^2S_{3/2}$ level to ground state [38].
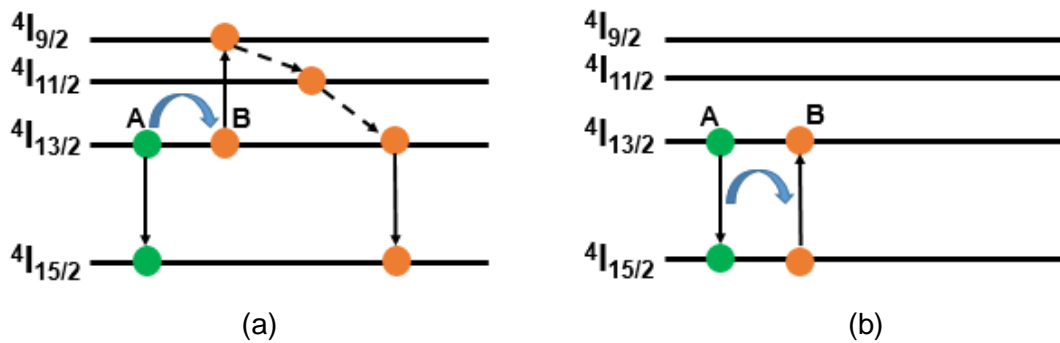
Figure 2.6: Schematic diagram showing ion-ion interactions between two neighbouring erbium ions. (a) and (b) represent co-operative upconversion and the energy migration process, respectively (adapted from [39]).

Energy migration

The energy released from a decay of erbium ion A from $^4I_{13/2}$ to ground state can be transferred to an unexcited erbium ion B and promote it to a $^4I_{13/2}$ level as shown in Figure 2.6 (b). Although the second ion B can still produce radiative emission, however, each energy transfer process will increase the probability of non-radiative transition. Thus, this process is still considered to be one of the processes that contributes to luminescence quenching [6]. Moreover, when the energy is transferred to the nearby erbium ion, it is probable that the erbium ion will be coupled with non-optically active sites. This will affect the amplification when an amplifier is built with materials having such detrimental processes are significant.

2.1.3.4 Excited state absorption (ESA)

Another factor that may contribute to luminescence quenching is excited state absorption (ESA). In this process, the excited erbium ion absorbs photons from the signal or pump which causes it to jump to a higher energy level (Figure 2.7) [40]. The ions lying at the higher energy level will then return to the metastable state by radiative transition or multiphonon relaxation. However, partly absorbed photons can disappear either in the form of heat or decay from the metastable to ground state with different wavelength emission [6].
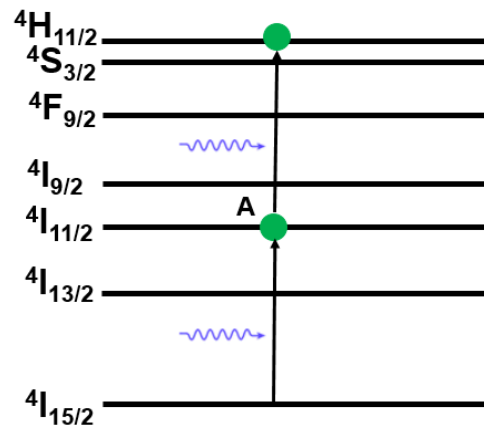
Figure 2.7: Excited state absorption of Er^{3+} ions. The excitied photons are here from 980 nm pump (adapted from [39]).

Since this process involves both a pump and signal photon, this causes maximum gain and pump efficiency to be affected. Typically, ESA is quite low when a pump of 980 nm is used and insignificant at 1480 nm. However, the ESA process is crucial at a shorter wavelength such as 800 nm because it can lead to poor pump efficiency and gain [41]. Hence, for an EDWA, a pump of 800 nm is definitely not a suitable choice.

2.2 Host materials for an EDWA

In the past few years, numerous studies have been done pertaining to a host material for erbium for EDWA application with the aim of producing optimal device performance. At a fundamental level, the performance of an EDWA largely depends on the host material for erbium. Generally, a waveguide amplifier should produce a high output gain with the shortest possible waveguide length for practical applications. This can be achieved by doping a host material with a high erbium concentration. Nevertheless, as the number of Er^{3+} ions per unit volume increases in the host material, the distance between erbium ions shortens, and they start to cluster beyond certain limits. Not all host materials doped with erbium are suitable for the fabrication of an EDWA as each host material has its limit for erbium doping concentration. Plus, although many materials have been identified as potential host materials for erbium, only a few material systems have demonstrated their ability to be an on-chip device for gain that is compatible with existing PIC technology. Several host materials for erbium doping and their suitability for EDWA application is compared and discussed in this section.

Silica-based waveguides can be the ideal material for building EDWAs for their excellent compatibility with well-developed silica-based fibre optics and microelectronics. However, as has been discussed before, silica has a serious issue with the solubility of Er^{3+} ions. The issue of solubility of Er^{3+} ions in silica can be mitigated by adding other oxide materials into the glass composition. Some key parameters obtained from previous reports about Er^{3+} ions doped into a SiO_2-based host material like aluminosilicate, phosphosilicate, SiO_2-GeO_2, oxyfluoride-silicate, soda lime silicate and SiO_2-HfO_2 are tabulated in Table 2.1. Table 2.1 highlights some of the vital characteristics for an EDWA based on various silicate based host materials. Among the properties shown are the refractive index, erbium concentration, bandwidth/full width half maximum (FWHM), lifetime, length of the waveguide, type of waveguide, loss, net optical gain and method of fabricating the waveguide.

Aluminosilicate displayed the characteristics of a good host material for erbium. Based on a buried waveguide that had been fabricated by Pan et al. [42], erbium doping concentration was 2.9×10^{20} cm^{-3}. It also displayed broad FWHM which was 50 nm. This waveguide produced a net optical gain of 1.0-1.1 dB/cm with a very low loss (0.05 dB/cm). The refractive index and lifetime were reported as 1.508 and 5 ms, respectively. However, this 20 cm long waveguide is a hindrance for a small integrated optical device.

Table 2.1: Some of the properties of an EDWA reported for silicate-based glass.

Property	Aluminosilicate	Phosphosilicate	SiO_2-GeO_2	Oxyfluoride-silicate	Soda lime silicate	SiO_2-HfO_2
Core refractive index	1.508	1.47	1.46	1.68	1.49	1.47-1.52
Erbium concentration (10^{20} cm^{-3})	2.9	0.4	500-600 ppm	1.1	0.7	0.3 mol%
FWHM / Bandwidth (nm)	50	~20	~33	21	Not reported	50
Lifetime (ms)	5	Not reported	Not reported	9	14	6.6-7.1
Waveguide length (cm)	20	7.5	6.45	1.85	5.9	Not reported
Waveguide type	buried	buried	ridge	channel	channel	slab
Loss (dB/cm)	0.05	0.17	0.06	1.0	0.1	0.8
Net optical gain (dB/cm)	1.0-1.1	0.67	0.16	0.92	0.76	Not reported
Method to fabricate EDWA	Physical vapour deposition	Plasma enhance chemical vapour deposition	Electron beam vapour deposition	Femtosecond laser inscription	Radio frequency magnetron sputtering	Sol-gel coating
References	[42]	[10,43,44]	[45]	[46,47]	[48]	[49]

A ridge waveguide (7.5 cm long) based on Er-doped phosphosilicate was fabricated by Shuto *et al.* using a plasma enhanced chemical vapour deposition (PECVD) method [44]. A net optical gain of 0.67 dB/cm and loss of 0.17 dB/cm were obtained from this waveguide. The concentration of erbium reported was only 0.4×10^{20} cm^{-3}. The FWHM reported from this work is ~20 nm with a refractive index of 1.47.

Nakazawa and Kimura fabricated a 6.45 cm long ridge waveguide based on Er-doped SiO_2-GeO_2. It produced very low gain (0.16 dB/cm) with loss of 0.06 dB/cm. This channel waveguide was fabricated using an electron beam vapour deposition technique and had FWHM of around 33 nm [45]. Among all the waveguides that have been reported from Table 2.1, it seems that the waveguide fabricated by this material had the lowest refractive index (1.46). This only leads to the conclusion that waveguides based on Er-doped SiO_2-GeO_2 are also unsuitable for the compact integrated amplifier.

Another SiO_2-based host which has been reported on is oxyfluoride-silicate (SiO_2-Al_2O_3-Na_2O-PbF-LaF_3). The 1.85 cm long channel waveguide that was fabricated using a femtosecond laser inscription technique by Thomson *et al.* produced loss (1.0 dB/cm) higher than its gain (0.92 dB/cm) [46]. The concentration of erbium that has been successfully doped into this host material was 1.1×10^{20} cm^{-3} with a lifetime of 9 ms. The refractive index and bandwidth were recorded as 1.68 and 21 nm, respectively [47].

Other than that, Ghosh *et al.* also doped erbium into a silicate host with a concentration of 0.7×10^{20} cm^{-3} and refractive index of 1.49 [48]. When compared with other host materials, the reported lifetime was highest at 14 ms. The optical gain obtained was 0.76 dB/cm with loss of 0.1 dB/cm for this 5.9 cm length channel waveguide. The guiding layer was deposited by using a radio frequency (rf) magnetron sputtering technique.

An erbium-doped SiO_2-HfO_2 slab waveguide that was fabricated using a sol-gel coating was also a potential material to be used for EDWA application. The reported bandwidth was high at 50 nm with loss of 0.8 dB/cm. The refractive index and lifetime recorded were 1.47-1.52 and 6.6-7.1 ms respectively [49]. There is no optical gain reported for the said material though. Failure to obtain gain from this material prevents it from being used for EDWA applications.

On the other hand, a few non-silicate based host materials were also used to study the suitability of the said material to be used for an EDWA. Some of the salient properties for an EDWA with a non-silicate host material are illustrated in Table 2.2. One of the many material types that can be a great host for erbium is tellurite glass. Many tellurite-based glass compounds are doped with erbium for EDWA applications such as TeO_2-ZnO-PbO-Er_2O_3 [50], TeO_2-WO_3-Na_2O-Er_2O_3 [51], TeO_2-ZnO-Na_2O [52] and TeO_2-GeO_2-Na_2O-ZnO-Er_2O_3 [19]. Erbium-doped tellurite glass is interesting due to its attractive features such as its high refractive index, the good solubility of erbium ions, wide band emission spectrum, high emission cross section at 1550 nm and low phonon energy (750 cm^{-1}) [50–52]. All these properties make tellurite glass a great candidate for an EDWA. Vu and Madden reported tellurite waveguide (ridge waveguide) with 5 cm long fabricated by a sputtering method could achieve a net optical gain as high as 2.8 dB/cm. Propagation loss was recorded as 0.6 dB/cm with an erbium concentration of 2.2 x 10^{20} cm^{-3}, fluorescence lifetime of ~1.3 ms and bandwidth of 40 nm [53]. The refractive index for this waveguide was also high (2.03) when compared with other materials with a similar net gain. This made it an ideal candidate for the low-cost miniature integrated optical system. Nevertheless, tellurite-based glass has a severe drawback in that it naturally has low thermal stability [20]. Additionally, without the presence of stabilising oxides, this material is chemically unstable. These attributes only make tellurite-based glass to be less than practical for applications [24].

Table 2.2: Some of the properties of an EDWA reported for non-silicate based materials.

Property	Tellurite glass	Phosphate glass	Bismuthate glass	Al$_2$O$_3$	Y$_2$O$_3$	Ta$_2$O$_5$	PMMA	Zirconia	ZSG
Core refractive index	2.03	1.56	1.94	1.65	1.9	2.1	1.53	2.08	1.75
Erbium concentration (10^{20} cm^{-3})	2.2	5.3	6250 ppm	1.17	2.3	2.7	0.36	0.88	0.8
FWHM / Bandwidth (nm)	40	28	40-50	80	Not reported	50	72	54	~25
Lifetime (ms)	1.3	4	2	7.6	~ 5	2.3	3.4	1.77	2.8
Waveguide length (cm)	5	1.0	6	5.4	3.9	2.3	1.6	6.5	4.7
Waveguide type	ridge	strip-loaded	ridge	channel	ridge	rib	rib	ridge	channel
Loss (dB/cm)	0.6	0.9	0.13	0.3	1.5	0.65	1.31	0.45	0.32
Net optical gain (dB/cm)	2.8	4.1	1.1	2	2.56	2.25	0.9	0.45	0.4
Method to fabricate EDWA	Rf magnetron sputtering	Rf sputtering	Rf magnetron sputtering	Sputtering	Sputtering	Rf magnetron sputtering	Spin coating	Sputtering	Sputtering
References	[53]	[54]	[55,56]	[57,58]	[59]	[60,61]	[62,63]	[64]	[65]

Another glass with good potential for EDWA application is phosphate glass. The refractive index, FWHM and lifetime recorded was 1.56, 28 nm and 4 ms, respectively. This guiding layer was fabricated by rf magnetron sputtering, and it was reported by Yan *et al.* to have the highest recorded gain per unit length of 4.1 dB/cm for a 1 cm length strip-loaded waveguide with loss of 0.9 dB/cm [54]. It was mainly because of the high erbium concentration (5.3 x 10^{20} cm^{-3}) in this glass matrix that contribute to the high gain achieved. A phosphate glass network is very flexible and open, with a very disordered linkage of the tetrahedron. This helps phosphate glass to integrate well with Er^{3+} ions [66]. The suitable environment for Er^{3+} ions in phosphate glass contributed to low clustering and low up-conversion effect. Nevertheless, phosphate-based glass has low chemical stability which can lead to degradation when exposed to air over time [67]. Furthermore, due to their lower chemical durability, techniques and procedures that involve a chemical reaction process during fabrication are deemed to be highly critical especially during wet etching in the standard photolithography process. As an example, phosphate glass reacts easily enough with molten salt baths and etchant when a diffusion mask needs to be removed, and this can lead to surface damage [3,68].

Bismuthate glass is also another potentially impressive glass host for erbium. It has a high refractive index (1.94) and broad bandwidth (40-50 μm). Ono *et al.* fabricated a ridge waveguide using rf magnetron sputtering with a length of 6 cm that produced 1.1 dB/cm gain and 0.13 dB/cm loss [55,56]. It also had a lifetime of 2 ms.

Apart from glass, ceramic such as aluminium oxide (Al_2O_3) could also be an attractive host. It had been employed extensively for both active and passive devices at 1550 nm. Al_2O_3 has a wide transmittance range which ranges from 200 nm to 7 μm, and its broad bandwidth (~80 nm) makes it suitable for integrated amplifiers that are capable of producing gain across a wide waveguide range [69]. Bradley *et al.* [57] reported that Al_2O_3-based EDWA (deposited by a sputtering method) with a length of 5.4 cm, high erbium concentration (1.17 x 10 ions/cm^{-3}) and moderate refractive index (1.65) produced gain as high as 2 dB/cm and loss as low as 0.3 dB/cm. The high fluorescence lifetime which was 7.6 ms resulted in a significant population inversion that led to the decay predominantly due to radiative emission [70]. Even though it has remarkable potential for EDWAs, this material is still currently incompatible with the economical low loss fibre pigtailing methods which are generally used with an SOS planar lightwave circuit (PLC) [71].

Another ceramic material that presents a good characteristic as a host for erbium is Y_2O_3. In recent years, it has received much attention due to its suitability as a host for laser and waveguide applications. It has magnificent thermal conductivity, low phonon energy (591 cm^{-1}), a large energy bandgap, high refractive index (1.9) and wide transparency range [69,72,73]. Furthermore, both trivalent erbium and yttrium have almost the same ionic radius and also Er_2O_3, and Y_2O_3 have a cubic crystal structure with an almost similar lattice constant making Er^{3+} ions easily doped into Y_2O_3 as the lattice mismatch between the two materials is very low [69]. Hoekstra *et al.* [59] constructed a ridge waveguide using the sputtering technique with a high erbium concentration reaching 2.3 x 10^{20} cm^{-3} and yielded gain of 2.56 dB/cm and loss of 1.5 dB/cm for a 3.9 cm length ridge waveguide. The lifetime obtained from this waveguide was approximately 5 ms. Yet, this material has a distinct disadvantage in that it has the tendency to crystallise due to its low crystallisation temperature that leads to high waveguide loss especially in the visible range [69,74]. The surface of the waveguide also becomes rougher at higher temperatures which is associated with larger grain size [69].

On the other hand, Er-doped Ta_2O_5 produced waveguide material that has the highest refractive index (2.1) [60,61] compared to the other host materials in Table 2.2 which makes it suitable for the production of ultra-compact and cost-effective integrated optical circuits. Ta_2O_5 also allows nearly absorption free transmission from 400 nm to 10 μm due to its large energy band gap of 4.2 eV [69]. In addition, they also have other interesting properties such as low phonon energy (100-450 cm^{-1}) [75] which may contribute to the high optical gain (2.25 dB/cm) with 0.65 dB/cm loss for a rib waveguide length of 2.3 cm as reported by Subramanian *et al.* [60]. This material is fabricated using rf magnetron sputtering and has a lifetime, FWHM and erbium concentration of 2.3 ms, 50 nm and 2.7 x 10^{20} cm^{-1}, respectively.

There are also many reports on the use of polymers as a host for erbium-doped waveguide amplifier. They have the broad bandwidth (72 nm) [63] and can be deposited at a relatively low temperature (200 °C) [10] which make them a likely host material for integrated optical devices. Le Quang *et al.* fabricated a rib waveguide with a length of 1.6 cm and a lifetime of 3.4 ms. This material was deposited on the substrate using the spin-coating technique. The produced gain (0.9 dB/cm) was lower than its loss (1.31 dB/cm) [62]. This was probably because the vibrational modes of the CH, OH and NH groups that are typically present in polymers quench strongly erbium emission [76]. Erbium concentration reported in this host material was 3.6 x

10^{19} cm^{-3}, the lowest among most non-silicate based reported hosts. One apparent problem was the difficulty of dissolving Er^{3+} ions because rare earth salts which were commonly used in processing and synthesis polymer waveguide have poor solubility in a polymer matrix [10]. On the other hand, the refractive index for this material was only 1.53 which is comparable to silicate-based materials. Another drawback of the polymer was their poor stability against aging, temperature and moisture [77].

Additionally, a few reports have mentioned erbium-doped zirconia (ZrO$_2$) for the purpose of EDWAs [64]. However, it has a broad bandwidth which is 54 nm and high refractive index (2.08). This material has an erbium concentration and a lifetime of 0.88 x 10^{20} cm^{-3} and 1.77 ms, respectively. This 6.5 cm long ridge waveguide that is fabricated using a sputtering technique is only able to produce gain at only 0.45 dB/cm with loss of 0.45 dB/cm. Another host material that has not really extensively been investigated is zinc silicate germinate (ZSG). It is probably due to their low gain (0.4 dB/cm) with loss of 0.32 dB/cm for a 4.7 cm length channel waveguide [65]. This material was fabricated using the sputtering method and has a refractive index, erbium concentration, FWHM and lifetime of 1.75, 0.8 x 10^{20} cm^{-3}, ~ 25 nm and 2.8 ms, respectively.

2.3 Methods used to fabricate EDWAs

In the past few years, a number of methods of fabrication have been investigated for rare earth doped glass waveguides. An EDWA can be fabricated by various methods and each has its own advantages and disadvantages. Method of fabrication is very important because it will affect the performance of the obtained EDWA. Among the fabrication methods for an EDWA that have been reported are radio frequency (RF) sputtering [65], sol-gel deposition [78], plasma enhanced chemical vapour deposition (PECVD) [44], rf magnetron sputtering [53], flame hydrolysis deposition (FHD) [79], ion exchange [80], femtosecond laser writing [81], ion implantation [82], focused proton beam writing [83], pulsed laser deposition (PLD) [84] and ultrafast laser plasma doping (ULPD) [24,85,86]. The next section will briefly describe some of the commonly used fabrication methods.

2.3.1 Sol-gel deposition

Sol-gel is a synthesis technique that involves a system that changes from a colloidal liquid form known as sol into a solid gel phase. The precursors required in this technique are usually metal compounds in an alcoholic solution (metal alkoxides), and the formation of sols takes place through the reaction of hydrolysis and

condensation. Sol is coated on a substrate in order to produce the thin film via a spin, spray or dip coating process. When sol is coated onto a surface, evaporation of solvent will occur, and this leads to the formation of an amorphous structure called gel. This comes into form by cross-linking of metal-organic groups, and this organic species can be annihilated by annealing the layer at a temperature between 300-500 ºC. The redundant solvent also decomposes when the layer is heated. This step is often referred to as the drying process [87]. The schematic sol-gel process is presented in Figure 2.8.
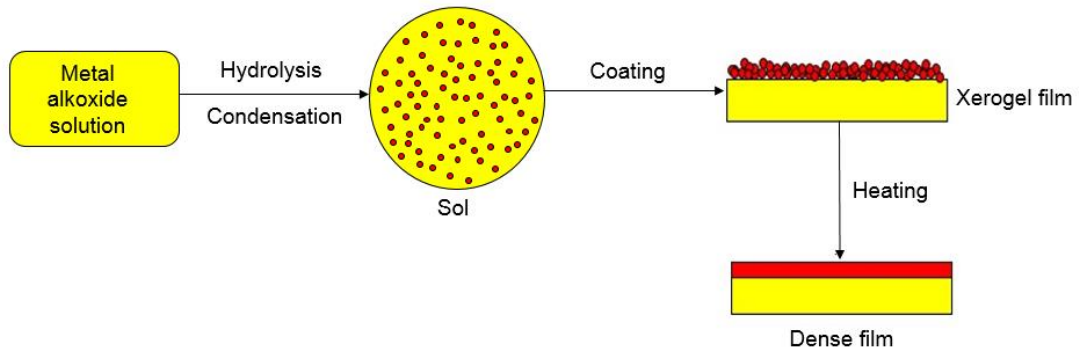
Figure 2.8: Schematic diagram of the sol-gel process (adapted from [88]).

Sol-gel deposition is one of the many techniques that is used in EDWA fabrication. The technique is quite common as it is a simple process due to low fabrication temperature, low-cost processing and has the ability to precisely control the stoichiometry at the molecular scale [89,90]. Nevertheless, the transformation from wet gel to dried gel reduces the film volume which can often lead to formations of cracks. The issue can be more critical in the thicker layer as the thickness is limited by the shrinkage of the gel thus giving way to mechanical stress to film. Depending on the chemical composition, when a certain critical thickness is achieved, the layer will start to crack, and when exceeding its capacity, the layer thickness can even fully delaminate from the substrate [91]. A few works which are related to the cracking problem from sol-gel deposition have been reported. An example is a report by Sloof *et al.* [78] who deposited Er-doped silica on a silicon substrate. The formed thin film cracked due to shrinkage during annealing as in Figure 2.9. Similar issues occurred for Zanetti *et al.* [90] where some of the samples developed cracks for thicker films. The cracking issue diminishes the optical quality of the fabricated thin films rendering the process to be unsuitable for the construction of quality optical waveguide. However, there are still a few reports of EDWAs with Er and Yb co-doped that is fabricated using this method and capable of yielding gain as high as 1.35 dB/cm [92], 1.15 dB/cm [93] and 1 dB/cm [94].
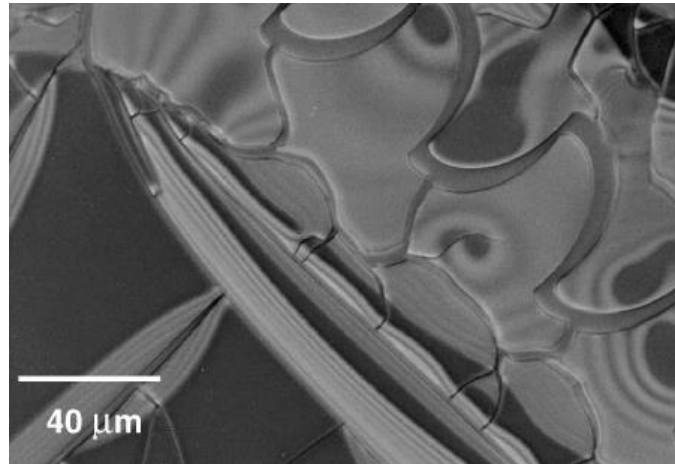
Figure 2.9: Shrinkage lead to the cracking problem [78].

2.3.2 Radio frequency (rf) sputtering

RF sputtering is a technique that is suitable for fabrication of a thin film for optical planar waveguides. It is a physical vapour deposition method that involves removing the material from a target (which acts as a source) and depositing it onto a substrate. The atoms are ejected from a target material by the energetic ion bombardment occurring from glow discharge plasma. The basic sputtering system consists of the cathode (target), an anode (substrate), power supply, vacuum chamber and gas supply which is represented in Figure 2.10. When the appropriate pressure is applied in the chamber and maintained, a glow discharge plasma can ignite when a high voltage is applied to the cathode. The plasma which normally consists of a positive argon ion is then bombarded onto the target. The atoms from the target are subsequently chipped out and ejected from the surface by the momentum transfer between incident ions and target atoms due to collisions. They then hit the substrate and adhere to its surface [95].

There are various sputtering deposition instruments available such as direct current (DC) and radio frequency (rf) sputtering. For conducting target material, it can be sputtered easily using a dc sputtering system, but for the non-conducting target material, it can only be sputtered when rf voltage is applied to the target. This is because, over time, positive charges will build up on the surface of the non-conducting target material and it will completely repel the incoming ion bombardment which can prevent a further deposition process. When alternating electrical potential which is rf voltage, supplied to the target, the target material surface can "clean" up the positive charge build-up for each cycle. At half cycle, the electron will reach the

target material to prevent charge build-up. At the other half cycle, at rf of 13.56 MHz (internationally used), ions with sufficient energy are then accelerated to the target surface causing sputtering [95].
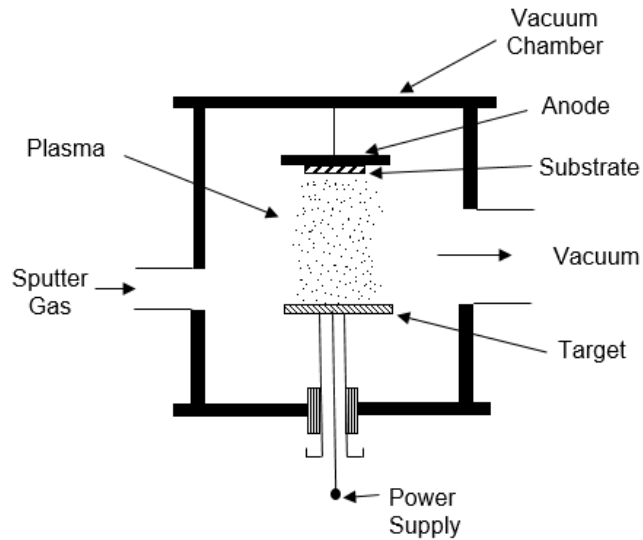
Figure 2.10: Schematic diagram of rf sputtering system (adapted from [96]).

For planar optical waveguide application, rf sputtering is preferred as most target materials are from a dielectric material. Among the materials that have reportedly been used for EDWA application and successfully fabricated using rf sputtering are Er-doped SiO_2-TiO_2 [97], Er-doped SiO_2-P_2O_5-HfO_2-Al_2O_3-Na_2O [98] and Er-doped zinc silicate germanate [65]. Still, an optical layer created using this technique reportedly had a porous and rough layer that only exacerbated the scattering loss [97,99].

2.3.3 Flame hydrolysis deposition (FHD)

Flame hydrolysis deposition (FHD) is one of the well-known techniques that can be used to produce an EDWA [93]. It was initially developed for optical waveguide and able to fabricate thick layers at high deposition rates (1 µm/min) [79,100]. The schematic diagram of FHD is displayed in Figure 2.11. The process involves precursor-like silicon tetrachloride $SiCl_4$ that is burned in a high temperature (1300-1500 °C) oxygen-hydrogen flame [79], resulting in fine silica particles that are usually called "soot" and hydrogen chloride. Soot is then deposited onto the substrate, and gaseous hydrogen chloride is extracted away. Later, the obtained porous soot layer is placed in a furnace and heated up to 1350 °C for consolidation. This layer is suitable for lower cladding. Further vapours introduced to the flame in addition to $SiCl_4$ cause soot to integrate with other precursors such as $POCl_3$, $GeCl_4$ and BCl_3. Erbium ions

is then incorporated onto soot with feed the torch with an aerosol of $ErCl_3$ solution (hydrous). There is an ultrasonic machine used in order to atomise the hydrous $ErCl_3$. The aerosol droplet is then delivered to the torch with Argon gas. The mixture undergoes another round of the consolidation process to produce a dense layer for the core by heating it up to 1350 ⁰C. The density of erbium in the film depends on the ultrasonic resonator intensity, erbium concentration in the solution and the flow rate of the Argon gas [101].
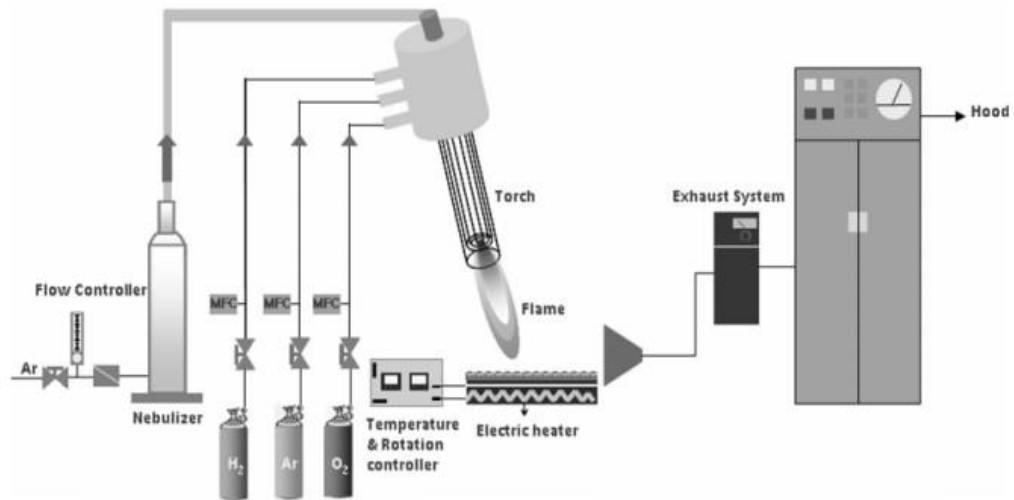
Figure 2.11: Schematic of flame hydrolysis deposition system [101].

FHD offers a reliable, economical, highly flexible and fast technique to produce a planar optical layer. However, the typical high temperature for the consolidation process needed in this method causes the doping density of erbium in the core layer to be limited to 0.45 wt. % ($\sim$4 x 10^{19} cm^{-3}) [10,43]. This is due to the natural characteristics of erbium that is sensitive and predisposed to clustering when exposed to high temperatures [102–104]. In view of the clustering issue, the length of the optical waveguide that had previously been reported was as high as 47.7 cm [43] which will not fulfil the aim of a miniature telecommunication device. Additionally, another study reported that the sintering temperature applied is high enough to make the dopant volatilise at the surface. This causes the degradation of dopant concentration and inhomogeneous composition throughout the film [105].

2.3.4 Plasma enhanced chemical vapour deposition (PECVD)

PECVD is a technique for depositing thin films from vapour (gas state) to solid state on a substrate. This technique is also reported as a choice for fabricating EDWAs. PECVD uses electrical energy to establish a glow discharge (plasma) where energy is transferred to the gas mixture. If electrical power with a sufficiently high voltage is

supplied to gas at a low pressure (<1.3 kPa), it will cause dissociation of gas reagents due to electron collision with a gas phase precursor and induce plasma generation consisting of ions, electrons, and electronically excited species [106]. It will then experience assorted chemical reactions near or at the surface of the substrate and later adhere to the substrate. The temperature of the electrons is very high, as high as 20,000 K or more, while, for temperatures, gas is maintained in a range of 25-350 ºC depending on the applied pressure. The substrate only requires moderate heating of less than 600 °C [107].

Figure 2.12 shows a typical PECVD setup for planar waveguide fabrication. The substrate is normally positioned on aluminium platen and being grounded. This setup forms a bottom electrode which is heated by resistance heaters placed in the bottom platen. On the other hand, another aluminium platen is located opposite the bottom platen and acts as a top electrode. The reagent gases with the inert carrier gas are supplied into the chamber at the region between the two electrodes. Silane (SiH_4) is commonly used as gas precursor [44]. For erbium doping, the dopants are often supplied by using a liquid source containing Er-chelate dissolved in an organic solution. Liquid Er-chelate is evaporated inside a stainless steel vessel that is heated to a constant temperature. Connecting tubes between plasma chambers with evaporator vessels are heated to avoid condensation. Argon and nitrous oxide (N_2O) gas are used as a carrier gas and oxidising agent respectively for erbium [108]. Introduction of the radio frequency signal to the top electrode subsequently initiates the plasma.
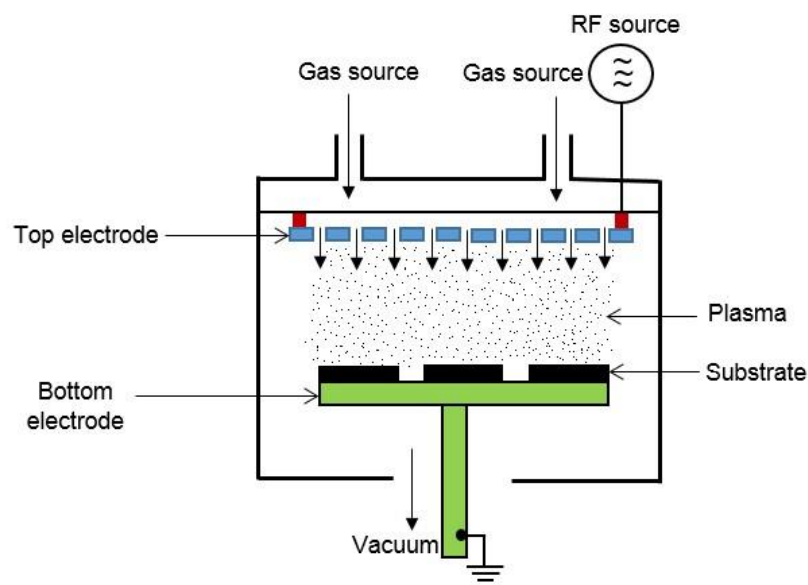
Figure 2.12: Schematic diagram of basic PECVD system (adapted from [109]).

There have been reports made on the fabrication of an EDWA by using PECVD [44,110–112] but the low vapour pressure of the erbium compound makes it difficult for it to be doped at high concentrations. This causes the internal gain achieved by this method is limited to 0.35 dB/cm [92,113]. Besides that, the use of silane is hazardous and requires strict safety precautions [114].

2.3.5 Ion implantation

Ion implantation is a standard process in the semiconductor industry and is now becoming commonly used in PIC fabrication methods as well. It is a process involving acceleration of energetic charged ions (keV to a few MeV) penetrating into 10-1000 nm below the substrate surface [115,116]. The presence of these ions can modify the chemical and/ or physical properties of the near-surface area on the solid substrate by transferring their momentum and energy to the nucleus of the atom and electron of the substrate.

Typically, ion implantation equipment consists of an ion source, analyser magnet, accelerator and sample chamber as shown in Figure 2.13. The ion source contains positively charged ions which are produced in a plasma discharge. They are extracted under a vacuum through high voltage pre-acceleration heading to an analyser magnet. This magnet facilitates the selection of the desired chemical species, charge state and isotope to achieve highly pure beams of ions. A beam of ions that passes through the narrow aperture can be effectively altered by adjusting the magnetic field precisely. This pure beam then accelerates and focuses on the substrate by using a series of electromagnetic lenses. By control, the beam current and accelerating voltage, concentration and depth of implanted ions can be obtained accurately [117].
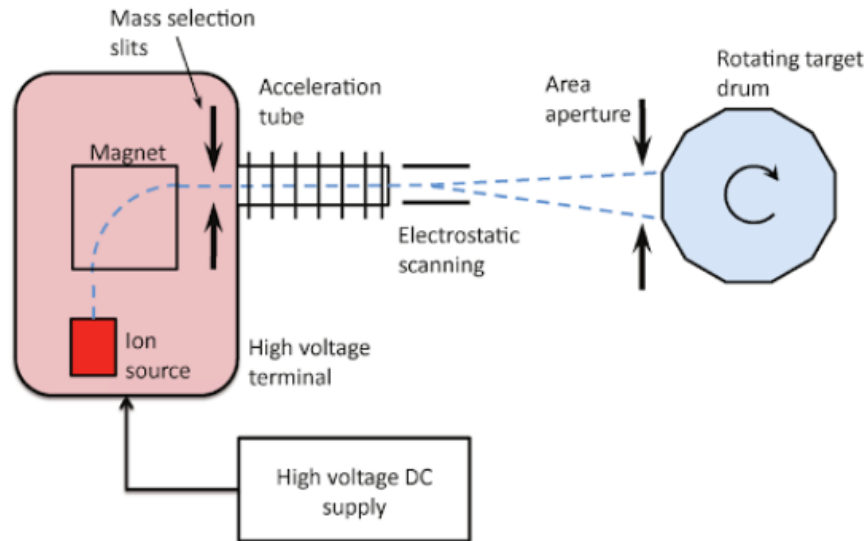
Figure 2.13: A schematic of the ion implantation system [117].

Since it is not like other doping methods such as diffusion, ion implantation grants independent control over the dopant concentration and implanted layer depth. The selection of dopant is also not limited due to the conventional solubility rule, and this allows any material to be used for implants into any substrate. Since this technique does not require high temperatures, [118], material size can be maintained because it does not involve thermal alterations. Because of this, surface degradation can be minimised. Moreover, because it is not a coating process, the substrate dimension can also be maintained. Minimum or no contamination on the substrate and also the material used for the implant can be achieved due to the highly pure beam originating from the analysing magnet. However, this technique has drawbacks in that only a maximum of one μm from the top surface substrate can be modified. Furthermore, usually, implantation of ions results in damage [119] at the end of the ion track inside the substrate, and this condition causes volume expansion which may result in decreased physical density and also the refractive index. This causes the confinement to be weak and leads to a tunnelling effect that can make the energy of the propagating beam leak.

2.4 Ultrafast laser plasma doping (ULPD)

ULPD is a novel doping technique that can be employed to dope optically active ion into the substrate. This technique is a new approach for producing a thin film for optical applications. The high-intensity laser pulse is employed to ionise, melt and evaporate the surface of the target material. This causes the explosive removal of

material which can also be called ablation and induce the plasma formation as shown in Figure 2.14.

Figure 2.14: Plasma plume generated by laser ablation of target material [120].

The plasma then expands in a perpendicular direction with the rate of a few km/s [24] to the heated substrate and strikes the surface. The interfacial reaction between the target plasma and substrate surface with the aid of thermal diffusion forms a modified layer consisting of a combination of the target material and the surface substrate. The thickness (nm to µm) and quality of the modified layer varies depending on the process parameter and type of target material and substrate used. The whole process occurring in ULPD is not yet fully understood and well documented. Although the mechanism in ULPD mimics the PLD technique, but some of the process involved has its own novelty and speciality that cannot be found in a common PLD technique.

2.4.1 Interaction between laser and target material

The choice of laser pulse duration is the chief parameter influencing the laser ablation process. For ULPD, femtosecond laser (fs-laser) is used to ablate the target material. The fundamental of this process is light-matter interaction and involves some complicated processes. When the fs-laser bombards the target material, the photon energy will be absorbed by atoms in the target material and later transfer the energy to the electron. The absorbed energy promotes an electron to be excited from its ground state to its excited state. The excitation mechanism is different for a metal, semiconductor and insulator. In metal, conduction and valence band are overlap which indicates that there is no threshold for the bridging of an electron from filled to

unoccupied states. In contrast, for a semiconductor, it has a small band gap, and if the photon energy is higher than the energy band gap, the electron can be promoted from the valence band to the conduction band. In material where the photon energy is lower than the energy band gap like an insulator, the energy transfer is fairly complex [121,122]. Generally, for an fs-laser, it has a high intensity which is in the range of 10^{12}-10^{19} W/cm^2 [123] and this leads to strong non-linear absorption. For an insulator, an electron in the valence band is excited to the conduction band by non-linear photoionisation, specifically by multi-photon ionisation and/or tunnelling ionisation. This process depends on laser intensity and frequency. The threshold intensity for the optical breakdown for this kind of ionisation varies significantly with the band gap of the target material because of a huge variation of absorption probability with band gap. However, linear absorption also occurs which is called avalanche ionisation [124]. The threshold intensity for the optical breakdown of this ionisation only involves small variation with the band gap.

2.4.1.1 Non-linear photoionisation

When a high intensity of a femtosecond laser interacts with an insulator, the bound electron will absorb a number of photons simultaneously (multi-photon energy), and they can be excited from the valence band to the conduction band as shown in Figure 2.15 (a). This process is called multi-photon ionisation or multi-photon absorption and is a multi-order and non-linear optical process. This process happens when the laser used is at low intensity (10^{12}-10^{16} W/cm^2) and high frequency.
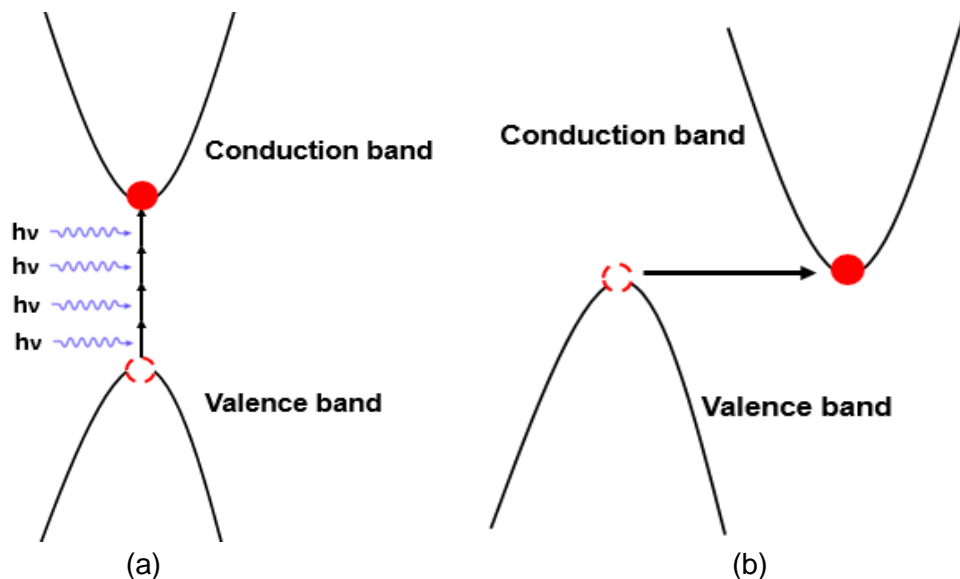
Figure 2.15: The non-linear photoionisation process that can be classified into two processes, i.e. (a) multi-photon ionisation and (b) tunnelling ionisation (adapted from [125]).

Whilst, tunnelling ionisation occurs when the laser is at high intensity (10^{17}-10^{19} W/cm^2) and low frequency. It happens when the strong field distorts the band structure and causes the potential barrier between the valence band and the conduction band to be reduced. This, in turn, enables the direct band to band transition of an electron from the valence to the conduction band through quantum tunnelling as shown in Figure 2.15 (b) [125]. The probability of the type of non-linear photoionisation will occur is described by the Keldysh parameter [126]:

$$\gamma = \frac{\omega}{e}\sqrt{\frac{m_e c n \varepsilon_0 E_g}{I}} \tag{2.2}$$

where ω is a laser frequency, e is an electron charge, m_e is an effective electron mass, c is the speed of light, ε_0 is the permittivity of free space, E_g is the energy band gap, and I is laser intensity. Tunnelling ionisation becomes dominant if γ is less than 1.5 and, if γ is more than 1.5, multi-photon ionisation will become superior. A combination of multi-photon and tunnelling ionisation mechanisms occurs when $\gamma \sim$ 1.5 [126].

2.4.1.2 Avalanche photoionisation

As shown in Figure 2.16, the electrons in the conduction band may also absorb photons by free carrier absorption. After the absorption of several photons repeatedly linearly, electron energy in the conduction band increases high so that it can overcome the band gap energy. This causes the electron to ionise bound electrons in the valence bands and produce two excited electrons in the minimum conduction band. These two electrons then experience free carrier absorption and impact ionisation. This process will occur repeatedly and continuously if the laser field is strong enough. In order to initiate this process, the existing electrons in conduction should be sufficient, and this seed electron is supplied either via multiphoton and/or tunnelling ionisation [125].

However, according to the investigation done by Kaiser *et al.*, they discovered that if the pulse duration is below 100 fs, avalanche ionisation is negligible and photoionisation is dominant. When a pulse duration of ~200 fs is used, impact ionisation becomes very important due to the presence of the strong electric field [127].
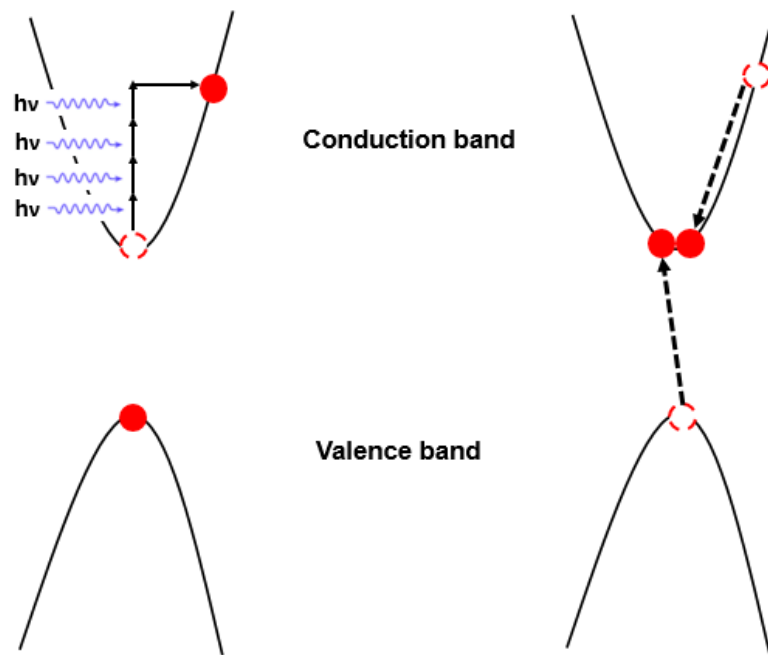
Figure 2.16: Schematic diagram showing the process of free carrier absorption and how it is continued by impact ionisation (adapted from [125]).

2.4.2 Ablation mechanism

There are two ablation mechanisms for the fs-laser pulse, i.e. a non-thermal mechanism (Coulomb explosion) and a thermal mechanism (phase explosion). For Coulomb explosion, which is a gentle type of ablation, this mechanism is normally dominant when the laser used is at low intensity near the ablation threshold. Emission of excited electrons from the target surface causes the production of the electric field of charge separation between highly ionised atoms with ejected electrons on the target surface. This phenomenon is called space-charge effect. The charge separation occurs when energy absorbed by the electron overrides Fermi energy (sum of electron binding energy for dielectrics with work function). This condition causes the surface region to have a high level of charging. If the surface region is not neutralised immediately compared to the time taken for the ion to interact with neighbouring ions via electrostatic repulsion, the charge formed on the dielectric surface of the target material will induce the production of emission ions by Coulomb's explosion. When the electron energy is higher than binding energy ions in the lattice, the resulting electric field will pull ions escape from the target results in the removal of several nanometers within the skin depth [128]. Apart from that, when a higher laser intensity is used to irradiate the target material, it can result in rapid overheating at the target material, and the temperature is much higher than boiling temperature (strong ablation). This is called phase explosion or explosive boiling [129]. Homogeneous nucleation of the material takes place at a remarkably high rate when

the temperature achieved is near to the critical temperature. This subsequently creates explosive boiling of the material which turns into a combination of liquid droplets and vapour [130].

2.4.3 Plasma formation and expansion

Laser pulse ionises the target material vapour and generates hot laser plasma namely plume that is located at or near the surface of the target material. The plume is expanding, and during the expansion process, plasma plumes cool down and transfer their energy in the form of heat into the liquid solution. Then, the laser-induced plasma interacts with a neighbouring liquid layer at the plasma-liquid interface by increasing the temperature higher than the boiling temperature of the liquid. As a consequence, plasma of liquid is created under a condition of standard pressure, and this is called plasma-induced plasma [131]. This results in an explosive ejection that contains metastable and energetic species (ions, atoms, electrons, molecules, particulates and molten droplets) with 3D adiabatic expansion directly in the forward direction to the substrate [132].

2.4.4 Doped layer formation

The energetic metastable species that travel with very high velocity penetrate into the surface substrate layer assisted by thermal diffusion [24]. The substrate is heated during the ablation process, and this is important because it can mediate the process by providing the activation energy required. Besides this, heating the substrate helps network modification of the substrate in a controlled manner. The species from the target material will first modify the molecular network of the substrate surface until a homogeneous layer mixture of species from the target material and substrate are formed [85].

2.5 Conclusion

In summary, an EDWA that inherits EDFA properties, but with a compact version, has a similar operation principle. The amplification of an EDWA is based on the stimulated emission of photon and Er^{3+} ion transition. Generally, a waveguide amplifier should produce a high output gain with the shortest possible waveguide length for practical applications, and this can be achieved by dope erbium at a high concentration. However, Er^{3+} ions tend to cluster at a high concentration. The clustering effect varies depending on the host material used. An erbium-doped phosphate glass channel waveguide exhibits the highest gain (4.1 dB/cm) compared to the other host materials due to the high solubility of Er^{3+} ions. Apart from that, tellurite glass, Zirconia and

Ta_2O_5 exhibit a high refractive index and this property is important for the production of on-chip integrated optical circuits. Moreover, a method to fabricate EDWAs also plays a significant role in determining high gain. Each method has its own advantages and disadvantages that can affect the performance of fabricated EDWAs. Due to various issues, a novel doping technique called ULPD is introduced and can offer a potential solution for erbium doping limitations and capable of modifying the optical layer refractive index.

CHAPTER 3
INSTRUMENTATION AND METHODOLOGY

This chapter explains the theory and principle pertaining to instruments used and experimental procedure involved in this thesis. The chapter begins with the details of a sample fabrication method that can be divided into two sections, which are the target glass preparation and discussions on the major instrumental technique used to fabricate the sample, which is femtosecond pulse laser deposition (fs-PLD). Subsequently, the explanation focuses on the instruments used for sample characterisation and analysis. The characterisation of the materials begins with prism coupler and photoluminescence spectroscopy, then x-ray diffraction (XRD) and x-ray photoelectron spectroscopy (XPS) are discussed. Following a brief description of Raman spectroscopy measurement, scanning electron microscope (SEM) and transmission electron microscope (TEM) and related studies are presented. An overview of TEM encompassing the relevant operation mode and working principle is presented together with a sample preparation. Next, this chapter continues with energy dispersive X-ray spectroscopy (EDX). The final part of this chapter is the discussion of the waveguide simulation work using COMSOL Multiphysics modelling software.

3.1 Sample fabrication

There are two major procedures for sample fabrication in this work. Starting with the target material preparation, referred to as the glass fabrication, which is then used as the "target" in the ULPD process using a femtosecond pulsed laser deposition (fs-PLD) system.

3.1.1 Target material preparation (glass fabrication)

Various techniques of glass preparation for optoelectronic applications are well known and widely documented, such as the melt-quenching technique [19], chemical vapour deposition (CVD) [133] and sol-gel [134] methods. Among the three, the melt-quenching technique is the most convenient and conventional. It is flexible enough for the maker to prepare a large number of glass compositions of tellurite, borate, silicate and phosphate oxide or non-oxide glass systems. Furthermore, melt-quenching allows for easy doping and co-doping of different types of active ions such as rare earth or transition metals. A disadvantage of the method, however, is that the fabricated glass lacks purity compared to glasses prepared with other techniques. Nevertheless, this issue can be mitigated by using a crucible made of noble metals

such as gold and platinum [133]. For the purpose of the study here, the bulk (target) glass was fabricated using the melt-quenching technique with a noble metal crucible, for the reasons given.

A schematic process of glass preparation is illustrated in Figure 3.1. In this study, the first step of the procedure was to weigh all the chemicals of each compound in the batch (15 g total weight) using a high-resolution balance ($\pm$0.0001 g, Oertling, NA 114). All the powder has 99.9995% purity and are from Alfa Aesar. Secondly, the precise weight of oxide mixtures was mixed thoroughly and transferred to a mortar for grinding for several minutes to obtain a uniform and fine powder mixture. Subsequently, the mixture was transferred to a gold crucible and placed inside a melting furnace at a temperature of 850 $^\circ$C for three hours in the presence of dry oxygen with a flow rate of around 2 ml/min during the melting process. The presence of dry oxygen was to purge the residual moisture in the furnace and to make sure there was no deficiency of oxygen in the glass. Oxygen deficiency can affect the overall stoichiometry of the obtained glass [135]. At the same time, a stainless steel mould was preheated inside an annealing furnace with a temperature close to the T_g of the tellurite glass for more than two hours. During the melting process, the gold crucible with the oxide melt in it was shaken for 5 minutes every hour to remove any gas bubbles and to obtain a homogenous mixture. After three hours, the gold crucible was taken out of the melting furnace, and the melt was immediately poured into the heated stainless steel mold. Next, this mold was reheated in an annealing furnace at a temperature of 300 $^\circ$C for 3 hours to eliminate internal stress and to further improve the fracture strength. The temperature of the annealing furnace was then slowly cooled down to room temperature at a rate of 0.5 $^\circ$C/min.

Weighting of total 15g oxide powder (TeO_2+ZnO_2+ Na_2O+Er_2O_3)	→	Glass melting (850 $^\circ$C, 3 hours)	→	Casting, quenching and annealing (300 $^\circ$C, 3 hours)	→	Polishing
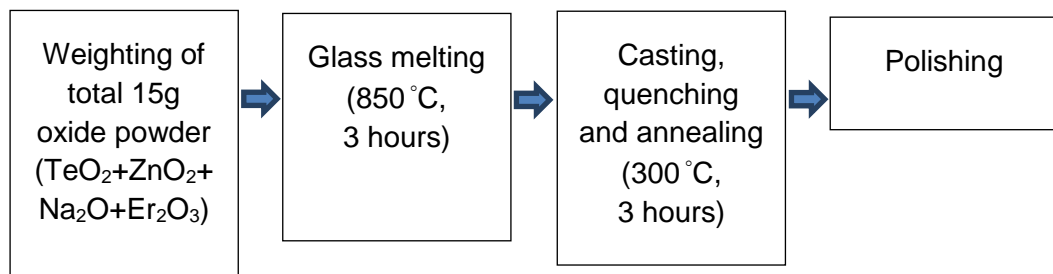
Figure 3.1: The schematic process of glass preparation.

It could be seen that the resulting glass was transparent and pinkish in colour as shown in Figure 3.2. Its dimensions in diameter and thickness were 2.3 cm and 0.5 cm respectively. The glass was polished using a polishing machine (Buehler, Motopol

2000) with various grades of silicon carbide paper (Buehler Grit P1200, P2400, P4000) in order to obtain a smooth and flat surface and also to make it fit inside the target holder that been used in fs-PLD (Figure 3.3). The smooth and flat surface of the target is really important in order to ensure that the plasma plume is directed upward from the surface of the substrate.

Figure 3.2: Example of a target glass prepared for this research which is transparent and pinkish in colour.

Figure 3.3: Target holder used during ULPD process.

Erbium-doped TZN glass targets with a molar composition of $79.5TeO_2$: $10ZnO:10Na_2O:0.5Er_2O_3$ were fabricated using oxide compounds and rare earth oxide of TeO_2, ZnO, Na_2O, and Er_2O_3 with an initial purity of higher than 99.99%.

3.1.2 Femtosecond pulsed laser deposition (fs-PLD)

The ULPD thin film samples were fabricated by customising a femtosecond pulsed laser deposition (fs-PLD) system. The simplified schematic diagram for the experimental setup for a typical fs-PLD system is shown in Figure 3.4. This system consists of a femtosecond (fs) laser, various optical components such as mirrors, polariser, beam expander and focusing lens to focus the laser beam onto the target glass, an ultra-high vacuum (UHV) chamber and associated system (vacuum pump, valves, pressure gauges and chiller), substrate and target that are positioned opposite and relatively close to each other and a heater to heat the substrate.
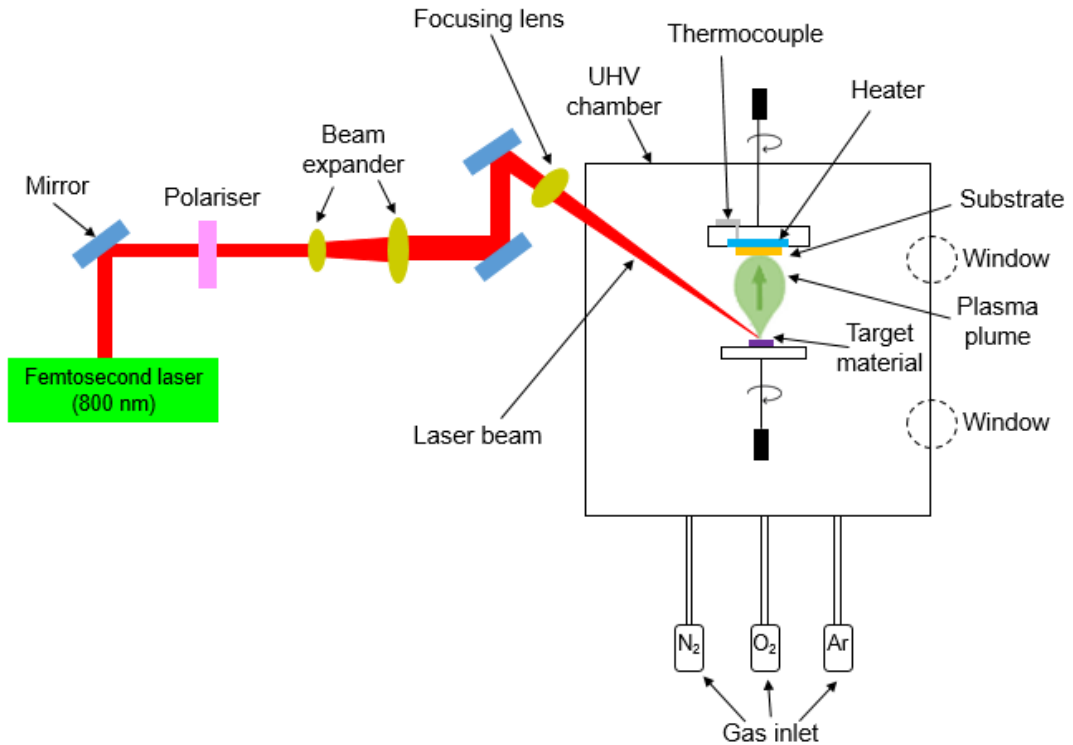
Figure 3.4: Experimental setup for fs-PLD.

A commercial Coherent Ti: Sapphire LIBRA laser with pulse duration 100 fs and wavelength centred at 800 nm was used in this work. Laser energies were precisely controlled by adjusting the polariser and the laser energy was measured using a Coherent LabMax-Top laser power and energy meter. The fs-laser beam was focused on to the target glass surface through a transparent window of the vacuum chamber at an incident angle of 60° (Figure 3.4). The target's surface needed to be polished before being placed into the target holder in order to obtain a flat surface that helps control the plasma plume direction which can affect the uniformity of the film produced. The target was then rotated and rasterised according to a set programme. This was to ensure that the laser could ablate the target surface uniformly. If the laser strikes to parts other than the target in the chamber, adjustment of target rastering needed to be done. Otherwise, the plasma plume obtained may contain elements other than the target material. The size and focus of the laser spot that hits the target needs to be controlled.

The substrate was then placed opposite the focused spot above the target at a distance of 70 mm. The substrate could be heated with a programmable heating element at a rate up to 50 °C per minute. The temperature was read using a digital output from a thermocouple located on top of the substrate, and a shutter was placed

about 1 cm beneath the substrate and between that and the target to control when and for how long the ablation process is active. The shutter would open only during the actual laser ablation process to avoid elements other than the target material getting onto the substrate.

After everything described above was set up and the necessary conditions were satisfied, the chamber lid was closed, and the chamber was evacuated to a vacuum until the pressure reached 9×10^{-5} Torr or lower. The substrate was then heated to a specific temperature at a ramp rate of 50 °C/min, and when the actual temperature neared the set temperature, background gas was released into the chamber at a set pressure. Just as all materials and setup were ready and stable, the target raster and rotator were turned on, and the laser shutter was opened for about 5 minutes so that the plasma plume could be checked. If the plasma plume was not very visible, it was due to poor focus. The focus had to be adjusted until the desired plasma plume was created. An uneven target surface could cause a non-stationary plasma plume. The plasma plume was also examined for flickering. If it flickered, it meant that the laser was misaligned with respect to the target and the laser was striking at places other than the target, i.e. target holder. On the other hand, by allowing laser ablate on the target, it could help to remove contamination from the target surface.

When satisfactory plume dynamics and target surface cleanliness were attained, the laser shutter was closed, followed by the target rotator and target raster. The chamber was then pumped down to the base pressure of 9×10^{-5} Torr or below to pump away any vapour phase contamination before refilling it to the operating pressure, and the ablation process timer was set accordingly soon after the operating pressure was reached. Meanwhile, the target raster, target rotation (40 rpm) and the substrate rotator (20 rpm) were set before the opening of the substrate and laser shutters.

During the experiment, checks were performed every 30 minutes. Those checks included gas pressure, fs-laser energy, substrate temperature and plume dynamics. The laser and substrate shutter was closed when the ablation process ended and, soon after that, the sample underwent rapid cooling to room temperature. When the temperature reached room temperature, the background gas flow was stopped, and the chamber vented using nitrogen gas to take the sample out.

3.2 Sample characterisation

The instruments involved in this study to investigate the optical, structural and physical properties of the ULPD processed samples are discussed below.

3.2.1 Prism coupler

Prism coupling is an efficient technique where a high index prism is used to couple a guided wave through a thin film by phase matching the incident wave and propagation mode. This technique can be used to measure refractive index and thickness of thin films [3]. This technique also enables us to ascertain if a thin film has the ability to guide light to any reasonable degree from the amount of attenuation experienced.

The method requires that a prism that has a higher refractive index than thin film to be measured was brought into contact with the sample as shown in Figure 3.5. The figure shows a minuscule air gap for clarity, and in practice, this can be typically between 100-200 nm between the thin film and prism depending on the surface roughness, and it is imperative to set a width gap between the prism and thin film as not to do so would affect the coupling efficiency [136]. This can be done by clamping the prism and the sample together with the help of a pneumatic pressure head. The function of the pressure head is to minimise the air gap between these two materials thus maximising coupling to a thin film.

The fundamentals of the measurement principle are as follows: a light beam is brought the incident to the face of the prism as shown in Figure 3.5 and refracted to the prism's base. At the base, the incident light is fully reflected. The incident angle of the light beam can be adjusted accordingly with a rotating table where prism, sample, photodetector, and coupling are mounted. At a particular angle where the phase matching condition is satisfied, the light is able to reach the thin film by tunnelling through the air gap between the prism base and thin film. The light then couples with the propagating modes in the thin film which causes the intensity to drop abruptly when reaching the photodetector as illustrated in Figure 3.6. A photodetector positioned on the output face of the prism can measure the relative intensity of the reflected beam at this position. Specific software was used to record and plot relative intensity versus angle of incident and then calculate the refractive index and thickness of thin film.
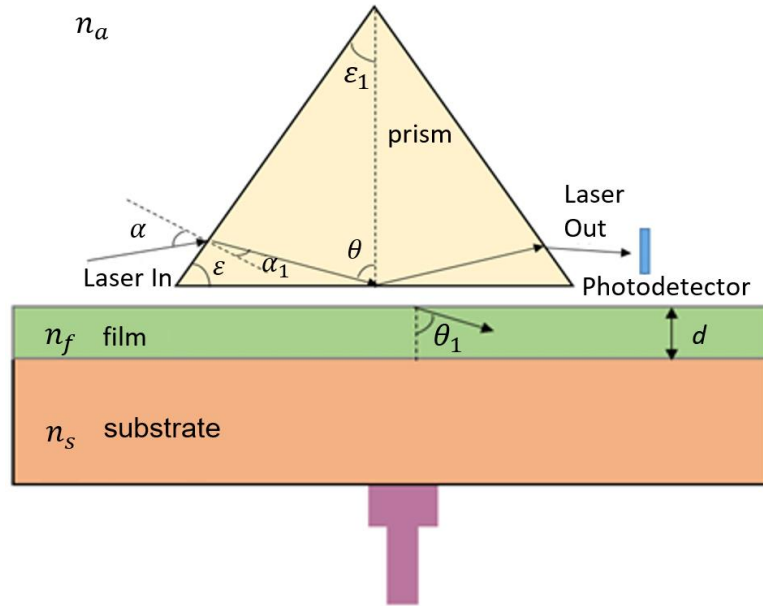
Figure 3.5: The schematic setup of the prism coupler [137].
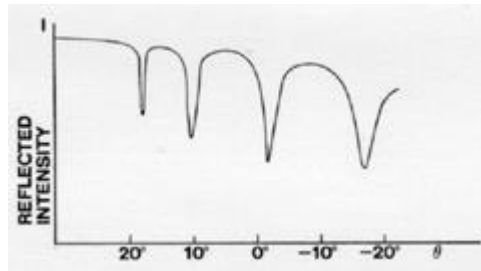
Figure 3.6: The typical spectrum from prism coupling experiment [138].

The phase matching condition happens when:

$$n_{prism} \sin \theta = n_{film} \sin \theta_1 \tag{3.1}$$

where n_{prism} and n_{film} are the refractive index for prism and film respectively. Equation (3.1) on the right is equal to effective index, $n_{eff,}$ of the propagation mode. Therefore,

$$n_{eff} = n_{prism} \sin \theta_1 \tag{3.2}$$

By applying Snell's law to the equation (3.2), it can be expanded as such [137]:

$$n_{eff} = n_{prism} \sin \left(\varepsilon + \sin^{-1} \left(\frac{\sin \alpha}{n_{prism}} \right) \right) \tag{3.3}$$

Where ε is the angle of the prism and α is a coupling angle. The value of the refractive index and the thin film thickness can further be calculated by using equation 3.4 [139,140]:

$$k_o d \left[n_{film}^2 - \left(n_{eff}^2 \right)_m \right]^{\frac{1}{2}} = p\pi + \gamma_{air} + \gamma_{substrate} + \Gamma_{prism} \tag{3.4}$$

where $k_o = \dfrac{2\pi}{\lambda}$, λ is a light wavelength, d is a film thickness, and p is a number of modes. For ζ_{air}, $\zeta_{substrate}$ and Γ_{prism}, they can be obtained by using the equation below. The formula to calculate γ_{air}, $\gamma_{substrate}$ and γ_{prism} are different for transverse electric (TE) and transverse magnetic (TM) modes. TE modes refer to the condition where the electric field is perpendicular to the direction of propagation (z-direction) while TM modes refer to when the magnetic field is perpendicular to the direction of propagation and parallel to the plane of the film [3].

$$\Gamma_{prism} = \sin(\gamma_{air}) \cos(\gamma_{prism}) e^{-2h\zeta_{x,air}} \tag{3.5}$$

$$\gamma_{air} = \begin{cases} \tan^{-1}\left(\dfrac{\zeta_{x,air}}{\zeta_{x,film}} \right) & \text{TE mode} \\[4mm] \tan^{-1}\left(\dfrac{\zeta_{x,air} n_f^2}{\zeta_{x,film} n_{air}^2} \right) & \text{TM mode} \end{cases} \tag{3.6}$$

$$\gamma_{substrate} = \begin{cases} \tan^{-1}\left(\dfrac{\zeta_{x,substrate}}{\zeta_{x,film}} \right) & \text{TE mode} \\[4mm] \tan^{-1}\left(\dfrac{\zeta_{x,substrate} n_f^2}{\zeta_{x,film} n_{substrate}^2} \right) & \text{TM mode} \end{cases} \tag{3.7}$$

$$\gamma_{prism} = \begin{cases} \tan^{-1}\left(\dfrac{\zeta_{x,air}}{\zeta_{x,prism}} \right) & \text{TE mode} \\[4mm] \tan^{-1}\left(\dfrac{\zeta_{x,air} n_{prism}^2}{\zeta_{x,prism} n_{air}^2} \right) & \text{TM mode} \end{cases} \tag{3.8}$$

$$\zeta_{x,air} = \sqrt{k_o^2 (n_{eff}^2)_p - k_o^2 n_{air}^2} \tag{3.9}$$

$$\zeta_{x,substrate} = \sqrt{k_o^2(n_{eff}^2)_p - k_o^2 n_{substrate}^2} \qquad (3.10)$$

$$\zeta_{x,air} = \sqrt{k_o^2(n_{eff}^2)_p - k_o^2 n_{air}^2} \qquad (3.11)$$

$$\zeta_{x,prism} = \sqrt{k_o^2(n_{eff}^2)_p - k_o^2 n_{prism}^2} \qquad (3.12)$$

The refractive index and thickness of the thin film can be determined by using the value of the known refractive index substrate, n_s, air refractive index, n_a and also an effective index, n_{eff}, obtained from the measurement. Nevertheless, a minimum of the two lowest modes is needed to propagate in the thin film so that a prominent, effective index can be obtained in order to calculate the refractive index and thickness of the thin film [137].

For this study, a Metricon 2010 prism coupler was used with a wavelength of 633 nm and prism with a refractive index of 1.9648. Pressure applied to the clamp sample and prism was 30-35 psi.

3.2.2 Photoluminescence (PL) spectroscopy

Photoluminescence is a spontaneous phenomenon related to the emission of light from a material after optical excitation. This simple and non-destructive technique is able to determine the emission properties of optically active ions dispersed in thin films.

Fundamentally, when the light of a sufficient energy impinges on a material, photons will be absorbed and electrons excited from ground states to higher energy levels. After some time, the excited electrons will return again to their ground states, and the absorbed energy is released via non-radiative and/or radiative transitions. Non-radiative transition creates phonons (heat or lattice vibration) while radiative transitions involve the emission of light (photons) with energy typically lower than excitation energy (Figure 3.7). The emission of energy in the form of light through radiative transitions like this is known as photoluminescence [141].
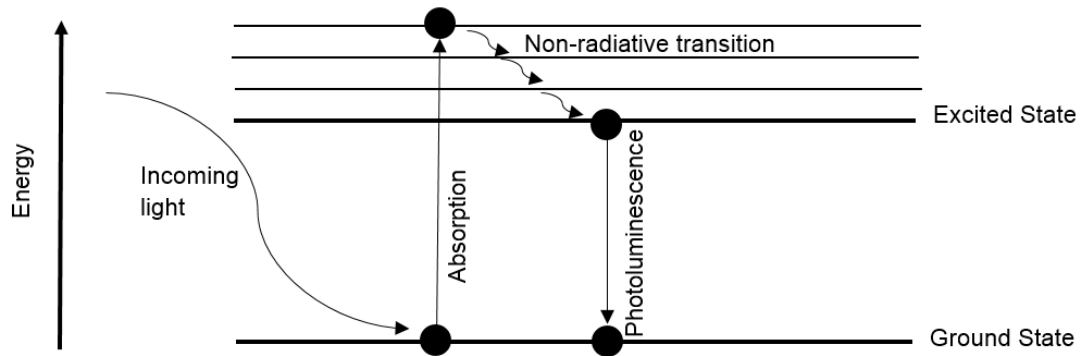
Figure 3.7: Schematic diagram for energy transition in a
photoluminescence process (adapted from [32]).

The block diagram of the PL spectroscopy setup is displayed in Figure 3.8. In this
work, an Edinburgh Instruments FLS920 spectrometer was used to obtain the
photoluminescence spectra. It comprises a light source, excitation and emission
monochromator, sample cell, and a cooled photomultiplier tube (PMT) detector for
the infrared light. Near infrared-red PMT is cooled by liquid nitrogen and the
temperature is maintained at -80 °C. The laser diode which produced the light beam
was focused onto the sample. The laser diode excitation wavelength of 980 nm was
used to obtain the emission from excited Er^{3+} ions in the range 1400-1700 nm which
is the emission bandwidth of Er^{3+} ions ($^4I_{13/2}$-$^4I_{15/2}$). The emission signal was collected
by the PMT detector, and emission intensities against wavelength were recorded and
plotted using a computer running a software tool named F900.
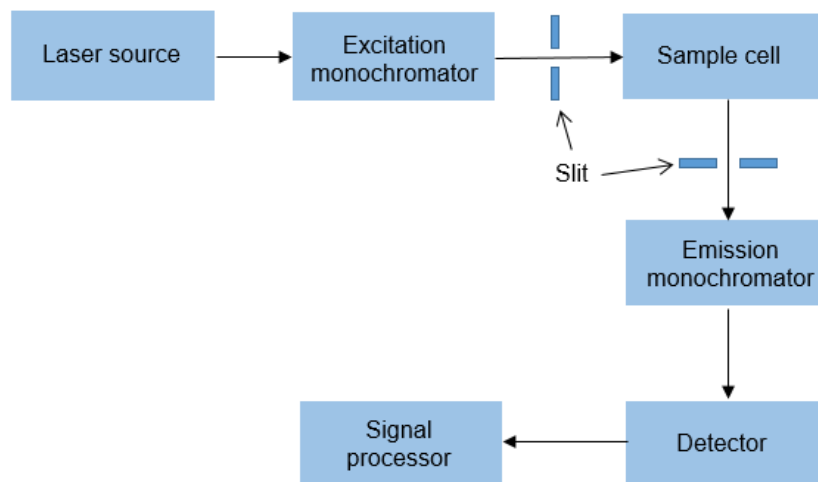
Figure 3.8: The block diagram for PL spectroscopy.

3.2.2.1 Time-resolved photoluminescence

Time-resolved PL was an extension of normal PL spectroscopy in which a short laser pulse is used for excitation. After pulse excitation, the PL process does not immediately stop but rather continues for a while until all the excited electrons reach the ground state. This technique measures the lifetime of an excited electron before it relaxes to a ground state. For these measurements, a laser pulse generator was used to generate the pulsed signals and the process could be examined using an oscilloscope. The pulsed laser source had a 100 ms period and a pulse width of 10 μs. The signal intensity was then recorded as a function of time and the lifetime obtained by fitting the intensity data with an exponential curve.

3.2.3 X-ray diffraction (XRD)

XRD is a non-destructive technique used extensively for material characterisation, primarily to study the chemical composition and crystallographic properties of material [142]. For this study, XRD was used to identify (if any) crystalline phases present in the doped layer. The appearance of defective crystallites that could contribute to propagation loss in the optical waveguide [143] in the fabricated doped layer needed to be avoided in this work. The basics of this technique rely on the diffraction of an X-ray beam on a crystal plane with a d-spacing as shown in Figure 3.9.
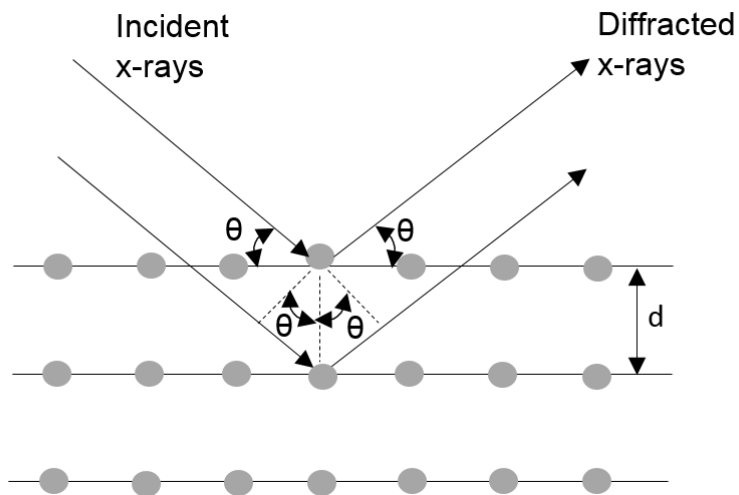
Figure 3.9: Schematic of a diffraction of X-ray from a crystal plane (adapted from [144]).

The interaction between incident X-ray and crystal plane creates constructive interference and a diffracted ray when Bragg's law is satisfied and expressed as:

$$2d \sin \theta = m\lambda \qquad (3.13)$$

where d is the spacing between two atomic planes, θ is the angle of incident, m is an order of reflection and λ is a wavelength of the incident light [142]. Crystal plane that interacts with X-ray can be ascertained by observing the angle at which the X-ray diffracts.

For a crystalline substance, the diffracted ray is in a particular direction and gives a high-intensity narrow peak (Figure 3.10), while, in the case of amorphous materials, the diffracted ray is in a random direction due to the random orientation of atoms which gives a broad peak or hump (Figure 3.11).
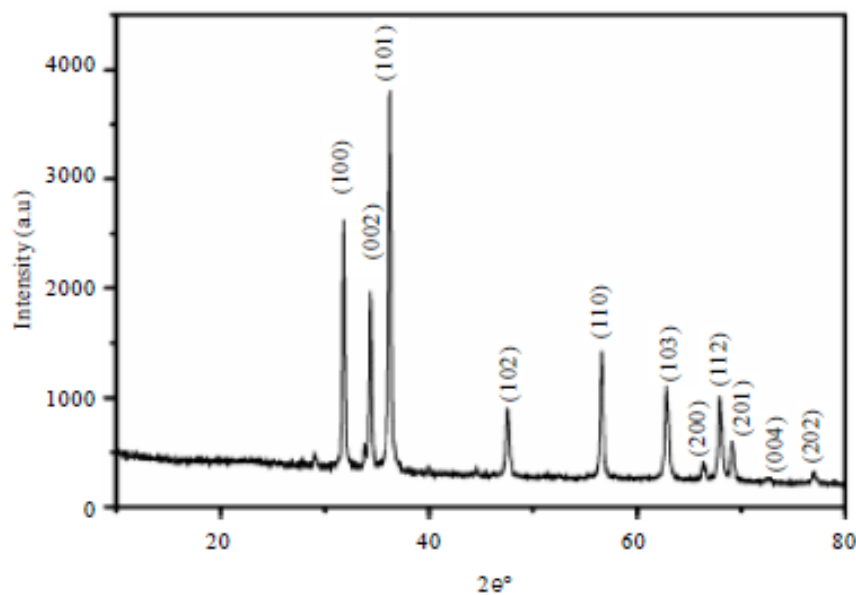
Figure 3.10: Example of XRD pattern of crystalline samples of ZnO nanoparticles [145].

Basically, XRD instruments can be divided into three basic elements which are an X-ray tube, a sample holder, and X-ray detector. X-rays are generated inside a cathode ray tube by heating the filament to produce an electron. When the electrons have enough energy, they will accelerate and hit the target material (Cu, Fe, Mo or Cr) and subsequently produce X-ray radiation. The X-ray pattern consists of a few components, but the most common are K_α and K_β. Between the two radiations, K_α is more profound and happens more often than K_β; therefore, K_α was used in the diffraction experiment. In order to obtain pure K_α radiation, a nickel foil filter was used to absorb K_β radiation and other radiation [146]. These X-rays were collimated and directed to the samples to be measured. The intensity of the reflected X-rays was detected by the detector as it rotated. The detector recorded and processed this reflected X-ray signal and converted the signal to a count rate [146].
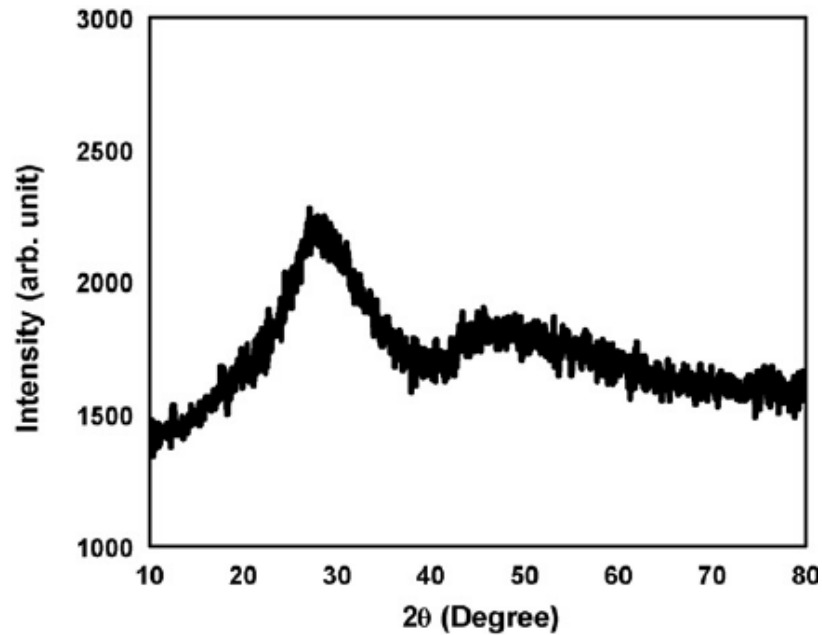
Figure 3.11: XRD pattern for amorphous samples of $23B_2O_3–5ZnO–72Bi_2O_3–xFe_2O_3/CeO_2$ glass [147].

In this work, samples were positioned on a glass slide in XRD (Phillips X'Pert) and were scanned using Cu K_α radiation with a wavelength of 0.15406 nm. It was scanned from 10° to 85° with a step size of 0.05°/s at room temperature in air.

3.2.4 X-ray photoelectron spectroscopy (XPS)

X-ray photoelectron spectroscopy (XPS) is a surface analytical technique which operates based on the photoelectric effect principle and is widely used for chemical analysis. XPS can be used in various ways to study and analyse glass material. More precisely, XPS can be employed to determine elemental composition, non-bridging and bridging oxygen concentration and contamination that may present within a glass.

XPS spectra can be procured by irradiating the sample with monochromatic X-rays done in a vacuum. When incident X-ray interacts with the sample, X-ray energy will be absorbed by the core electron of an atom that is located between 0-10 nm from the top surface. If photon energy is adequate or large enough, the core electron can escape from the atom as shown in Figure 3.12. An emitted electron that has its own kinetic energy is known as a photoelectron, and the phenomenon is called the photoelectric effect. The kinetic energy of an emitted photoelectron is given by the equation shown below:

$$KE = h\upsilon - BE - \phi \tag{3.14}$$

where $h\upsilon$ is the x-ray energy used, BE is the binding energy of the ejected electron and ϕ is the minimum energy needed to remove an electron from solid (work function). Since ϕ can be eliminated through calibration causing equation 3.14 to be [148],

$$KE = h\upsilon - BE \tag{3.15}$$
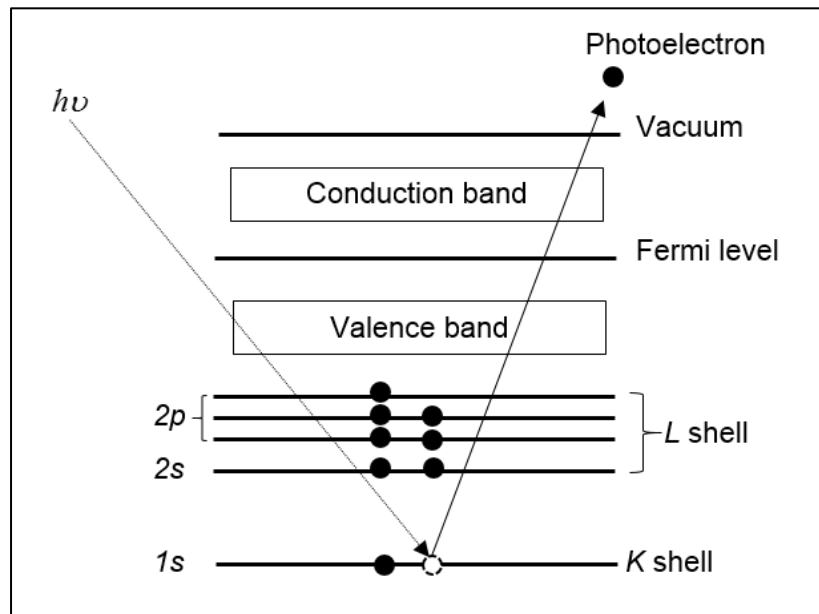
Figure 3.12: Schematic diagram of the photoelectric effect process (adapted from [149]).

Each element which is associated with each core atomic orbital has a characteristic set of peaks based on the relevant binding or kinetic energy in XPS spectra as shown in Figure 3.13. However, when plotting, discussing and comparing results, it is often preferable to use binding energy as the ordinate in the spectra. This is due to the position of any photoelectric effect for binding energy is independent from the X-ray source used, allowing for easier data analysis and data comparisons with other literature [150].

Not all the peaks in XPS spectra are due to electron ejection from direct interaction with the incident photon. The most common signal that also comes along with a photoelectron signal is Auger electron and plasmon loss peak. Auger electrons are generated when a vacancy in the inner shell caused by the photoelectric effect is filled by an electron at the outer shell, resulting in the emitting of energy. The energy will

be released in the form of a photon or can be transferred to another electron which can be ejected from the atom. This second ejected electron is called an Auger electron. Plasmon loss, on the other hand, is the loss of specific energy due to the interaction between a photoelectron and other electrons at the surface region of the sample. For an insulator sample, a fairly sharp peak is present in the range of 20-25 eV binding energy higher than the main peak [151].
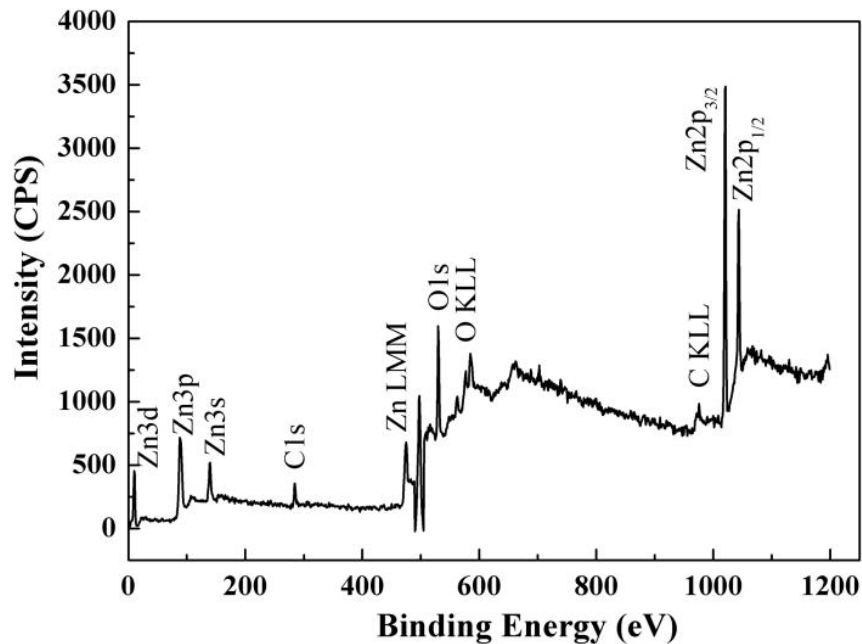
Figure 3.13: An example typical XPS spectrum for a ZnO thin film [152].

For qualitative analysis, XPS is undoubtedly very useful and reliable; however, for quantitative analysis, XPS is not that accurate. Although the amount of electrons collected is proportional to the total electrons present in the sample, but the single measurement which is often reported as atomic concentration has an error of around 10% [153]. This means that elemental concentration obtained cannot be assumed *a priori* [151].

Although XPS is a surface analytical technique, elemental concentration as a function of depth can also be obtained. This XPS depth profile can be determined by integrating a sequence of ion beam sputtering with XPS analysis. Ion beam sputtering is employed to etch the material from the sample surface for a certain period before it is turned off. Later, an XPS measurement is made from the surface that has been etched. The cycle of material removal and spectrum acquisition is continued until profiling is reached to the required depth (Figure 3.14) [153].
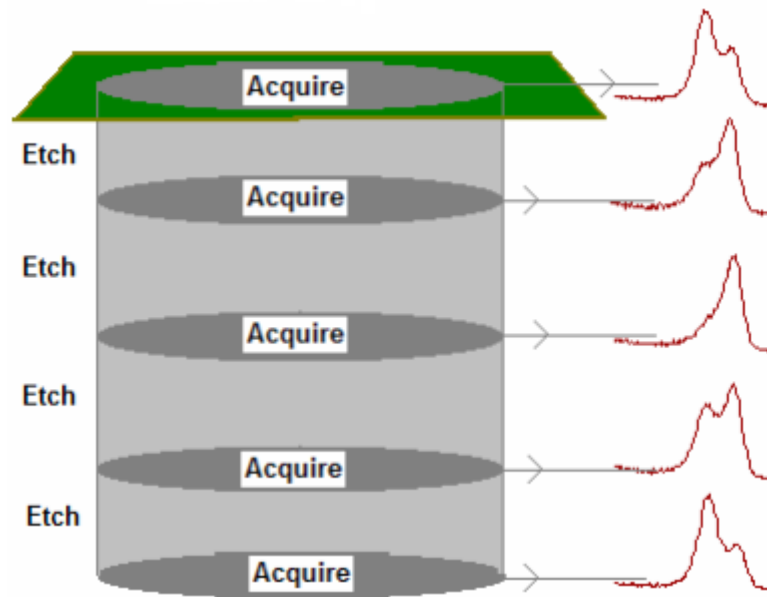
Figure 3.14: XPS depth profile [153].

Figure 3.15 shows a schematic diagram of basic components of XPS. These include a photon source, electron energy analyser, detector, and data analysis system [154]. In this work, XPS measurements were performed with K-alpha XPS instrument (Thermo Scientific) at National EPRSC XPS Users' Service (NEXUS) at Newcastle University by Dr Jose Portoles and Dr Billy Murdoch. The measurement was done using Al K_{α} (1486.6 eV) in an ultra-high vacuum (HPV) chamber in which the pressure was around 5 x 10^{-9} mbar. For survey spectra, a pass energy of 150 eV with a step size of 0.4 eV was used while, for high-resolution spectra, a pass energy of 40 eV with a step size of 0.1 eV was employed. On the other hand, for depth profiling, ion beam sputtering was done by bombarding the surface using monatomic Ar^+ with the energy of 4 eV and a high current setting. Data analysis and peak fitting were performed using CasaXPS software. A Shirley background subtraction and a mixed Gaussian-Lorentzian function were utilised to fit all the peaks in the obtained spectrum. All the binding energies of the photoelectron spectra in this work reportedly used a C 1s peak at 285 eV as a reference in order to maintain consistency and correction for sample charging. The C 1s peak is an adventitious peak that is obtained from unavoidable hydrocarbon contaminants in a vacuum. Generally, this peak is accepted to be independent of the chemical state of the material under study [155,156].
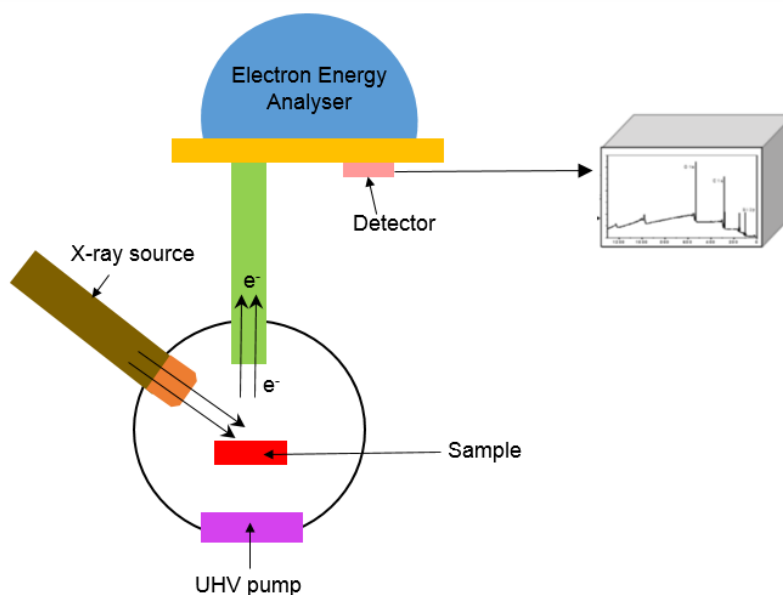
Figure 3.15: Schematic diagram of basic components of XPS.

3.2.5 Raman spectroscopy

Raman spectroscopy is a spectroscopic technique that involves light scattering from the coupling of optical with lattice or molecular vibrational modes [157]. It is based on the Raman effect that has been used extensively to investigate the internal structure of the molecule.

This technique requires a monochromatic light source, usually a laser with a wavelength in the range of near ultraviolet to infrared, to be projected onto a sample. The incident photons from the laser can be scattered elastically or inelastically. When incident photon impinges the sample, the photon energy will excite electrons to the virtual state. The electrons will then emit a photon when they return to the stable ground state. For elastic scattering, the incident and scattered photons have the same amount of energy. This kind of scattering is called Rayleigh scattering. For inelastic scattering, also known as Raman scattering, the scattered light has a different energy from an incident photon. It is due to the interaction of laser light with a phonon that allows energy to be shifted up or down. This phenomenon is known as the Raman effect. The amount of energy gain or loss by a photon is dependent on the nature of vibration (chemical bond or phonon) characteristic of the material. In Raman spectra, Raman intensity versus wavenumber shift in a unit of cm^{-1} are often plotted. Raman scattering can be divided into two types which are Stokes-Raman and Anti-Stokes-Raman scattering. Stokes-Raman scattering happens when the reemitted photons have lower energy than the absorbed photons. The reverse scenario is called Anti-

Stokes-Raman scattering where the inelastically scattered photons have higher energy than the absorbed photons [158]. Understanding of this scenario can be better illustrated in Figure 3.16.
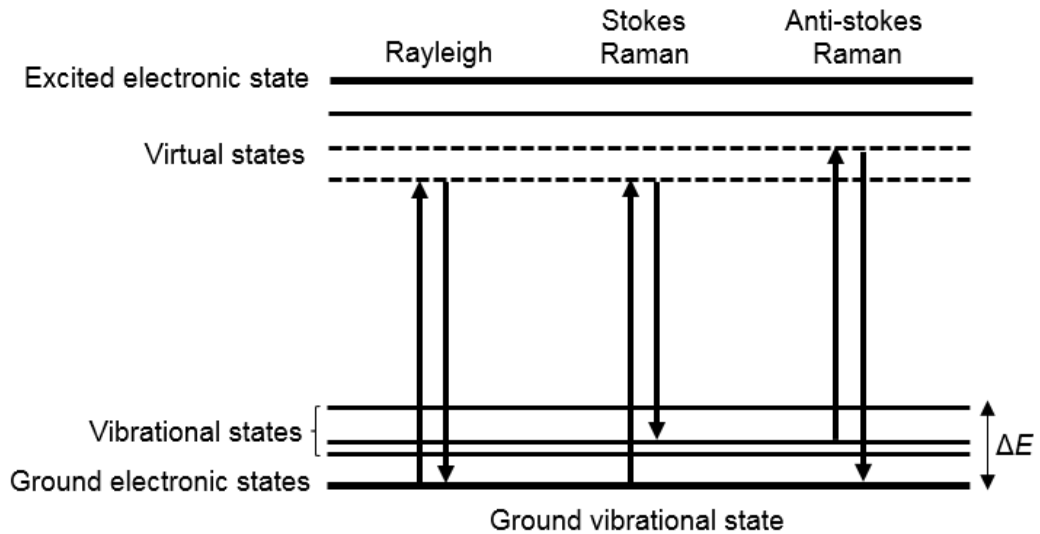
Figure 3.16: Energy level diagram for Rayleigh scattering and Raman scattering [159].

For Raman scattering, there are two types of vibrational modes of molecules which are bending and stretching vibrations. Bending vibration is a type of vibration that involves changes in bond angle with the bond length remaining the same. On the other hand, stretching vibration involves vibration that causes the change in bond length but not bond angle. This vibration can further be classified into two groups which are symmetric and asymmetric vibrations. For symmetric vibration, the bond length of the functional group moves in the same direction and vice versa for asymmetric vibration [160].

Raman scattering is normally 1000 times weaker than Rayleigh scattering. It makes Rayleigh scattering to have much higher probability event compared to Raman scattering [161]. On the other hand, a Raman signal is also weaker compared to a PL signal. The PL signal can produce strong background and can even cover a Raman signal fully [162]. Therefore, choice of excitation wavelength is very critical especially for samples that have luminescence species. This is very important in order to minimise the noise from a PL signal.

Figure 3.17 exhibits the schematic diagram of the Raman spectroscopy system. A Renishaw inVia Raman microscope with a laser excitation wavelength of 514 nm with

a power of 25 mW was used in this work. The instrument consisted of a monochromator, laser source, detector, microscope, filter and a data processing unit. The light beam passed through a monochromator and focused onto the sample with the aid of a microscope. The signal scattered from the sample was reflected to a filter to remove Rayleigh scattering. After that, Raman scattering was collected by the detector. The intensities and the wavelength of the signal were recorded to gain Raman spectra with the help of the data processing unit.
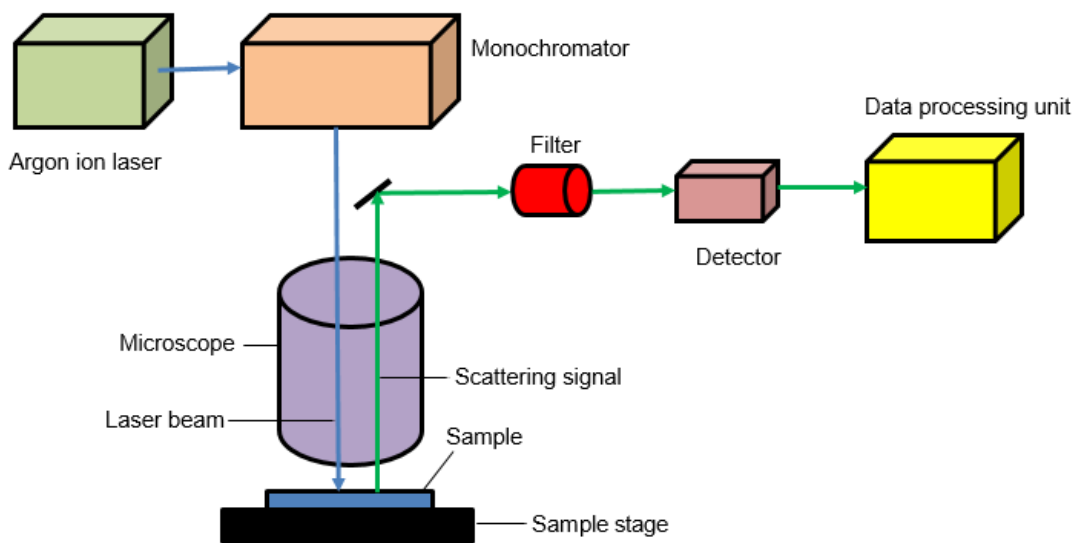
Figure 3.17: Schematic diagram of Raman spectroscopy system.

3.2.6 Scanning electron microscopy (SEM)

Scanning electron microscopy is one of the electron microscope technique that is capable of capturing sample surface images in high resolution. The topography of the doped layer is ascertained by SEM as it is a crucial factor in determining the quality of the thin film. It is also used to obtain thickness for each layer in the samples.

A typical SEM system is illustrated in Figure 3.18. The electron beam is generated from an electron gun fitted with a tungsten filament (cathode) when a high voltage is applied. It is then accelerated towards an anode in the SEM. After that, the electron beam is passed through one or two condenser lenses to reduce the diameter of the beam. The electron beam is essentially focused down to 1000 times its original size. It is later passed through scanning coils to form a raster scan over the surface of the sample. Next, the electron beam passes through the final objective lens which is the heart of SEM as it focuses the electron beam onto the specimen surface [163–165].

The selected portion of radiation is collected by a detector and signal which are then converted into intensity changes and duly displayed on a computer monitor.

When an electron beam strikes the surface of the sample, it will interact with the atoms in the sample and produced various signals including backscattered electrons (BSE), secondary electrons (SE), Auger electrons, x-rays and heat [166,167]. However, SE and BSE are commonly used for imaging purposes.
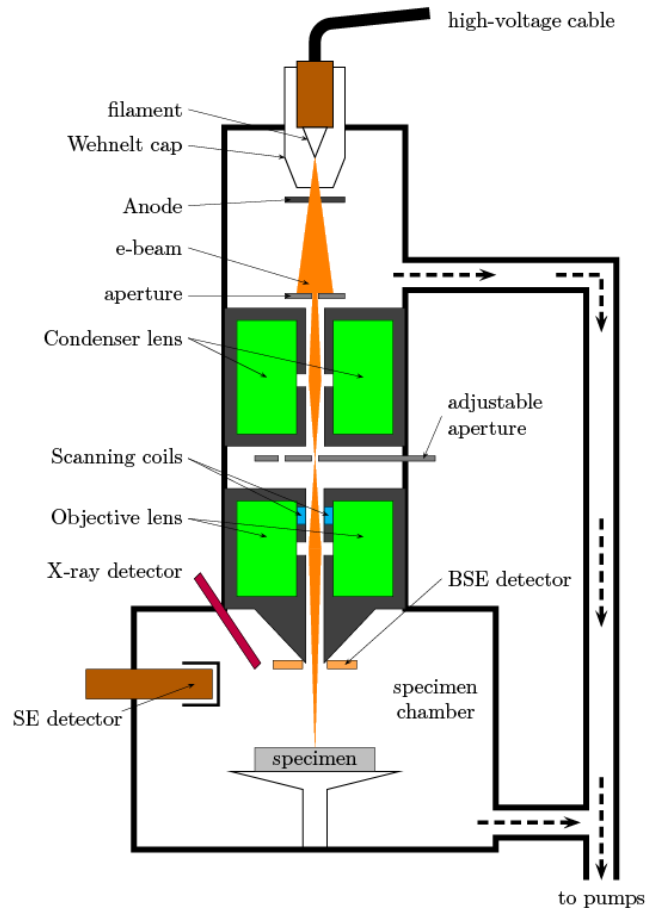
Figure 3.18: Schematic diagram of the SEM [163].

SEs are created from inelastic scattering when an electron from a beam collides with an atom in a sample and causes the collided atom to ionise. The freed electron from the ionisation process is a secondary electron. SEs are generated close to the sample surface (Figure 3.19) and defined as having an energy below 50 eV. These electrons originated from the region that has the depth of a few nanometers from the sample surface due to their low energy. For BSE, it is formed from elastic scattering that has energies above 50 eV. As BSE has a higher energy than SE, it has more interaction depth (Figure 3.19). An important aspect of BSE scattering is that its yield depends on the mean atomic number in the sample. Since the heavy elements in (high atomic

number) BSE are stronger than light elements (low atomic number), regions that are condensed with heavy elements seem lighter in appearance [164,167,168]. Therefore, BSE is most suitably used to study a sample that consists of many areas that have their own different chemical compositions such as a multi-layer thin film sample.
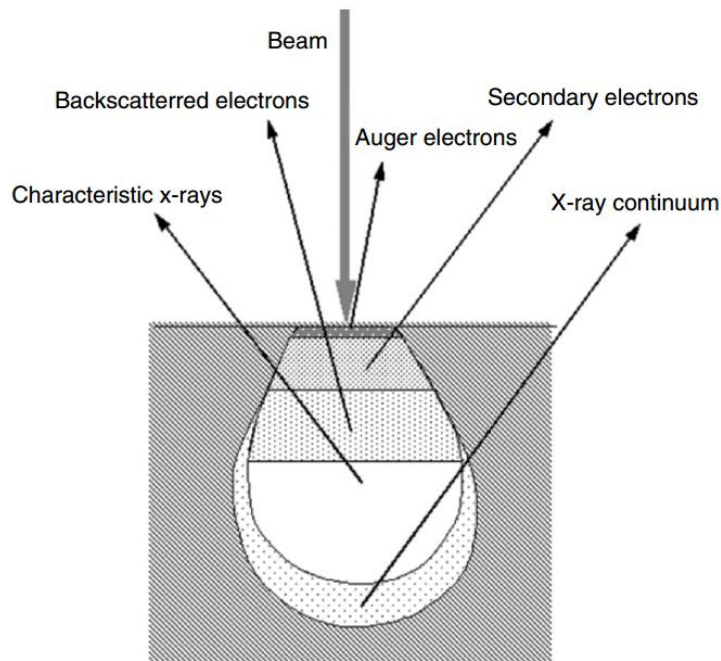
Figure 3.19: The schematic of the depth of electron beam penetrating the sample [167].

There are some problems that could affect the quality of the image obtained. One of the main problems when inspecting a non-conducting sample is charging effect. In SEM, the sample is being bombarded by electrons, and, in the case of non-conducting samples, it causes an accumulation of static electric charges on the sample surface. When the quantity of electrons that accumulate is too large, it affects the incoming electron beam and the image produced becomes blurry, distorted, abnormal or becomes very bright. For metals, they allow electrons to move inside them, and when they are grounded, the additional electron will be removed, and no charge will accumulate. However, for the non-conducting sample, they do not have a medium to remove the additional electron. This problem can be reduced by coating a layer of conducting material such as carbon that helps to ground the charge built up on the surface. Other than that, BSE mode can also be used during measurement as BSE mode is less affected by the charging effect due to higher energy than SE [169].

In this work, a Hitachi SU8230 field emission (FE)-SEM was used to determine the topography of a cross-section of the samples. Before measurement began, all the samples were inserted into Hitachi ZONESem in order to do rapid surface cleaning and eliminate hydrocarbon contamination from samples. This system used ultraviolet (UV) radiation and ozone in a simple, dry process at room temperature. It is capable of doing minimal etching of specimens which have carbon structures and surface sample cleaning in only a few minutes [170].

As the doped layer was a dielectric material, all of the images were taken using a BSE detector to avoid electron charging. BSE was also used to detect the contrast between each layer. The voltage of the electron beam was set to 10 kV. However, for surface imaging for the film obtained, a Hitachi TM3030 Bench Top SEM was used in this work, and the set voltage was 5 kV.

3.2.7 Transmission electron microscopy (TEM)

TEM is an electron microscopy technique where the high energy of an electron beam is transmitted through an extremely thin sample and interacts with the sample when the electron beam passes through it. TEM can be used to observe features such as crystal structure, grain boundaries, defects and film thickness. TEM is capable of providing a higher resolution image compared to SEM and able to operate at a high magnification ranging from 600x to 10^6x. It is also able to generate diffraction information and images from the same sample through a scattering process by the high energy electron [171].

3.2.7.1 Electron scattering

When a primary electron passes through the sample, some of the electrons will penetrate through sample unscattered (direct beam), and some of them will collide with an atom in the sample and be scattered as shown in Figure 3.20. Scattered electron experiences two types of scattering which are elastic and inelastic. Elastic scattering occurs when a primary electron collides with the nucleus of an atom without energy loss (or energy loss in the only small fraction) and is deflected at a wider angle from inelastic energy ($\theta_{el} > 1$). The element that has a higher atomic number (larger nucleus) makes more electrons experience elastic scattering. On the other hand, inelastic scattering is a result of the collision of a primary electron with electrons that surround the nucleus. This form of scattering involves higher energy loss and deflects at a smaller angle ($\theta i_{el} < 1$) compared to elastic scattering [172]. Both forms of scattering give out unique information about the sample [173]. Elastic scattering

increases contrast and image resolution due to scattered electrons only come from one point which is the nucleus while, for inelastic scattering, it affects the TEM image quality. Resolution and contrast are decreased due to inelastic scattering because this type of scattering originates from various points. In addition, the inelastic scattering also causes radiolysis effect, whereby it can cause changes to the structure of the specimen or mass loss [174].
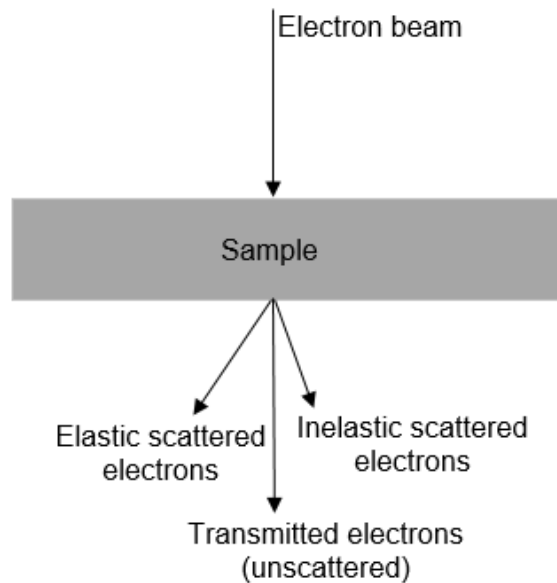
Figure 3.20: Interaction electron beam with the sample in TEM (adapted from [175]).

TEM quality is very much dependent on the thickness of a sample as a thin sample reduces the effect of inelastic scattering and increases the unscattered electrons that penetrate the sample. Typically, the sample must be provided in the thickness range of 10 nm to 1 µm.

3.2.7.2 TEM operating mode and working principle

Generally, there are two operation modes in TEM which are the imaging and diffraction modes. For the imaging mode, it can be categorised into three modes which are: bright field (BF), dark field (DF) and phase contrast (High-resolution TEM (HRTEM)). BF is the most common mode used where the region that has significantly higher atomic weight will appear darker, and conversely, a region with lower atomic weight will be lighter in appearance. BF only allows the direct beam to pass and block the diffracted beam as shown in Figure 3.21 (a)). Image contrast that occurs is formed by the different thickness and/or atomic number. For DF, the approach is completely opposite to BF. The direct beam is blocked and the selected diffracted beam is

allowed to pass as illustrated in Figure 3.21 (b). The diffraction region of the sample will appear in a lighter shade, while, relative to its surroundings, the remaining region of no specimen appears to be a darker shade [176]. On the other hand, phase contrast that is often synonymous with HRTEM needs a thinner sample and incident electron beam with higher energy. HRTEM needs more than a single beam which is a combination of direct and diffracted beam to form an image (Figure 3.21 (c)). When more beams are collected, the image produced will be of higher resolution. The image that forms is the direct result of interference from several diffracted beams with an incident beam allowing for phase contrast to appear. The interference pattern which is in a fringe type unveils the crystal periodic nature [177]. For diffraction mode, it is regularly associated with selected area electron diffraction (SAED). It is used to analyse the crystallography of the material. The diffraction pattern is created when electron scatter enters the periodic atomic structure. According to the equation (3.13), diffraction obeys Bragg's equation and, in the diffraction pattern image obtained, is in a reciprocal space. When a parallel beam goes through the sample, at the rear focal plane of the objective as shown in Figure 3.22, there will be a diffraction pattern depending on the structure and orientation in the sample. Three diffraction patterns that may be achieved are: single crystal, polycrystalline and amorphous. For the single crystal, the diffraction pattern is made of the discrete spot (Figure 3.23 (a), while polycrystalline and amorphous create many concentric ring patterns (Figure 3.23 (b)) and a diffuse ring pattern (Figure 3.23 (c)) respectively [178].

(a)   (b)   (c)
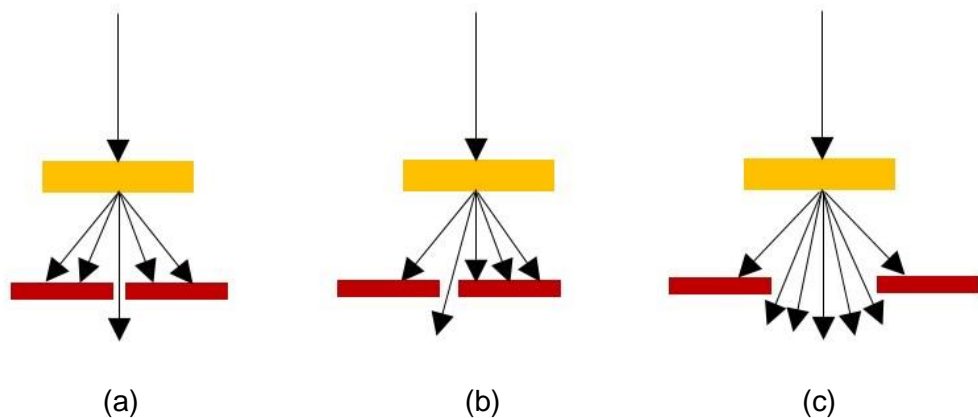
Figure 3.21: Beam paths for (a) bright field (b) dark field (c) HRTEM) [176].
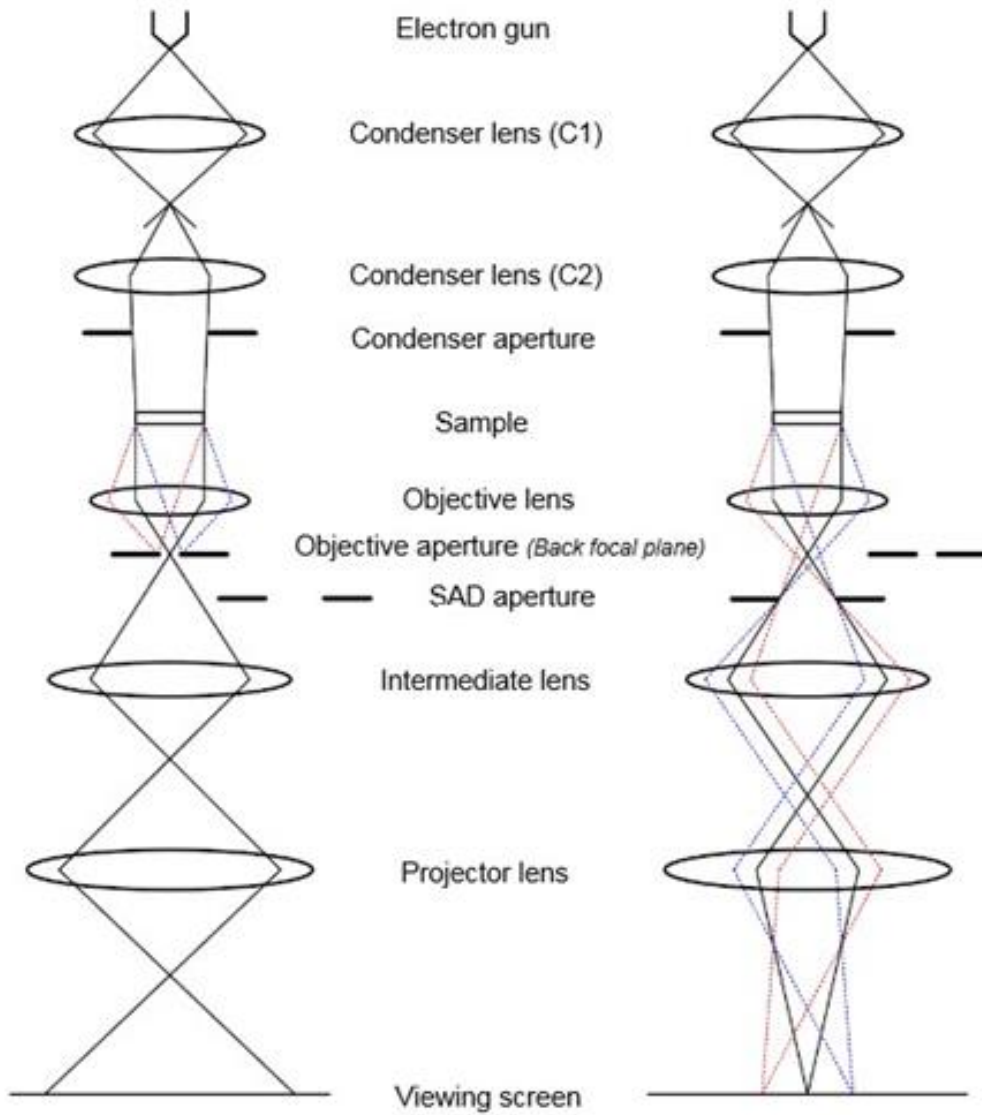
Image   Diffraction pattern

Figure 3.22: TEM beam path for imaging and diffraction mode [179].
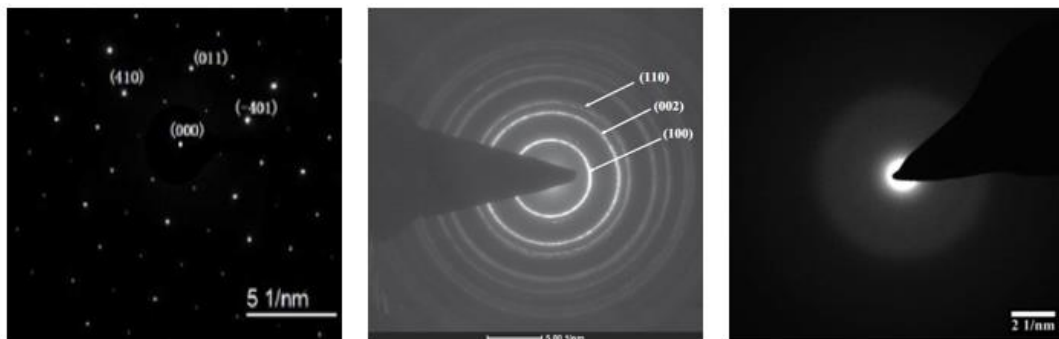
(a)   (b)   (c)

Figure 3.23: Example of diffraction pattern in TEM for (a) single crystal (boron carbide (B_4C)) [180] (b) polycrystalline (Al-doped ZnO) [181] (c) amorphous (EDTS) [24].

A typical diagram of TEM configuration is shown in Figure 3.22. It consists of an electron source, system of condenser lens, objective lens, intermediate lens, projector lens, lens aperture and detector. The electron beam, which is generated by a field emission gun (FEG), is accelerated under high voltage been focused on the sample with the help of condenser lens and condenser aperture. The transmitted electron is later focused by an objective lens and duly magnified by the intermediate lens. The image is then enlarged by a projector lens. For diffraction pattern as in SAED, the objective lens is used to focus the diffraction pattern on the back focal plane of the objective lens. The sample area where the diffraction pattern is created is limited by placing a selected area aperture as shown in Figure 3.22. For BF, DF and HRTEM, images are formed by opting for the most suitable objective aperture size and placed in the most optimum location based on the desired mode. In this work, FEI Tecnai TF20 was used for TEM measurement, and it was performed by Dr Zabaeda Aslam from Leeds Electron Microscopy and Spectroscopy Centre (LEMAS).

3.2.7.3 Scanning transmission electron microscopy (STEM)

STEM offers an alternative imaging technique other than conventional TEM which involves a tiny convergent electron beam that can scan over an area of interest on the sample. Imaging capabilities for the STEM are better as the instrument comes attached with multiple detectors that function to collect a wider range of the possible signal. However, image acquisition for the STEM is relatively slower than TEM as the sample is scanned by raster fashion [182].

In general, STEM comprises a lens system, electron gun, and various detectors as shown in Figure 3.24. The main aim of the lens system is to focus a beam into a tiny spot beam (probe) on the sample. Scan coil, on the other hand, is used to scan the probe on the sample's area of interest in a raster pattern. The various scattered signal is then collected, and later a magnified image is formed. There are various signals that can be possibly detected in the STEM, but the most commonly detected signals are [182]:

i. A transmitted electron with lost energy when travelling through the sample and the energy is measured by electron energy loss spectroscopy (EELS).

ii. X-rays that are from electron-excited in the sample (EDX).

iii. A transmitted electron that leaves the sample at an angle of less than 10 mrad with respect to the optic axis and the signal can be detected by BF detector.

iv.   A transmitted electron that leaves the sample at an angle of around 10-50 mrad with respect to the optic axis and the signal is collected by an annular dark field (ADF) detector.

v.   A transmitted electron that leaves the sample at an angle of more than 50 mrad with respect to the optic axis. It can be detected by a high field annular dark field (HAADF) detector.
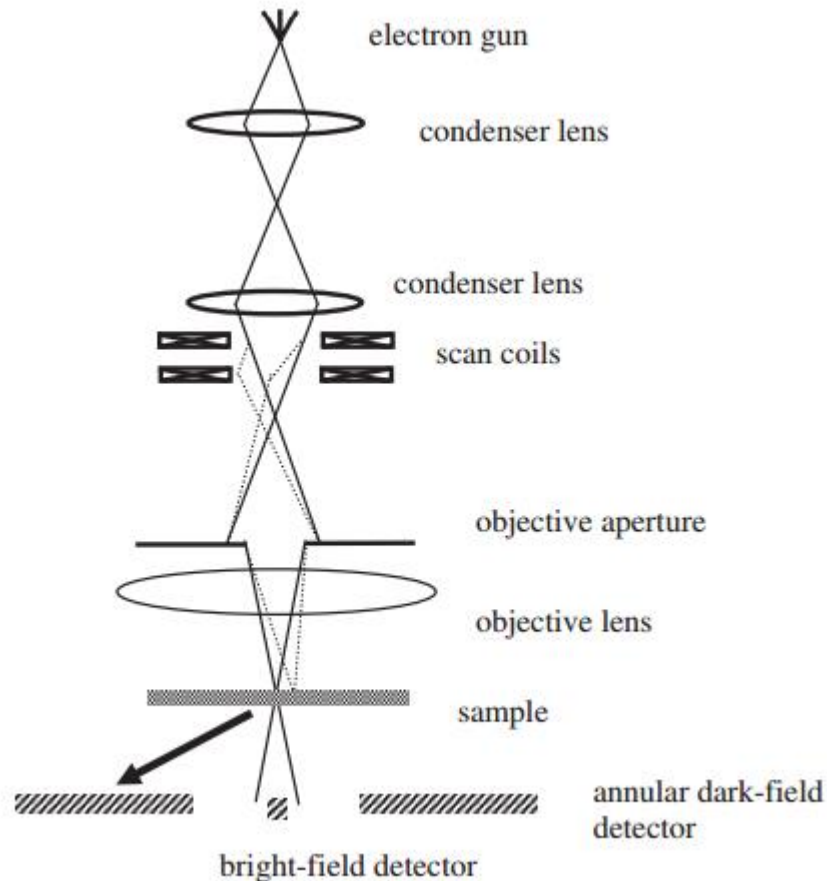
Figure 3.24: Schematic diagram of STEM setup [183].

By using STEM-HAADF, image contrast created is directly related to atomic number. The region that has more atomic weight appears lighter as an atom is deflected at a larger angle and the reverse is true for less atomic weight [183]. For this work, samples were measured by Dr Zabaedah Aslam using an FEI Titan3 Themis 300 with X-FEG 300 kV S/TEM with S-TWIN objective lens, a monochromator (energy spread approx. 0.25 eV) and multiple HAADF/ADF/BF STEM detectors.

3.2.7.4 Sample preparation for TEM

TEM needs an extremely thin sample to enable transmission of the electron. Sample thickness should be less than 100 nm for high-resolution imaging. Therefore, TEM samples need to be prepped using special techniques which, in turn, often depend on the type of sample and also the property of interest. TEM sample preparation is immensely important because it influences the quality of the TEM image. There are a few possible techniques for preparing TEM samples such as focused ion beam (FIB), tripod polishing and conventional method [184–186]. Among the listed techniques, FIB is the primarily used technique to prepare a cross-section TEM sample and it also often yields the best TEM samples in terms of speed, homogeneity, and thinness [187]. In this work, FIB and conventional method were used to prepare samples for TEM measurement.

The FIB system works in a similar fashion to SEM except instead of an electron beam to focus on a sample, it uses a finely focused ions beam. The FIB is integrated with a field emission gun scanning electron microscope (FEGSEM) for sample imaging. The configuration of SEM and FIB is shown in Figure 3.25. Basically, the operation of FIB is initiated with a liquid metal ions source (LMIS) which is placed in contact with a tungsten needle as shown in Figure 3.26. In general, the ion source used in an FIB system is gallium (Ga) due to its low melting point (near room temperature) and its capability to be focused to a very fine beam spot size (typically < 10 nm in diameter) [188]. When a huge electric field is applied to the tungsten needle tip, emission of positive ions is formed. The ions are then duly extracted and accelerated by a voltage of a few kiloelectron volts. After that, the ions are focused onto a specific region and high energy of typically around 5-50 keV causing the beam to mill at a predetermined location. Higher milling rates can be achieved by increasing the beam current (> 50 nA) [189]. As the beam bombards the sample, a secondary electron is also sputtered out and is collected to form an image. Nevertheless, before the milling process, ion beam-assisted chemical vapour deposition deposits a layer of platinum. The deposited metal is used as a sacrificial layer, to shield the sample top surface from damage due to ion irradiation.
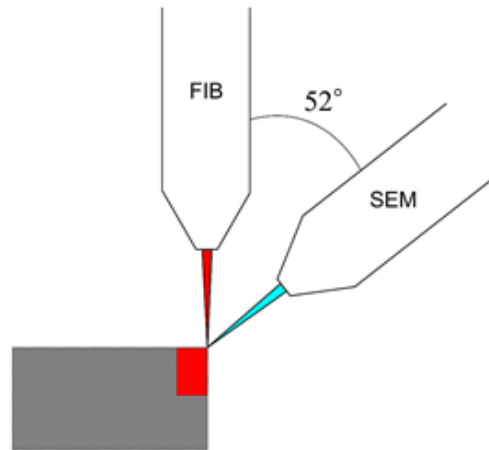
Figure 3.25: Schematic diagram of FIB-SEM geometry [190].
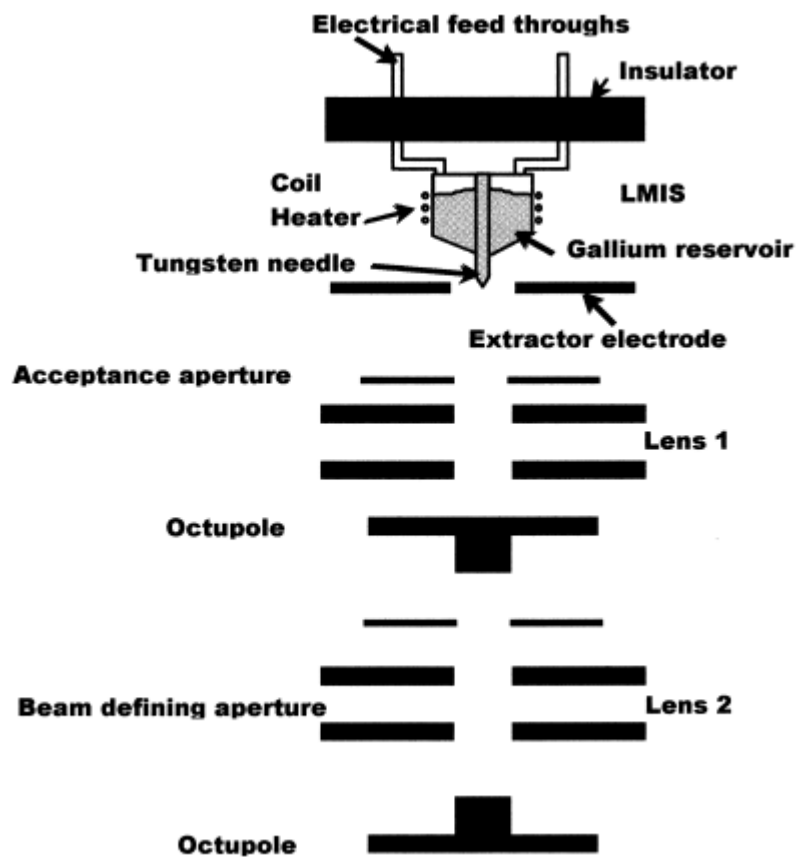
Figure 3.26: Schematic of FIB and LMIS setup [189].

For this work, an FIB procedure was performed by using an FEI Nova 200 NanoLab with the *in-situ* lift-out procedure. The ion beam operates at beam currents between 5 to 0.1 nA with voltages between 30 and 5 kV. The procedure started by locating the area of interest on the sample. The sample top surface was then deposited with platinum. Next, the ion beam was used to remove the material so that the sample became a thin slice. Later, it was cut around to ensure it could be hoisted up easily

and moved to a sample grid using a micromanipulator. The thin slice on the sample grid was then sliced thinner using an ion beam and polished finely. The result was a thin layer with a thickness of less than 100 nm.

This FIB TEM sample preparation was done by Mr John Harrington at the Leeds Electron Microscopy and Spectroscopy Centre (LEMAS). Even though FIB is a favourable method however conventional TEM sample preparation was employed due to delays in accessing the FIB system due to its upgrading. At that time, only a conventional method was available for TEM sample preparation.

This method started by removing two sections from the sample using an ultrasonic cutter and cleaning them with acetone. Next, two films' faces were glued together using epoxy resin. Additional silicon wafers then sandwiched the two glued films. Then, the same ultrasonic cutter was used to bore a hole through the middle of the layers to get a core that was a tube-like shape for the sample wafers. The core was then coated with epoxy resin and placed into a copper tube. Next, using a diamond blade saw, the core was cut into individual sections of about 1 mm thick. The resultant sample grid was then grown down to 250 µm thickness with a high finish on both sides. The wafer was then thinned right at its centre using a dimple grinder. A 2-4 µm thickness was attained, and it was confirmed by measuring its transparency using an optical microscope. The same amount of material was removed from the faces of both samples. Lastly, by using precision ion polishing (PIPS) two Ar-ion guns, further materials were removed from the sample until a minute hole was seen in the middle of the sample.

This conventional TEM sample preparation was done by Mr Stuart Micklethwaite at the Leeds Electron Microscopy and Spectroscopy Centre (LEMAS).

3.2.8 Energy dispersive X-ray spectroscopy (EDX)

EDX is used mainly to identify a sample's elemental composition including contaminants. It usually comes integrated with the SEM or STEM. Principally, the two machines work similarly, and both machines measure samples concurrently. Various signals are produced when energetic electrons interact with the surface of the material. One such signal is the characteristic X-rays. These are generated when an electron that is situated in an inner electron shell is excited to a higher energy level. The resultant hole will be filled by an electron from a higher state and an X-ray will be emitted in this process. The X-ray energy produced takes the character of the

particular element from which it is emitted. The X-ray spectrum is then captured to gain data on the elemental composition of the specimen under study. A higher peak in a spectrum means that the element of the sample is more concentrated. Identified elements are then processed from the spectrum and reported in an atomic percentage (atomic %) or weight percentage (weight %). However, the EDX analysis will not give information about chemical compounds formed among the detected individual elements [167,169,191].

Even EDX is often integrated with SEM or STEM; however, there are some differences between those two. The major difference between EDX analysis in STEM and SEM is the spatial resolution as exemplified in Figure 3.27. Usage of the thinner sample and higher accelerating voltage in STEM causes interaction volume to be 10^8 times smaller than SEM [192]. It is reported that the local chemical composition of a material measured by EDX-STEM has an accuracy of approximately 10 times better than EDX-SEM [193].
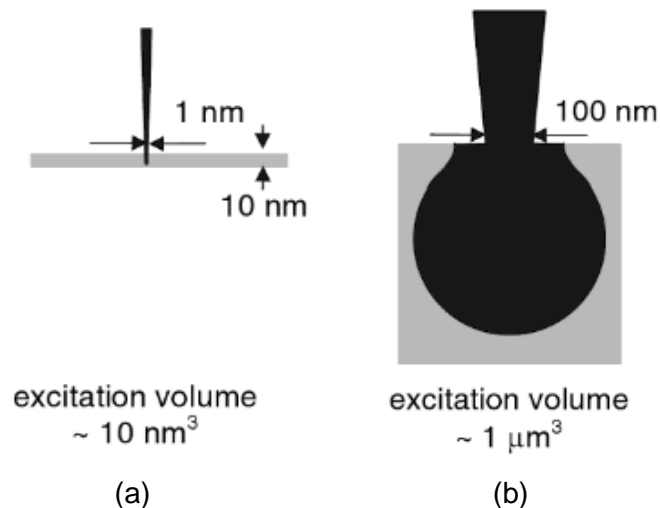
Figure 3.27: Schematic diagram of beam interaction volume in (a) STEM (b) SEM [192].

In this work, for EDX-SEM, an Oxford Instruments 80 mm^2 X-Max energy dispersive X-ray (EDX) detector was built together with a Hitachi SU8230 field emission (FE)-SEM while an FEI Super-X 4-detector EDX system was attached with a FEI Titan3 Themis 300 for EDX-STEM measurement. Both setup instruments used Aztec software for data analysis.

3.3 Computer simulation using COMSOL Multiphysics Modelling Software

Computer simulation, which is typically based on mathematical modelling and calculation, is a very useful tool to predict the outcome of some reactions. It can be

used to study the complex relationship between various variable factors. COMSOL Multiphysics Modelling Software (finite-element analysis) was used to investigate the effect cladding thickness for diffused and ridge channel waveguides in this thesis.

CHAPTER 4

DOPING TeO$_2$-ZnO-Na$_2$O-Er$_2$O$_3$ INTO A SILICA-ON-SILICON (SOS) SUBSTRATE

This chapter describes the doping of TeO$_2$-ZnO-Na$_2$O-Er$_2$O$_3$ (Er-TZN) glass into SOS substrate to form an EDTS layer by varying ULPD process parameters such as fs-laser energies, substrate temperature, fs-laser repetition rate, ablation period and oxygen gas pressure, and their structural, physical and optical properties. Five series of samples were prepared and analysed in this chapter with the aim of obtaining the best possible process parameters in terms of the EDTS layer properties listed above.

4.1 Dependence of laser pulse energy on Er-TZN doping into SOS substrate

Table 4.1 reports the details of four samples, A(50), A(60), A(80) and A(100) fabricated with different fs-laser energies 50 µJ, 60 µJ, 80 µJ and 100 µJ, respectively while maintaining all other process parameters.

Table 4.1: The parameters used to dope Er-TZN into SOS substrate by using various fs-laser energies.

Process parameters	Operating conditions
Substrate	Silica (t=1 µm)-on-silicon (SOS)
Target material	79.5TeO$_2$-10ZnO-10Na$_2$O-0.5Er$_2$O$_3$ (Er-TZN)
Fs-laser energy (sample name)	50 µJ (A50), 60 µJ (A60), 80 µJ (A80) and 100 µJ (A100)
Fs-laser repetition rate	1.0 kHz
Substrate temperature	570 °C
Ablation period	4 hours
Background gas pressure	70 mTorr O$_2$

Figure 4.1(a) displays a backscattered (BSE) cross-section SEM image for bare SOS substrate while Figure 4.1(b)-4.1(d) presents the images of the cross-section for samples doped with Er-TZN by using fs-laser energies of 50 µJ, 60 µJ, and 80 µJ, respectively. Differences, in contrast, could be seen clearly in every micrograph which meant that every layer had a varying density and thickness. Elemental composition of the EDTS layer obtained from EDX-SEM as shown in Table 4.2 proved that the EDTS consisted of combinations of elements from the target material and also silica from the substrate surface. It means that cations such as Te, Zn, Na, and Er were removed from the target material and penetrated into silica thereby modifying the original silica network during the ULPD process. Progressive increase in the concentration of elements of the target glass is clearly evident in the EDTS with an

increase in laser energy. Line scan and area scan of elements for the sample A80, obtained with EDX-STEM as reported in Figures 4.2 and Figure 4.3, respectively, also showed that the EDTS consisted of a mixture of Er-TZN with silica.

(a)

(b)

(c)

(d)
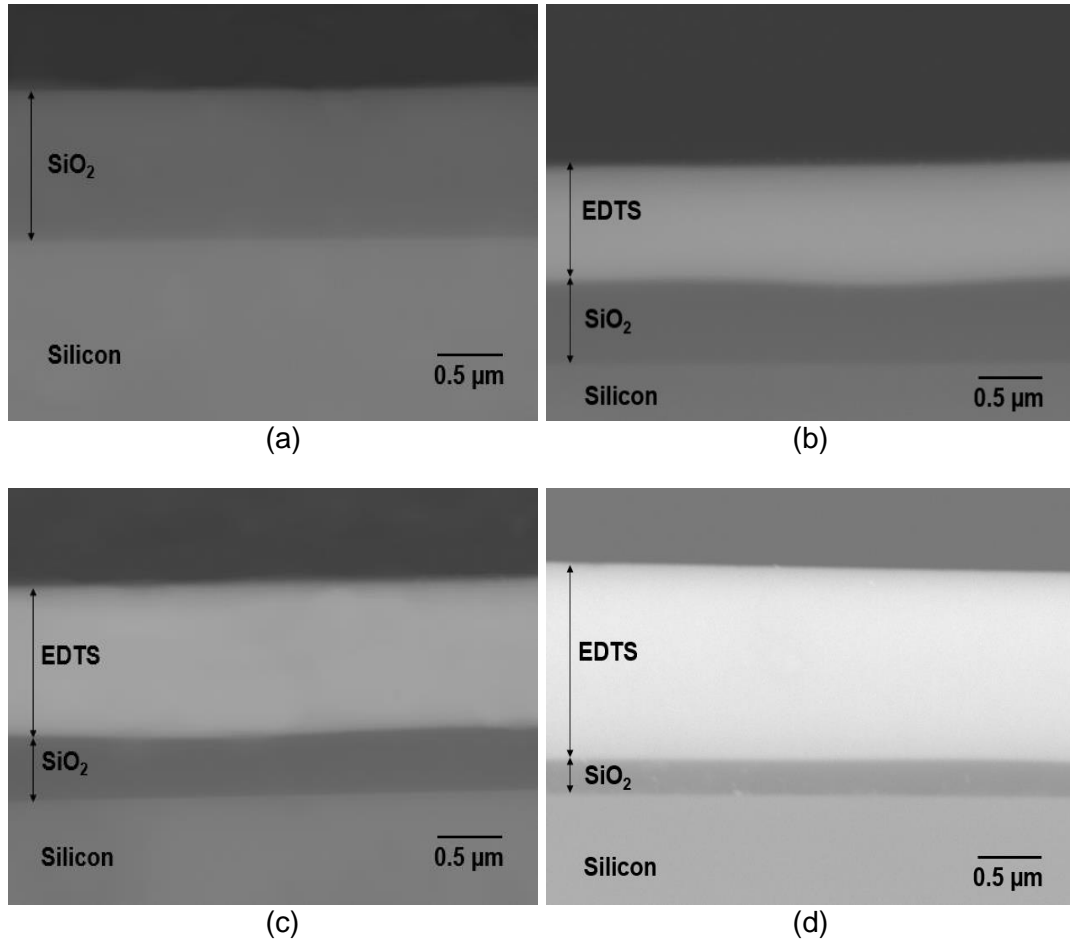
Figure 4.1: Backscattered cross-section SEM image of (a) bare SOS substrate, and samples doped with Er-TZN by using the fs-laser energy of (b) 50 µJ (A50), (b) 60 µJ (A60) and 80 µJ (A80).

Table 4.2: Elemental concentration of the EDTS layer with different fs-laser energies measured by EDX-SEM.

Element	Elemental concentration (at. %)		
	Sample A50	Sample A60	Sample A80
O	61.01	58.77	57.10
Si	21.47	21.16	17.90
Na	8.57	10.74	12.96
Zn	6.77	6.91	8.10
Te	1.74	1.96	3.39
Er	0.44	0.46	0.55
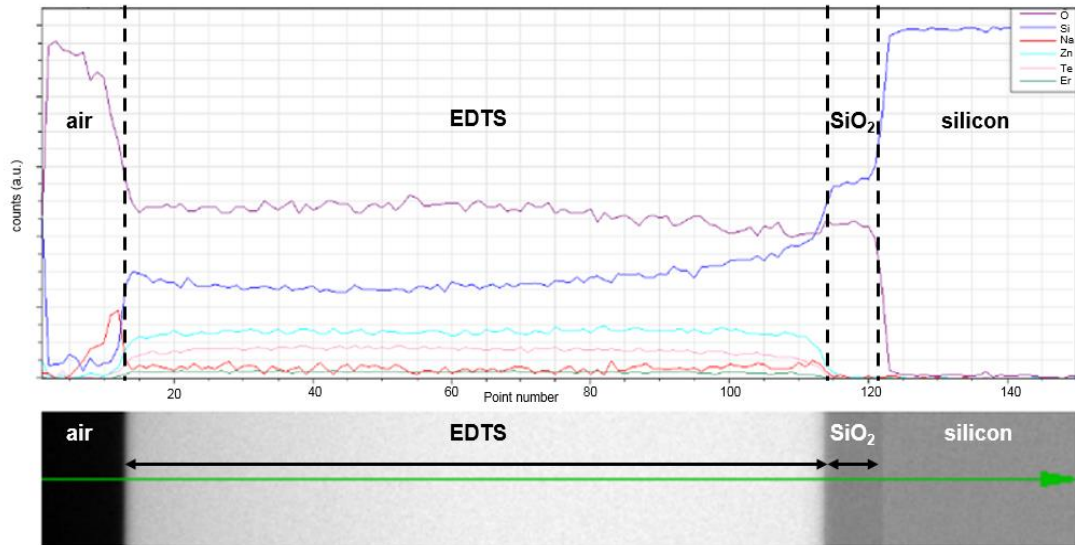
Figure 4.2: Line scan determined by EDX-STEM for sample A80.
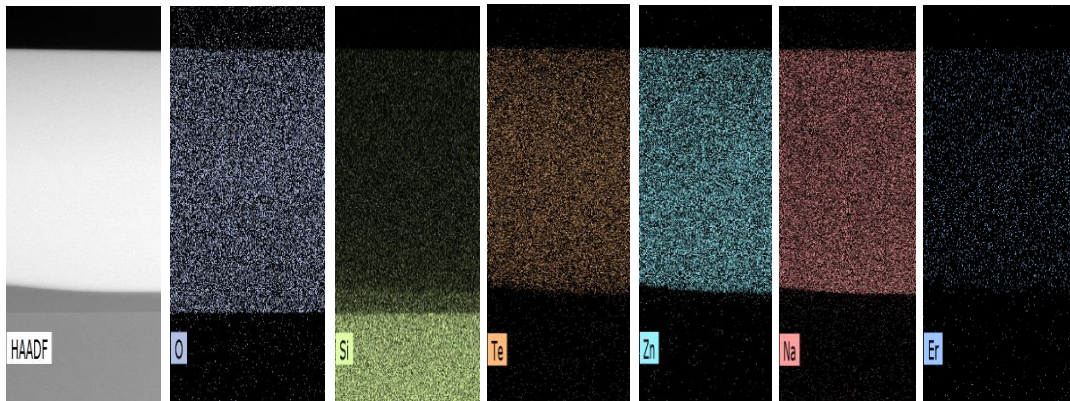
Figure 4.3: Area scan obtained by EDX-STEM for sample A80.

From the cross-section backscattered SEM images (Figure 4.1 (b)-(d)), the EDTS looked brighter than silica and silicon layers. This is attributed to the presence of heavy elements such as Er and Te in the EDTS which resulted in a stronger average backscattered electron flux. Conversely, the silica layer enriched with a light element like oxygen appeared darker compared to silicon and the EDTS. All samples did not show any detectable clustering of Er^{3+} ions in SEM images. In order to further prove that the EDTS did not have any clustering of Er^{3+} ions, a sample fabricated with the fs-laser energy of 80 µJ underwent TEM and STEM measurement due to the better resolution image compared to SEM. Figure 4.4 (a) shows the bright-field TEM while Figure 4.4 (b) is the STEM-HAADF. Both images did not present any detectable of Er^{3+} ion clusters in the EDTS.
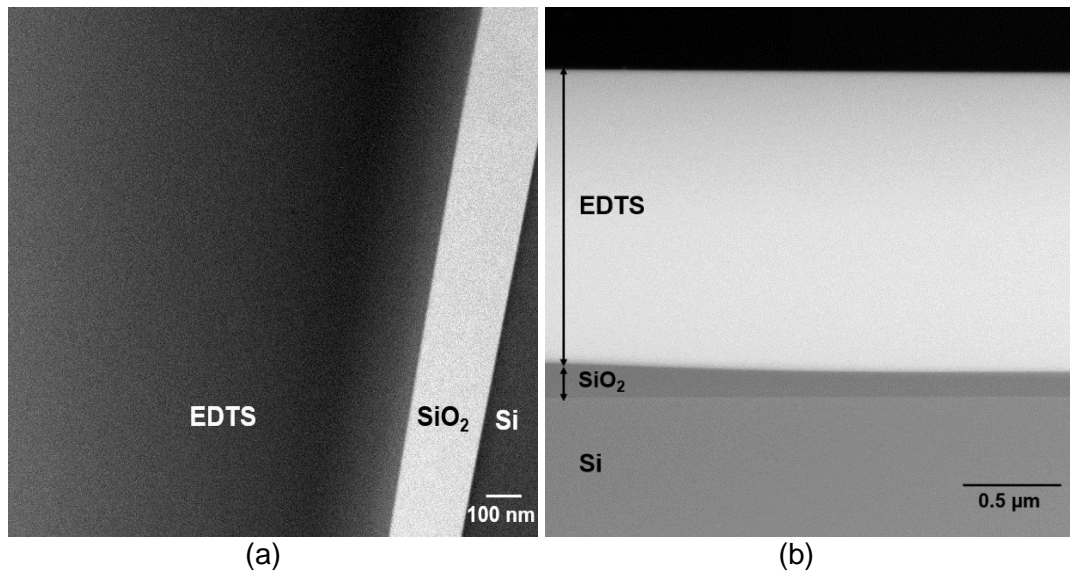
Figure 4.4: (a) The bright-field TEM image (b) STEM-HAADF image, of the sample prepared using 80 μJ (A80).

Formation of the EDTS layer is a result of the impact and dissolution of the high energy laser produced plasma plume at the heated substrate material. The heated substrate provides activation energy needed to mediate the process and later to dynamically break and remake the strong Si-O-Si covalent bond in silica. This helped high energy ions and nanoparticles from the target glass to penetrate into the host glass network and modify the original silica structure at the molecular level. The structural modification of laser plasma-silica substrate and formation of a well-defined metastable EDTS layer has been previously reported [24,26,86]. This is applicable to SOS substrate materials but at a lower temperature compared to silica glass [85]. Further discussions on temperature dependence are provided in Section 4.2. An additional feature of the process, the expansion of silica due to doping of Er-TZN into it, is observed clearly in Figure 4.5. The cross-section shows in three different areas namely, (a) the fully exposed middle of the sample, (b) the region close to the shadow of the substrate holder and, (c) the area of the sample where the substrate is fully shadowed by the substrate holder. The expansion of the silica layer upwards on the formation of ETDS is clearly evident. The thickness gradient in section (b) might be due to the effect of the edge of the substrate holder which reduces the incident plasma density.
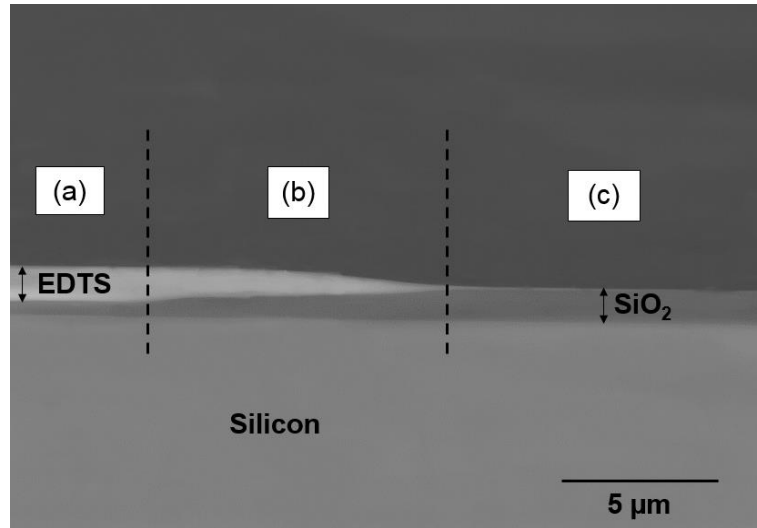
Figure 4.5: Backscattered SEM image for sample A60 taken to show the expansion of silica due to Er-TZN doping. It is divided into three main parts which are (a) the fully exposed middle of the sample (b) region close to the shadow of the substrate holder and (c) the area of the sample where the substrate is fully shadowed by the substrate holder.

Besides that, it is noticed by EDX-SEM (Table 4.2) that the concentration of Zn, Na, Te, and Er are increased when higher fs-laser energy is employed which is consistent with the volume increment of target glass that has been removed during ablation. It is also observed that concentration of Te in the EDTS is quite low even though TeO_2 is a major component in the target material. This is due to the fact that Te is the most volatile element and structurally unstable in Er-TZN. This could have caused its depletion during its transport towards the substrate [24,194,195]. Other than that, Zn which is more volatile than Na [196] also contributes to its lower density compared to Na in the EDTS.

The EDTS layer refractive index of the samples was measured using a prism coupler (at 633 nm) and reported in Table 4.3. The refractive index increased in tandem with the laser energy increment as more elements are ablated from the target material and integrated with the host material. This also confirms the increase in density of the layer discussed earlier. The increase in thickness of the EDTS layer with laser energy is visible from the SEM images shown in Figure 4.1 (b)-(d) and confirmed by the data reported in Table 4.3. This increase in depth which is due to a higher incident ion flux from the laser produced plasma at higher energies. The prism coupler measurement also confirmed the increase in EDTS thickness with incident fs-laser energy on the target material (Table 4.3). On the other hand, the thickness of the pristine silica layer became lowered due to the modification of the silica surface which had transformed

to the EDTS layer progressively especially when higher laser energy was used. However, further higher laser energies (above ~80 µJ) led to cracks and ruptures of the doped layer due to high surface strain. This could be ascertained clearly when laser energy as high as 100 µJ was used as illustrated in Figure 4.6. No further characterisations of the sample prepared at 100 µJ s (A100) were carried out as it was considered damaged.

Table 4.3: Thickness of the EDTS layer and undoped silica underneath the EDTS and the refractive index of the EDTS for samples A50, A60, and A80.

Sample	EDTS thickness measured with SEM (µm)	EDTS thickness measured with prism coupler (µm)	SiO₂ thickness below EDTS layer measured with SEM (µm)	Refractive Index
A50	0.81 ± 0.06	0.83 ± 0.05	0.56 ± 0.06	1.5587 ± 0.0004
A60	1.05 ± 0.02	0.99 ± 0.04	0.43 ± 0.02	1.5690 ± 0.0003
A80	1.56 ± 0.08	1.56 ± 0.04	0.22 ± 0.07	1.6172 ± 0.0005
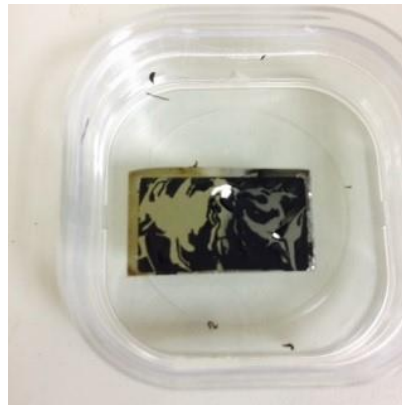
Figure 4.6: EDTS layer cracked and ruptured when fs-laser energy 100 µJ was used.

The difference in the thickness measured by the prism coupler and SEM results from the non-uniform thickness across the surface of the layer. The uneven thickness could be seen under low magnification SEM as shown in Figure 4.7 (a)-(c). The thickness measurement using SEM and prism coupler were made around the middle of the sample to be comparable. However, the exact location could not be determined very accurately for these two separate measurements. Hence, the measured thickness for both instruments showed small differences.
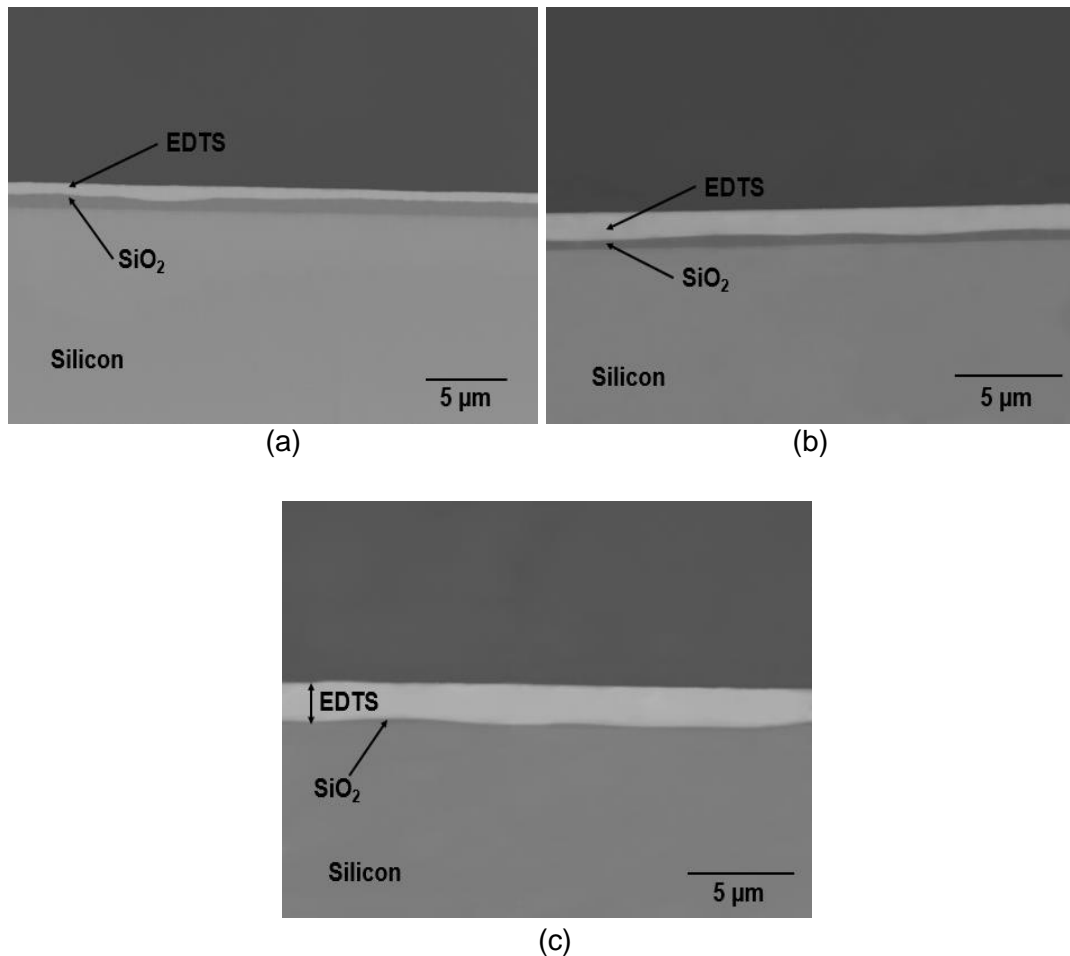
Figure 4.7: Backscattered cross-section SEM image of low magnification for samples doped with Er-TZN by using (a) 50 µJ (A50), (b) 60 µJ (A60) and (c) 80 µJ (A80) fs-laser energy.

The XRD patterns of the SOS substrate and samples A50, A60 and A80 are displayed in Figure 4.8. These samples did not show any sharp crystalline peaks except the peak at $2\theta = 69°$ which corresponded to the underlying silicon, Si (100) of the SOS substrate. This proved the amorphous nature of the EDTS layer. The broad silicon peak is probably due to the defects that originates from the effects of thermal oxidation of silicon. At the interface region of Si-SiO$_2$, there will be at least one layer of silicon atoms that are bonded both with oxygen and silicon atoms. These silicon atoms are in the intermediate oxidation states (+1, +2, +3, depending on the number of oxygen atoms they are bound) [197,198]. The presence of these silicon atoms with intermediate states are source of defects [199] which can make the intermediate layer become disordered. As the beam penetration depth is probable limited to the intermediate layer, this results in the producing of broad peak in XRD patterns. On the other hand, around 30°, an additional amorphous halo away from the silica halo (peaked around 22º), relating to the amorphous nature of the material became more

visible when higher laser energy was used. This halo that appeared around $2\theta = 30°$ matched with other reported silicate glasses such as SiO_2-ZrO_2 [200], calcium silicate [201] and SiO_2-MgO-CaF_2-CaO-SrO-SrF_2 [202]. This indicated that when doping concentration became higher in silica and transformation of silica matrix to silicate glass became much more obvious. In sample A50, due to a lower concentration of Er-TZN compared to other samples fabricated with higher laser energy, the silicate halo is relatively weak. The amorphous nature of the EDTS layer is also confirmed by selective area electron diffraction (SAED) as shown in Figure 4.9. It was captured from the centre of the EDTS layer that displayed a hollow ring. The diffraction pattern showed that no long-range order existed in the EDTS layer as was expected from the XRD measurement. This clearly points to the conclusion that the resultant modified layer is amorphous in nature.

Photoluminescence (PL) emission spectra were measured using a 980 nm diode laser as the excitation source. The PL emission band peaked at around 1535 nm resulting from the $^4I_{13/2} \rightarrow$ $^4I_{15/2}$ transition that, excited by a 980 nm laser diode, was recorded for all samples. The PL emission spectra obtained for samples prepared with different fs-laser energies are reported in Figure 4.10. All samples displayed identical spectral shape with two peaks at wavelengths of 1535 and 1543 nm. The appearance of the second peak has been said to be due to the Stark splitting effect of the two energy levels involved [31]. From Figure 4.10, it can be seen that PL intensity increased with laser energy for fabrication and this is due to an increase in Er^{3+} ions concentration. Other than that, full half width maximum (FWHM) obtained from emission spectra for all samples are 20 nm as reported in Table 4.4. FWHM and emission spectra obtained are identical to erbium-doped silicate glasses such as soda lime silicate, phosphosilicate and borosilicate reported before [203,204]. This confirmed again that Er-TZN had permeated into the silica glass network and transformed it into silicate glass. The PL lifetime difference also varied with laser energy as shown in Table 4.4. The decline in the PL lifetime with an increase in laser energy can be attributed to the higher Er^{3+} ions concentration. The increase of Er^{3+} ions density in the EDTS reduces the average spacing between Er-Er ions and this leads to the quenching effect because of energy migration between Er^{3+} ions [204].
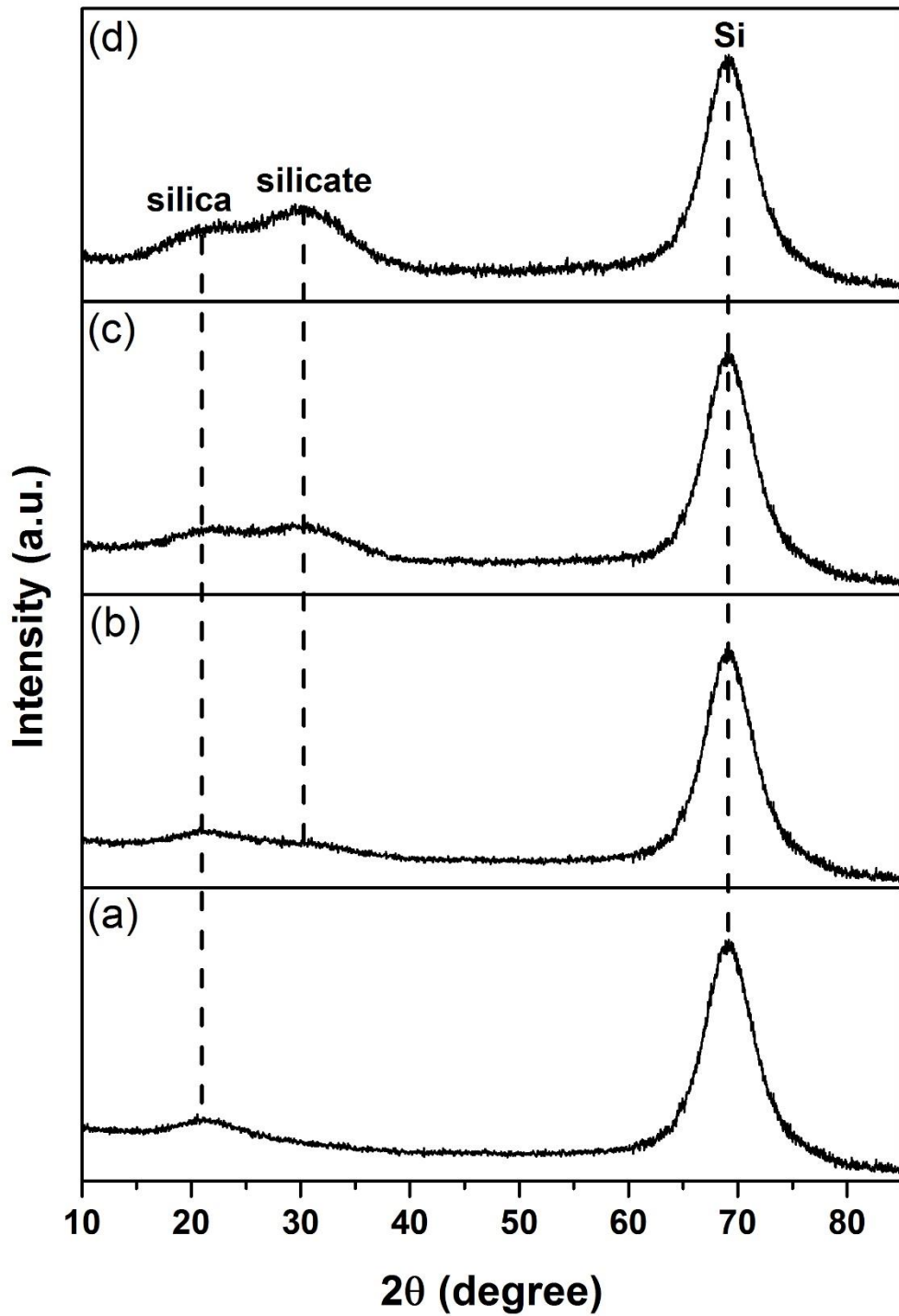
Figure 4.8: XRD patterns for (a) SOS substrate, and samples prepared by using fs-laser energies of (b) 50 µJ (A50), (c) 60 µJ (A60), and (d) 80 µJ (A80). The $2\theta = 69°$ peak is from silicon of the SOS substrate underneath the silica layer and the EDTS.
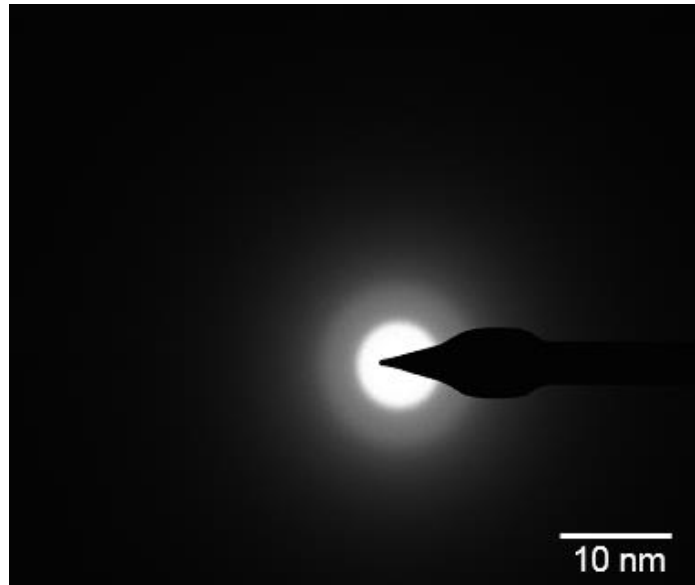
Figure 4.9: SAED captured in the centre of the EDTS for sample fabricated by 80 μJ fs-laser energy.
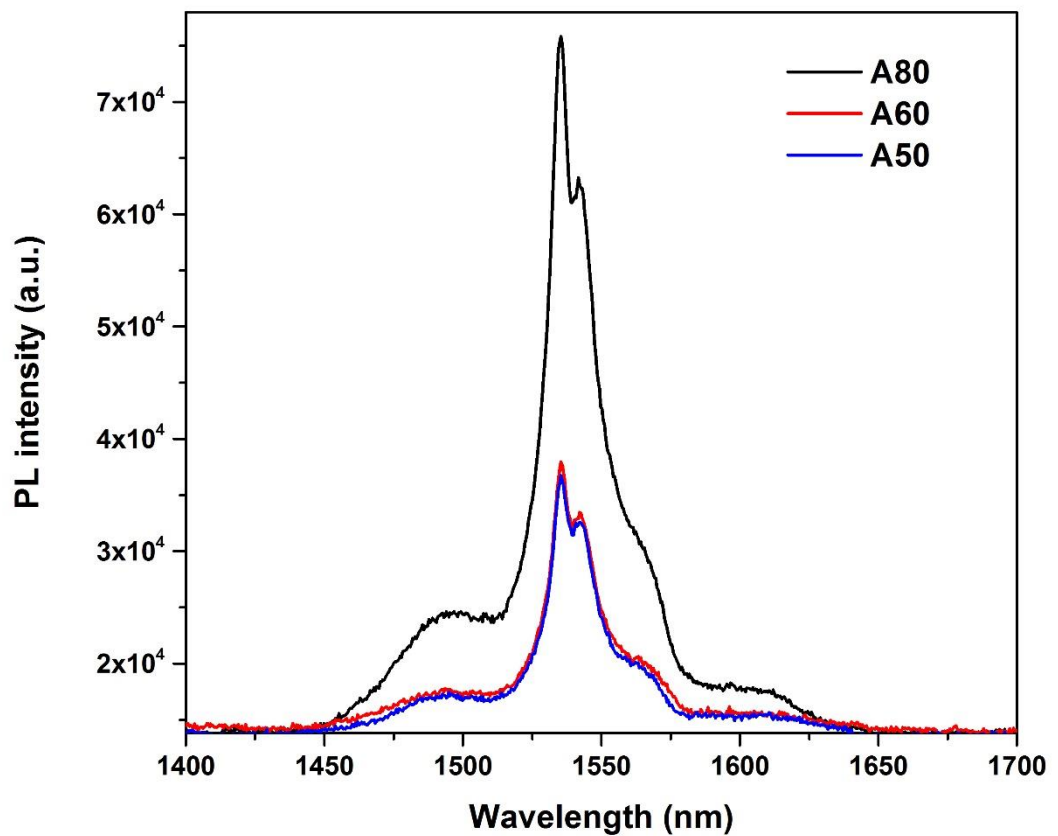
Figure 4.10: Photoluminescence spectra obtained with emission peaked around 1535 nm for samples fabricated at various fs-laser energies. The excitation wavelength used was 980 nm.

Table 4.4: FWHM and photoluminescence lifetime obtained from samples that had been prepared with different fs-laser energies.

Sample	FWHM (nm)	PL lifetime (ms)
A50	20	12.29
A60	20	12.21
A80	20	10.79

4.2 Dependence substrate temperature on the EDTS

The substrate temperature is found to be of utmost importance to allow Er-TZN to penetrate into a silica glass network. Strong -O-Si-O- covalent bonds can be modified by the incoming plasma plume when appropriate temperatures are used to heat the substrate. Thus, three samples with different substrate heating temperatures were prepared and are reported in Table 4.5 with the other process parameters used. Figure 4.11 (a)-(c) showed backscattered cross-section SEM for samples fabricated when substrates were heated at temperatures of 400 °C, 570 °C and 700 °C.

Table 4.5: List of parameters employed to dope Er-TZN into SOS substrate by using various substrate temperatures.

Process parameter	Operating conditions
Substrate	Silica (t=1 µm)-on-silicon (SOS)
Target material	$79.5TeO_2$-$10ZnO$-$10Na_2O$-$0.5Er_2O_3$ (Er-TZN)
Fs-laser energy	50 µJ
Fs-laser repetition rate	1.0 kHz
Substrate temperature (sample name)	400 °C (B400), 570 °C (B570) and 700 °C (B700)
Ablation period	4 hours
Background gas pressure	70 mTorr O_2

From Figure 4.11 (a), it could be concluded that the doping process did not succeed at 400 °C, it only resulted in a deposited layer on the substrate. The thickness of the original silica layer (Table 4.6) remained at ~1 µm proving that no doping process actually happened for sample B400. This indicated that a temperature of 400 °C is not sufficient enough for the incoming plasma plume to modify the strong covalent bonds of silica. The film formed on the SOS is only Er-TZN glass film with compositions as presented in Table 4.7 where Te concentration is much higher than Si. Figure 4.11 (a) and top view image (Figure 4.12 (a) and (b)) captured under an optical microscope, however, demonstrates the poor surface quality of the film thus formed. The surface appears very rough with clusters of microparticles. Such film is not suitable for an EDWA as it would cause large surface scattering and ultimately

propagation loss for laser signals. On the other hand, the data in Table 4.7 showed that the sample where the substrate was heated at 700 °C had lower Te concentration compared to the sample prepared at 570 °C. This is due to the volatility of Te [194,195] which caused severe depletion through evaporation at a high temperature. However, the high temperature used to heat up the substrate gave way to more elements from the target glass except for Te to penetrate the silica. It is noted that the higher temperature caused the bond silica to be weakened and increased the reaction among the elements contained in the plume (except Te) with silica.

(a)   (b)

(c)
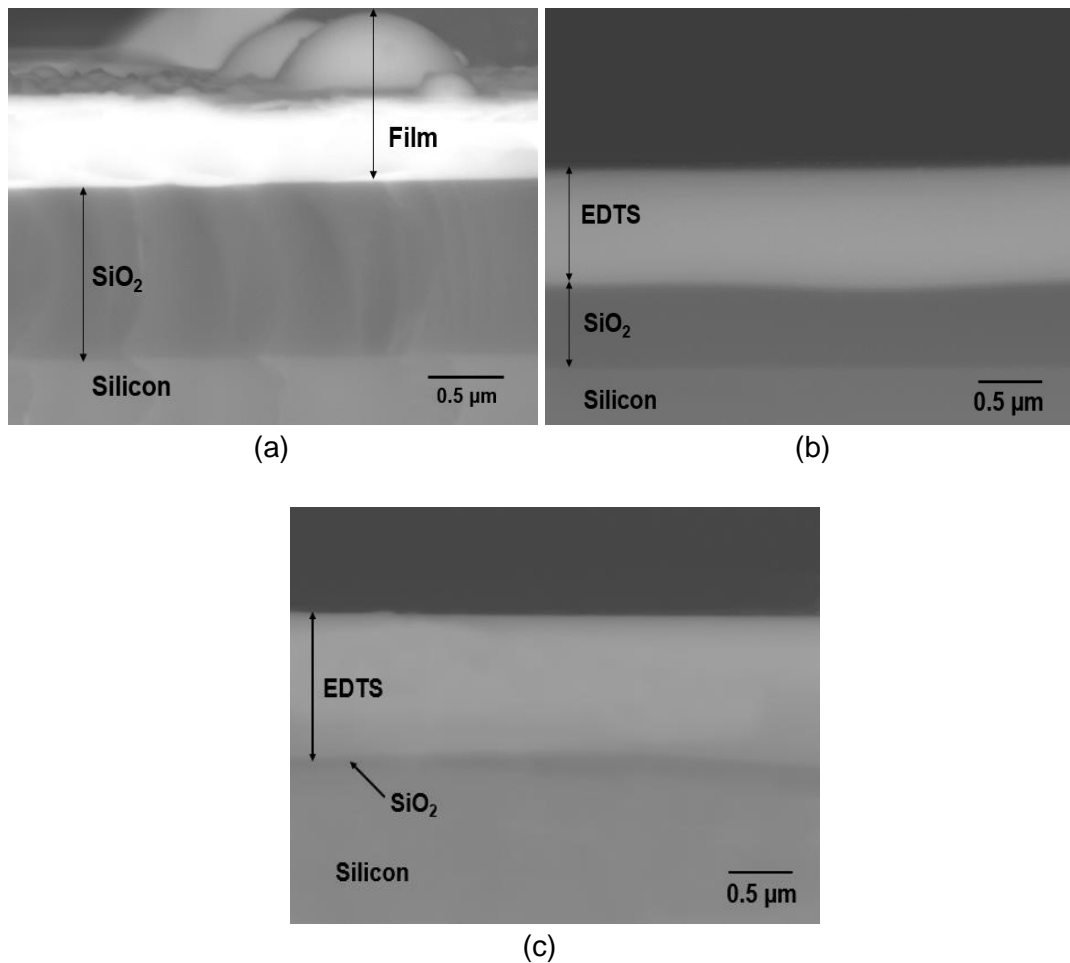
Figure 4.11: Backscattered cross-section SEM image of samples doped with Er-TZN when substrate was heated at (a) 400 °C (B400), (b) 570 °C (B570) and (c) 700 °C (B700).

As shown in Table 4.6, the thickness and the refractive index of sample B(400) could not be accurately determined by the prism coupler due to its rough sample surface. On the other hand, the higher temperature used, caused the materials from Er-TZN (except Te) could penetrate more into silica and this caused a thicker EDTS. The reduced concentration of Te in sample B700, which is a heavy element in the EDTS, caused the refractive index to decline. Therefore, the concentration of Te in the EDTS

is vital as it can control the increase of the refractive index which, in turn, can contribute to the design of integrated optical waveguides using the ULPD approach presented in this thesis.

Table 4.6: Variation upper layer and remaining silica layer thickness and refractive index prepared at different substrate temperatures.

Sample	EDTS thickness measured with SEM (μm)	EDTS thickness measured with prism coupler (μm)	SiO$_2$ thickness below EDTS layer measured with SEM (μm)	Refractive Index
B400	-	-	1.03 ± 0.03	-
B570	0.81 ± 0.06	0.83 ± 0.05	0.56 ± 0.06	1.5587 ± 0.0004
B700	1.10 ± 0.03	1.10 ± 0.01	0.22 ± 0.06	1.5285 ± 0.0002

(a)   (b)
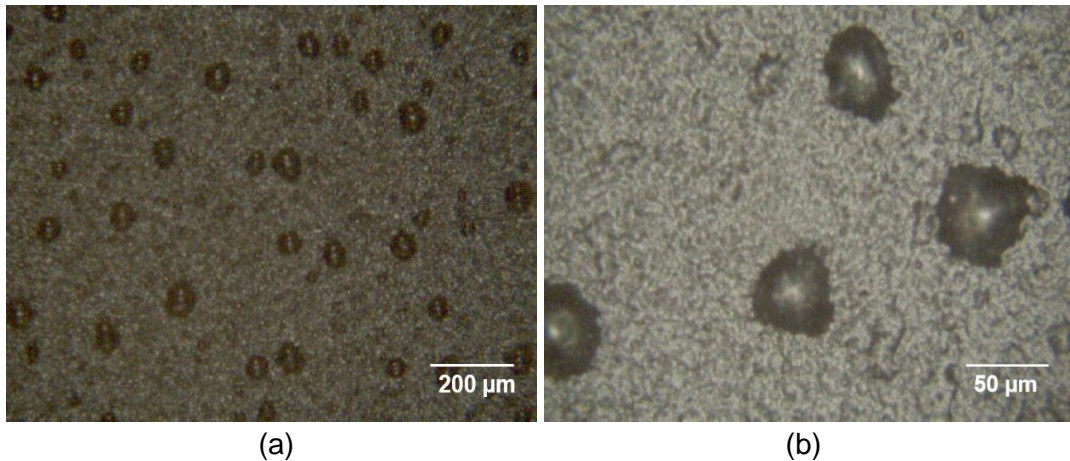
Figure 4.12: Top view surface for sample B400 obtained from optical microscope with different magnifications.

Table 4.7: The percentage of components existing in the upper layer of SOS substrate for samples that were fabricated using different substrate temperatures.

Element	Elemental concentration (at. %)		
	Sample B400	Sample B570	Sample B700
O	50.69	61.01	60.91
Si	1.67	21.47	20.99
Na	7.94	8.57	9.68
Zn	6.60	6.77	7.14
Te	32.21	1.74	0.73
Er	0.89	0.44	0.55

Figure 4.13 shows the XRD patterns of SOS doped with Er-TZN when the substrate was heated to 400 °C, 570 °C, and 700 °C. For samples B570 and B700, the EDTS obtained are amorphous while, for B400, it clearly shows that the deposited film is crystalline with a distinct peak at *2θ* = 19.16°, 28.86°, 49.02° and 59.68°. For peaks 19.16° and 59.68°, they refer to $Zn_2Te_3O_8$ based on the ICCD reference code: 04-012-2189 with each having miller indices of ($\bar{1}11$) and (332) while, for peaks 28.86° and 49.02°, they matched with Na_2TeO_3 with miller indices of (022) and (242), respectively (ICDD reference code:00-035-1263).

PL emission spectra for a substrate heated by various temperatures are represented in Figure 4.14. It is clear that for sample B400, spectrum shape obtained is different from sample B570 and B700. FWHM for sample B400 is broader in comparison to samples B570 and B700 and is almost similar to reported tellurite glasses [53,205,206]. For sample B570 and B700, the obtained FWHM is 20 nm, and this is similar to FWHM of other silicate glasses as discussed in Section 4.1. Table 4.8 also reports the PL lifetime for samples B400, B570 and B700. Sample B400 had the lowest PL lifetime (5.26 ms) compared to sample B570 (12.29 ms) and B700 (11.12 ms). The obtained PL lifetime for erbium-doped tellurite glass obviously is much lower than erbium-doped silicate glass as reported for other erbium-doped tellurite glasses which are TeO_2–GeO_2–Na_2O–ZnO–Er_2O_3 [19], TeO_2-WO_3-Na_2O-Er_2O_3 [51] and TeO_2–WO_3–Na_2O-Nb_2O_5-Er_2O_3 [207]. The lower PL lifetime for sample B400 is due to it being essentially a tellurite host material with stoichiometry similar to the target glass. It is well known that PL lifetime also depends strongly on host material [208,209] which is closely related to the refractive index of the host material based on the Judd-Ofelt theory. According to the theory, lifetime has an inverse relationship with refractive index [210–212]. Because tellurite glass has a higher refractive index than silicate glass, therefore it exhibits a lower lifetime, and this is the main reason that PL lifetime for sample B400 was far lower than for samples B570 and B700.
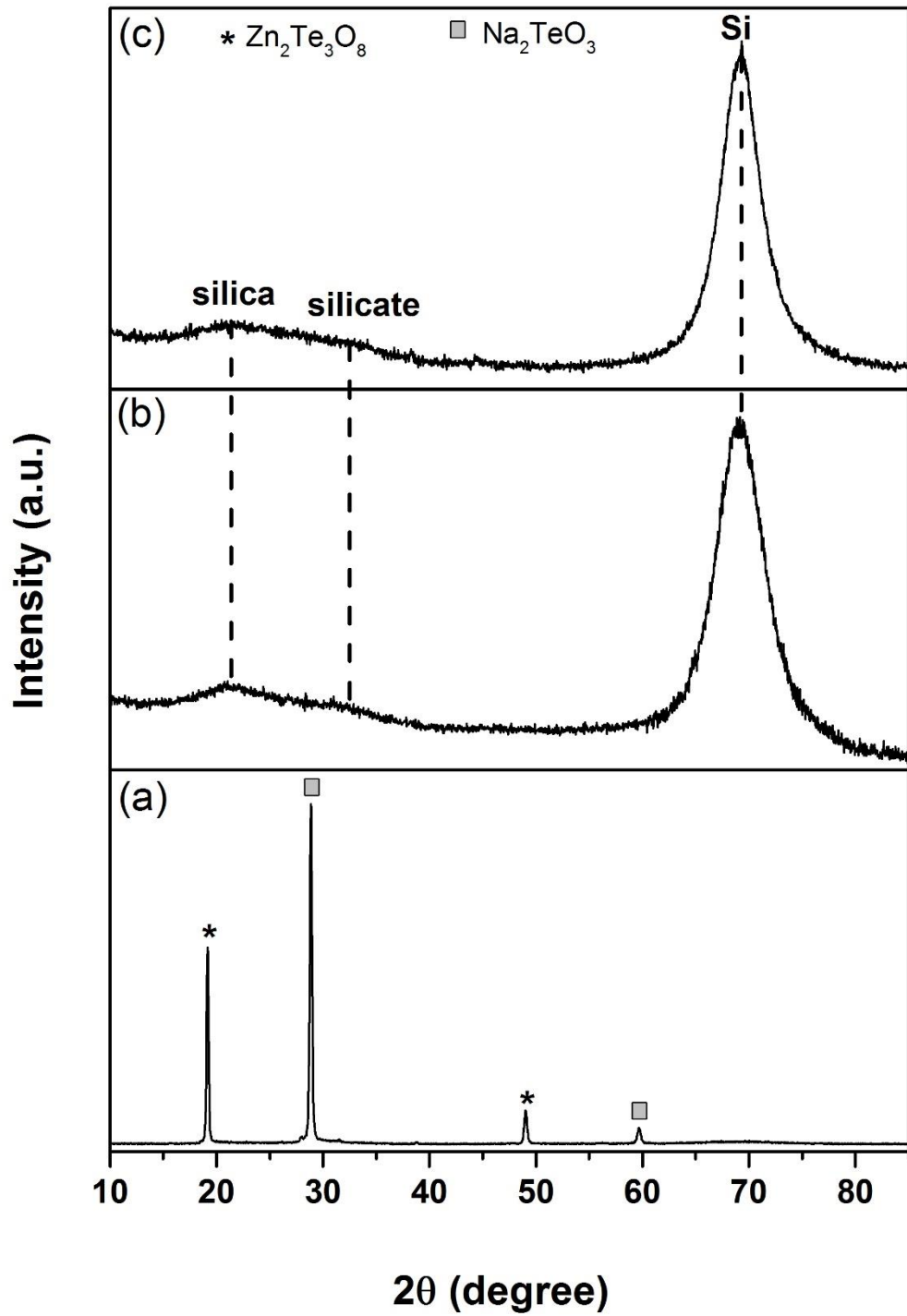
Figure 4.13: XRD patterns for samples prepared using temperature of (a) 400 °C (B400), (b) 570 °C (B570) and (c) 700 °C (B700).
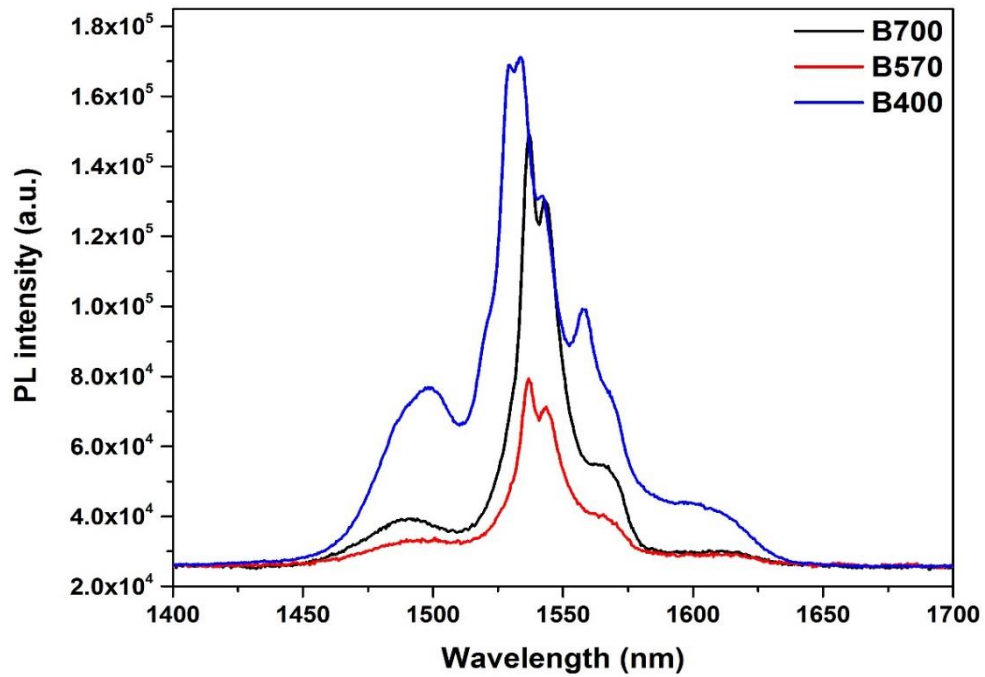
Figure 4.14: PL spectra of upper layer prepared at different substrate temperatures.

Table 4.8: FWHM and PL lifetime for film fabricated at different substrate temperatures.

Sample	FWHM (nm)	PL lifetime (ms)
B400	38	5.26
B570	20	12.29
B700	20	11.12

4.3 Dependence fs-laser repetition rate on the EDTS

The effect of fs-laser repetition rate on EDTS properties was also analysed. Both samples were prepared according to parameters detailed in Table 4.9 and samples C0.5 and C1 were named according to the fs-laser repetition rates (0.5 kHz and 1 kHz) used.

Table 4.9: List of parameters used to dope Er-TZN into SOS substrate by using various fs-laser repetition rates.

Process parameter	Operating conditions
Substrate	Silica (t=1 µm)-on-silicon (SOS)
Target material	$79.5TeO_2$-$10ZnO$-$10Na_2O$-$0.5Er_2O_3$ (Er-TZN)
Fs-laser energy	50 µJ

Fs-laser repetition rate (sample name)	0.5 kHz (C0.5) and 1.0 kHz (C1)
Substrate temperature	570 °C
Ablation period	4 hours
Background gas pressure	70 mTorr O_2

The different repetition rates used in this work for sample preparation were 0.5 kHz and 1 kHz. Only two repetition rates are reported due to the limitation on the fs-PLD instrument used for this work. The XRD measurement results in Figure 4.15 showed that both samples are amorphous in nature. As seen in Figure 4.16 (a) and (b) and also in Table 4.10, the EDTS layer thickness produced for samples 0.5 kHz is 0.412 µm which is almost half of the thickness of the sample fabricated using an fs-laser 1 kHz (0.806 µm). When the repetition rate is doubled, the collision cascade density is expected to increase as the plasma fluence is higher [213]. Therefore, the thickness of the doped layer is increased when a higher repetition rate is used. The refractive index of the EDTS also increases when a higher fs-laser repetition is used as illustrated in Table 4.10. This phenomenon is well predicted as more elements from the target material are removed and interacted with the silica. Therefore, the doping concentration is higher for 1 kHz as measured using EDX-SEM in Table 4.11. As there is more Er content in the EDTS for sample C1, the PL intensity for this sample is higher when compared to sample C0.5 (Figure 4.17). The FWHM for these two samples are almost the same (19-20 nm) and matched with other erbium-doped silicate glass. Again, due to the lower Er density in the EDTS for sample C0.5, the PL lifetime is longer at 14.07 ms as compared to sample C1 which is only 12.29 ms.
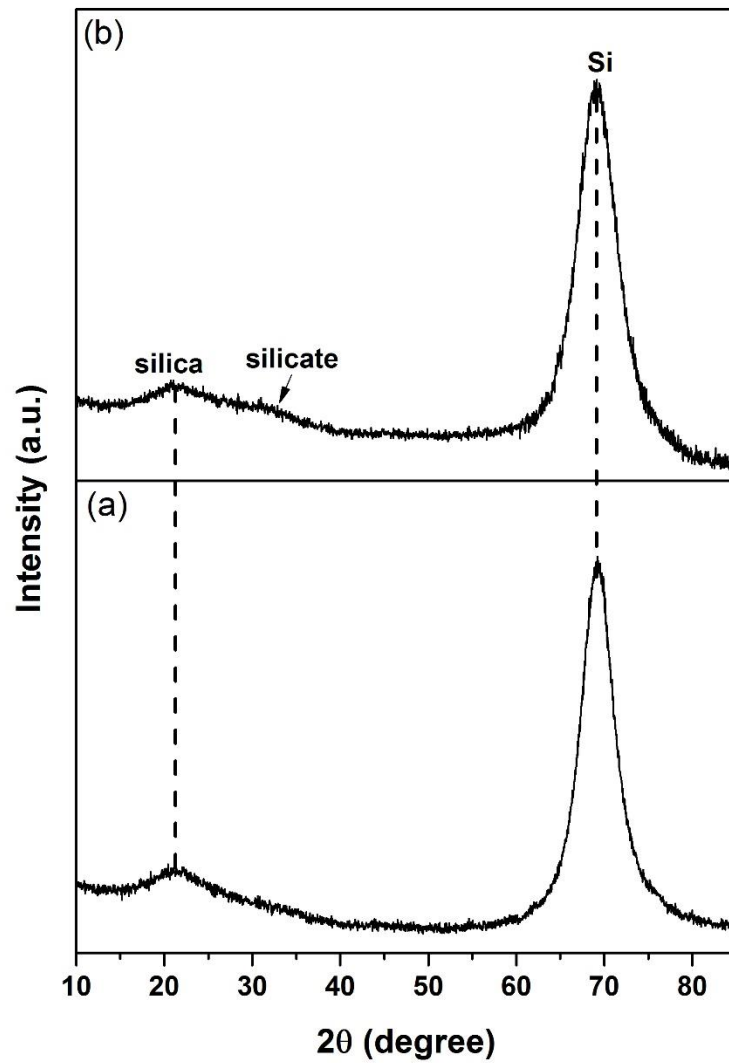
Figure 4.15: X-ray diffraction patterns of samples prepared by using two different fs-laser repetition rates: (a) 0.5 kHz (C0.5) and (b) 1.0 kHz (C1).
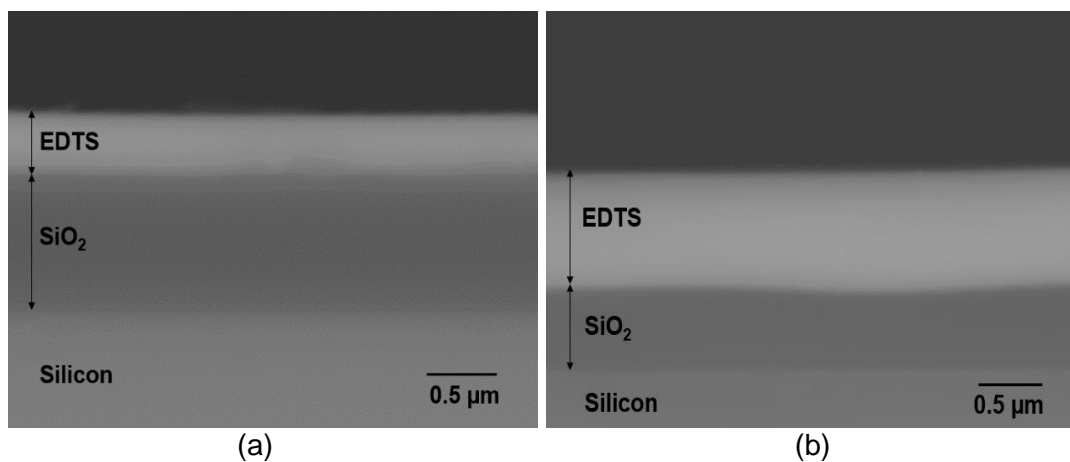
Figure 4.16: Backscattered cross-section SEM image for samples doped with Er-TZN by using fs-laser repetition rates of (a) 0.5 kHz (C0.5) (b) 1.0 kHz (C1).

Table 4.10: Thickness of the EDTS layer and remaining silica layer underneath the EDTS and the refractive index of the EDTS prepared at different fs-laser repetition rates.

Sample	EDTS thickness measured with SEM (µm)	EDTS thickness measured with prism coupler (µm)	SiO$_2$ thickness below EDTS layer measured with SEM (µm)	Refractive Index
C0.5	0.41 ± 0.09	0.47 ± 0.03	0.83 ± 0.06	1.5300 ± 0.0003
C1	0.81 ± 0.06	0.83 ± 0.05	0.56 ± 0.06	1.5587 ± 0.0004

Table 4.11: Elemental composition of the EDTS layer measured by EDX-SEM for samples C0.5 and C1.

Element	Elemental concentration (at. %)	
	C0.5	C1
O	62.57	61.01
Si	29.78	21.47
Na	4.17	8.57
Zn	2.13	6.77
Te	1.06	1.74
Er	0.29	0.44
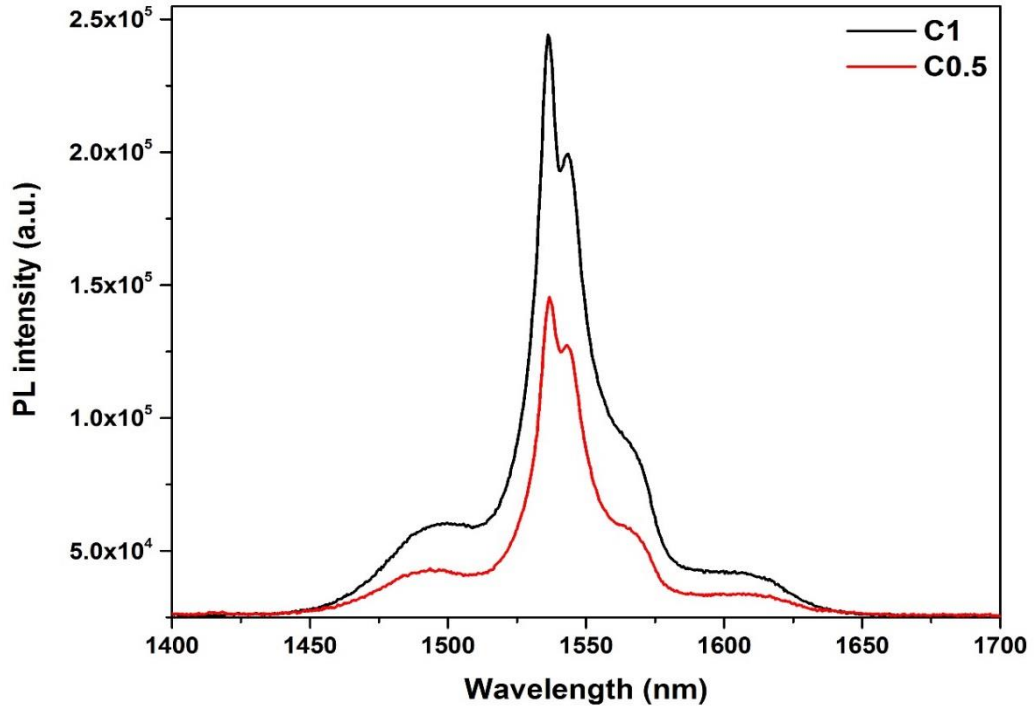
Figure 4.17: PL pattern of the EDTS layer prepared with fs-laser repetition rates of 0.5 kHz and 1.0 kHz.

4.4 Dependence ablation period on the EDTS

Two types of substrates were used to study the influence of different ablation periods on the properties of the EDTS. The substrates used were SOS and silica on silicon-on-insulator (SOI) substrate. For the substrate silica on SOI, three different silica thicknesses were used which were 10 nm, 15 nm, and 25 nm.

4.4.1 Silica-on-silicon (SOS) substrate with silica thickness of 1 μm

Four samples were prepared with SOS substrate having 1 μm silica layer. The ablation period was varied between four to ten hours. Parameters used in this experiment are summarised in Table 4.12. Sample ID of F4, F6, F8, and F10 with respect to the ablation period of 4 hours, 6 hours, 8 hours and 10 hours are also included in Table 4.12.

Table 4.12: List of parameters used to dope Er-TZN into SOS substrate using different ablation periods.

Process parameter	Operating conditions
Substrate	Silica (t=1 μm)-on-silicon (SOS)
Target material	$79.5TeO_2$-$10ZnO$-$10Na_2O$-$0.5Er_2O_3$ (Er-TZN)
Fs-laser energy	50 μJ

Fs-laser repetition rate	1.0 kHz
Substrate temperature	570 °C
Ablation period (sample name)	4 hours (F4), 6 hours (F6), 8 hours (F8) and 10 hours (F10)
Background gas pressure	70 mTorr O_2

Figure 4.18 (a)-(c) showing a backscattered cross-section SEM for three samples fabricated with different ablation periods (4, 6 and 8 hours). The EDTS layer thickness measured using SEM and also the prism coupler are listed in Table 4.13. As anticipated, the thickness of the EDTS increased when a longer ablation period was used as more elements from Er-TZN entered into the silica. Unfortunately, sample F10 broke into pieces in the UHV chamber during the process. This could have been due to a substrate which exceeded its limit and could no longer withstand the bombardment of a high energy plume. At a certain limit, the substrate became fragile and finally shattered. No characterisation could be done for this sample.

Interestingly, in sample F8, the silica layer was completely modified, and small crystallites appeared at the interface between the silicon and the EDTS. This phenomenon could have happened due to the failure of elements from Er-TZN to penetrate into the silicon and accumulate at the silicon border. Elements from Er-TZN, which is rich with oxygen, would have difficulty to modify the silicon and subsequently crystallised at the interface due to oxygen deficiency at the interface. Furthermore, the resultant EDTS layer for this sample had an adhesion problem. This can be seen in Figure 4.19 where the film disengaged slightly from silicon when conventional TEM sample preparation was done for that sample. The problem did not persist for other samples that had no small crystallite on the interface as shown in Figure 4.4 previously.

Wax that was used to stick the sample back to back, which is one of the conventional procedures to prepare a TEM sample, is believed to have pulled the doped layer away from the substrate. This case is often associated with intrinsic tensile stress that might have been due to lattice mismatch between the film and substrate, incorporation of foreign atoms, crystallite coalescence at the grain boundaries, a variation of interatomic spacing with crystal size and phase transformation [214,215]. Figure 4.20 shows the line scan EDX-STEM that is performed at the area. It clearly showed that the black area in the image to be the empty space with very high noise surrounding the area.

(a)

(b)

(c)
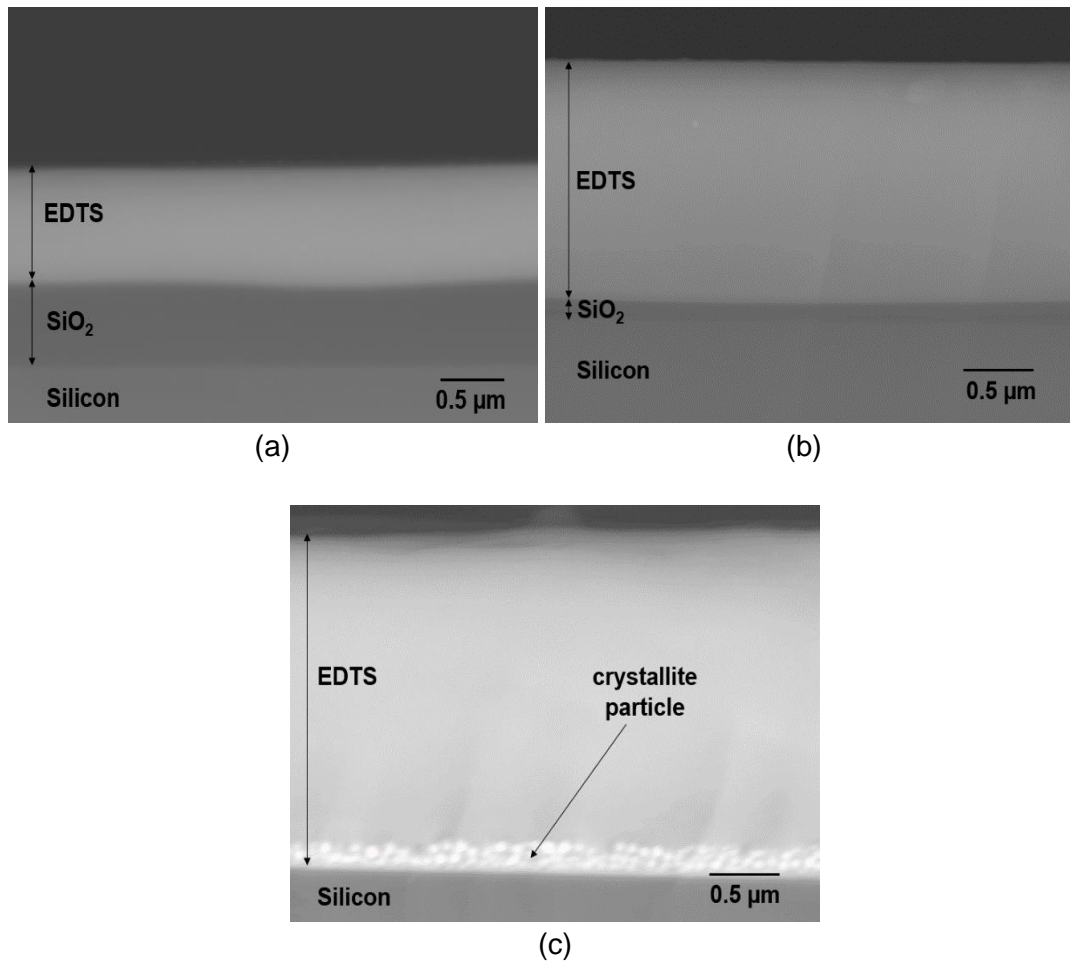
Figure 4.18: Backscattered cross-section SEM image of samples doped with Er-TZN when target had been ablated for (b) 4 hours (F4), (b) 6 hours (F6) and (c) 8 hours (F8).

Table 4.13: Thickness of the EDTS layer and remaining silica layer underneath the EDTS and the refractive index of the EDTS prepared with different ablation periods.

Sample	EDTS thickness measured with SEM (µm)	EDTS thickness measured with prism coupler (µm)	SiO_2 thickness below EDTS layer measured with SEM (µm)	Refractive Index
F4	0.81 ± 0.06	0.834 ± 0.05	0.56 ± 0.06	1.5587 ± 0.0004
F6	1.36 ± 0.03	1.307 ± 0.05	0.11 ± 0.03	1.5915 ± 0.0005
F8	1.94 ± 0.02	1.928 ± 0.05	-	1.6172 ± 0.0003
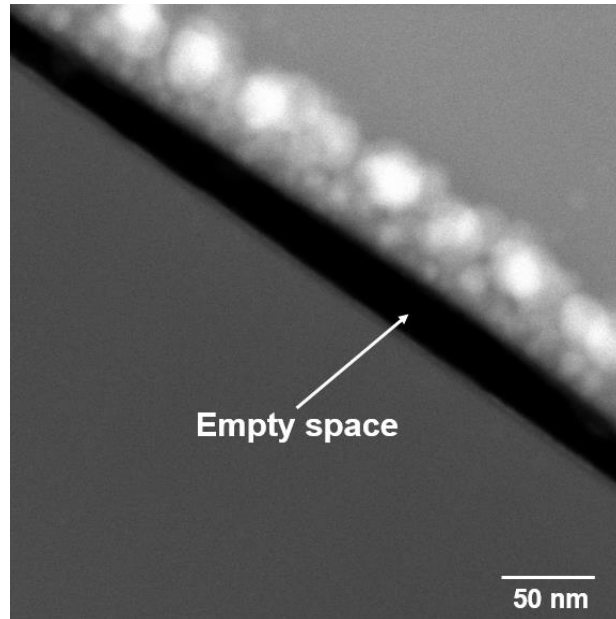
Figure 4.19: Doped layer is observed been peeled off after conventional TEM preparation. The black area between the film and silicon substrate is an empty space.
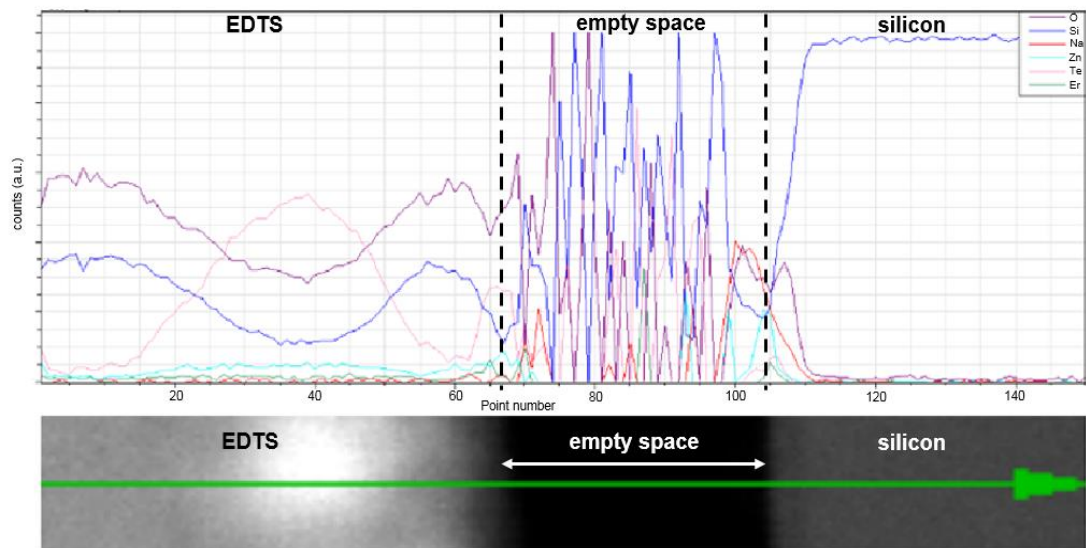
Figure 4.20: Line scan obtained from EDX-STEM showing that no element was detected at the empty space between the film and silicon substrate.

Despite this, the primary element for a crystallite particle is Te as the line scan shown in Figure 4.20. In order to investigate more about the element that might be present for the small crystallite, an area scan measurement using EDX-STEM was made. Figure 4.21 (a) – (g) shows the cross-section and the area scan for an element that is present in the sample. This small crystallite was identified again to be Te as shown in the area scan in Figure 4.21 (d). Te concentration is at the highest around the area where the small crystallite accumulated. The point scan measured from EDX-SEM also showed that Te concentration is as high as 8.81 at. % in the area as illustrated

in Figure 4.22 and Table 4.14. Commonly, Te concentration in a typical EDTS is within the range 1-3 at. % depending on the parameter used. Apart from the adhesion issue, the presence of crystallite particles needed to be avoided as it would only contribute to the escalation of optical propagation loss for waveguide application [216].

(a)

(b)

(c)

(d)

(e)

<div align="center">(f)   (g)</div>
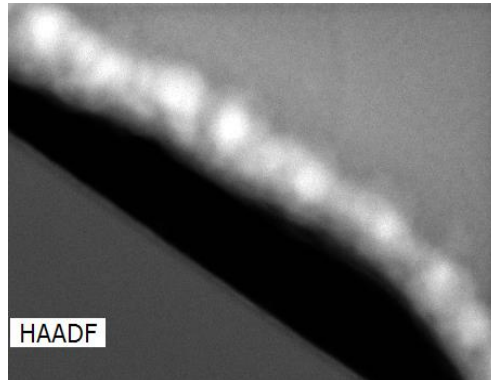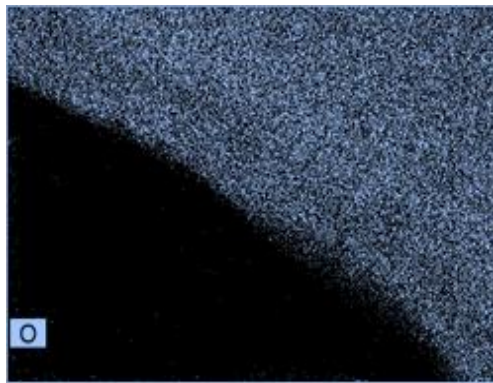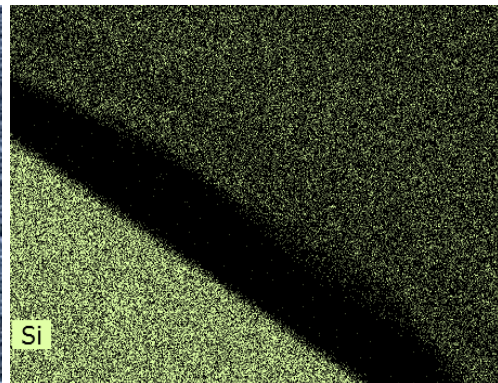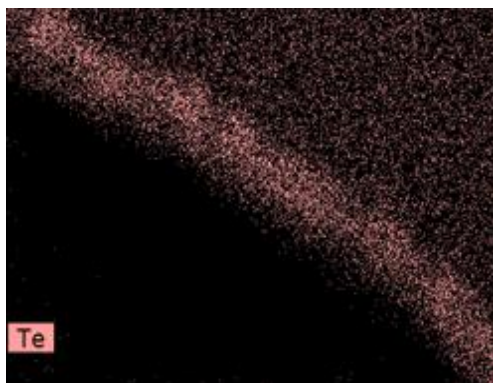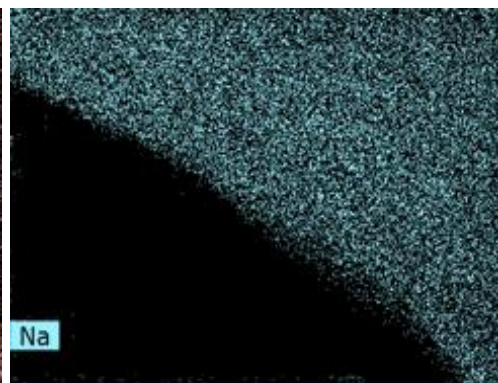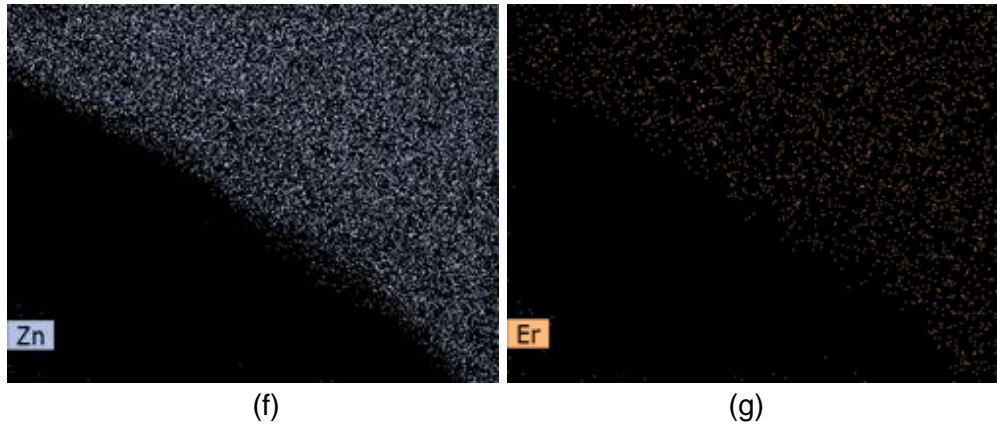
Figure 4.21: Area scan measured by EDX-STEM for sample F8 with (a) the area being measured. The distribution of species present in it are (b) oxygen, (c) silicon, (d) tellurium, (e) sodium, (f) zinc and (g) erbium.
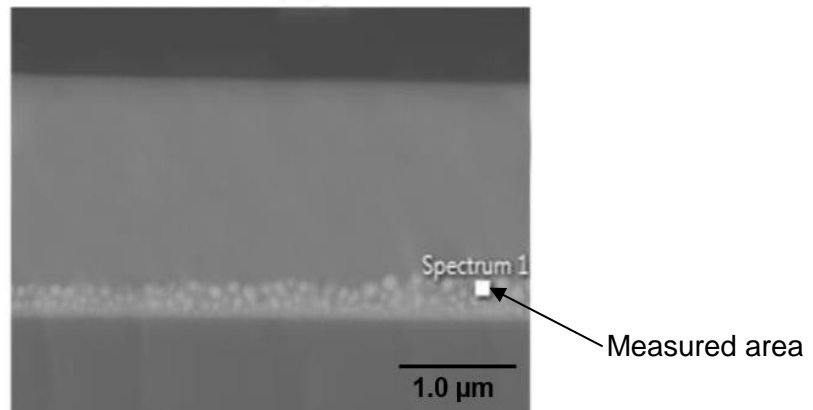
Figure 4.22: Point EDX-SEM measurement done at crystallite particle accumulation area.

Table 4.14: Elemental concentration at measured area shown in Figure 4.22 obtained by EDX-SEM.

Element	Atomic percent (at. %)
O	51.05
Si	27.64
Na	6.78
Zn	4.69
Te	8.81
Er	1.03

The prism coupler measurement also showed that the EDTS refractive index increased in parallel with the ablation period increment (Table 4.13). This was due to the increased amount of elements from Er-TZN entering the silica over time, as exemplified in Table 4.15.

Table 4.15: Elemental density of the EDTS layer measured by EDX-SEM for different ablation period samples.

Element	Elemental concentration (at. %)		
	Sample F4	Sample F6	Sample F8
O	61.01	60.96	57.81
Si	21.47	19.24	18.50
Na	8.57	10.50	11.45
Zn	6.77	6.86	7.98
Te	1.74	1.82	3.15
Er	0.44	0.62	1.11

From the XRD patterns, as shown in Figure 4.23, the halo around 30ºC is more visible for the longer ablation period because EDTS network that better resembles a silicate network due to the entrance of a generous amount of materials from Er-TZN into silica. However, for sample F8, a few peaks pointed to the presence of crystallite particle in the EDTS which are believed originated from small crystallite located at the border of the EDTS and silicon. For these patterns, twelve peaks which corresponded to 2θ of 23.05º, 27.62º, 38.40º, 40.44º, 43.31º, 46.22º, 49.62º, 51.28º, 56.88º, 62.95º, 63.74º and 82.19º were observed. All peaks corresponded to Te (ICCD reference code: 00-036-1452) and this matched with the inference of Te crystal formation on analysing EDX-SEM and EDX-STEM.

The PL spectra as exhibited in Figure 4.24, showed that the PL intensity increased with ablation period. The intensity of the sample with an ablation period of 8 hours to be the most followed by those with 6 and 4 hours. This is a direct consequence of the increase in Er^{3+} ions with a longer ablation period. All samples had similar FWHM which was ~20 nm while the PL lifetime decreased with ablation period as shown in Table 4.16. This decrease clearly indicates that the ablation period not only affects the thickness of the layer but also the doping concentration. The decrease in lifetime is a direct consequence of an increase in Er^{3+} ion concentration and associated concentration quenching discussed in Section 4.1.
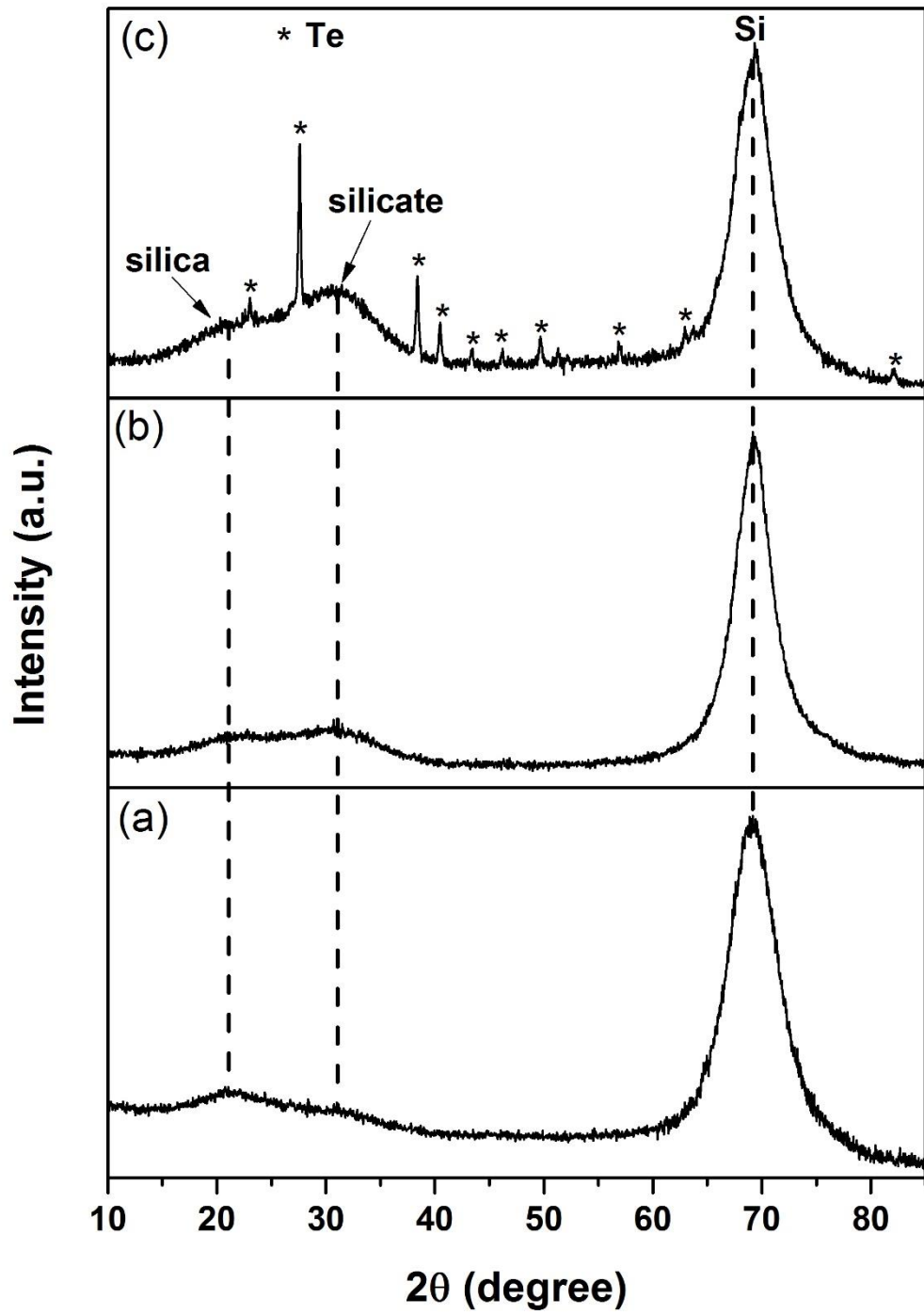
Figure 4.23: XRD patterns for the EDTS layer prepared by ablating the Er-TZN for (a) 4 hours (F4), (b) 6 hours (F6) and (c) 8 hours (F8).
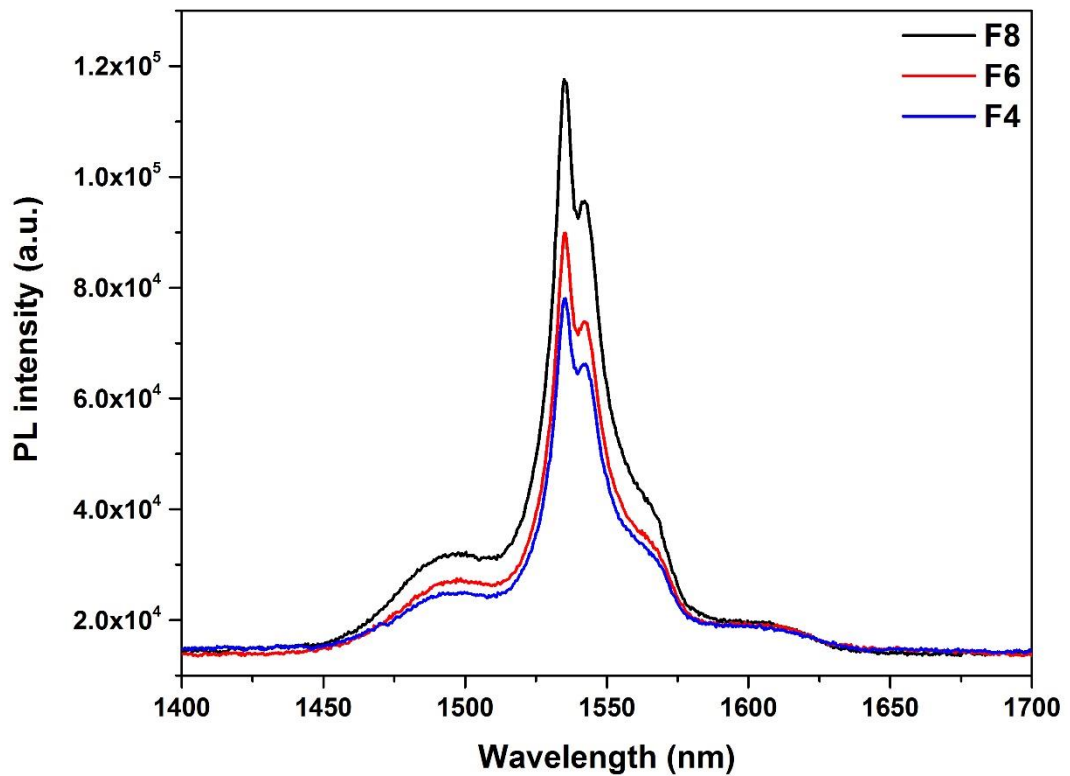
Figure 4.24: Comparison of the photoluminescence intensity of the EDTS layer with ablation period.

Table 4.16: FWHM and PL lifetime for sample fabricated using different ablation periods.

Sample	FWHM (nm)	PL lifetime (ms)
F4	20	12.29
F6	20	10.69
F8	20	9.71

4.4.2 Silica on silicon-on-insulator (SOI) substrate

This section reports on the results for the samples prepared using silica on silicon-on-insulator (SOI) with various silica thicknesses used as substrates. The silica thicknesses were 10, 15 and 25 nm. As the thicknesses of the silica were very low and varied, the ablation period for each was very short and differed depending on the silica thickness. The parameters used to fabricate the samples are tabulated in Table 4.17. Samples with different silica thicknesses 10 nm, 15 nm and 25 nm are labelled as G10, G15, and G25.

Table 4.17: List of parameters used to dope Er-TZN into silica on SOI substrate using different ablation periods and silica thicknesses.

Process parameter	Operating conditions
Substrate	Silica (t=10 nm, 15 nm and 25 nm) on silicon-on-insulator (SOI)
Target material	$79.5TeO_2$-$10ZnO$-$10Na_2O$-$0.5Er_2O_3$ (Er-TZN)
fs-laser energy	50 µJ
Repetition rate	1.0 kHz
Substrate temperature	570°C
Ablation period (sample name)	2 minutes for 10 nm (G10), 6 minutes for 15 nm (G15) and 11 minutes for 25 nm (G25)
Background gas pressure	70 mTorr O_2

Cross section images for these three samples were recorded under bright-field TEM as the EDTS layer created for each sample was extremely thin. The images obtained are shown in Figure 4.25 (a)-(c). On observing these images it is evident that there are some darker regions/spots in the EDTS layer. It can be concluded that the mixing of Er-TZN and silica is not homogeneous in these samples. The very short process duration has caused the elements of Er-TZN to be crystallised or phase separated within the silica. Further tuning of the laser pulse energy and duration of the process would be required to optimise such very thin EDTS layers.

(a)   (b)
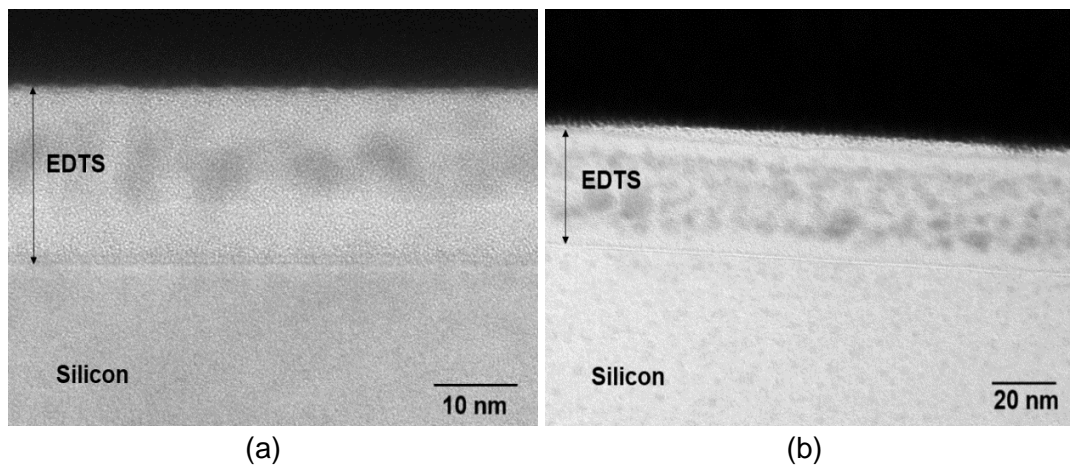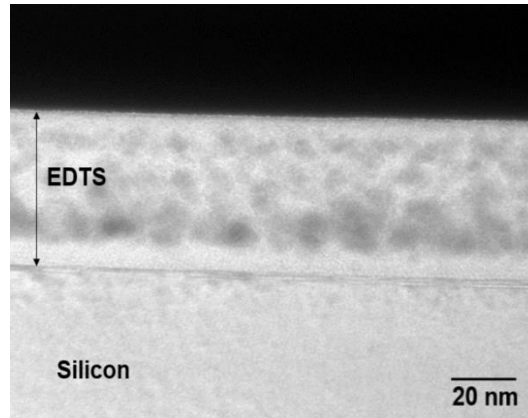
(c)

Figure 4.25: Bright-field image of the sample prepared using different silica thicknesses on SOI substrate. For (a), it is the sample which has an initial silica thickness of 10 nm while (b) and (c) have initial silica thicknesses of 15 nm and 25 nm.

Because of the very low concentration of elements from Er-TZN and their uneven distribution in the EDTS due to the very short ablation period, quantitative estimations from EDX-STEM are prone to errors. Furthermore, the very low concentration of elements from Er-TZN in sample G10 resulted in the area scan for this sample having too much noise contributing to unreliable and inaccurate results. Therefore, an area scan to detect the presence of species from Er-TZN in the EDTS was only done for samples G15 and G25 (Figure 4.26 and Figure 4.27). Comparing the image contrast in Figure 4.26 and Figure 4.27, it can be inferred that more Er-TZN elements are present in the EDTS layer when the ablation period is longer. A line scans, as shown in Figure 4.28 and 4.29, also confirmed the presence of Er-TZN elements in the doped layer. Iridium presence is due to the use of it as a surface protective layer when FIB sample preparation was performed. Furthermore, the thickness of the upper layer as shown in Table 4.18 increased from the initial thickness. It could be ascertained that there is an expansion of the silica layer because of the doping process. For this sample set, PL characterisation could not be done accurately because of the very thin EDTS and very low PL intensity.
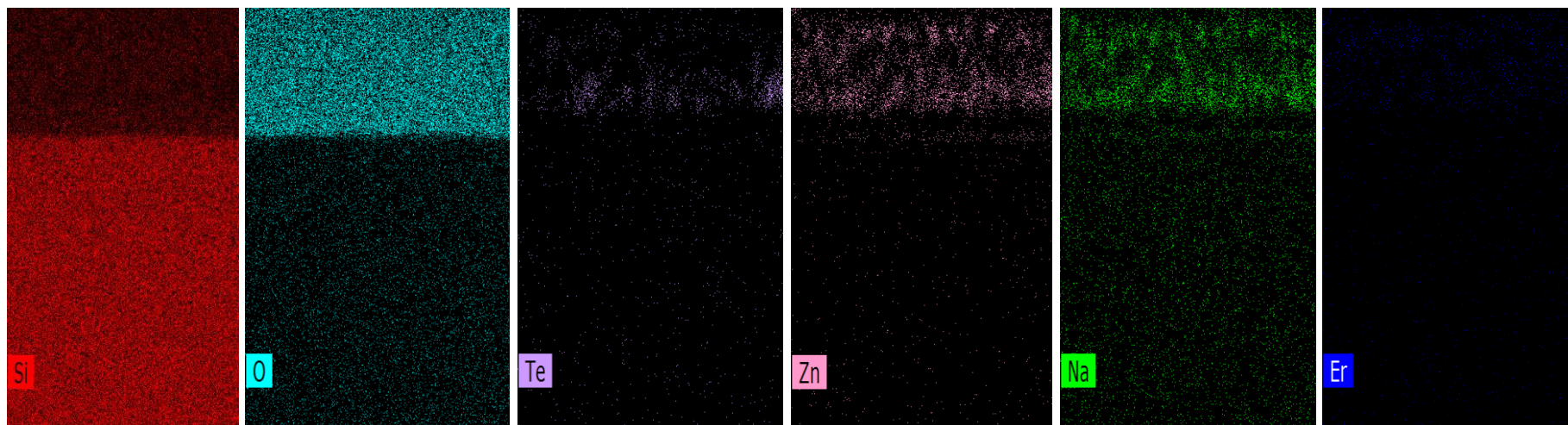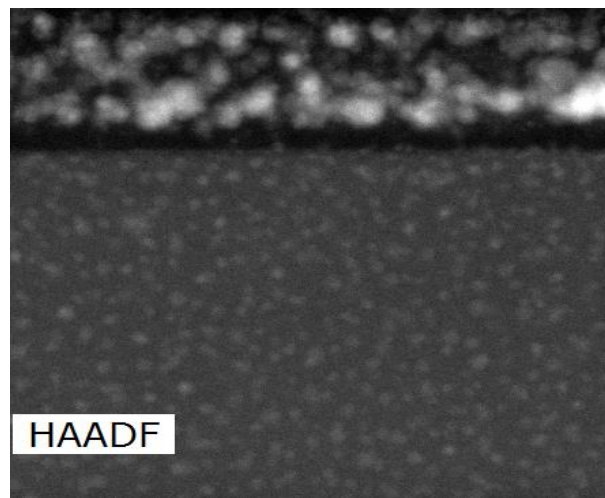
Figure 4.26: Area scan for sample using silica (15 nm) on SOI substrate that underwent an ablation period of 6 minutes (G15).
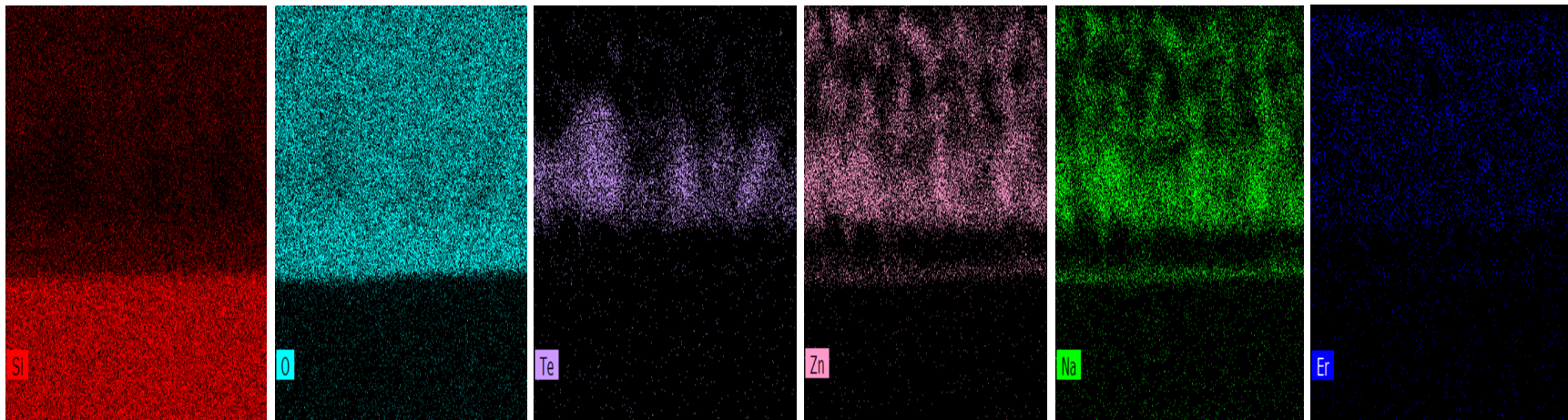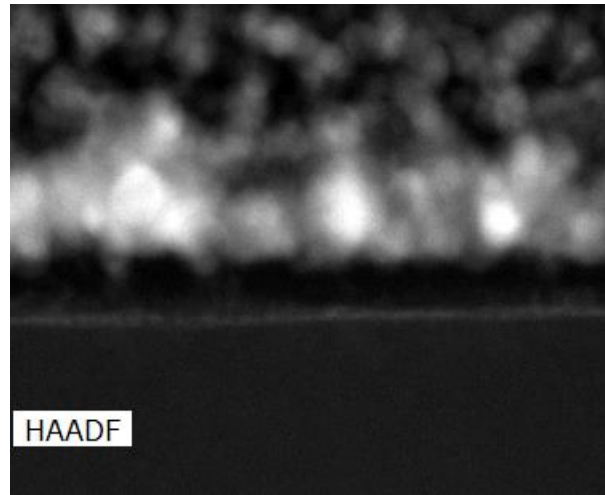
Figure 4.27: Area scan for sample using silica (25 nm) on SOI substrate that underwent an ablation period of 11 minutes (G25). .
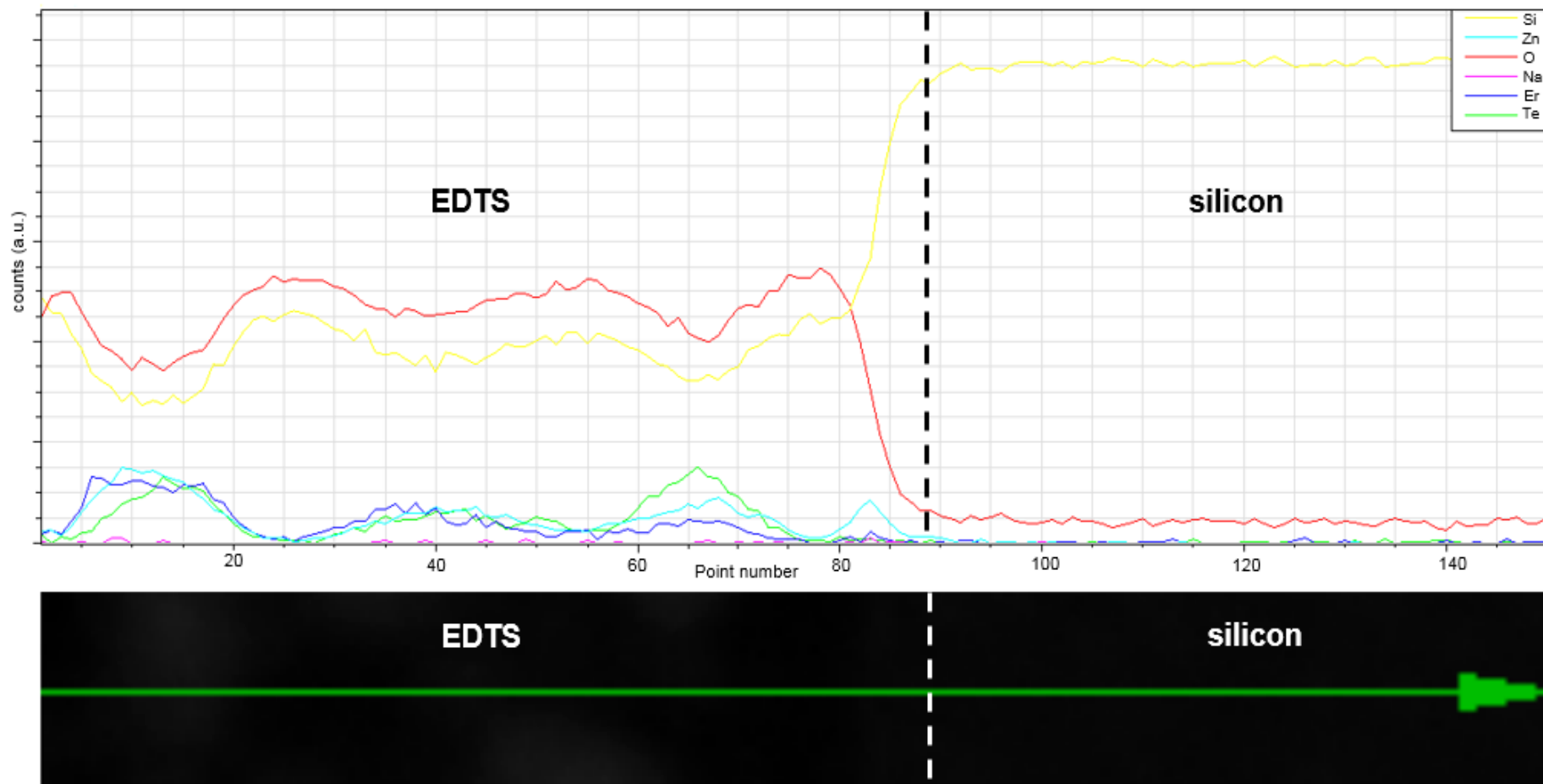
Figure 4.28: Line scan of the sample using silica (15 nm) on SOI substrate that underwent an ablation period of 6 minutes (G15).
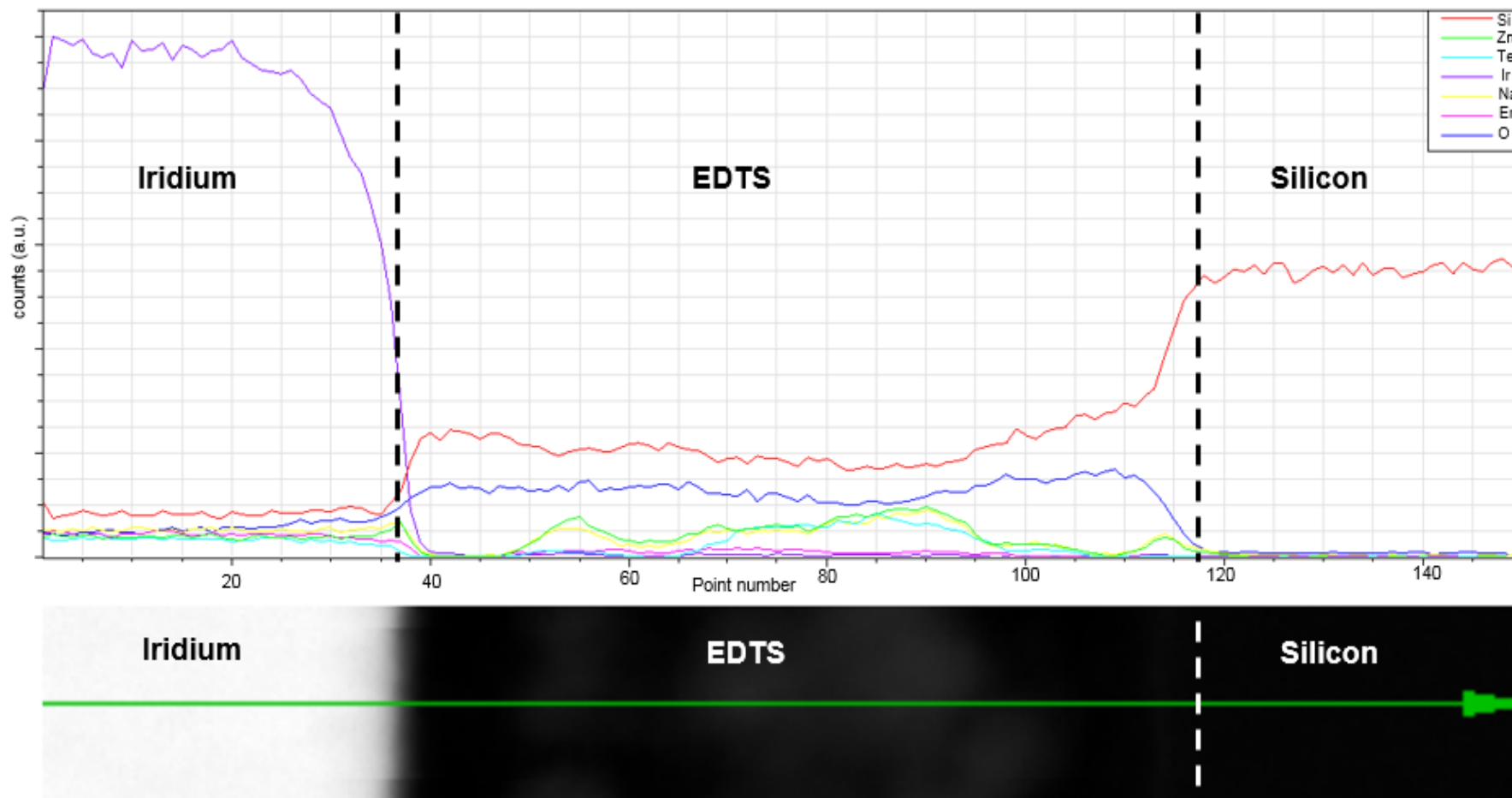
Figure 4.29: Line scan of the sample using silica (25 nm) on SOI substrate that underwent an ablation period of 11 minutes (G25).

Table 4.18: EDTS layer thickness for different ablation periods used for different silica thicknesses on SOI substrate determined by TEM.

Sample	EDTS thickness measured with TEM (nm)
G10	24.0 ± 0.4
G15	40.2 ± 0.1
G25	65.3 ± 0.4

4.5 Dependence ambient oxygen gas pressure on the EDTS

The ambient gas pressure in the process chamber is an important parameter in the ULPD technique. Generally, plasma plume can be distributed much more widely with background gas pressure during the ablation process. For this work, since the target material used was oxide glass and the substrate was SiO_2, oxygen was chosen as the background gas to ensure a surrounding rich with oxygen thus facilitating the formation of defect free Er-TZN and SiO_2 glass formation. Even though ambient pressure does not affect the path or laser beam absorption, the produced plasma plume characteristics depended heavily on it. Parameters selected to study the relationship between background oxygen gas pressure and EDTS characteristics are reported in Table 4.19. Samples with the names H50, H70, H90, and H100 represent those prepared at oxygen gas pressures of 50 mTorr, 70 mTorr, 90 mTorr and 100 mTorr respectively. As shown in Figure 4.30 (a)-(d) and Table 4.20, the EDTS layer thickness increased when low oxygen gas pressure was used. This is a direct consequence of the surging kinetic energy of the plasma plume at lower pressures. The collision between ablated species (Er-TZN) with O_2 species during the flight to substrate became fewer at lower pressures which, in turn, allowed for more elements from Er-TZN to reach the substrate and gained enough energy to penetrate into the silica layer [217]. The outcome is that the penetration of Er-TZN elements into silica became more aggressive thus increasing the EDTS thickness at lower oxygen gas pressures.

Table 4.19: List of parameters used to study the relationship between background oxygen gas pressures and EDTS properties.

Process parameter	Operating conditions
Substrate	Silica (t=1 µm)-on-silicon (SOS)
Target material	$79.5TeO_2$-$10ZnO$-$10Na_2O$-$0.5Er_2O_3$ (Er-TZN)
fs-laser energy	50 µJ
Repetition rate	1.0 kHz
Temperature	570°C
Ablation period	4 hours

Background gas pressure (sample name)	50 mTorr (H50), 70 mTorr (H70), 90 mTorr (H90) and 100 mTorr (H100) O_2
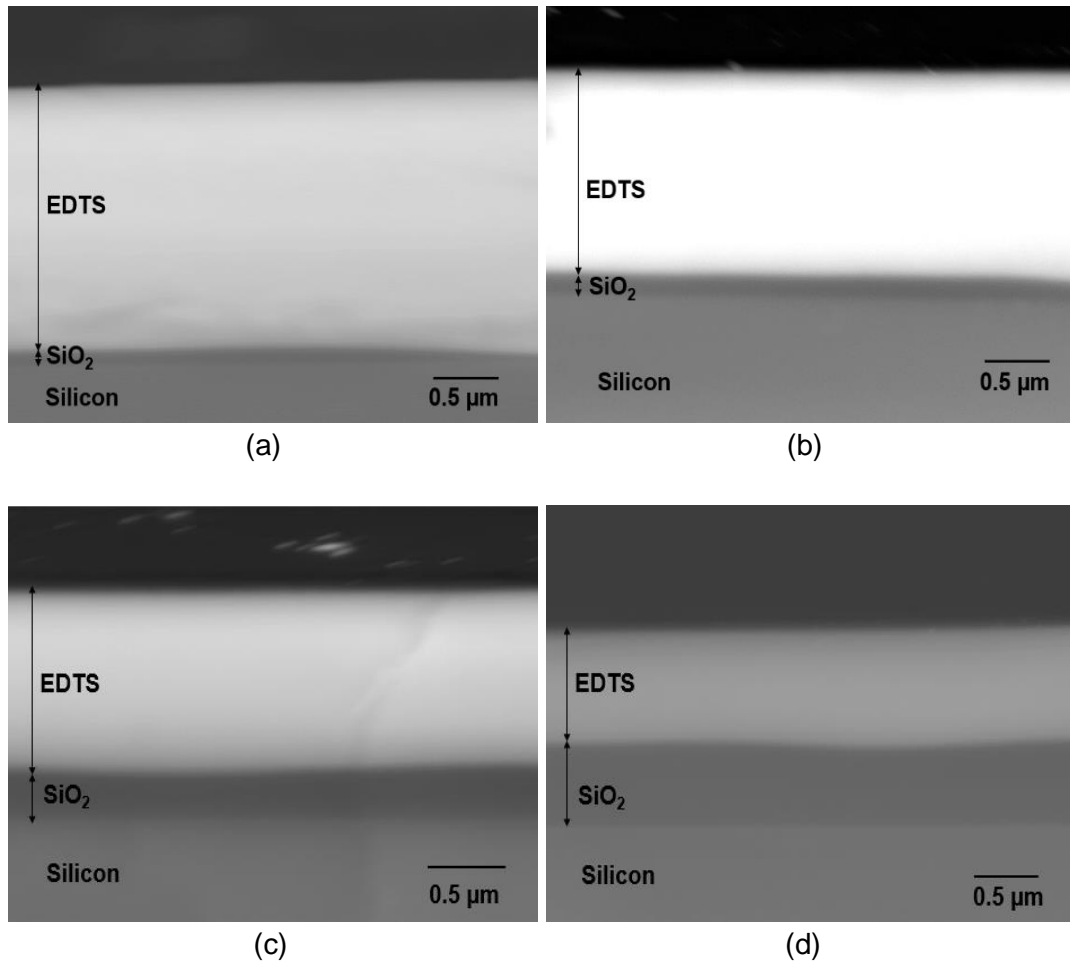
Figure 4.30: Backscattered cross-section SEM image of SOS doped with Er-TZN using background oxygen gas pressures of (a) 50 mTorr (H50), (b) 70 mTorr (H70), (c) 90 mTorr (H90) and (d) 100 mTorr (H100).

The reduction in the measured refractive index and lower EDTS thickness as a result of lower doping concentration at higher O_2 pressures was also verified by the prism coupler measurement results reported in Table 4.20. This variation seems reasonable because low gas pressures correspond to a higher kinetic energy of ablated materials which also correlates to higher plasma density at the substrate. The resulting plasma density is believed to obey Beer's law behaviour which is given by

$$D = D_0 e^{-P\sigma t}$$ (4.1)

where D_o is the initial plasma density at the target, P is ambient gas pressure, σ is the total cross section for plasma-to-ambient gas collisions and t is the distance from

the target. The density of the plasma might be exponentially decreased as the background gas pressure increases [218,219]. Consequently, more elements from Er-TZN can be integrated with silica on the substrate surface when lower O_2 gas pressure is used. This inverse relationship between refractive index and background process gas pressure is also reported before for pulsed laser deposited thin films [220–223]. The oxygen deficiency and increased of Te, Zn, Na and Er concentration for low oxygen gas pressures is also evident from the data reported in Table 4.21.

Table 4.20: EDTS layer and remaining silica thickness underneath the EDTS and the refractive index measured by SEM and prism coupler for the sample prepared using various oxygen gas pressures.

Sample	EDTS thickness measured with SEM (µm)	EDTS thickness measured with prism coupler (µm)	SiO$_2$ thickness below EDTS layer measured with SEM (µm)	Refractive Index
H50	1.86 ± 0.03	1.71 ± 0.01	0.07 ± 0.01	1.6484± 0.0001
H70	1.64 ± 0.09	1.67 ± 0.03	0.13 ± 0.03	1.6356 ± 0.0009
H80	1.12 ± 0.07	1.18 ± 0.01	0.27 ± 0.03	1.5990 ± 0.0003
H100	0.81 ± 0.05	0.85 ± 0.02	0.57 ± 0.05	1.5987 ± 0.0003

Table 4.21: Elemental composition of the EDTS layer measured by EDX-SEM for samples prepared at different oxygen gas pressures.

Element	Elemental concentration (at. %)			
	Sample H50	Sample H70	Sample H90	Sample H100
O	55.15	57.29	60.52	62.16
Si	20.01	20.46	21.01	22.63
Na	11.19	10.41	9.89	7.85
Zn	8.91	7.62	5.88	5.23
Te	3.38	2.92	1.98	1.60
Er	1.36	1.30	0.72	0.53

The XRD patterns shown in Figure 4.31 shows that samples fabricated with oxygen pressures of 70 mTorr, 90 mTorr, and 100 mTorr are amorphous with a diminishing halo of silicate with increasing oxygen gas pressure. This relative decrease in silicate halo is caused by a lesser concentration of Er-TZN element that enters into silica at higher gas pressures. Nevertheless, for sample H50, it exhibited a mixed amorphous-crystalline phase. There are crystallite peaks at angle 2θ of 23.05º. 27.62º, 38.40º,

40.44º, 43.31º, 46.22º, 49.62º, 51.28º, 56.88º, 62.95º, 63.74º and 82.19º which referred to Te (ICDD reference code: 00-036-1452). Those crystallite peaks are attributed as resulting from crystallite particles which are present at the interface between the EDTS and silicon as shown in Figure 4.32. As the thickness is slightly uneven throughout the whole sample, at certain areas, Er-TZN approached silicon and formed these crystallite particles.

The PL spectra for all samples in this section still retained the line shape like other erbium-doped silicate glasses [203,204] and as illustrated in Figure 4.33. They also had FWHM of ~ 20nm (Table 4.22). As anticipated, samples H50 and H70 had the highest PL intensity and lowest PL lifetime caused by very high numbers of Er^{3+} ions compared to samples H90 and H100.
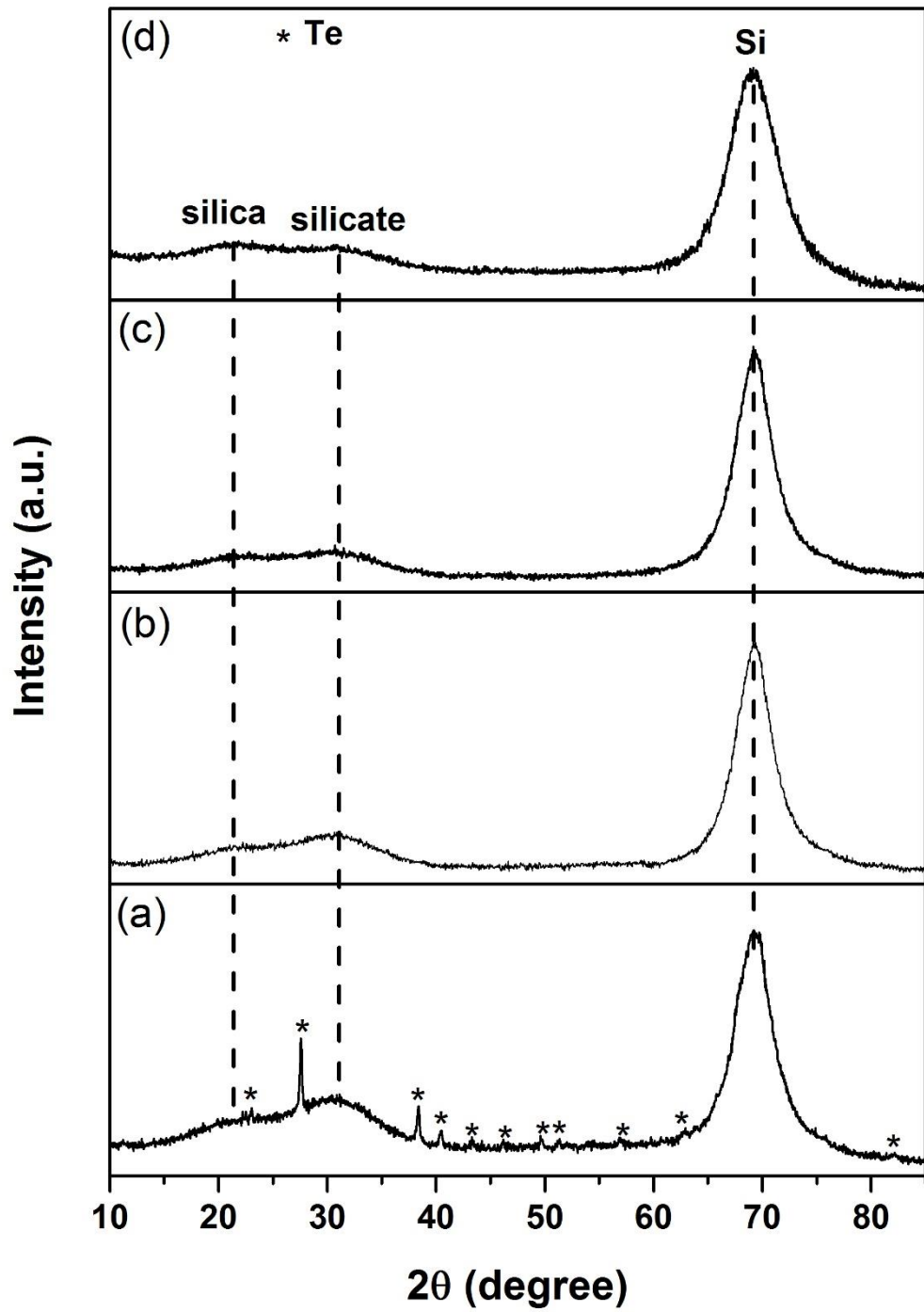
Figure 4.31: XRD patterns for samples prepared by using background oxygen gas pressures of (a) 50 mTorr (H50) (b) 70 mTorr (H70) (c) 90 mTorr (H90) (d) 100 mTorr (H100).
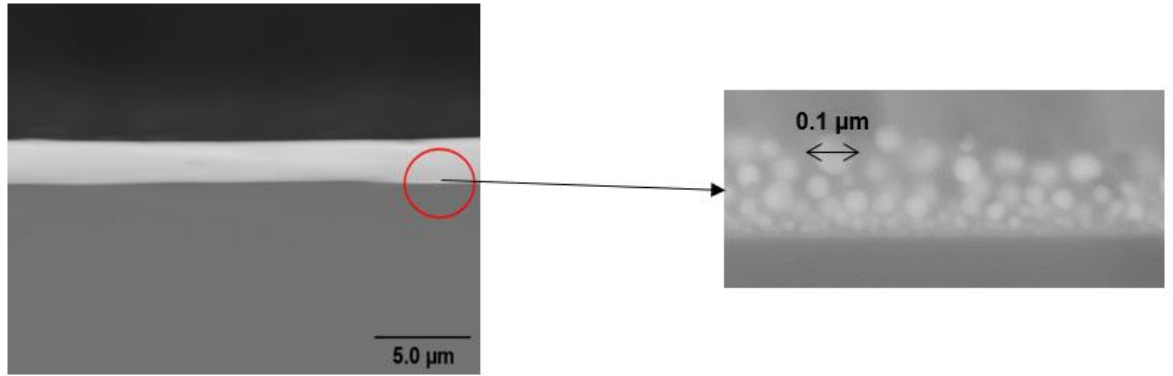
Figure 4.32: Crystallite particle at the interface between silicon and the EDTS at a certain area when 50 mTorr oxygen gas pressure was used. The appearance of crystallite particles is not visible for samples H70, H90 and H100 under the same magnification.
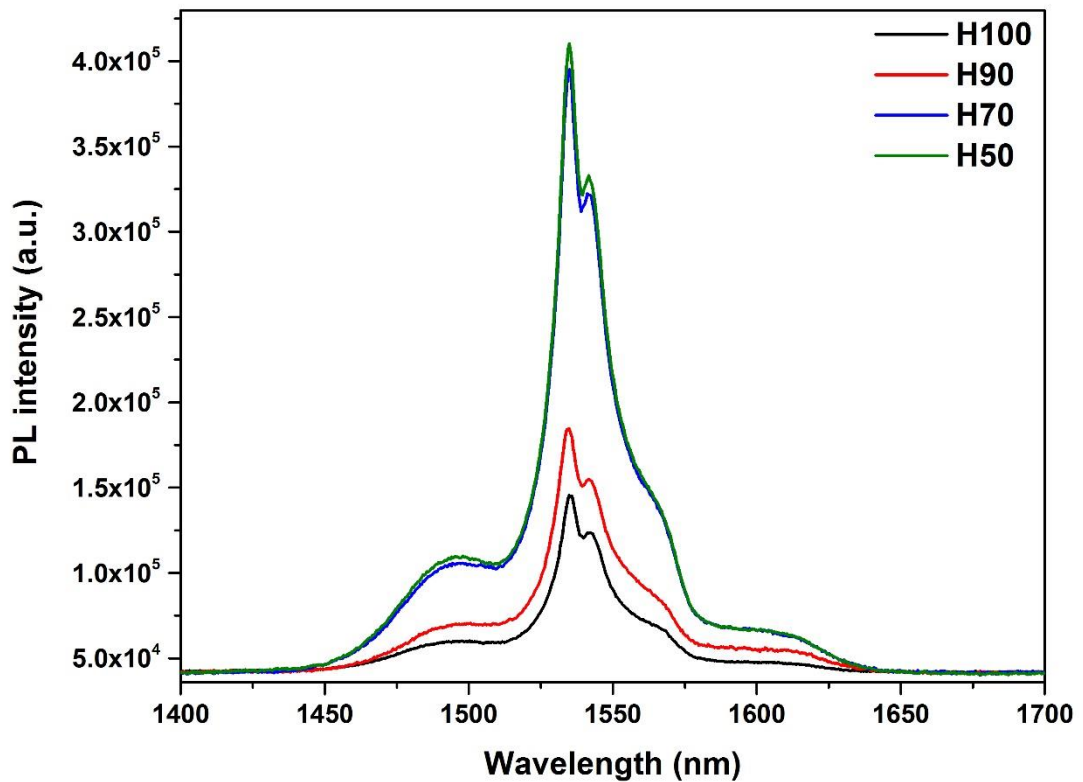
Figure 4.33: PL pattern of the $^4I_{13/2}$-$^4I_{15/2}$ transition of erbium ions with varying oxygen gas pressures.

Table 4.22: FWHM and lifetime for sample fabricated using different oxygen gas pressures.

Sample	FWHM (nm)	PL lifetime (ms)
H50	20	9.34
H70	20	9.39
H90	20	10.25

H100	20	10.64

4.6 Conclusion

This chapter clearly demonstrates that the process parameters are closely related to the properties of the EDTS. The energy of the fs-laser plays an important role because it affects the dynamics of layer formation. EDTS thickness and refractive index increased when a higher fs-laser was used due to more elements of Er-TZN managing to get into the silica. The substrate heating is also significant because it provides the activation energy required to initiate the doping process and dynamically break Si-O covalent bonds in the SiO_2. This assists the high energy ions from Er-TZN in penetrating into the silica and modifies the original silica structure network resulting in a well-defined metastable homogeneous EDTS layer. However, when Er-TZN approaches silicon in the substrate, crystallite particles of Te are formed at the interphase between the silica and the silicon due to a lack of oxygen. For other process parameters such as different fs-laser repetition rates and ablation periods, both process parameters exhibit a linear relationship between EDTS thickness and refractive index. Nevertheless, as higher oxygen pressure is used, fewer elements can gain access into the silica, and this contributed to a lower EDTS thickness and refractive index. On the other hand, the failure to obtain a homogeneous EDTS layer for a very thin layer of silica on SOI suggests that further parameter optimisation is required.

CHAPTER 5

X-RAY PHOTOELECTRON SPECTROSCOPY (XPS) AND RAMAN SPECTROSCOPY OF AN EDTS ON SOS SUBSTRATE

Although certain optical and physical properties have been extensively studied for an EDTS on a silica-on-silicon substrate in Chapter 4, its chemical properties, on the other hand, are yet to be fully understood. In this chapter, a chemical analysis of an EDTS was carried out using X-ray photoelectron spectroscopy (XPS). This technique can be employed to elucidate the elemental surface composition and the oxidation state of the cations [224,225]. Indeed, XPS is also able to resolve the contribution of bridging oxygen (BO) and non-bridging oxygen (NBO) peak in O 1s core level spectra in binary glasses [226–228] and also a complex oxide glasses system [224,229,230]. The survey scan mode for XPS is utilised to detect the presence of elements on the EDTS surface. However, Er 4d peak could not be detected in the XPS survey scan, so the high-resolution scan is used instead to determine the elemental concentration in the EDTS. The value obtained is then compared with EDX results. Based on the XPS analysis obtained, a structural network of the EDTS could be estimated. Also, depth profiling during XPS measurement can investigate the distribution of various elements in the EDTS as a function of EDTS layer thickness. In addition, a Raman spectroscopic study is also conducted to investigate the structural properties of the EDTS.

5.1 XPS study of silica-on-silicon substrate

Table 5.1 shows the elemental composition of the top surface of SOS substrate measured by XPS and EDX-SEM. Ideally, the elemental composition of SiO_2 is 66.67 at. % for O and 33.33 at. % for Si. Unfortunately, the value that was measured by XPS had a huge difference from the ideal case which is supposedly 61.73 at. % for O and 38.27 at. % for Si. This caused the relative error for Si and O to be 7.41% and 14.82%, respectively. This similar case was also observed by Smith [231] for SnO_2. Based on stoichiometry, the actual atomic concentration should have been 33.33 at. % for Sn and 66.66 at. % for O. However, the measured value obtained from XPS was 38.61 at. % and 61.39 at. % for Sn and O respectively. Thus the relative error obtained for Sn was 7.92 at. % and O was 15.85 at. %. Other than SnO_2, Smith also studied a few other materials such as K_2SO_4, ZnO, ZrO_2, Al_2O_3 and MoO_3 [231]. All of them showed the concentration of oxygen to be less than the expected value based on stoichiometry. The result of 100% normalisation caused the concentration cation species to overestimate the true value. This phenomenon might have occurred due

to oxygen loss which contributed to the residual error obtained in the analyses. Radiation-induced oxygen loss which occurred from maximum valency oxides has been observed on surface analysis using X-ray beams [231,232]. This is most likely the cause of inaccuracy in the elemental quantification from XPS analysis of an inorganic compound containing oxygen.

Table 5.1: Elemental concentration of silica surface on silicon substrate measured by XPS and EDX-SEM.

Elements	XPS	EDX-SEM
O	61.39	74.48
Si	38.61	25.52

Table 5.1 also shows a comparison of the EDTS elemental composition measured by XPS and EDX. There is a difference in the value of the elemental concentration between EDX and XPS. Apart from the limiting factor experienced by XPS, the difference in value may also be due to the limitation of EDX having the unfortunate reputation as a method of semi-quantification [233] rather than absolute quantification. However, the error from actual value is less for XPS than EDX [234].

5.2 XPS and Raman study of the EDTS surface prepared using different background oxygen pressures

From the XPS survey scan, as shown in Figure 5.1, surface EDTS once again proved that it is a mixture of elements from target materials (except erbium) and silica from the substrate. Unfortunately, the Er concentration is too low to be detected in survey spectra. Erbium that is commonly detected from an Er 4d peak is overshadowed by the more prominent background Si 2s peak due to much higher Si concentration compared to Er. The absence of a distinctive peak other than peaks for carbon (C 1s) and species from silica and Er-TZN (except erbium), in the survey spectra, showed that no contaminant was present at the surface of the EDTS. Moreover, the intensity of Na 1s, Te 3d and Zn 2p were the highest for sample H50, and this confirms that, at a low O_2 pressure, more elements from the target gets embedded into the substrate. The determination of elemental compositions from the XPS survey data is according to the assumption that adventitious carbon levels, morphology and surface sensitivity across the survey spectrum are consistent for all samples.
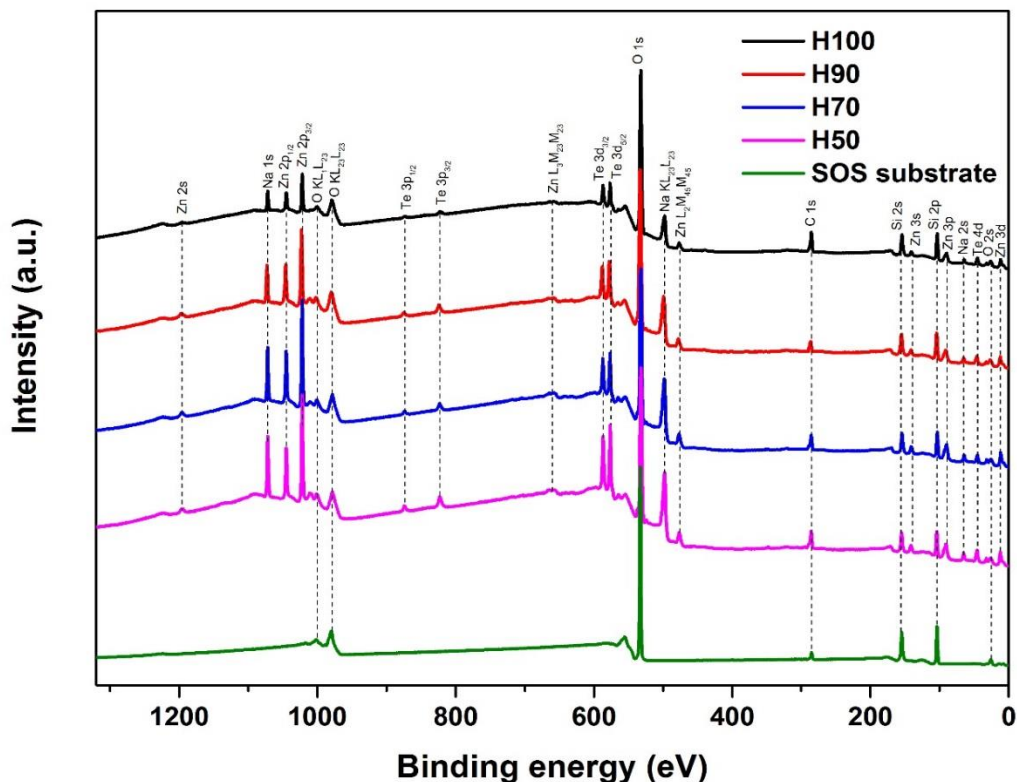
Figure 5.1: XPS survey scans from the surface of the SOS substrate and samples H50, H70, H90 and H100 using monochromatic Al Kα (1486.6 eV).

As the survey scan failed to detect the presence of erbium, a high-resolution scan for core level of O 1s, Si 2p, Te $3d_{5/2}$, Zn 2p, Na 1s and Er $4p_{3/2}$ was carried out to determine the elemental composition present at the EDTS surface. The elemental quantification obtained from the high-resolution scan for core level O 1s, Si 2s, Te 4d, Na 1s, Zn 2p and Er $4p_{3/2}$ are shown in Table 5.2. Even though the exact value for elemental concentration could not be obtained accurately because of oxygen loss as described previously, the presence of elements from silica and target material at the EDTS surface indicated there is a mixing of elements from the target material and the substrate surface (SiO_2). Table 5.2 clearly shows an increase in O and Si elements and also the decline of Te, Zn, Na and Er species for samples prepared with higher O_2 pressure. This condition caused the decrease of the refractive index as tabulated in Table 4.20.

Table 5.2: Elemental composition of the EDTS layer for samples H50, H70, H90 and H100 obtained from a high-resolution scan.

Elements	Sample H50 (at. %)	Sample H70 (at. %)	Sample H90 (at. %)	Sample H100 (at. %)
O	54.94	55.83	58.61	61.97
Si	23.74	24.85	26.81	27.53
Na	10.07	9.47	6.75	4.52
Zn	6.61	6.02	4.44	3.61
Te	3.47	2.86	2.77	1.78
Er	1.17	0.97	0.62	0.59

Figure 5.2 (a)-(d) show the high-resolution scan and the fitted peak for O 1s spectra. As seen in Figure 5.2 (a)-(d), the spectra consisted of bridging oxygen (BO) and non-bridging oxygen (NBO) components which are situated at the binding energy (BE) of ~532 eV and ~530 eV respectively. An oxygen atom that is bonded with two network formers is called bridging oxygen (e.g., -Si-O-Si-) while non-bridging oxygen represented oxygen that is attached with only one network former and another one with the network modifier (e.g., -Si-O: Na). Apart from BO and NBO peak, there is a Na $KL_1L_{2,3}$ peak at ~536 eV which arose due to the Auger process and is not associated with O 1s. The assessments pertaining to the NBO and BO peaks are consistent with electronegative and electron density arguments. The values for electronegativity for oxygen, silicon, tellurium, zinc, sodium, and erbium are 3.44, 1.90, 2.10, 1.65, 0.93 and 1.24, respectively. BO peak always has higher BE than NBO as BO is bonded with a glass former such as Si and Te which has higher electronegativity compared to Na and Er that are glass modifiers. Higher electronegativity atoms such as Si and Te, will attract electrons towards them when forming bonds with O [224]. This makes the surrounding BO electron density decrease and ultimately causes the repulsive force experienced by the outer electron to also decrease. Due to this, the attractive force that pulls inner electrons from the nucleus increases and higher energy is required to eject BO's orbital photoelectron from O 1s orbital. As a result, BE for BO is higher. For NBO though, this situation is reversed, and this made the NBO to have a lower BE [155].

The best fitting result for BE from the O 1s spectra corresponding to BO and NBO is reported in Table 5.3. From Figure 5.2 and Table 5.3, it can be seen that BO looked more dominant than NBO in the EDTS network. The position of the BO and NBO

peak of O 1s spectra from this work is just like other silicate glass that has been reported on [225,228,229]. It again proved that elements from the target material had been penetrated and mixed with a silica layer resulting in a silicate compound. The concentration of Si that acted as a primary glass former in the EDTS network is far higher than other cations which caused BO to be dominant in the EDTS. However, the amount of NBO increases when a lower background gas pressure is used due to more modifier atoms being present in the doped layer. The increment of these modifier atoms also caused O 1s signal shift to lower BE as shown in Figure 5.2 and Table 5.3. This is because the increment of modifier density increases the electron population at the oxygen atom that can bring down its binding energy. As a consequence, the sample that had a higher modifier concentration exhibited lower BE.

Figure 5.3 shows a deconvoluted Si 2p core level peak with different oxygen gas pressures. Each Si 2p peak consisted of two peaks which are $2p_{1/2}$ and $2p_{3/2}$ due to spin-orbit splitting. These two peaks had been fitted with area ratio $2p_{1/2}/2p_{3/2} = \frac{1}{2}$ based on the theory of splitting of the 2p level [235]. The BE for both peaks for samples prepared at different O_2 pressures is shown in Table 5.4. Si $2p_{1/2}$ and Si $2p_{3/2}$ appeared to be shifted to lower BE for a sample fabricated using lower O_2 pressure. The drop of the BE is believed to be attributable to a Si atom which is attached to an NBO atom. NBO bonded with Na, Zn or Er has higher ionicity compared to Si which is attached with BO by the covalent bond. This caused oxygen to relax its attractive potential against the Si atom which, in turn, resulted in an increase in electron density in the Si-O tetrahedron. Correspondingly, an increase in electron density on a Si atom caused BE for Si 2p to decrease [229,236]. Therefore, with the increase of Na, Zn, and Er in the EDTS due to the lower use of O_2 pressure, the BE for Si 2p decreased. Although Te had a higher electronegativity than Si and the possible Si-O-Te bond might cause electron population decrease in Si, but its lower concentration than Na and Zn might overshadow its role.
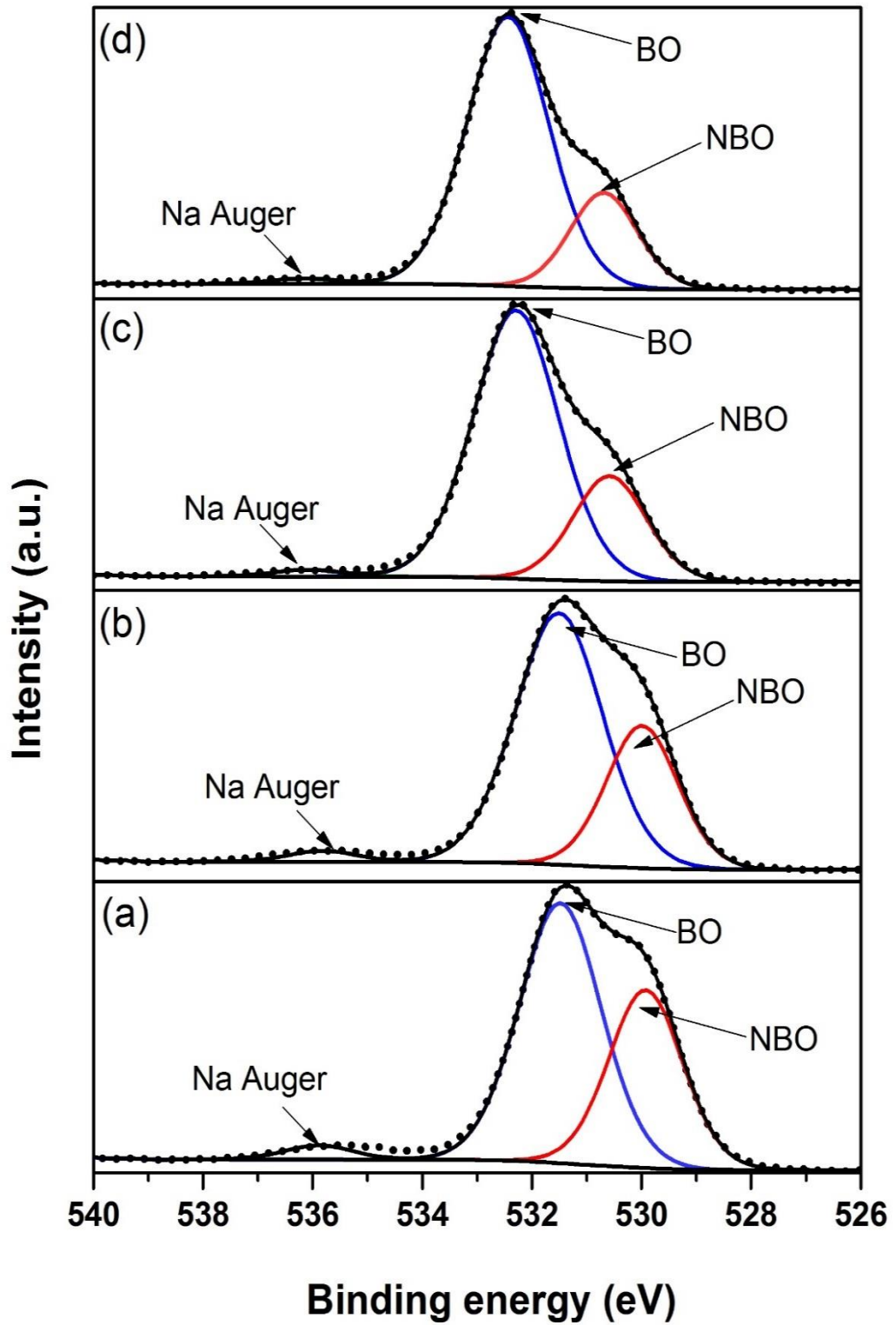
Figure 5.2: High-resolution core level spectra of the O 1s of the surface of the EDTS layer for samples (a) H50, (b) H70, (c) H90 and (d) H100.

Table 5.3: Fitted peak information for BO and NBO resulting from O 1s core level of the EDTS for samples H50, H70, H90 and H100.

Sample	Peak position (eV)		Area (%)	
	BO	NBO	BO	NBO
H50	531.48	529.93	61.90	38.10
H70	531.51	529.99	68.35	31.65
H90	532.29	530.58	74.84	25.16
H100	532.44	530.69	77.44	22.56
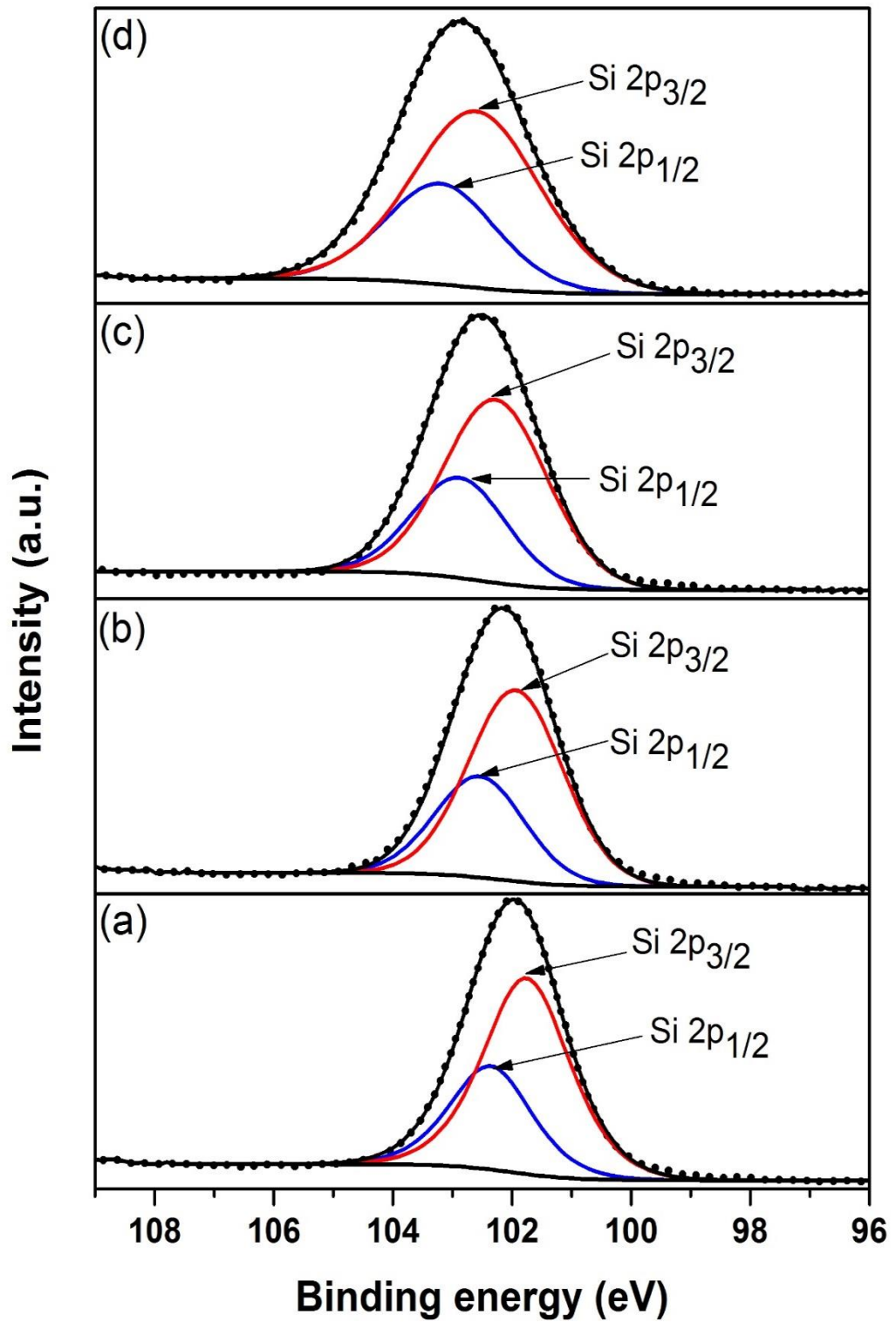
Figure 5.3: High-resolution Si 2p spectra of the surface of the EDTS layer for samples (a) H50, (b) H70, (c) H90 and (d) H100.

Table 5.4: XPS binding energy for the core levels of Si 2p, Na 1s and Zn 2p for samples H50, H70, H90 and H100.

Sample	Si 2p		Na 1s	Zn 2p	
	Si 2p$_{1/2}$	Si 2p$_{3/2}$		Zn 2p$_{1/2}$	Zn 2p$_{3/2}$
H50	102.35	101.75	1071.67	1044.82	1021.74
H70	102.54	101.94	1071.35	1044.43	1021.34
H90	102.88	102.28	1070.86	1044.11	1021.02
H100	103.20	102.60	1070.55	1043.84	1020.77

Meanwhile, no deconvolution was done for Na 1s (Figure 5.4) as it had no spin-orbit splitting for orbital S. From Table 5.4 and Figure 5.4, Na 1s peak was observed to shift to lower BE which corresponds to the increase in background gas pressure. It is strongly believed that Na, which is the most electropositive element in the doped layer, will lose the attractive force towards electrons which made electrons congregate at NBO. Due to this, the electron density was lower around Na, and it further increased the attractive force between the nucleus and O 1s electrons and also binding energy. Consequently, the sample with the higher concentration of Na tended to exhibit higher binding energy.

On the other hand, Zn 2p was also fitted like peak Si 2p except that it did not need to be deconvoluted because peak Zn 2p$_{1/2}$ and Zn 2p$_{3/2}$ are far from one another and do not overlap (Figure 5.5). From Table 5.4, peak Zn 2p shifted to the opposite direction from Si 2p. In an EDTS, it is assumed that the Zn atom acts as a modifier agent to make chemical bonds with Si and Te through the NBO. Like Na, Zn also loses the attractive force towards electrons due to its high electropositivity. This caused the electron density to be lessened around Zn and also caused Zn to move towards higher BE. Zn reduction in a sample prepared with a higher gas pressure caused the H100 sample to have the lowest binding energy.
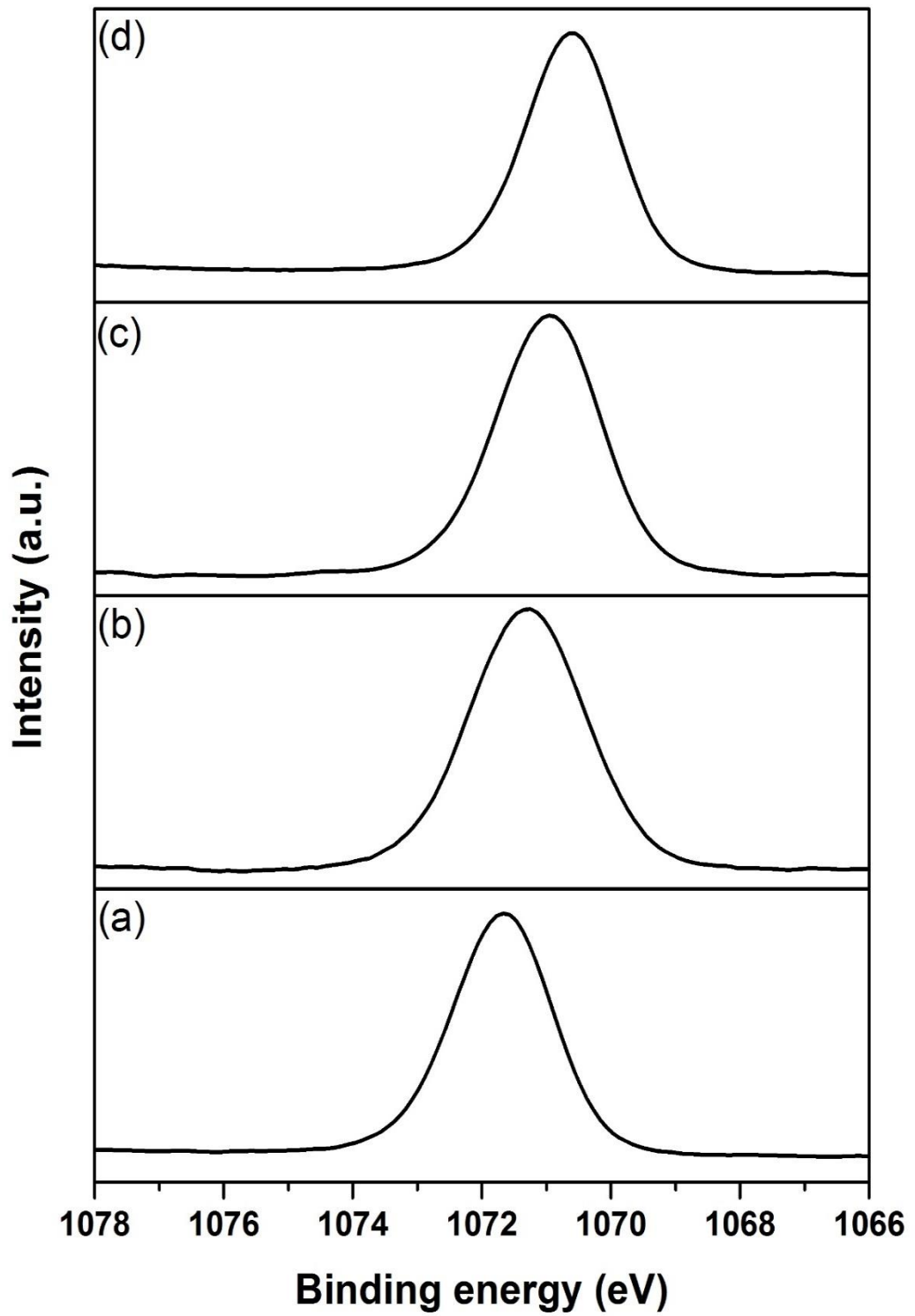
Figure 5.4: High-resolution Na 1s spectra of the surface of the EDTS layer for samples (a) H50, (b) H70, (c) H90 and (d) H100.
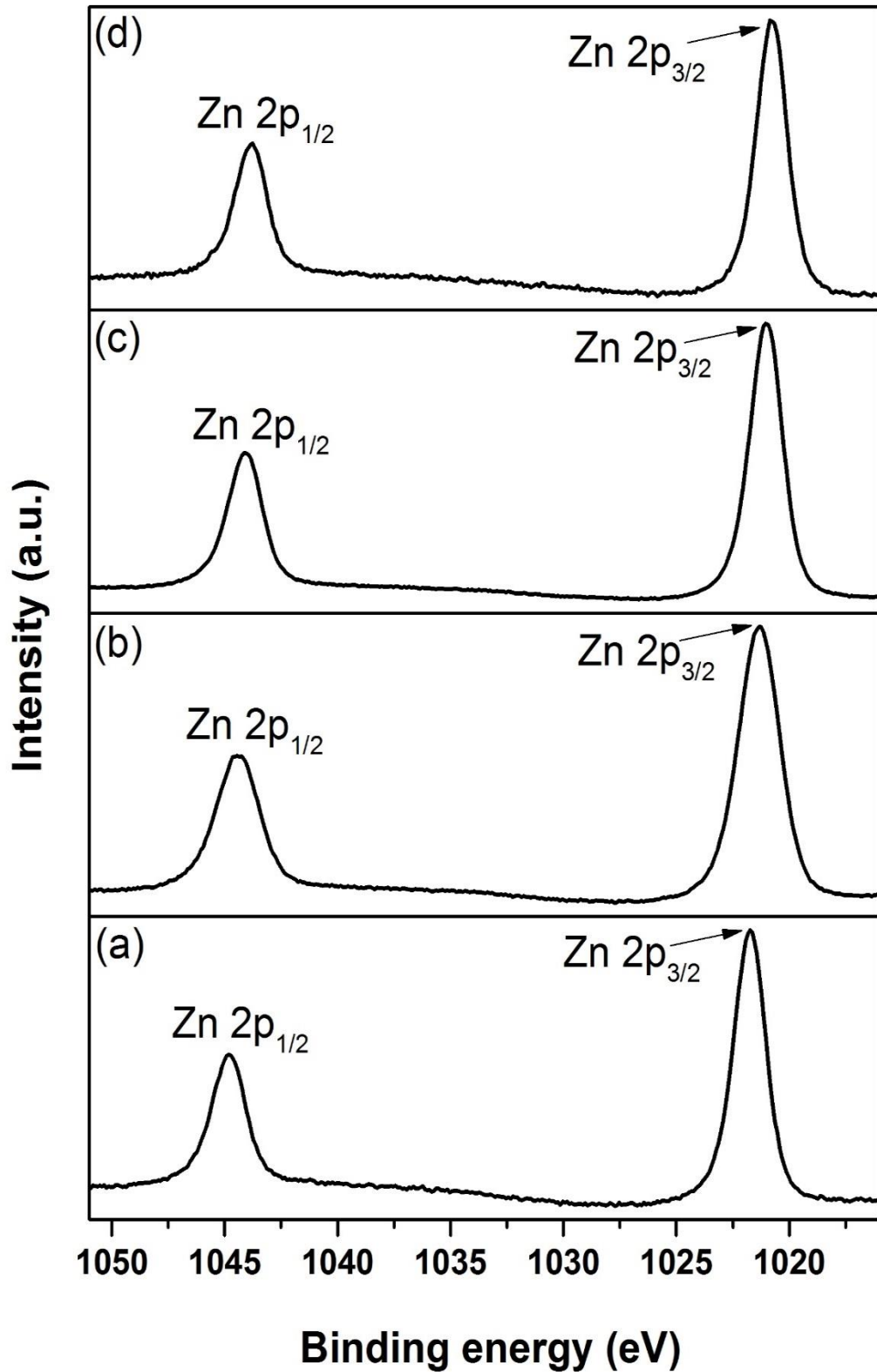
Figure 5.5: Zn 2p photoelectron peaks of the samples (a) H50, (b) H70, (c) H90 and (d) H100 showing the spin-orbit split into the Zn $2p_{3/2}$ and Zn $2p_{1/2}$ levels.

For Te $3d_{5/2}$ spectra, there are two distinct peaks that corresponded to Te oxide and Te metal as shown in Figure 5.6. The Te oxide peak is deconvoluted into two corresponding of TeO_4 and TeO_3. TeO_4 indicated that Te is bonded to BO while for TeO_3, Te is often associated with NBO. As clearly shown in Figure 5.6 and Table 5.5, the number of Te bonded to NBO is far higher compared to BO, and this clearly shows the difficulty of Te making a bond with Si-O to form the bond of Si-O-Te. It would be easier for Te to bond with Si if there is a modifier element close to it because it requires the agent to break the strong bond of Si-O-Si. However, the number of BO is higher for samples prepared with a lower background gas pressure. This is probably because Te has higher kinetic energy at lower gas pressures and is more capable of breaking Si-O-Si bonds by itself and attaching to BO. Therefore, sample H50 has the highest number of TeO_4. Nevertheless, the total TeO oxide increased in tandem with background gas pressure as an amount of oxygen is higher and this condition facilitated Te participating in the main glass network.

Interestingly, there is a Te metal peak detected in the EDTS as shown in Figure 5.6. Because the EDTS is amorphous in nature [24,85] and the presence of Te metal appeared to be undetectable by XRD, it is assumed that one or more Te atoms are situated in the interstitial site, and their sizes are below the XRD detection limit (< 5 nm) [237,238]. The total amount of these Te atoms present in the interstitial sites is supposed to be quite low because the entire range should fit into an interstitial site that had limited space. Due to this, the total size of these crystallite particles in the EDTS is below the XRD detection limit.

BE shift for Te metal showed a similar trend to that of Te oxide. The decline of BE for Te metal with background gas pressure increment is believed to be related to particulate size. The use of high pressure caused a higher incidence of collision to occur by vapour species, and the nucleation and growth of these vapour species promoted the formation of nanoparticulates. Increased gas pressure caused the velocity of vapour species to decrease, which in turn, caused the particulates to become larger when they reached the substrate. With the presence of background gas, ultrafine particulates are formed from vapour species instead of liquid droplets [239]. Based on Figure 5.6 and Table 5.5, such smaller particulates result in higher measured BE, and this kind of relationship has been reported in some literature [240–242]. These phenomena have to do with the relaxation energy of atoms involved. When a photoelectron leaves the core level, an electron-hole will be formed. This causes the atoms to be in an unstable state. It will return to its stable state through

the process of reorganisation or charge distribution (relaxation). Eventually, an electron in the surrounding will fill the hole and so the photoemission process takes place. Relaxation can be divided into two way which are a rearrangement of electrons from the atom (intra-atomic relaxation) and extra-atomic relaxation corresponding to the movement of electrons among neighbouring atoms [243]. This relaxation energy is produced due to the movement of electrons to the lower energy level which helps increase the kinetic energy of the ejected photoelectron and, at the same time, decrease the binding energy [244,245]. When the particle size become smaller, the number of overlapping energy levels decreases, and the band gap becomes larger. The relationship between the energy band gap and particle size can be simplified by the Brus equation [246,247] (with the assumption that nanoparticles are in a spherical form):

$$E_g^* = E_g^{bulk} + \frac{h}{8r^2}\left(\frac{1}{m_e^*} + \frac{1}{m_h^*}\right) - \frac{1.8e^2}{4\pi\varepsilon_s\varepsilon_0 r} \tag{5.1}$$

Here, E_g^* is the band gap of the nanoparticle, E_g^{bulk} is the band gap of the bulk material (for Te is 0.33 eV), h is the Planck constant, r is the nanoparticle radius, m_e^* is the effective mass of electrons, m_h^* is the effective mass of holes, e is the standard unit charge, ε_0 is the permittivity of free space and ε_s is the relative permittivity of the solid. From equation (5.1), again it shows that band gap increases when the particle size is decreased. The broader band gap makes it more difficult for electrons to travel to the lowest occupied level and this causes the likelihood of the relaxation process to be low. When the relaxation process decreases, it causes the kinetic energy of the photoelectron to decrease and instead increases binding energy [248]. Therefore, sample H50 had the highest binding energy for the Te metal component compared to other samples.

The area percentage of Te metal appeared to be higher when a lower gas pressure was used (Table 5.5). The presence of more elements from the target material due to the use of lower background gas pressure made it harder for Te to incorporate with the main glass network.
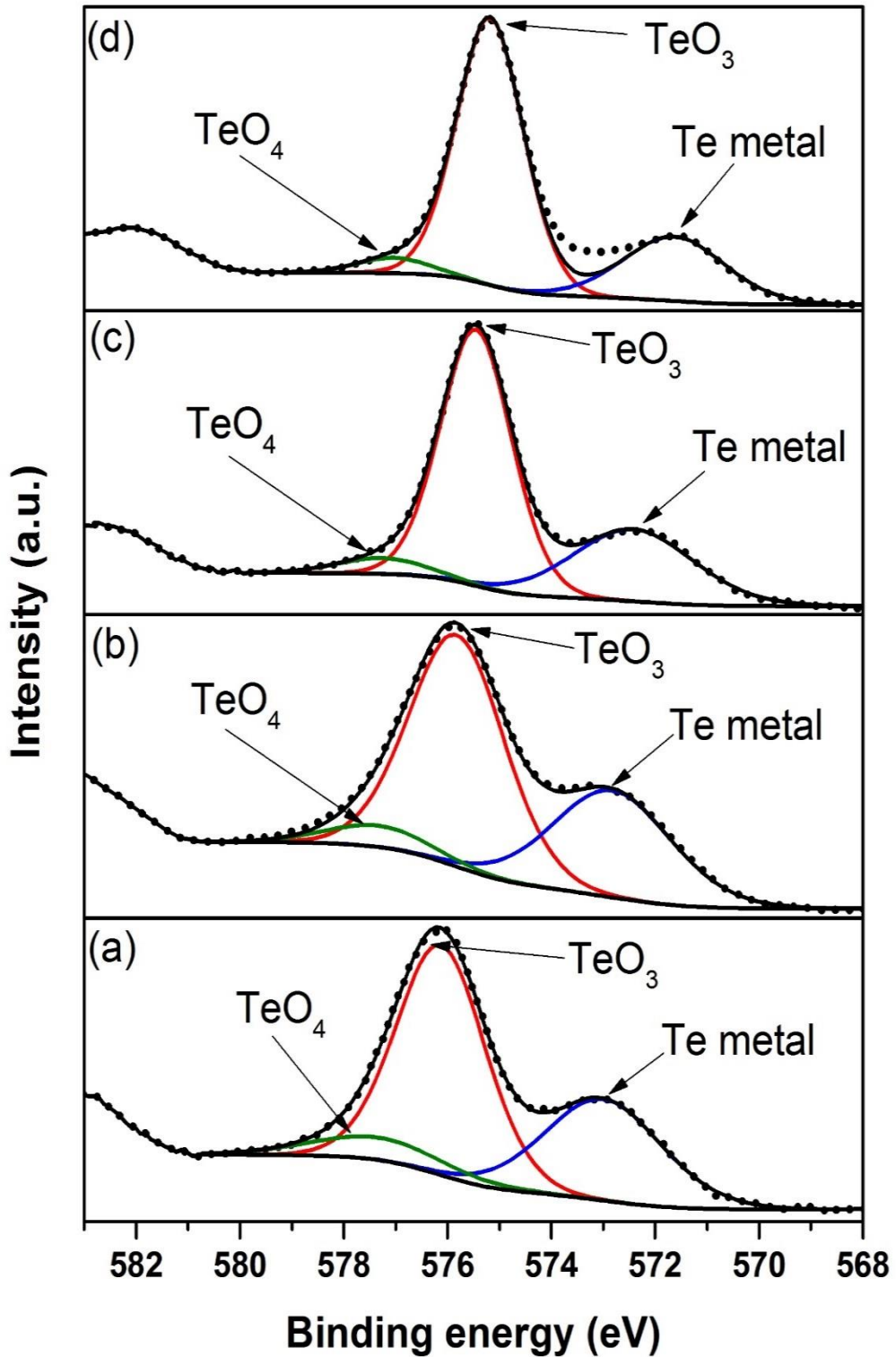
Figure 5.6: Te 3d$_{5/2}$ spectrum of the surface of the EDTS layer for samples (a) H50, (b) H70, (c) H90 and (d) H100. The fitted peak suggests that the EDTS contains Te metal and two forms of Te oxide which are TeO$_3$ and TeO$_4$.

Table 5.5: Peak positions (eV) and area percentage (%) for the component in core level Te $3d_{5/2}$.

Sample	Te $3d_{5/2}$					
	Peak position (eV)			Area (%)		
	Te oxide (TeO$_4$)	Te oxide (TeO$_3$)	Te metal	Te oxide (TeO$_4$)	Te oxide (TeO$_3$)	Te metal
H50	577.34	576.13	573.01	8.35	57.97	33.68
H70	577.33	575.82	572.83	7.02	59.69	33.29
H90	577.26	575.45	572.41	4.96	64.45	30.59
H100	577.04	575.18	571.63	4.36	69.97	25.67

Figure 5.7 shows the high-resolution XPS spectra of Er $4p_{3/2}$. From the spectra, it can be deconvoluted into two components. The peak which has higher BE corresponded to the Er trivalent ions (Er^{3+}) while the peak associated with Er metal is situated at lower BE energy. Er^{3+} is believed to contribute to the formation of an Er-O bond and participate with the main glass network. Like Te, Er metal, which also consists of one or several Er atoms, is predicted to be situated in an interstitial site, and their size is below the XRD detection limit. Figure 5.7 and Table 5.6 also indicate that Er metal was much higher compared to Er^{3+} and its concentration seemed to increase with decreasing background gas pressure as more Er was present in the EDTS. Competition became increasingly intense among target material cations to form a bond with the oxygen in the silica making it easier for the majority of Er atoms to position themselves in interstitial sites especially when lower background gas pressure was used. However, BE for each component of each sample shows almost the same value. This may be due to a very low concentration of erbium that did not impact significantly on the amount of electron density.
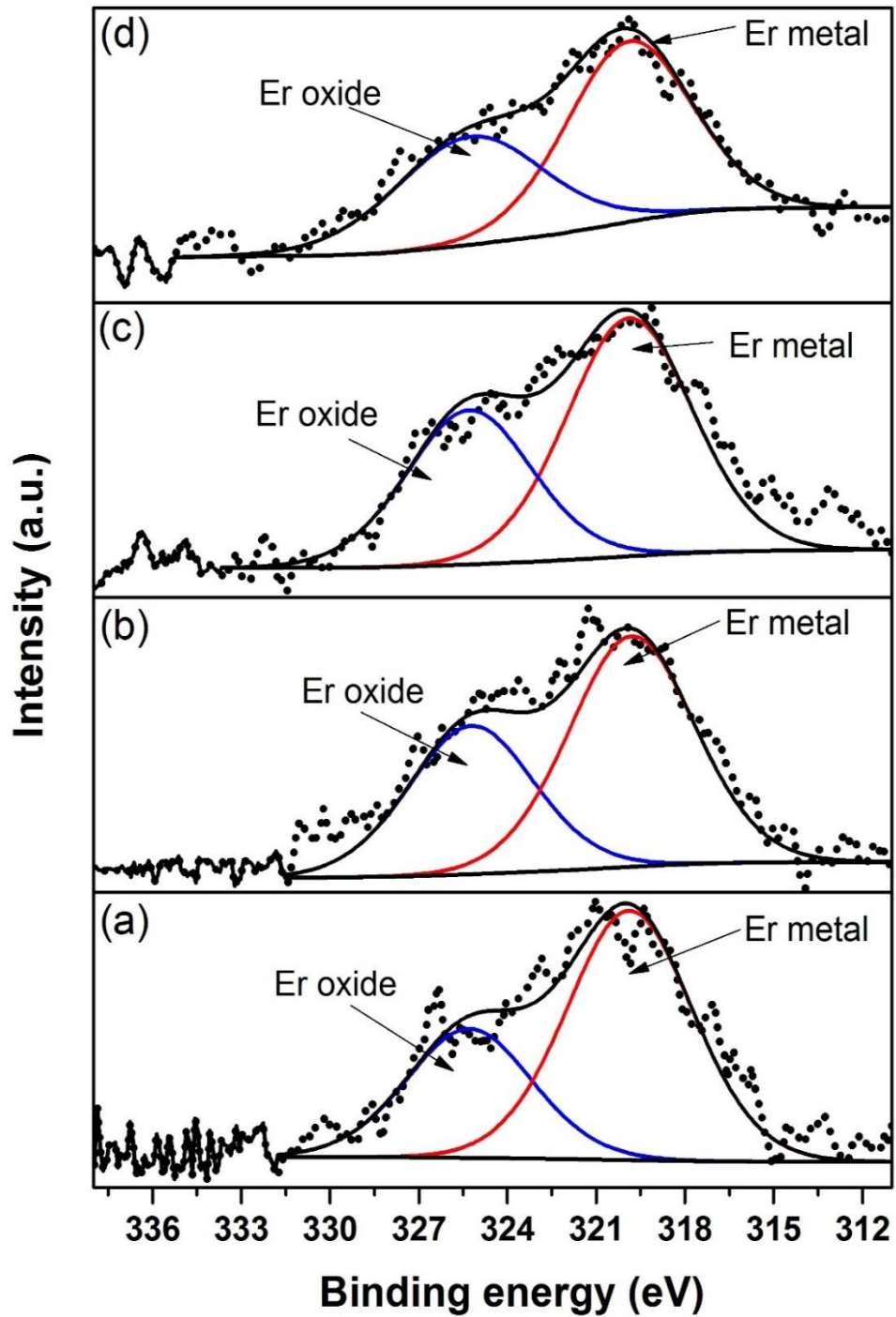
Figure 5.7: Er 4p$_{3/2}$ core level spectra with peak fitting for samples prepared with oxygen gas pressures of (a) 50 mTorr (H50), (b) 70 mTorr (H70), (c) 90 mTorr (H90) (d) 100 mTorr (H100).

Table 5.6: Peak parameter (peak position (eV) and area percentage (%)) derived from fitting Er $4p_{3/2}$.

Sample	Peak position (eV)		Area (%)	
	Er oxide	Er metal	Er oxide	Er metal
H50	325.26	319.89	34.09	65.91
H70	325.29	319.88	36.02	63.98
H90	325.29	319.85	39.69	60.31
H100	325.30	319.81	41.37	58.63

Subsequently, depth profiling was done to investigate the trend of semi-quantification values as a function of etching time or EDTS depth. Figure 5.8 displays the depth profile for sample H70. It was found that the concentration of all the elements, except Er, were almost consistent and this clearly showed that the distribution of elements for O, Te, Zn, Na, and Si are almost uniform in the EDTS. Figure 5.8 also showed that, other than Er, all species from tellurite glass mixed well with silica. However, as the EDTS is too thick and the etch rate is low, the etching process could not reach the interface between the EDTS and silica. Nevertheless, the depth profiling done was only a survey scan at every 30 s. Thus, the element Er failed to be detected.

Due to the failure of detecting erbium through conventional depth profiling, sample H70, later on, was etched for 120, 240, 360, 480, 600 and 720 s and high-resolution for each core level O 1s, Si 2p, Na 1s, Te 3d, Zn 2p and Er $3d_{3/2}$ were scanned at particular etch times/depths. However, the concentration of Er obtained was very high, at a value considered not quite logical. A probable explanation for this is that some of the argon used to etch the EDTS surface had unexpectedly been implanted into the EDTS. Because the BE peak for Ar 2s is almost equal to Er $4p_{3/2}$ and the concentration is believed to be higher than Er in the doped layer, this caused its peak to overlap with Er. This, once again, caused a failure to detect Er, but from Figure 5.9, it still shows that elements other than Er are fairly consistent.
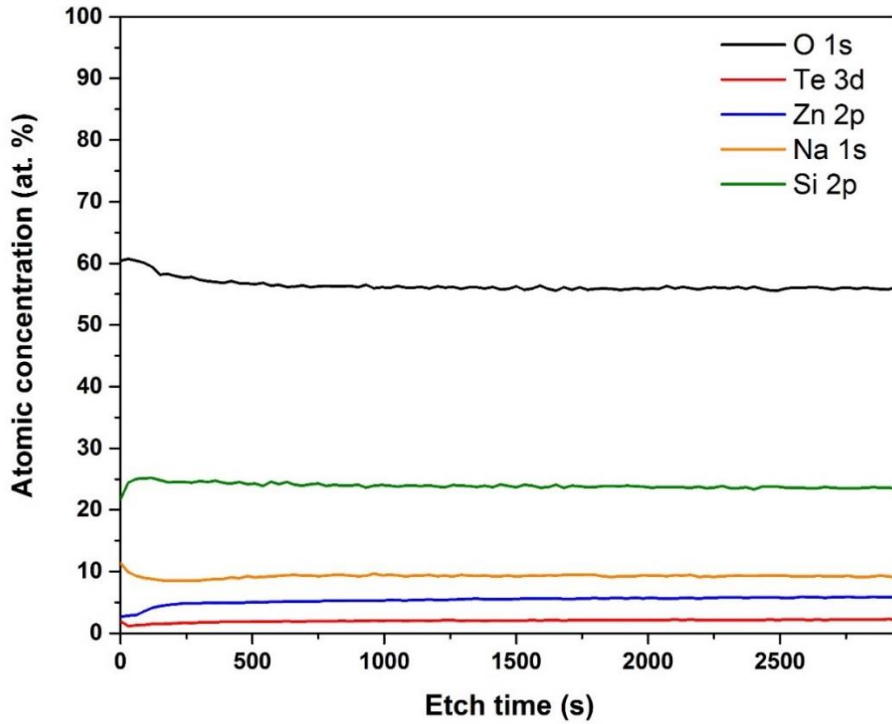
Figure 5.8: XPS depth profile for sample H70. The in-depth distributions of silicon, oxygen, tellurium, zinc and sodium are reported.
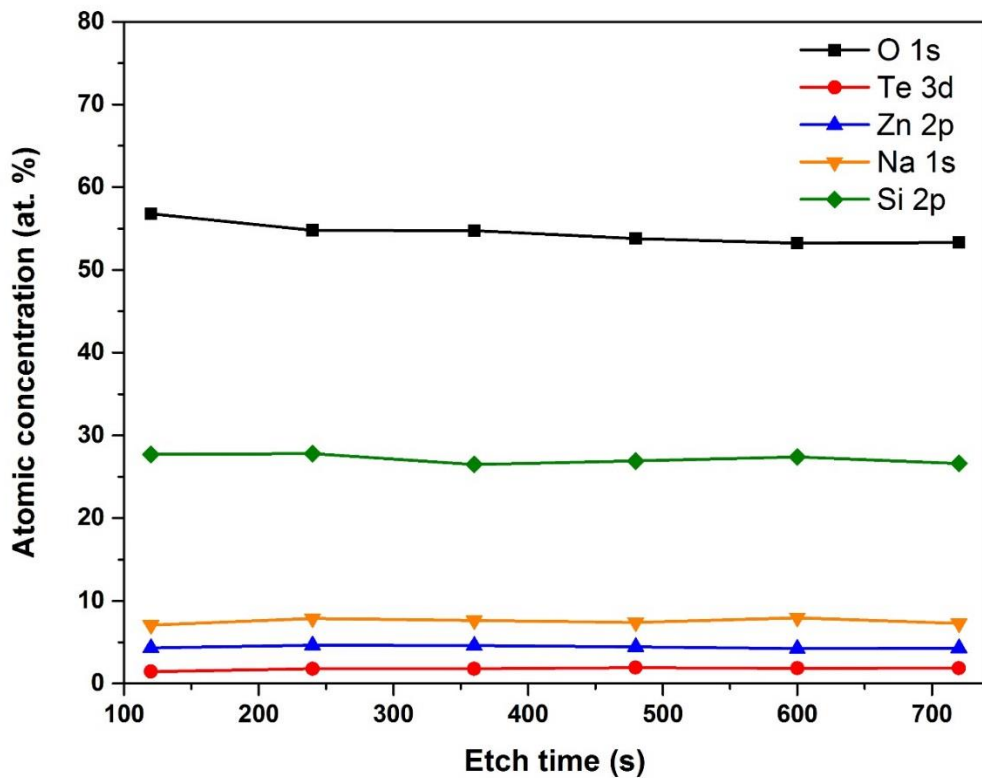
Figure 5.9: The concentration of silicon, oxygen, tellurium, zinc, and sodium obtained from a high-resolution scan when etching for 120, 240, 360, 480, 600 and 720 s.

Besides that, a Raman study was also done in order to further investigate the structural properties of the EDTS. Figure 5.10 shows the Raman spectra for SOS substrate and samples H50, H70, H90, and H100. All samples including the SOS substrate reported the peak of the wavenumber of 521 cm^{-1} attributed to single crystalline silicon [249,250] derived from the substrate. This peak appeared to be the lowest for sample H50 because the EDTS for this sample was the thickest which, in turn, caused the signal from the Si substrate to be weak. However, there were peaks at the wavenumber 122 and 141 cm^{-1} for sample H50 which corresponded to metallic tellurium that matched with the XRD result (Figure 4.31) [251,252]. For peaks located at a high wavenumber, 1160 and 1544 cm^{-1}, these two peaks are linked with erbium fluorescence emission [253].

Next, the Raman spectra for sample H70 were deconvoluted into eight Gaussian bands (A, B, C, D, E, F, G, and H) and the results are shown in Figure 5.11. The peak at energies lower than 200 cm^{-1} is named band A, and is considered a boson peak [254,255]. The Raman peak observed near band B (272 cm^{-1}) is associated with a bending vibration of the TeO_3 trigonal pyramid (tp) [256–258]. The appearance of TeO_3 is also detected by XPS as shown in Figure 5.6. Band C, which is in the range of 430-500 cm^{-1}, is commonly associated with Si-O-Si bending of Q^4 species [249,259,260]. The peak around band E (590-650 cm^{-1}) is attributed to the Si-O-Si bridges (bending vibration) between two Q^2 species [259,261]. The emergence of a peak in the region of band F (770-790 cm^{-1}) and G (900-1000 cm^{-1}) are often assigned as antisymmetric Si vibration in tetrahedral oxygen cage (Q^4) [249,259,262] and Si-O-Si stretching of Q^2 components, respectively [259,263]. As mentioned before, the bands at a higher frequency that are located at band H (~1160 cm^{-1}) and I (~1544 cm^{-1}) are associated with Er-related fluorescence while the prominent peak at band D (521 cm^{-1}) is referred to silicon from the substrate.
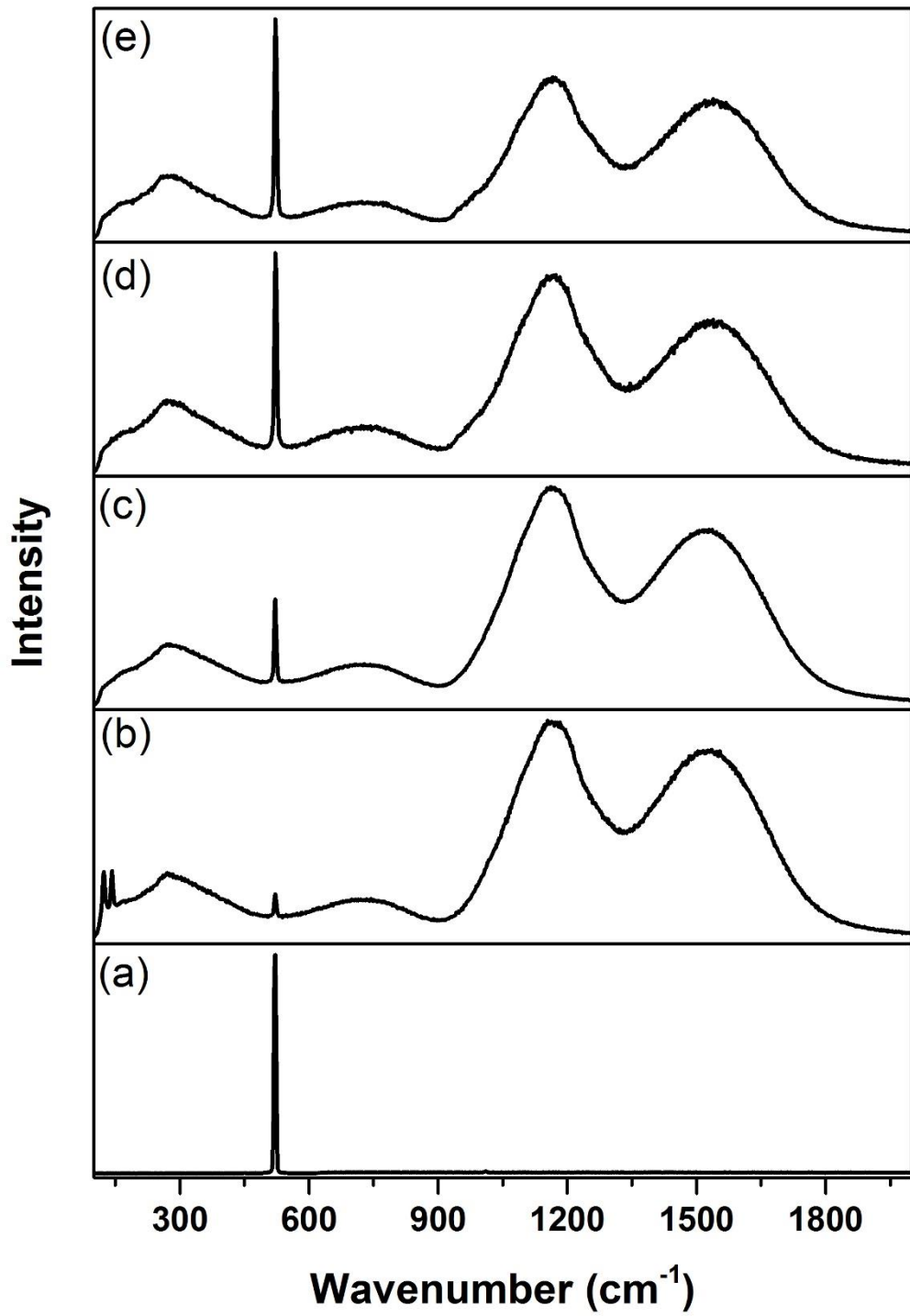
Figure 5.10: Raman spectra of (a) SOS substrate and samples (b) H50, (b) H70, (c) H90 and (d) H100.
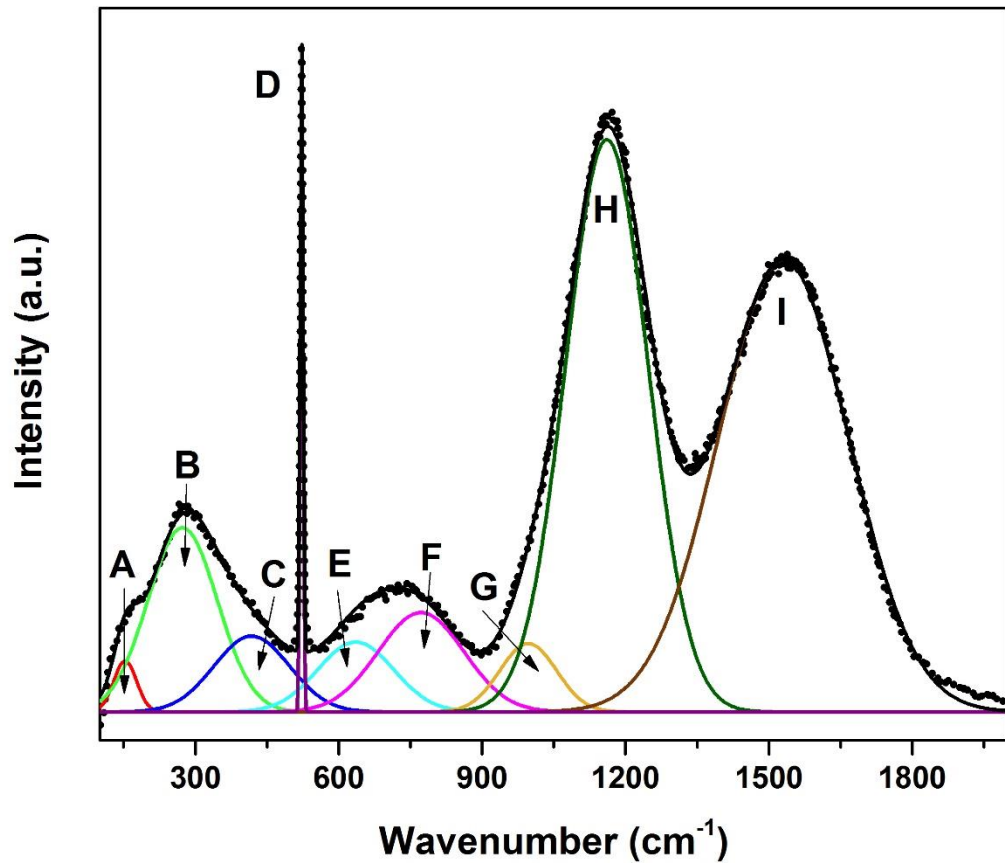
Figure 5.11: The deconvolution Raman spectra for sample H70.

5.3 XPS and Raman study of the EDTS surface fabricated at various SOS substrate temperatures.

Figure 5.12 shows the XPS survey scan for samples that were fabricated using different substrate temperatures. Obviously, for sample B400, Te peak is the highest compared to other samples, and this proved that tellurite is the host network for the upper layer. The absence of Si in the sample B400 also proved this. Because the Si element is absent or very low in the surface layer of sample B400, this allowed the peak for Er 4d (168 eV) to be detected in the survey scan. For sample B700, Te peak is very low, and this validates the discussion in the previous chapter (Section 4.2).
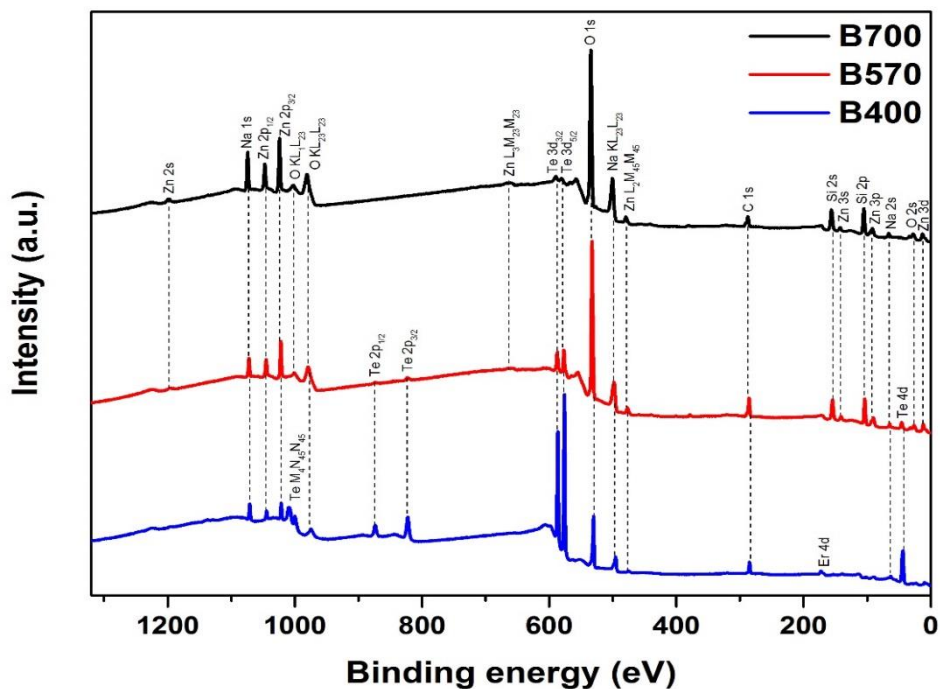
Figure 5.12: XPS survey scan for samples B400, B570 and B700.

Table 5.7 tabulates the element concentration for the surface layer of samples B400, B570, and B700 which are calculated using a high-resolution scan of O 1s, Si 2p, Na 1s, Zn $2p_{3/2}$, Te $3d_{5/2}$ and Er $4p_{3/2}$. Again, even though the value for the element concentrations derived from XPS is slightly different from EDX-SEM but the trend is still quite similar. The presence of element Si, which could be detected in high-resolution scans, indicated that few Si atoms managed to diffuse into the deposited layer for sample B400.

Table 5.7: Elemental composition of the EDTS layer for samples B400, B570 and B700 obtained from a high-resolution scan.

Elements	Sample B400 (at. %)	Sample B570 (at. %)	Sample B700 (at. %)
O	52.24	58.51	58.40
Si	1.85	28.90	28.79
Na	10.18	5.72	7.08
Zn	6.95	3.50	4.57
Te	27.08	2.89	0.59
Er	1.70	0.48	0.57

Figure 5.13 shows a high-resolution scan of Te $3d_{5/2}$ for a sample fabricated with different substrate temperatures. Interestingly, the high-resolution scan of Te $3d_{5/2}$ for B400 is slightly different from that of the EDTS. No Te metal could be detected for this deposited layer, and this indicated that the amount of oxygen is sufficient in the layer. Surprisingly, TeO_3 is dominant in this network. The peak that located at ~574 eV is normally attributed to tellurium sub-oxide [264,265]. For the B700 sample, the very low density of the EDTS made the scan results to have much noise and made deconvolution processes difficult possibly causing it to be less accurate. NBO which is dominant in the deposited layer structure was also detected in high-resolution O 1s as shown in Figure 5.14.

Figure 5.15 shows the Raman spectra of samples prepared at different substrate temperatures. Both samples B570 and B700 showed the typical EDTS on silica-on-silicon Raman spectra. However, the peak around ~250-280 cm^{-1} associated with TeO_3 seems more pronounced for the B570 sample compared to the B700. This might be due to higher Te density in B570. For B400, the Raman spectra is a bit different from others. The Si peak is invisible for this sample. Since the Raman spectrum for K400 is somewhat different, this spectrum had been deconvoluted into seven Gaussian bands (A, B, C, D, E, F, and G) and its results are depicted in Figure 5.16. The presence of a peak at 258 cm^{-1} at location A is allocated to trigonal pyramid TeO_3 (tp) unit (bending vibration) while band B, which consisted of wavenumber 381 cm^{-1}, corresponded to Zn-O vibrations [256,257]. The observed peak at 532 cm^{-1} (band C) is assigned to the vibration bond in the Te-O-Te bridging structure between various Te-based structural units. This band originated from the stretching modes and symmetrical bending of continuous chains of TeO_4, TeO_{3+1} and TeO_3 polyhedra at the shared corner [256]. The peak located around 660 cm^{-1} (band D) resulted from the asymmetrical stretching vibrations of the Te-O bond in TeO_4 trigonal bipyramids (tbps) units. Band E which consisted of a peak of 786 cm^{-1} is assigned to the asymmetric vibrations of linkages related to the TeO_3 structural units [266,267]. As mentioned before, bands F and G are Er^{3+} ion PL emission related.
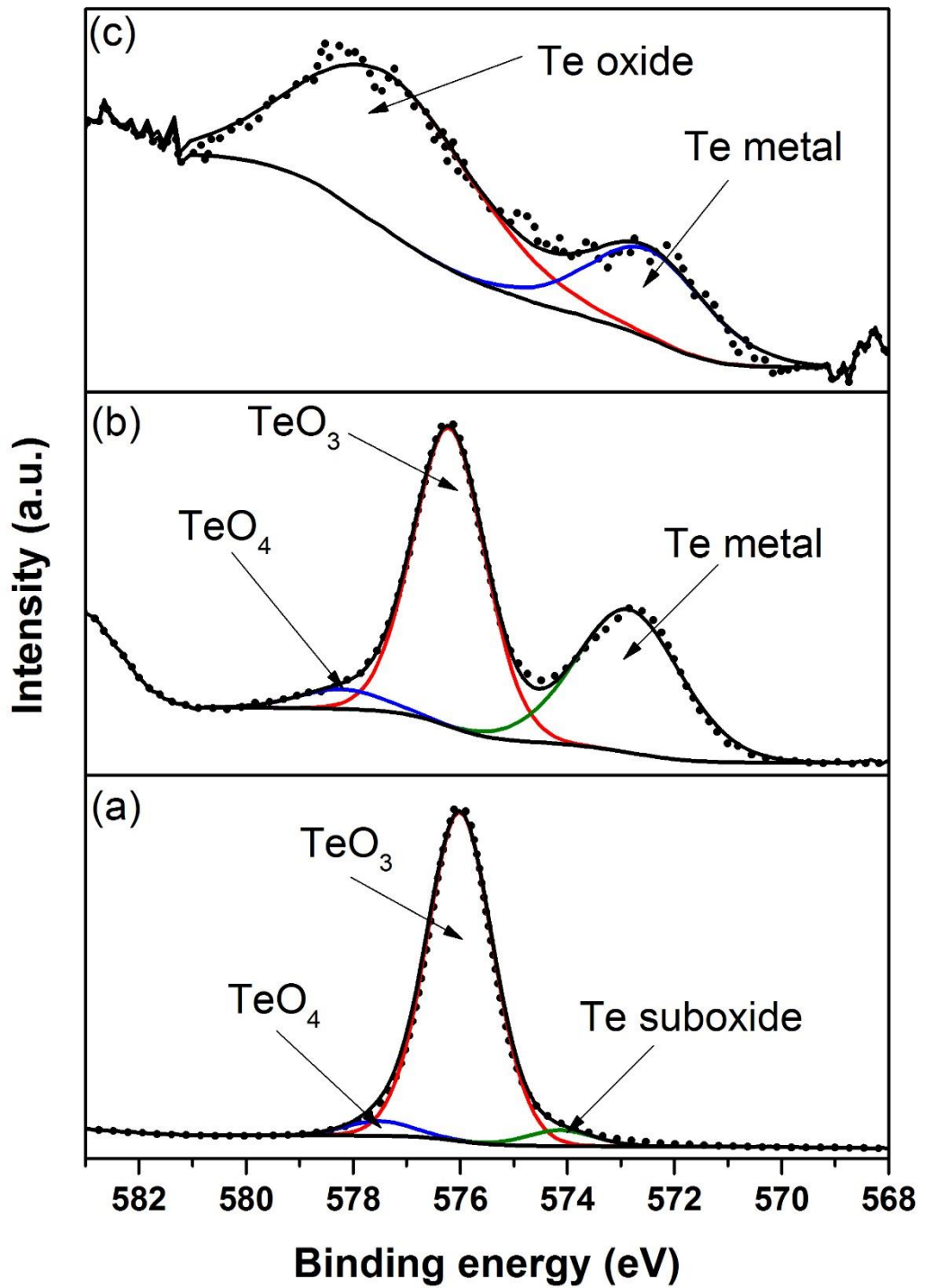
Figure 5.13: Te 3d$_{5/2}$ spectra of the surface of the EDTS layer for samples (a) B400, (b) B570 and (c) B700.
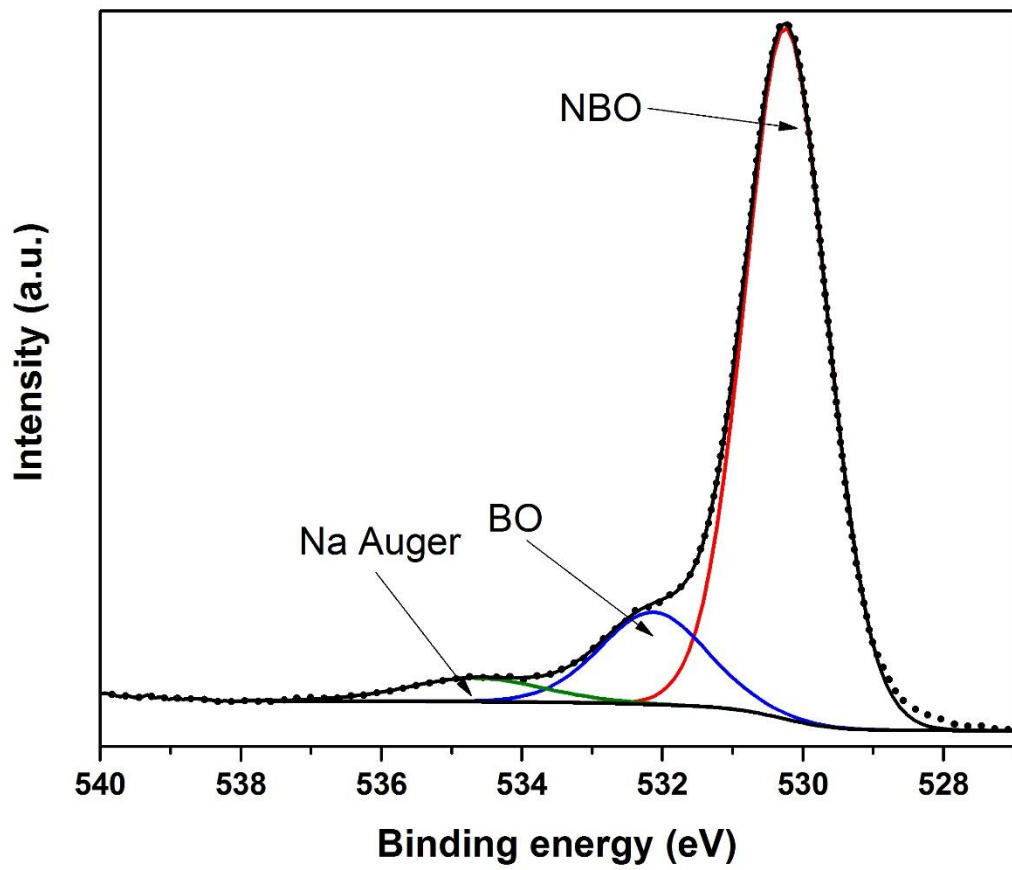
Figure 5.14: High-resolution spectra of O 1s for sample B400. This clearly shows that NBO is dominant in the network.
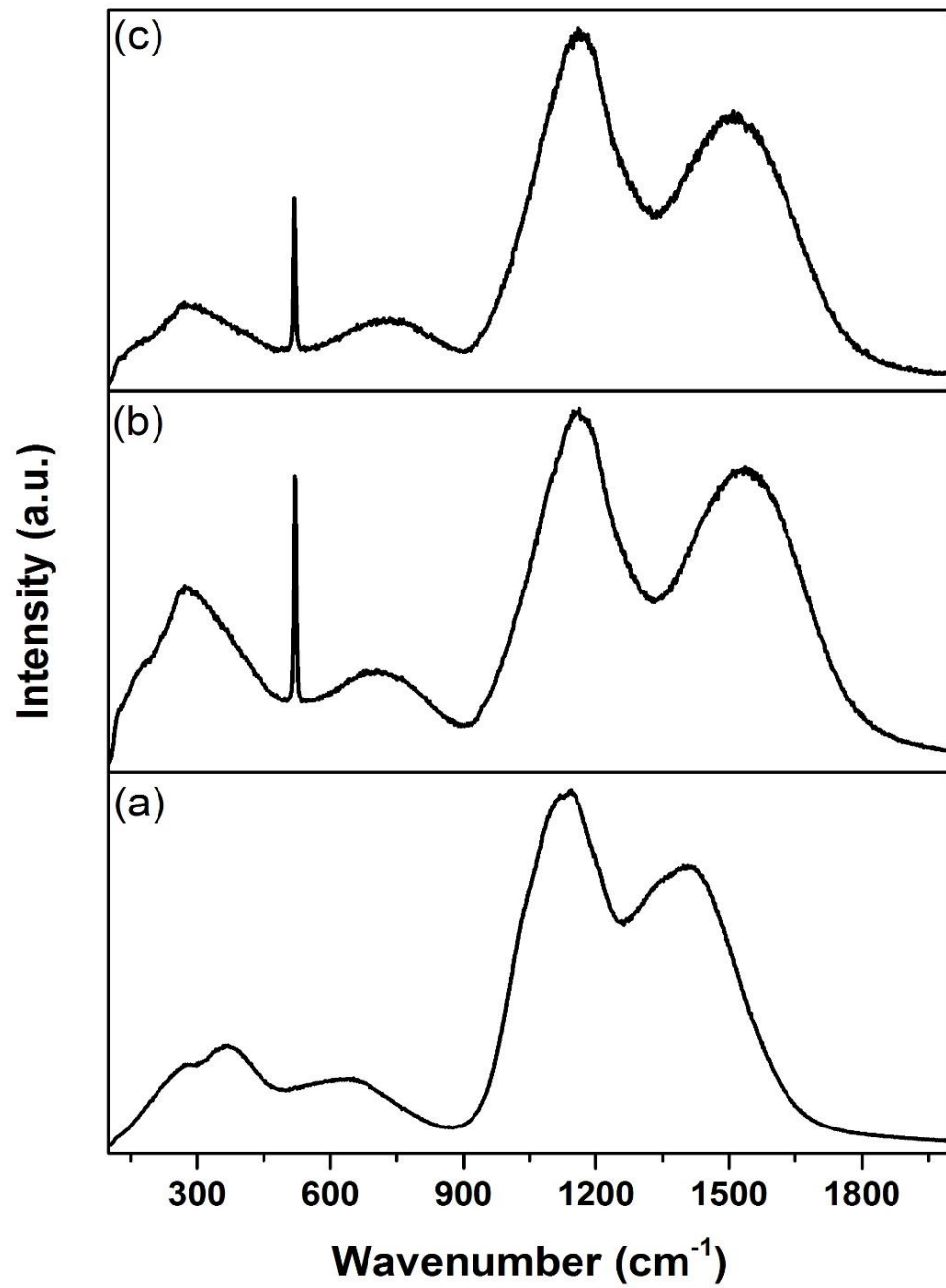
Figure 5.15: Raman spectra of samples (a) B400, (b) B570 and (c) B700. Both B570 and B700 samples show typical EDTS Raman spectra.
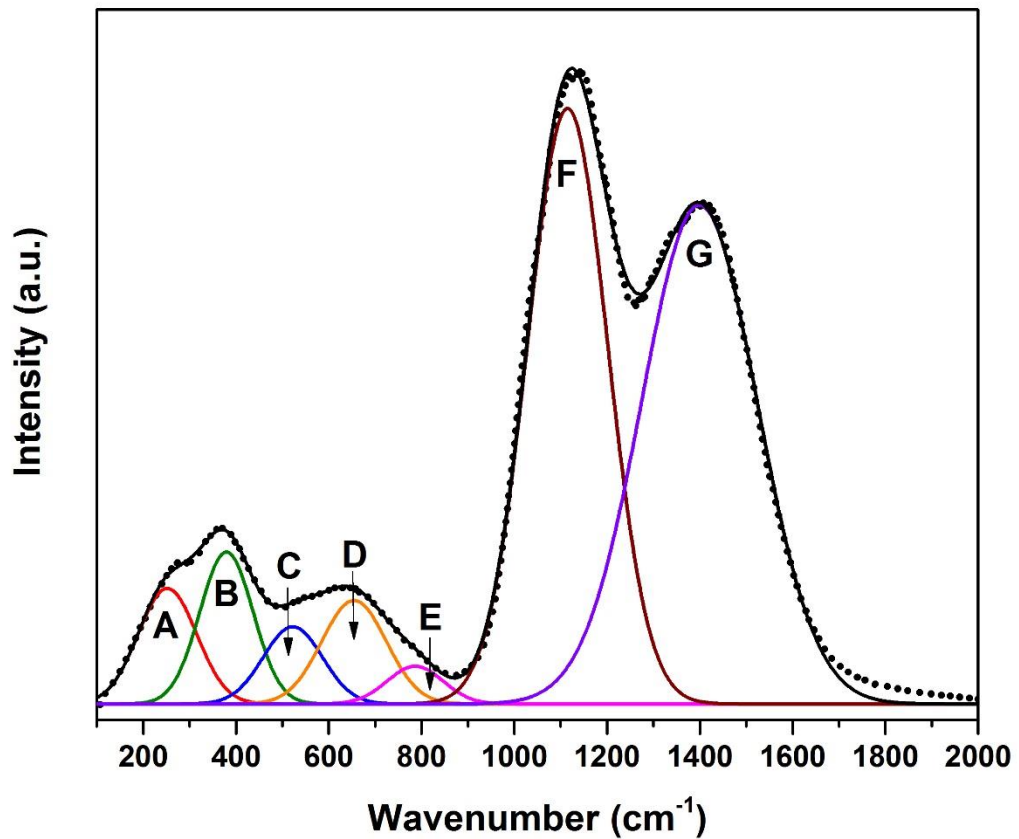
Figure 5.16: Deconvolution of Raman spectra of sample B400 in various Gaussian
bands. The bands investigated in this work labelled as
A, B, C, D, E, F and G are marked.

5.4 Elemental concentration of the EDTS surface fabricated using silica on silicon-on-insulator (SOI) substrate.

A very thin EDTS made it hard for the elemental concentration measurement to be carried out by EDX-STEM. Alternatively, the XPS measurement could measure elemental concentration on this thin EDTS surface. Table 5.8 shows the elemental concentration in samples G10, G15, and G25. As expected, the species from Er-TZN increased when thicker silica was used due to the longer ablation period.

Table 5.8: Elemental composition of the EDTS layer for samples G10, G15 and G25 obtained from a high-resolution scan.

Elements	Sample G10 (at. %)	Sample G15 (at. %)	Sample G25 (at. %)
O	59.63	59.17	58.22
Si	37.70	34.44	32.95
Na	2.12	4.29	5.48
Zn	0.32	1.42	2.50
Te	0.08	0.20	0.30
Er	0.15	0.48	0.55

5.5 Conclusion

The XPS study in this chapter contributes to a better understanding of the chemical composition and the local structure of the EDTS layer. According to the curve fitting of O 1s core spectra, it is noticed that bridging oxygen (BO) is more dominant compared to non-bridging oxygen (NBO) in the EDTS network. Result fitted peak of Te $3d_{5/2}$, and Er $4p_{3/2}$ exposed the presence of Te and Er metals in the EDTS, and from these findings, it is believed that they are situated in the interstitial site. From the XPS measurement also, it gives the concentration of each element present in the upper layer of the sample. However, the concentration of each element obtained through XPS might be less precise due to oxygen loss. Besides this, XPS depth profiling performed proves that the EDTS consists of a homogeneous mixture of elements from the target material and silica from the substrate. On the other hand, Raman spectra obtained also give a deeper understanding about the structure properties of the upper layer on the substrate and, in particular, substantiate the presence of Te metal and TeO_3 structural units in the material.

CHAPTER 6

DOPING TeO$_2$-ZnO-Na$_2$O-Er$_2$O$_3$ (Er-TZN) INTO SILICON NITRIDE (Si$_3$N$_4$)-ON-SILICON SUBSTRATE

The success of Er-TZN doping into silica has inspired the extension of the ULPD technique to other substrate materials, which is the subject of this work. Among various available substrates, Si$_3$N$_4$-on-silicon seems an interesting candidate due to the fascinating properties of Si$_3$N$_4$ such as its high refractive index (1.99), and the fact that it is also a Si-based material like SiO$_2$ which compatible with CMOS processing. A number of process parameters have been varied to ensure that the resulting doped layer at least replicates the quality of the EDTS. The process parameters investigated were different substrate temperature, type of background gas, fs-laser energy, fs-laser repetition rate, background gas pressure and ablation period.

6.1 Substrate temperature

Five samples were fabricated with different substrate temperatures following the procedures reported for ULPD before. These samples are labelled as K470, K520, K570, K600 and K650 based on the applied substrate temperatures of 470 °C, 520 °C, 570 °C, 600 °C and 650 °C, respectively. All process parameters used to prepare these samples are listed in Table 6.1.

Table 6.1: The parameters used to dope Er-TZN into Si$_3$N$_4$-on-silicon substrate by using various temperatures to heat the substrates.

Process parameters	Operating conditions
Substrate	Si$_3$N$_4$ (t=1 μm)-on-silicon
Target material	79.5TeO$_2$-10ZnO-10Na$_2$O-0.5Er$_2$O$_3$ (Er-TZN)
Fs-laser energy	50 μJ
Fs-laser repetition rate	1.0 kHz
Substrate temperature (sample name)	470 °C (K470), 520 °C(K520), 570 °C (K570), 600 °C (K600) and 650 °C (K650)
Ablation period	4 hours
Background gas pressure	70 mTorr O$_2$

As discussed previously in Chapter 4, the substrate temperature is a significant parameter in ULPD because it activates the mobility of the ablated species so that it penetrates into the substrate and modifies the host Si$_3$N$_4$ network. Before further optimisation of the process can be undertaken, however, a suitable temperature needs to be identified. Figure 6.1 (a) shows a backscattered (BSE) cross-sectional

SEM image for a Si_3N_4-on-silicon substrate prior to ULPD trials while SEM images for samples K470, K520, K570, K600 and K650 are shown in Figure 6.1 (b)-(f). As Figure 6.1 (b) illustrates, deposition of Er-TZN onto the substrate has occurred. The layer formed on the Si_3N_4 substrate appeared uniform and smooth. However, it appears that only a small amount of the Er-TZN has successfully penetrated the Si_3N_4. This signifies that a temperature of 470 °C is not high enough to break the Si-N bond. Only a few of the energetic elements of the Er-TZN have managed to enter into the Si_3N_4 molecular network as can be seen around the materials interface. On the other hand, according to the SEM images of Figure 6.1 (c) – (f), for samples that were fabricated with a higher temperature of 520 °C - 650 °C, it is found that the Er-TZN successfully penetrated the Si_3N_4. From the cross-sectional SEM, it can be seen that at the edge of sample K600, as shown in Figure 6.2, doping occurred. Nevertheless, from all of the images of the doped layer, it is clear that the doping was not as uniform as doping silica with Er-TZN. Although elements from the target material managed to penetrate the Si_3N_4, it is discretely distributed as depicted by the grayscale variations in the doped layers. This largely inhomogeneous layer appeared to be partly porous, and, in certain areas, there was an accumulation of specific elements. The SEM images of the surface of the doped layer also show that it is very uneven and rough as shown in Figure 6.3.

(a)　　　　　　　　　　(b)
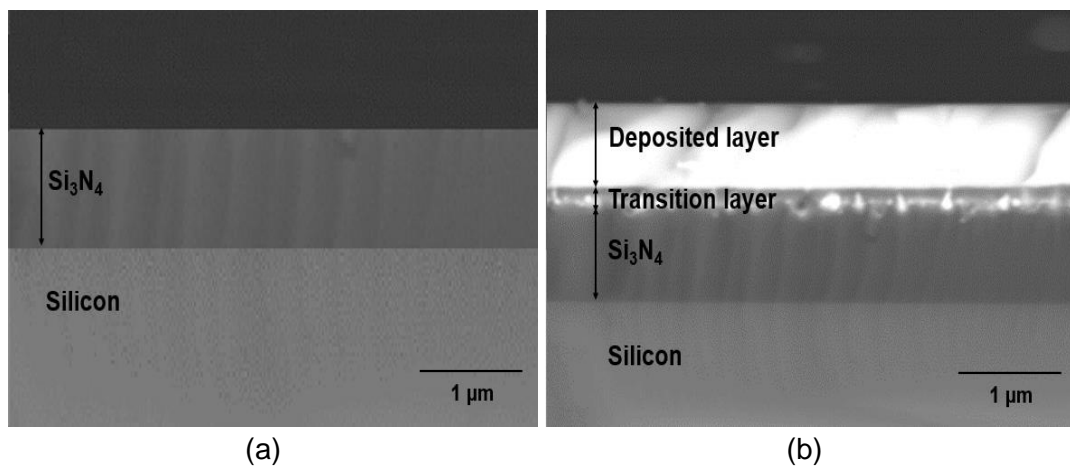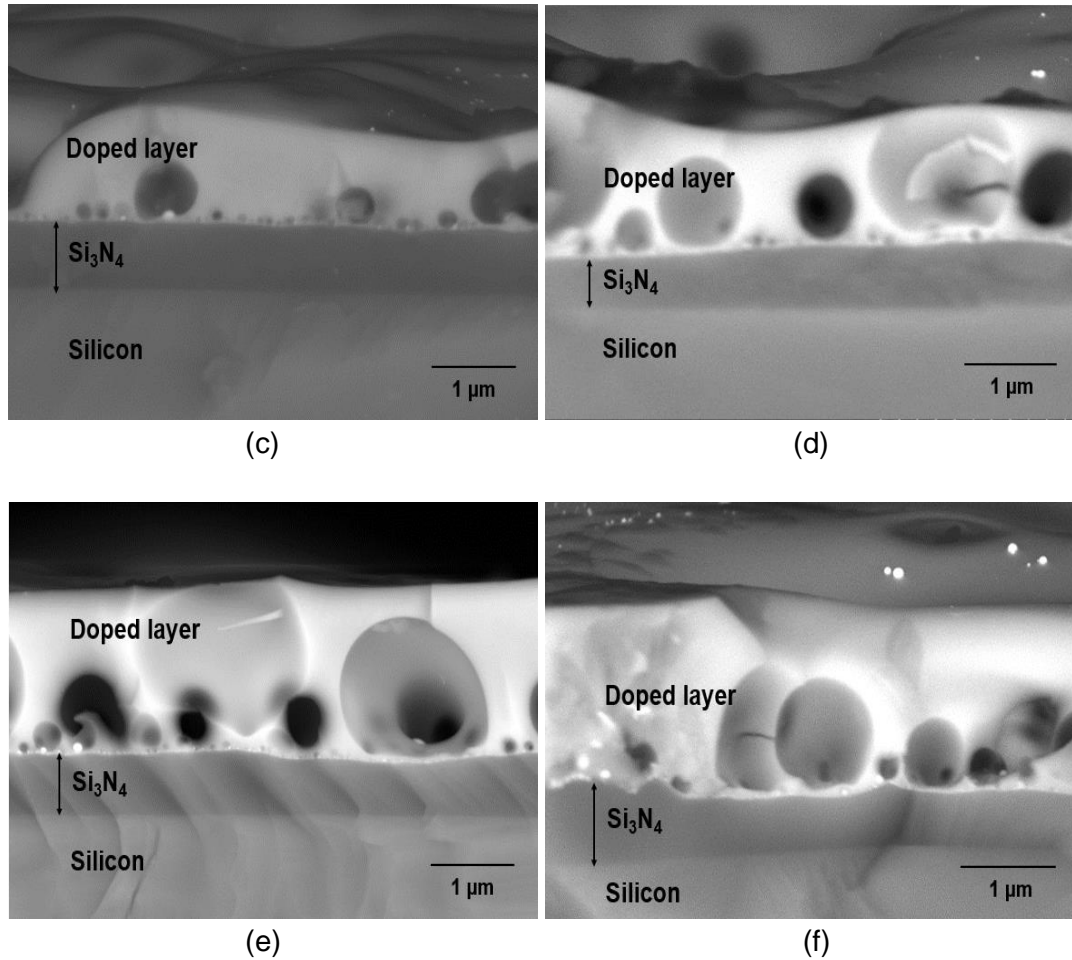
Figure 6.1: Backscattered cross-sectional SEM images of (a) bare Si$_3$N$_4$-on-silicon substrate, and samples doped with Er-TZN into Si$_3$N$_4$-on-silicon when substrate was heated at (b) 470 °C (K470) (c) 520 °C (K520), (d) 570 °C (K570), (e) 600 °C (K600) and 650 °C (K650).
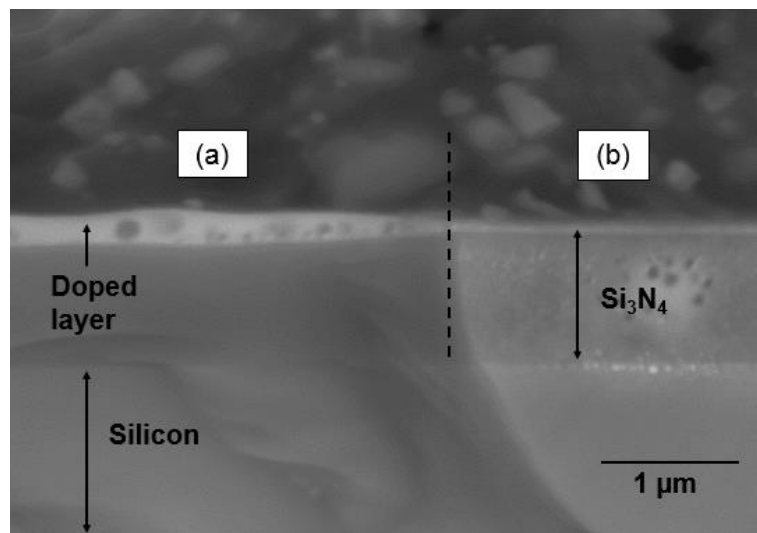
Figure 6.2: Doping of Er-TZN into silicon nitride at the sample edge for sample K600. It is divided into two main parts which are (a) the formation of a doped layer on Si$_3$N$_4$ and (b) an area where substrate has been covered by the substrate holder.
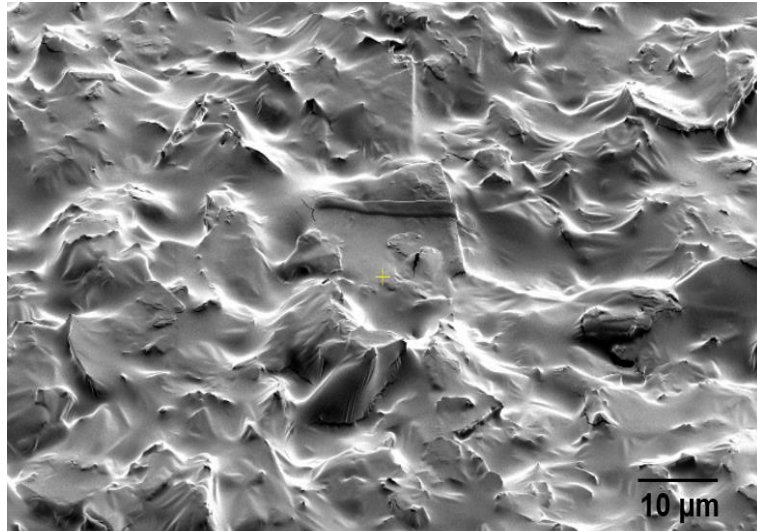
Figure 6.3: SEM surface morphology of the top surface of the doped layer for sample K600.

The thicknesses of the upper layers for all of the samples are summarised in Table 6.2. For sample K470, the thickness of the Si_3N_4 underneath the upper layer was less than the original thickness of 1 μm, and this indicated that doping had occurred, even though there was only a small amount on the Si_3N_4 surface. For samples K520, K570, K600 and K650, the upper layer thicknesses cannot be precisely determined and have large errors due to their very rough surfaces. However, the estimated thickness obtained showed a linear relationship between thickness and the temperature used to heat the substrate. Additionally, the thickness of the Si_3N_4 underneath the doped layer became smaller with an increase of substrate temperature. This meant that the material target could react with the Si_3N_4 more thoroughly at higher temperatures. The refractive index and thickness, which were measured using a prism coupler in this thesis, could not be measured due to the uneven surface of the doped layer.

Table 6.2: Thickness of upper layer and Si_3N_4 underneath, measured by SEM for samples K470, K520, K570, K600 and K650.

Sample	Thickness (μm)	
	Upper layer	Si_3N_4 under upper layer
K470	1.1 ± 0.1	0.87 ± 0.04
K520	1.5 ± 0.4	0.74 ± 0.03
K570	1.5 ± 0.3	0.66 ± 0.03
K600	1.8 ± 0.3	0.60 ± 0.05
K650	2.0 ± 0.3	0.57 ± 0.09

Figure 6.4 shows two different positions in the K470 sample measured by EDX-SEM in order to obtain the elemental concentrations at these particular positions, and the

results are shown in Table 6.3. Because the upper layer of the sample K470 is only a deposited layer, it is expected to have the properties of tellurite-based glass used as a target material. The high concentration of Te at position 1 confirmed this. For position 2, which is located near the interface of deposited region and Si_3N_4 but within the Si_3N_4 have some elements from the target material, mostly oxygen. The smaller atomic size of oxygen compared to Te, Zn, Na and Er enabled a few energetic ions/atoms of oxygen to successfully penetrate the Si_3N_4 and oxidise some of it. However, it is evident that the lower temperatures hindered deeper modification of the Si_3N_4 layer further. An area scan done for the sample to determine the distribution of elements in sample K470 is shown in Figure 6.5.The negligible presence of elements Si and N in the upper layer confirms that the upper layer consists of just elements from Er-TZN. Apart from this, the area scan obtained also shows an intermediate region between the deposited layer and Si_3N_4 composed of Si, O, Te, Zn, Na, Er and N.
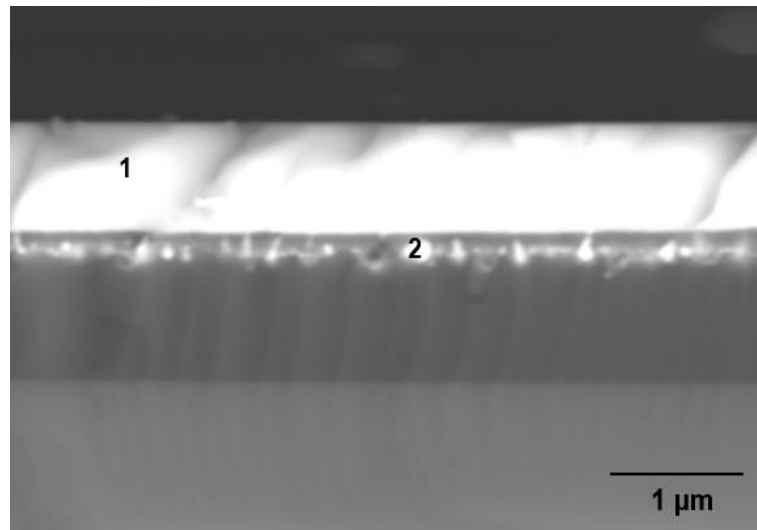
Figure 6.4: EDX-SEM measurement at two different locations for sample K470.

Table 6.3: Elemental concentration of sample K470 at two locations as shown in Figure 6.4.

Element	Concentration (at. %)	
	Position 1	Position 2
O	58.79	15.86
Si	2.25	39.49
Te	23.7	2.83
Zn	5.78	1.23
Na	8.45	1.54
Er	0.65	0.02
N	0.38	39.03

(a)   (b)   (c)   (d)   (e)   (f)   (g)   (h)
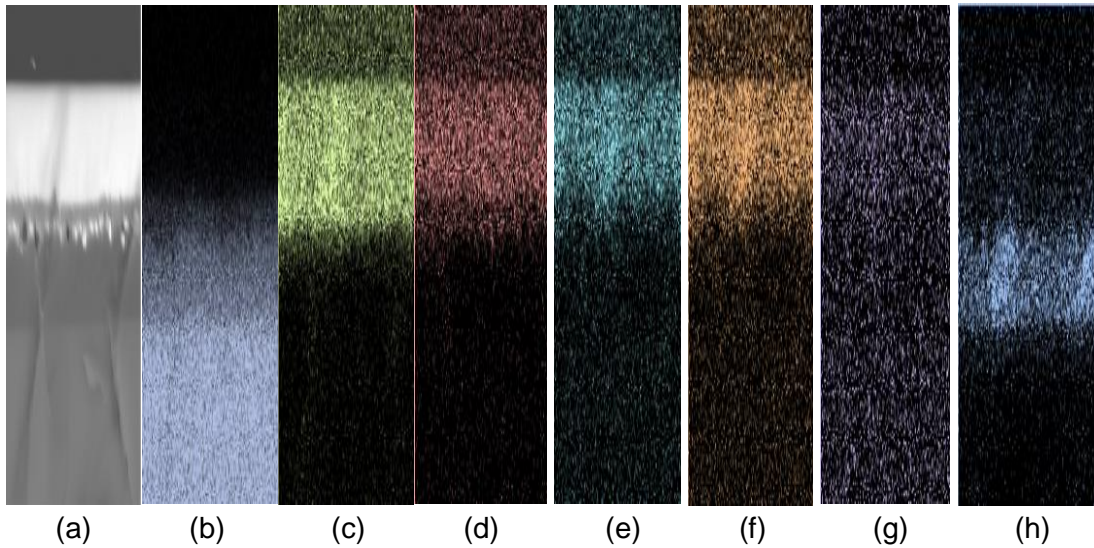
Figure 6.5: Area scan measured by EDX-SEM for sample K470 with (a) the area being measured. The distribution of species present in it which were (b) silicon, (c) oxygen, (d) tellurium, (e) sodium, (f) zinc, (g) erbium and (h) nitrogen.

Figure 6.6 shows the EDX-SEM measurement results performed at several locations in the doped layer for samples prepared at a higher temperature, i.e. 600 °C. The composition at each position is also provided in Table 6.4. Clearly, the elements are distributed unevenly. Surprisingly, the concentration of N in the doped layer is very low when compared to its concentration in Si_3N_4 which is supposedly around ~57.1 at. % . It is considered that nitrogen was lost in the form of nitrogen gas when the tellurite glass reacted with Si_3N_4 and this phenomenon was also reported by Watanabe *et al.* [268].

For the darkest regions in the doped layer, it is found that the concentration of Te is higher than that at the other positions. This is likely due to Te accumulation at position 1 but, as discussed previously in Chapter 4 (Section 4.4.1), Te accumulation should show as a brighter region because Te is a heavy atom. To identify the reason for this discrepancy, an area scan was performed to view the entire elemental distribution present in the K600 sample. Interestingly, through the area scan (Figure 6.7), it was discovered that the Te had an even distribution over the entire doped layer. Concentration elements other than Te were very low in the dark regions. The area scan for Er is less obvious because of its very low concentration, resulting in a lot of noise in the scan results. The scarcity of elements Si, O, Zn, Na, Er and N in the dark areas caused at. % for Te to be higher in these regions.
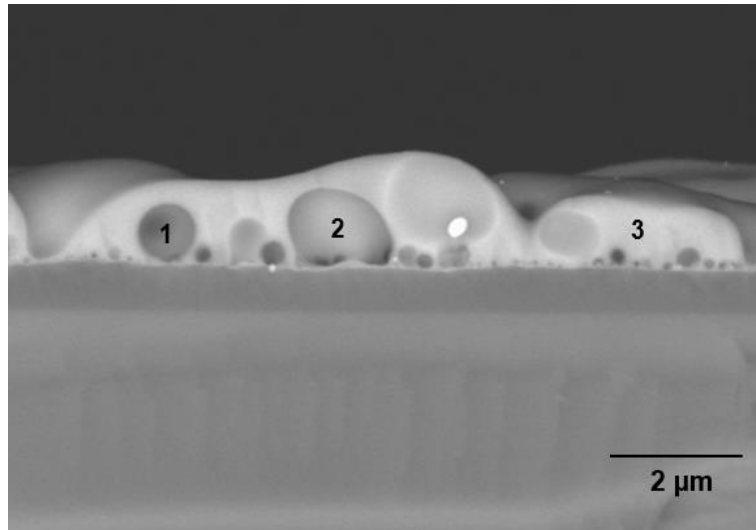
Figure 6.6: EDX-SEM measurement at two different locations for sample K600.

Table 6.4: Elemental concentration of sample K600 at two locations as shown in Figure 6.6.

Element	Concentration (at. %)		
	Position 1	Position 2	Position 3
O	34.52	41.17	63.17
Si	38.10	37.39	17.59
Te	19.64	9.15	4.79
Zn	1.84	5.73	3.22
Na	3.89	5.75	8.14
Er	0.55	0.79	0.91
N	1.46	0.02	2.18

(a)   (b)
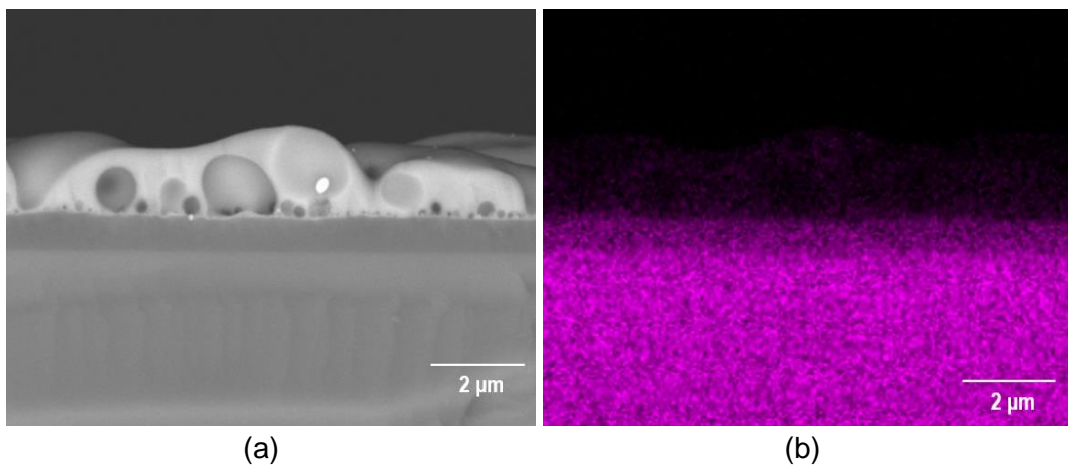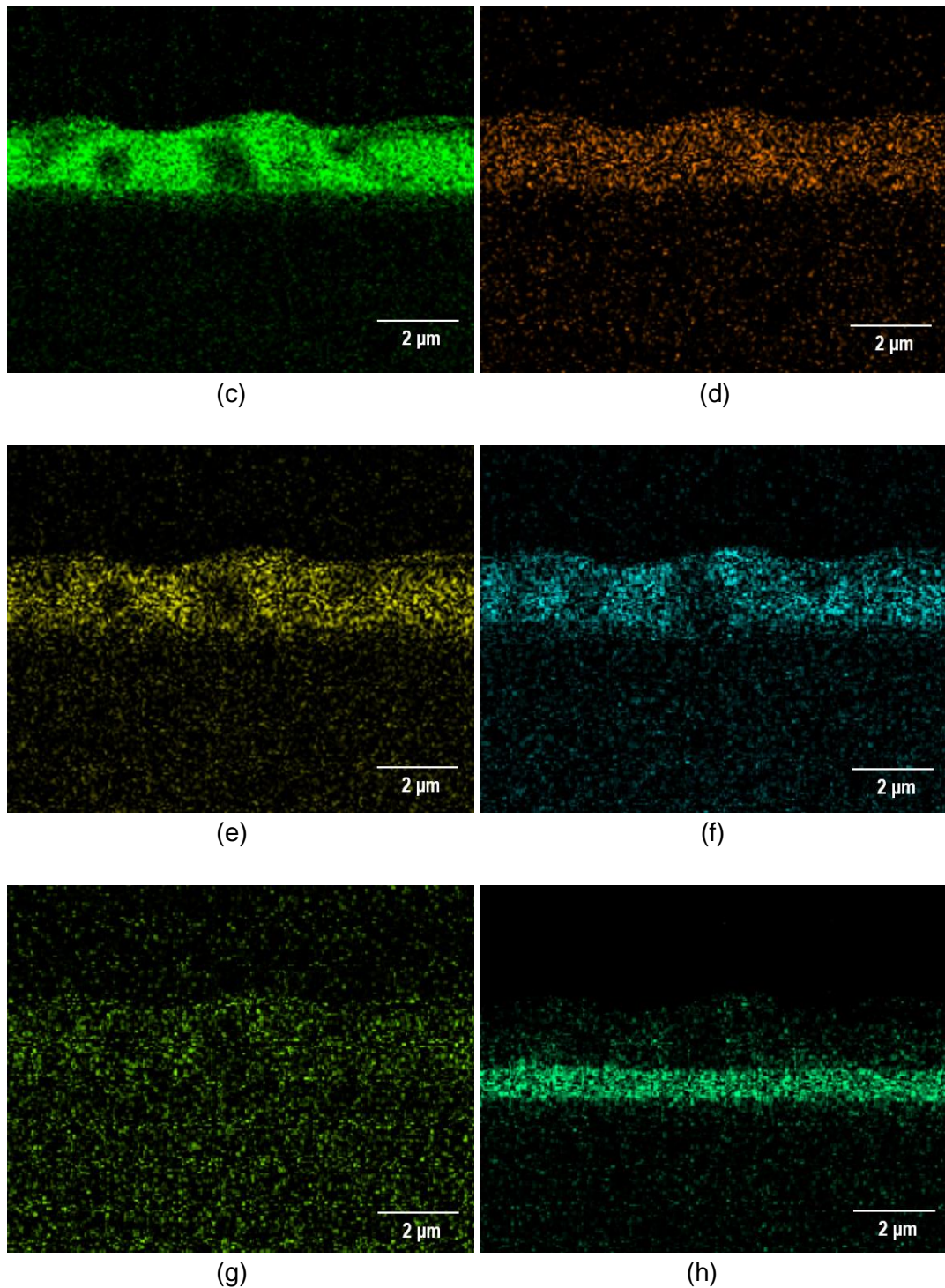
Figure 6.7: Area scan measured by EDX-SEM for sample K570 with (a) the area being measured. The distribution of species present in it which were (b) silicon, (c) oxygen, (d) tellurium, (e) zinc, (f) sodium, (g) erbium and (h) nitrogen.

Failure to obtain a very uniform doped layer, such as is the case with the EDTS, was probably due to the substrate temperature not being sufficiently high. The melting temperature of Si_3N_4 (1900 °C) is higher than that for silica (1710 °C). Therefore, higher temperatures might be required to allow the dissolution of Er-TZN into Si_3N_4 with homogeneous layer formation. However, one of the limitations of the equipment

used in this research was that it could only reach 650 °C. Additionally, the failure to obtain homogeneous doped layers might be due to the SiO_2 amorphous network which is somewhat different to that of Si_3N_4. Unlike the local structure of silica which contains adjustable and flexible -Si-O-Si- bridging bonds, Si_3N_4, on the other hand, consists of- Si-N-Si- bonds that is rendered rigid as nitrogen requires bonding with three Si rather than two to form a stable configuration. As a consequence, its network structure is much more constrained compared to silica [269]. This made it difficult for the elements from Er-TZN to diffuse into Si_3N_4 and modify it. A higher temperature would be expected to help loosen the strong Si-N bonds. Furthermore, the more rigid Si_3N_4 structure caused it to have higher internal stress levels and therefore to crack more easily. This problem was not observed for samples fabricated using a silica-on-silicon substrate. Figure 6.8 (a)-(b) shows the surface images of samples that used different substrates (SiO_2 and Si_3N_4) with the same process parameters and target material. The images were taken under an optical microscope near the edge of the doped layer. This clearly shows that the undoped Si_3N_4 layer on silicon cracked after the sample fabrication process.

Silica-on-silicon substrate	EDTS	Si_3N_4-on-silicon substrate	Doped layer
	50 µm		50 µm
(a)		(b)	
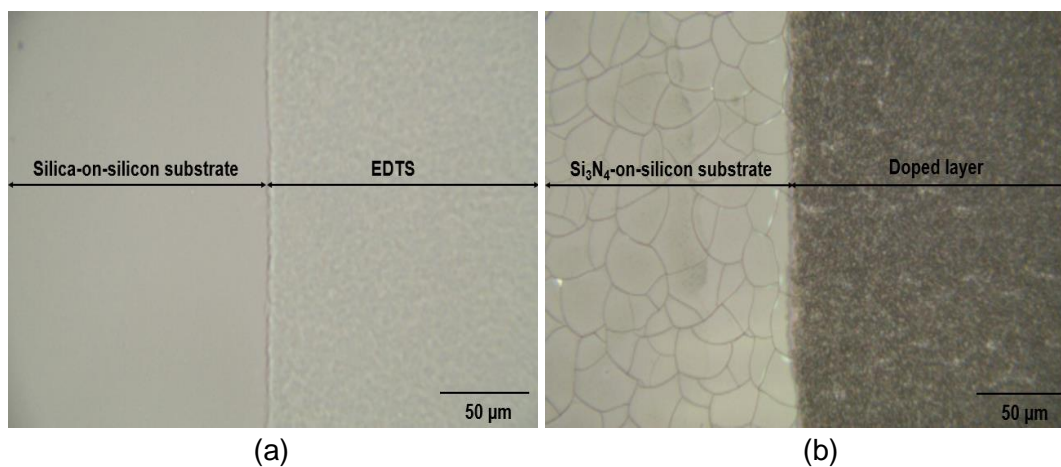
Figure 6.8: Surface image was taken by optical microscope for samples fabricated with the same process parameters and a target material for (a) silica-on-silicon and (b) Si_3N_4-on-silicon substrate.

Figure 6.9 shows the XRD patterns of the substrate and samples K470, K520, K570, K600 and K650. The patterns show that all samples are in a mixed amorphous-crystalline phase. The indexed peaks assigned to the possible crystalline structures are also shown in Figure 6.9. The 2θ peak located at approximately ~69° is a crystalline Si (100) peak that originates from the silicon substrate. For sample K470, there are eleven peaks detected which are 23.38°, 27.87°, 38.63°, 40.61°, 43.61°, 46.42°, 48.73°, 49.95°, 57.24°, 63.11° and 65.98° that corresponds to Te (ICCD

reference code: 00-036-1452). It is believed that the appearance of Te crystallite peaks is attributable from the transition layer between the deposited and Si_3N_4 layers. On the other hand, for the doped layer of samples K520-K650, the intensity and number of crystalline peaks increase when higher substrate temperatures are used. This is because crystallisation occurs more easily at high temperatures [270,271]. The crystalline peaks for SiO_2 (ICCD reference code: 00-039-1425) and Na_2Zn_3 $(SiO_4)_2$ (ICCD reference code: 00-012-3700) start to appear when the sample is heated at 600 °C and become more pronounced at higher temperatures. In addition, for the doped layer, the crystalline phase of Te also increases in both number and intensity with respect to increasing temperature.

Figure 6.10 presents the Raman spectra for the Si_3N_4-on-silicon substrate and samples fabricated with various substrate temperatures. The Raman spectra for sample K470, which is comprised of tellurite-based glass, was different (Figure 6.10 (a)) compared to samples prepared at higher temperatures. From Figure 6.10 (b)-(f), all Raman spectra showed metallic tellurium peaks (122 and 141 cm^{-1}). This indicates that the tellurium cluster is likely to form within this doped layer and coincides with the findings from XRD. However, these two peaks are less pronounced in sample K470. This suggests that most of the Te in this sample is present in oxide form rather than metallic form. The stoichiometry of the Er-TZN is better preserved in the deposited film than in the doped layer. The Raman spectrum for K470 is similar to those for sample B400 (Figure 5.15 (a)) excepting the peak for metallic tellurium because both of them are deposited layers of tellurite-based. The assignment of all the peaks in this sample has already been discussed in the previous Chapter 5 (Section 5.3). The decrease of the Si peak intensity from samples K520 to K650 indicated that the thicknesses of the doped layer increase for samples fabricated at higher substrate temperatures. The Raman spectra for samples K520, K570, K600 and K650 (Figure 6.10 (b)-(e)) are similar to the EDTS (without Te metal), and only the appearance of peaks at 122 and 141 cm^{-1}, in fact, distinguished them. Therefore the assignment of all other peaks in the spectra is the same as discussed in Chapter 5 (Section 5.2) for the EDTS as the contribution of N is not detectable.
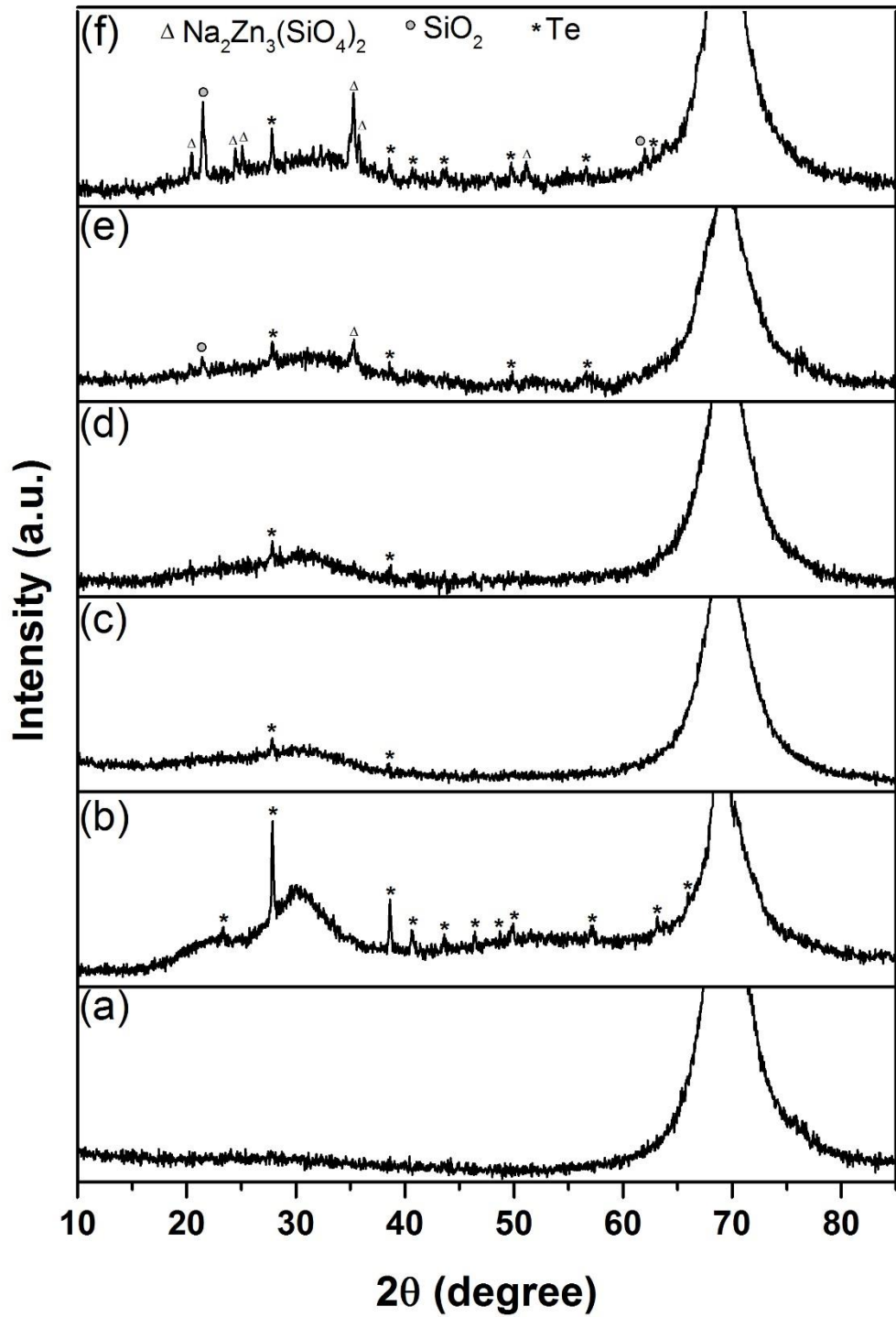
Figure 6.9: XRD patterns of (a) Si_3N_4-on-silicon substrate and samples (b) K470, (c) K520, (d) K570, (e) K600 and (f) K650.
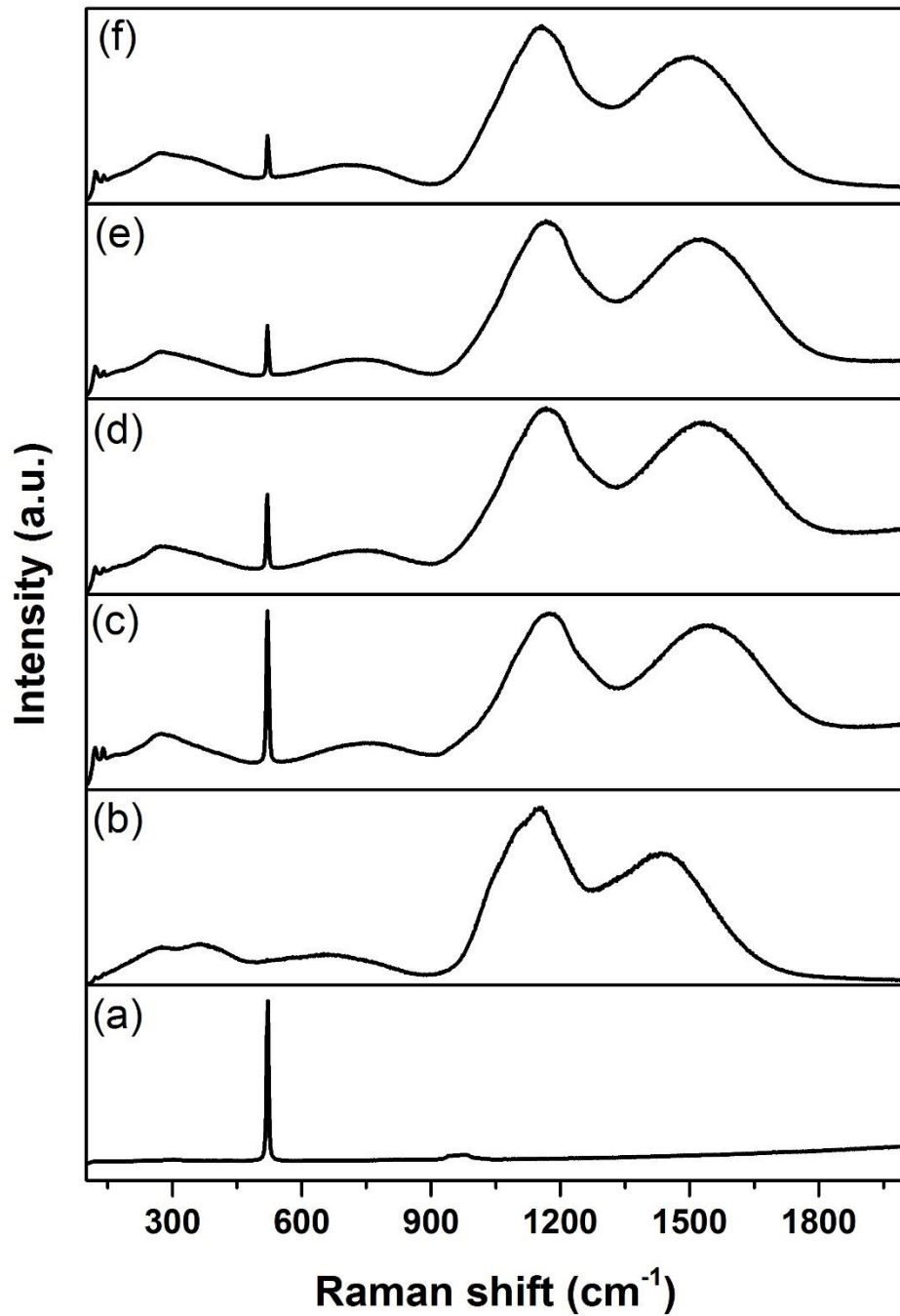
Figure 6.10: Raman spectra of (a) Si_3N_4-on-silicon substrate and samples (b) K470, (c) K520, (d) K570, (e) K600 and (f) K650.

Figure 6.11 displays the XPS survey spectrum for the sample prepared using a substrate temperature of 570 °C. The spectrum pattern obtained resembles that of

the EDTS. The absence of the element nitrogen confirmed that nitrogen is released when Er-TZN reacts with Si_3N_4. The distinct peak of N 1s that is expected at a binding energy of around 398 eV is not observed in the obtained spectra. Therefore, it is evident that nitrogen is present only in very small quantities, or is virtually absent in the doped layer. The presence of Si in the spectral survey verified once again that Er-TZN had successfully entered into the Si_3N_4 layer and formed a predominantly silicate-based layer.
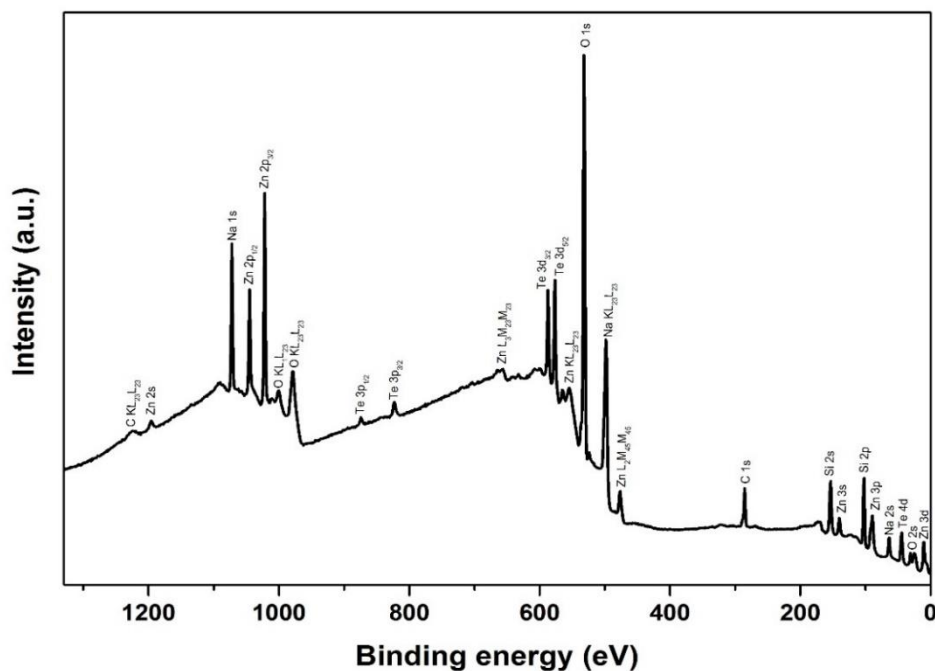
Figure 6.11: XPS survey spectrum for the sample prepared using a substrate temperature of 570 °C.

PL emission spectra for the samples are shown in Figure 6.12. For the K470 sample, the FWHM of the spectra is broader compared to others, which also indicated that the upper layer is a tellurite-based material. The low PL lifetime (4.97 ms) and a FWHM value of around 33 nm (Table 6.5) obtained are comparable to that reported for tellurite glass [53,272]. On the other hand, as shown in Table 6.5, samples K520, K570, K600 and K650 had a PL lifetime of between 9 and 10 ms and FWHMs of 20 nm, and this indicated that the doped layer is silicate based, as with the EDTS. If the doped layer is Si_3N_4 based, it will show a lower lifetime, in the range of 0.2-7 ms with a FWHM broader than a typical erbium-doped silicate base material [273–275]. From Table 6.5, the higher PL intensity and lower lifetime of samples prepared at higher substrate temperatures signifies that the Er density is higher in the doped layer when the substrate is heated to a higher temperature.
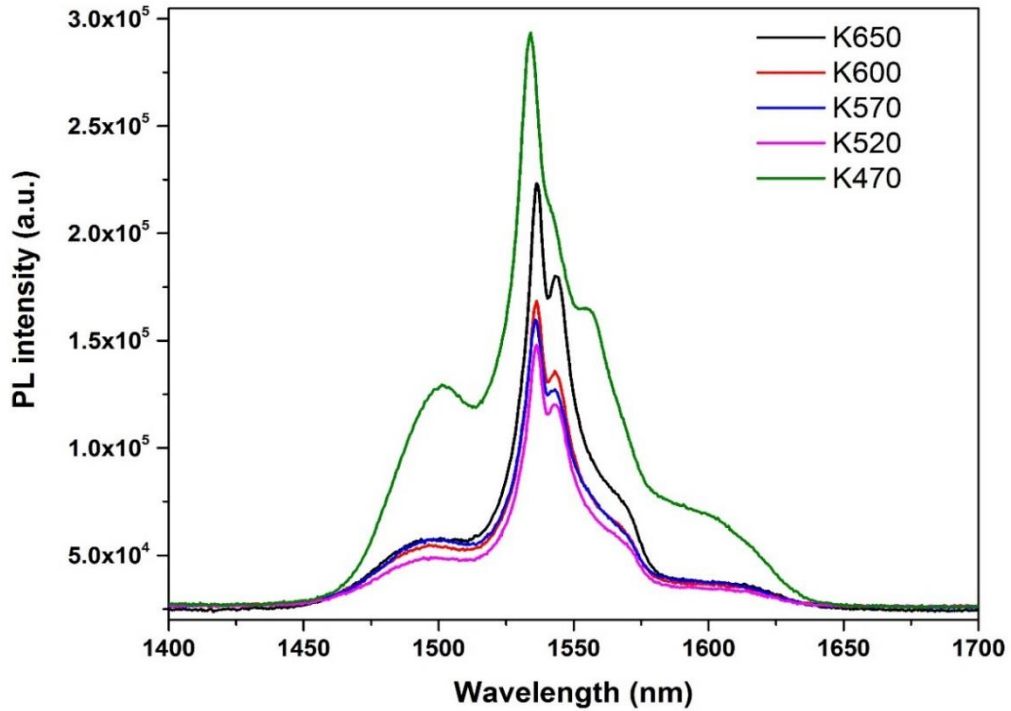
Figure 6.12: Room temperature PL spectra of samples K470, K520, K570, K600 and K650. The broad shape for sample K470 indicates it has a different host from the others.

Table 6.5: PL lifetime and FWHM of samples K470, K520, K570, K600 and K650.

Samples	PL lifetime (ms)	FWHM (nm)
K470	4.97	33
K520	10.43	20
K570	9.94	20
K600	9.71	20
K650	9.59	20

6.2 Ambient atmosphere

Another important condition in the ULPD technique is an ambient atmosphere in the chamber, as this can influence the behaviour of the plasma plume which can, in turn, affect the characteristics of the doped layer obtained. The ambient atmosphere determines the plume particle dynamics (velocity, scattering, collision and kinetic energy) and the amount of time that particles remain in the plume [276–278]. The process can be carried out under high vacuum or in the presence of another background gas that can be inert, reactive or a mixture of different gases [279]. Four samples were fabricated under different ambient atmospheres, and the process parameters used to prepare all of these samples are reported in Table 6.6. The

sample that was fabricated in a vacuum is labelled SV while SO, SN and SA represent oxygen, nitrogen and argon environments, respectively.

Table 6.6: The parameters used to dope Er-TZN into Si_3N_4-on-silicon substrate under different ambient atmospheres.

Process parameters	Operating conditions
Substrate	Si_3N_4 (t=1 µm)-on-silicon
Target material	79.5TeO_2-10ZnO-10Na_2O-0.5Er_2O_3 (Er-TZN)
Fs-laser energy	80 µJ
Fs-laser repetition rate	1.0 kHz
Substrate temperature	650 °C
Ablation period	4 hours
Background gas pressure (sample name)	Vacuum – 6 x 10^{-5} Torr (SV), 70 mTorr O_2 (SO), 70 mTorr N_2 (SN) and 70 mTorr Ar (SA)

The micrographs obtained, Figure 6.13 (a)-(d), show the doped layer on Si_3N_4-on-silicon with different background atmospheres whilst the thickness of each doped layer together with the Si_3N_4 layer underneath it are presented in Table 6.7. It can be seen that the doped layer under vacuum (SV) is the thinnest among all of the samples. The thinner doped layer recorded for the SV is believed to be related to the plume dynamics during the process. In such high vacuum conditions, when the laser ablates the target, the generated plume leaves the target with very high energy towards the substrate surface. The bombardment of these very energetic particles/ions onto the substrate/doped layer surface induces these particles to be re-sputtered or reflected when they bombard the substrate of the already formed film [280,281].

(a)   (b)
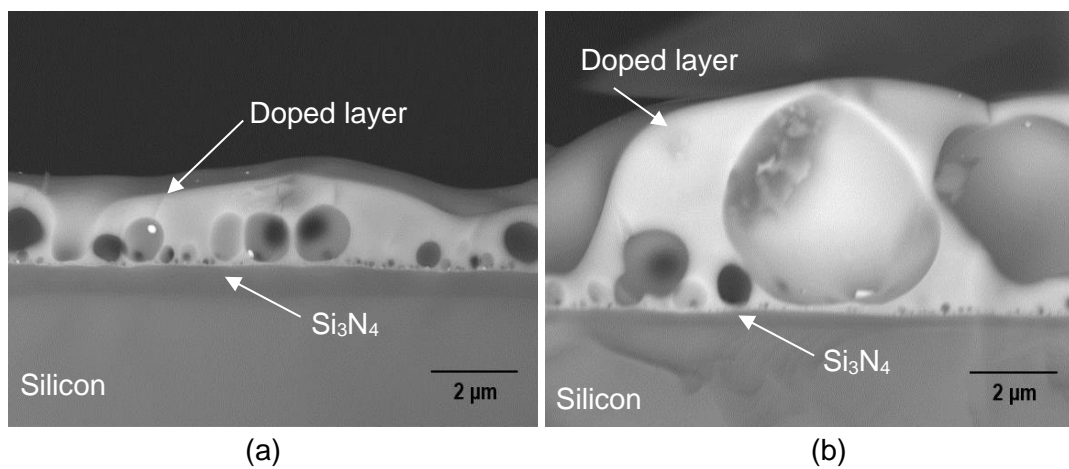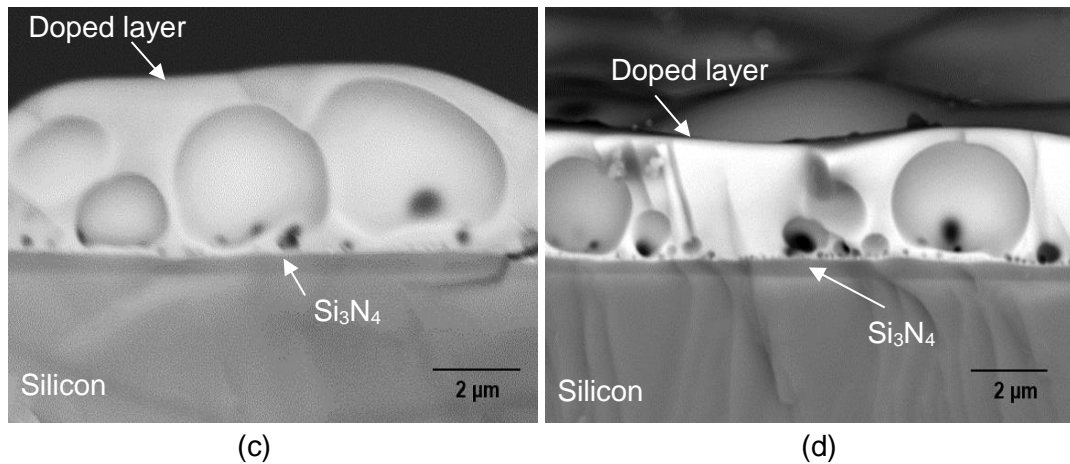
Figure 6.13: Backscattered cross-section SEM image of samples doped with Er-TZN under (a) vacuum (SV) and a background gas of (b) oxygen (SO), (c) nitrogen (SN), and (d) argon (SA).

Table 6.7: Thickness of upper layer and Si_3N_4 underneath measured by SEM for samples SV, SO, SN and SA.

Sample	Thickness (µm)	
	Upper layer	Si_3N_4 under upper layer
SV	2.1 ± 0.2	0.62 ± 0.04
SO	5.4 ± 0.4	0.34 ± 0.04
SN	4.5 ± 0.3	0.35 ± 0.05
SA	3.0 ± 0.2	0.40 ± 0.06

The very high kinetic energy of a particle in the plasma plume can be reduced by deliberately introducing a background gas in the chamber at low pressures. The presence of the background gas creates collision events that occur between the ablated particle and background gas that will scatter the plumes from their initial trajectories [282,283] and increase the residence time of particles in the plume. This gives ample time for the particles to nucleate, agglomerate and enlarge their sizes prior to reaching the substrate [284]. As a consequence, they will be less mobile on the substrate surface [283].

Since the argon atom is bigger than the nitrogen and oxygen atoms, the probability of a collision incident between particles in the plume with Ar atoms is higher, resulting in a shorter mean free path and bigger particle size. Therefore, a thinner layer is produced than for the samples fabricated under O_2 or N_2 atmospheres. The mean free path can be estimated by using equation 6.1 [284,285]:

$$\lambda_m = \frac{k_B T}{\sqrt{2}\pi x^2 P} \tag{6.1}$$

where k_B is the Boltzmann constant, T is the temperature of the gas, x is the collisional cross-section and P is the gas pressure. The mean paths for the Ar and O_2 environments are estimated to be around 1.767 x 10^{-7} m and 2.475 x 10^{-7} m respectively, and it is predicted to be higher under vacuum conditions [284]. For the N_2 atmosphere, it is expected that the mean free path is quite similar to that of O_2 because both have almost similar mass density. However, it appears that the thickness of the doped layer for sample SO is higher than that of SN although SN is fabricated with a lighter background gas. This is probably because O_2 is more reactive than N_2 and chemical reactions between O_2 and particles within the plume may have occurred. It is anticipated that the reaction between O_2 from the background gas with the ablated particles will form single monoxide or multioxide molecules. These heavier monoxide or multioxide molecules experience less scattering to the flank side compared to lighter elements [286]. This might be the cause of the doped layer for the SO samples being thicker than that for the SN samples.

The surfaces of the doped layers for the samples prepared under various environmental conditions were recorded by SEM and shown in Figure 6.14 (a)-(d). Figure 6.14 (a) displays a surface image sample prepared in a high vacuum environment while those prepared under oxygen, nitrogen and argon atmospheres are presented in Figure 6.14 (b) – (d). Among the images, the surface layer for SV seems to be relatively smoother. This was probably due to the particles that travelled to the substrate directly from the target (without or with very few collisions), and this resulted in the sizes of the particles which impinged on the substrate being smaller. The size of a bump on the surface increases when heavier gas is used. In addition, a heavier gas increases the residence time of the particles in the plume which makes the particle become bigger, the collisions between the background gas and the particles in the plume become more severe, leading to an increased broadening of the plume angular distribution. For a heavy background gas, the broadening is more critical than for a light gas. Light species in the plume tend to be much more scattered than heavy species, and this leads to the appearance of large particles on the film [280].

Figure 6.15 (a)-(d) shows the XRD patterns of the doped layers on Si_3N_4-on-silicon fabricated in different atmospheres. The patterns show that all samples are still in a mixed amorphous-crystalline phase. The indexed peaks assigned to the possible

crystalline structures are also shown in Figure 6.15 (a)-(d). The sample prepared in an oxygen environment clearly exhibited a higher intensity of crystalline peak, which indicated a greater degree of crystallinity [287]. This is probably attributable to the interaction of oxygen gas with species in the plume. The energy exchange and heat generation associated with the oxidation process expedited the crystallisation of the doped layer and improved the crystallinity [288]. On the other hand, the longer residence stays time for plume particles in the argon atmosphere could also have enhanced the building of a more stable crystal bridge [289] and subsequently, therefore, increased the crystalline phase (Figure 6.15 (d)). Furthermore, the high interaction of ablated species with the argon atoms eventually increased the plasma plume temperature, which also helped to increase the crystallisation [290].

(a)　　　　　　　　　　　　　(b)

(c)　　　　　　　　　　　　　(d)
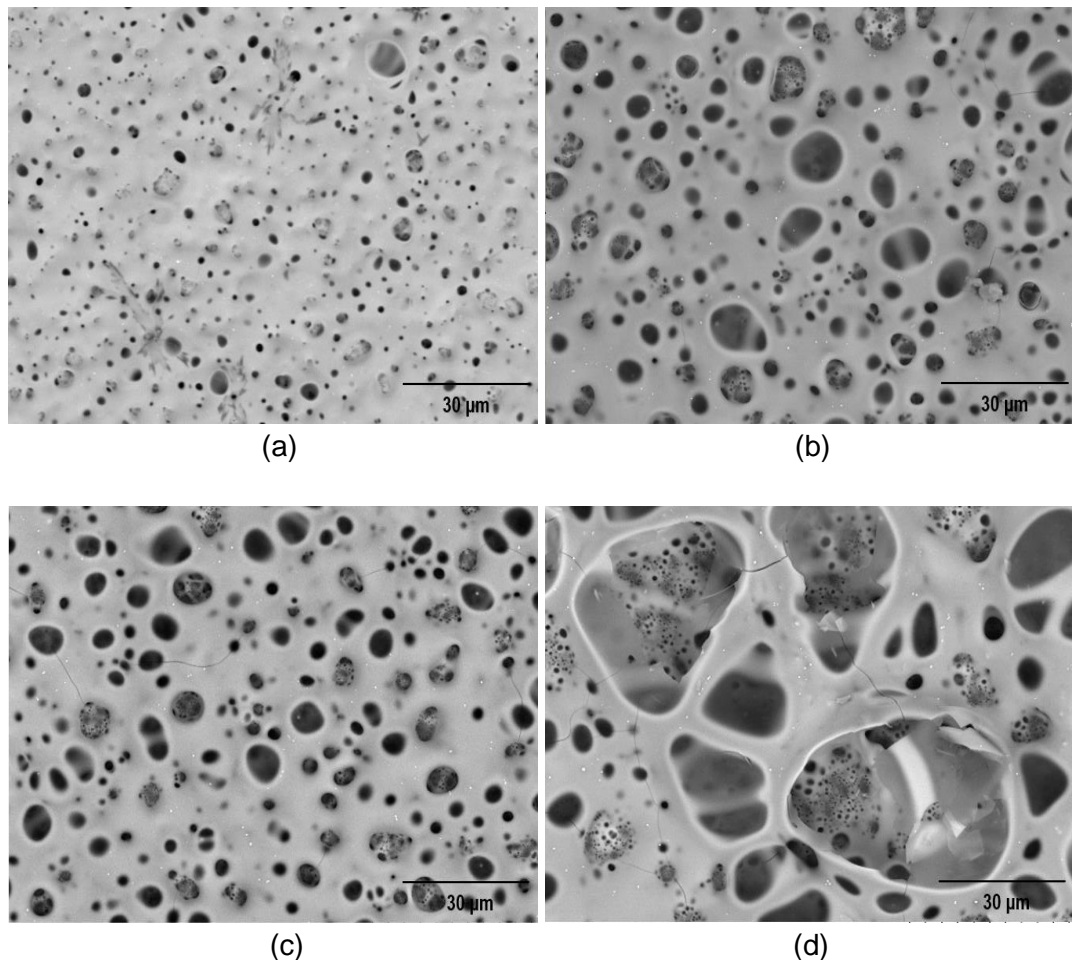
Figure 6.14: SEM micrograph for the surface of doped layers prepared under (a) vacuum (SV), (b) oxygen (SO), (c) nitrogen (SN) and argon (SA).

Figure 6.16 presents the Raman spectra for the samples doped under a vacuum and with various types of background gas. All the spectra exhibited a similar pattern, except the intensity of the Si peak (521 cm^{-1}), which depended on the thickness of

the doped layer. As mentioned before, the Si peak will be more pronounced for the thinner film.

The PL spectra for samples SV, SO, SN and SA are shown in Figure 6.17. The PL intensity for each sample corresponds to the amount of Er^{3+} ions embedded in the doped layer. The sample fabricated in a vacuum atmosphere (SV) experienced re-sputtering incidents, causing a reduction of Er^{3+} ions in the doped layer. However, all samples still exhibited silicate-based characteristics according to the FWHM and PL lifetime, as listed in Table 6.8. As expected, the PL lifetime had an inverse relationship with PL intensity.
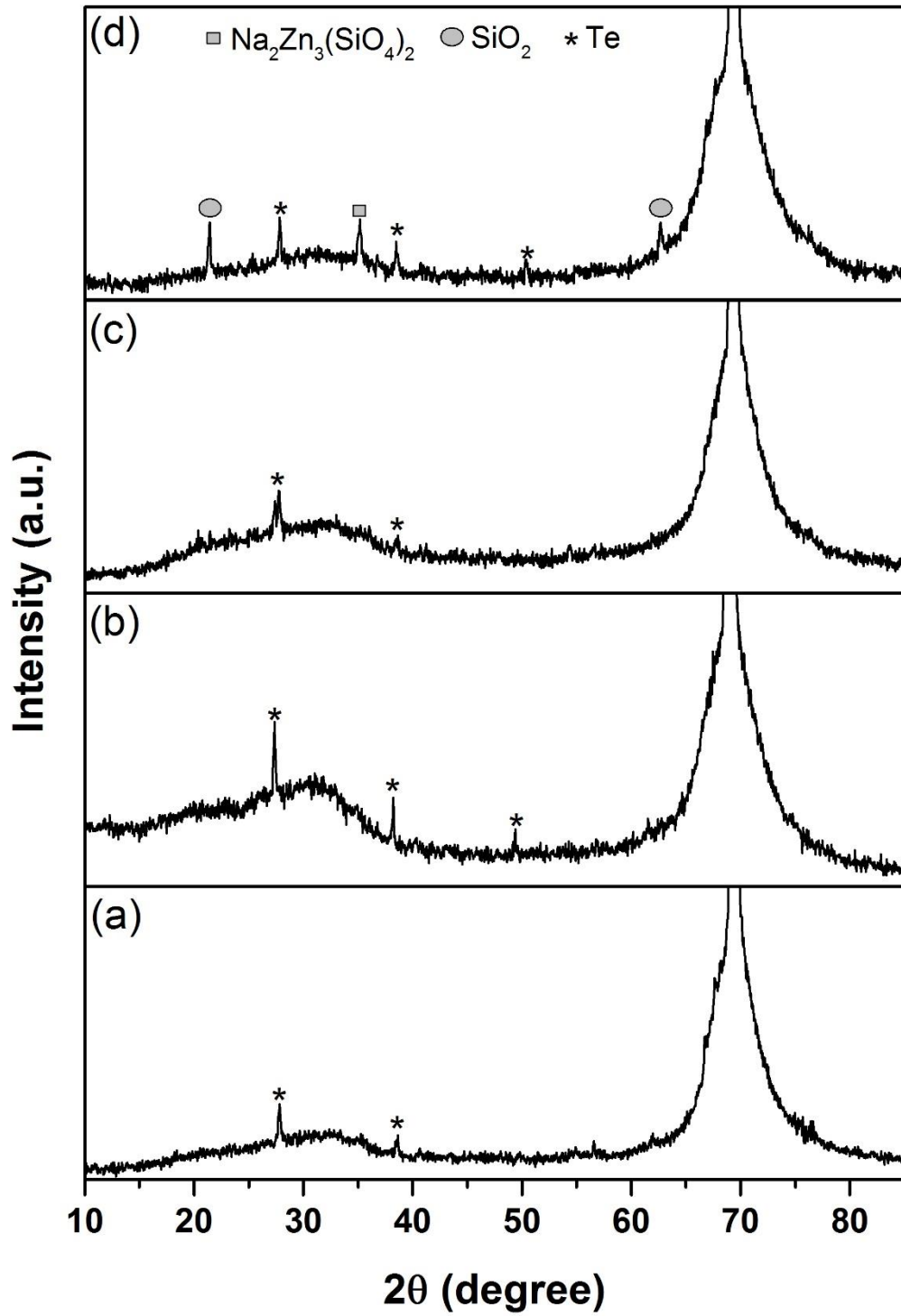
Figure 6.15: XRD patterns of doped layer on Si₃N₄-on-silicon fabricated under (a) vacuum (SV), (b) oxygen (SO), (c) nitrogen (SN) and (d) argon (SA) environment.
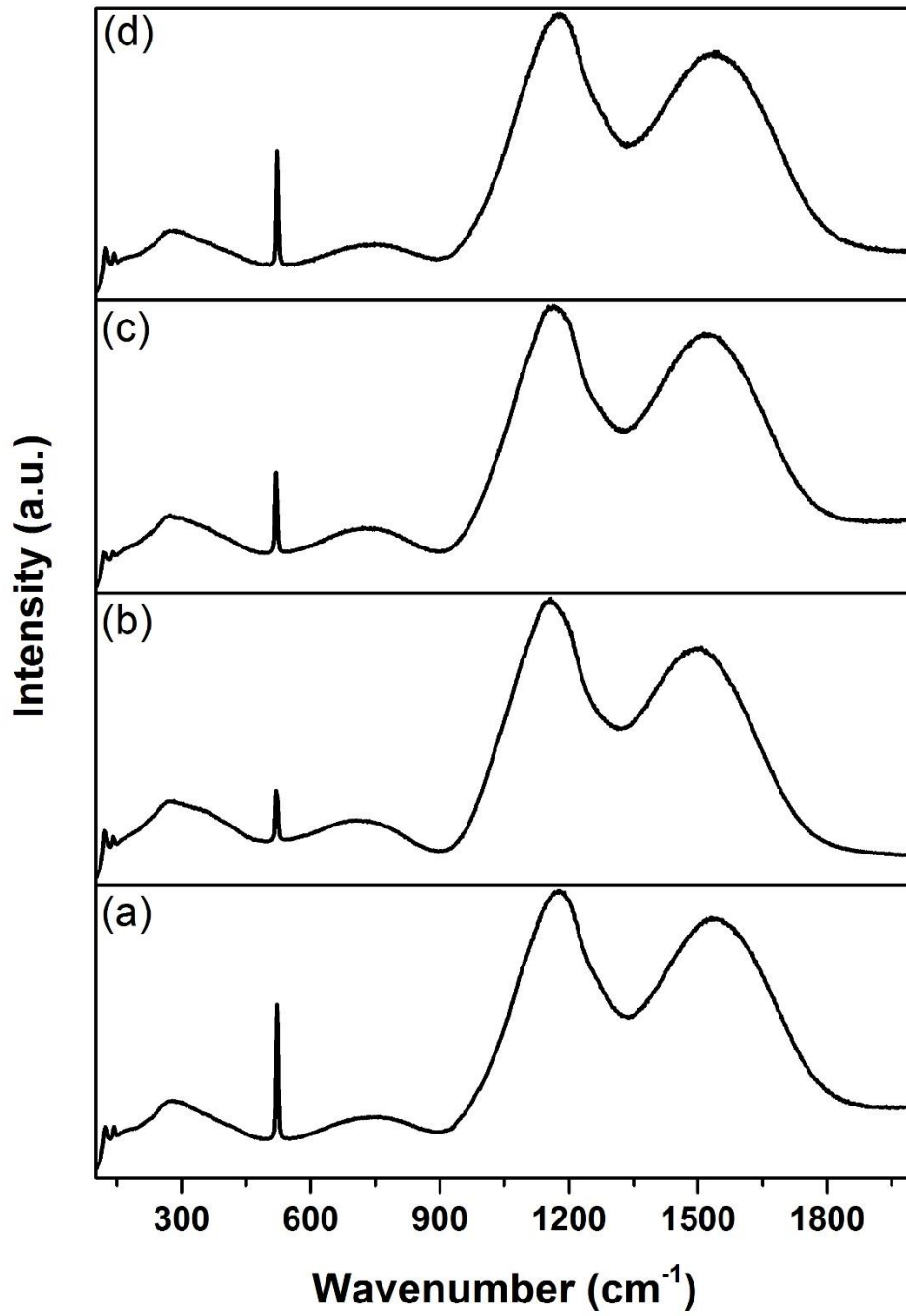
Figure 6.16: Raman spectra for samples doped under (a) vacuum (SV), (b) oxygen (SO), (c) nitrogen (SN) and (d) argon (SA) environment.
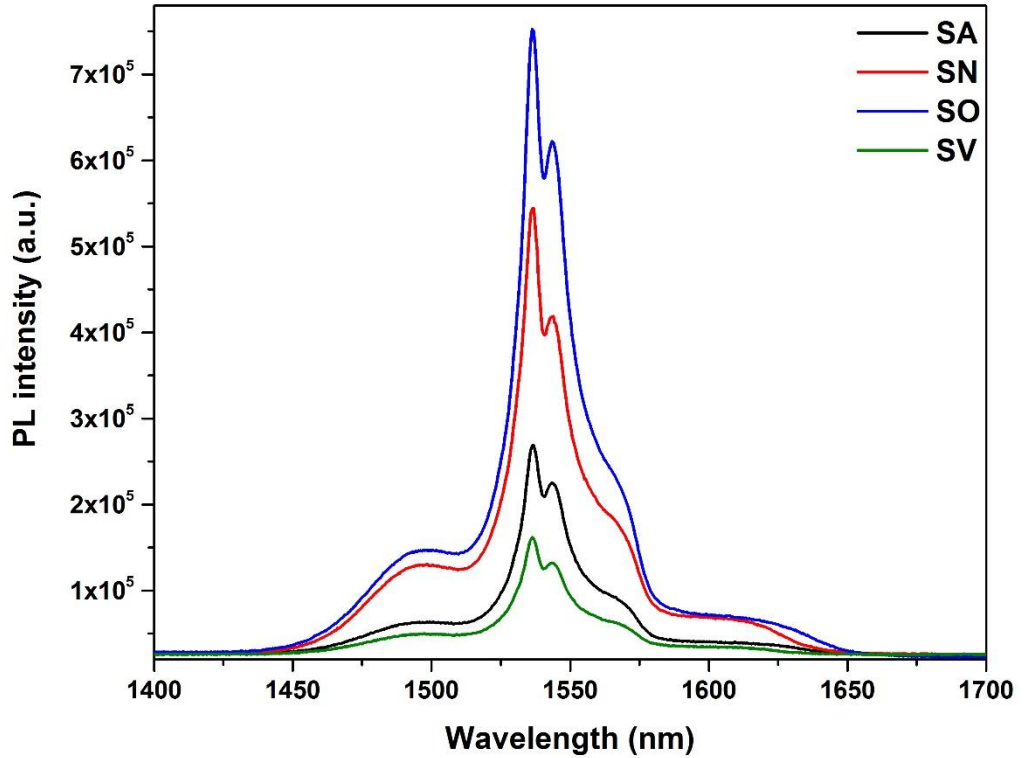
Figure 6.17: PL spectra for samples SV, SO, SN and SA.

Table 6.8: PL lifetime and FWHM for doped layer prepared under different atmospheres.

Samples	PL lifetime (ms)	FWHM (nm)
SV	10.55	20
SO	8.45	20
SN	8.89	20
SA	10.43	20

6.3 Fs-laser energy

Trialling of the process parameters continued by using various fs-laser energies to achieve a homogenous doped layer. Five samples were fabricated and labelled according to the fs-laser energy used. Sample N30 represents the sample fabricated with 30 µJ laser energy whilst the higher fs-laser energies at 40, 50, 60 and 80 µJ are labelled with codes N40, N50, N60, and N80 respectively. Table 6.9 exhibits the process parameters used to prepare samples employing different fs-laser energies.

Table 6.9: List of process parameters utilised to dope Er-TZN into a Si_3N_4-on-silicon substrate with different fs-laser energies.

Process parameter	Operating conditions
Substrate	Si_3N_4 (t=1 µm)-on-silicon
Target material	$79.5TeO_2$-$10ZnO$-$10Na_2O$-$0.5Er_2O_3$ (Er-TZN)
Fs-laser energy (sample name)	30 µJ (N30), 40 µJ (N40), 50 µJ (N50), 60 µJ (N60) and 80 µJ (N80)
Fs-laser repetition rate	1.0 kHz
Substrate temperature	650 °C
Ablation period	4 hours
Background gas pressure	70 mTorr O_2

Figure 6.18 (a) - (e) shows SEM images of cross-sections for samples fabricated using different fs-laser energies. Table 6.10 gives the thickness of the doped layer, measured by SEM, for all samples. The images (Figure 6.18 (a)-(e)), together with the values stated in Table 6.10, clearly show that the higher fs-laser energy resulted in an increased thickness of the doped layer, as expected. This scenario is the same as that seen for the EDTS. However, lower energy ablation using fs-laser energies of 30 and 40 µJ led to a more uniform layer and particle size reduction. This is because higher fs-laser energy caused the plasma plume to be denser and enhanced the molecular interactions that led to the formation of bigger particles [291]. Furthermore, when a higher fs-laser energy is used on the target material, the absorption depth becomes larger, and this could lead to superheating of a large volume. As a result of this heating process, the volume could transform into the melt phase due to rapid expansion thus increasing the number of molten droplets or particulates ejected from the target [292]. The very high measurement error for the thickness of sample N80 compared to the other samples indicates that the surface of this sample is very rough. The large particle size that results from the use of high fs-laser energy causes the surface doped layer to be very rough.
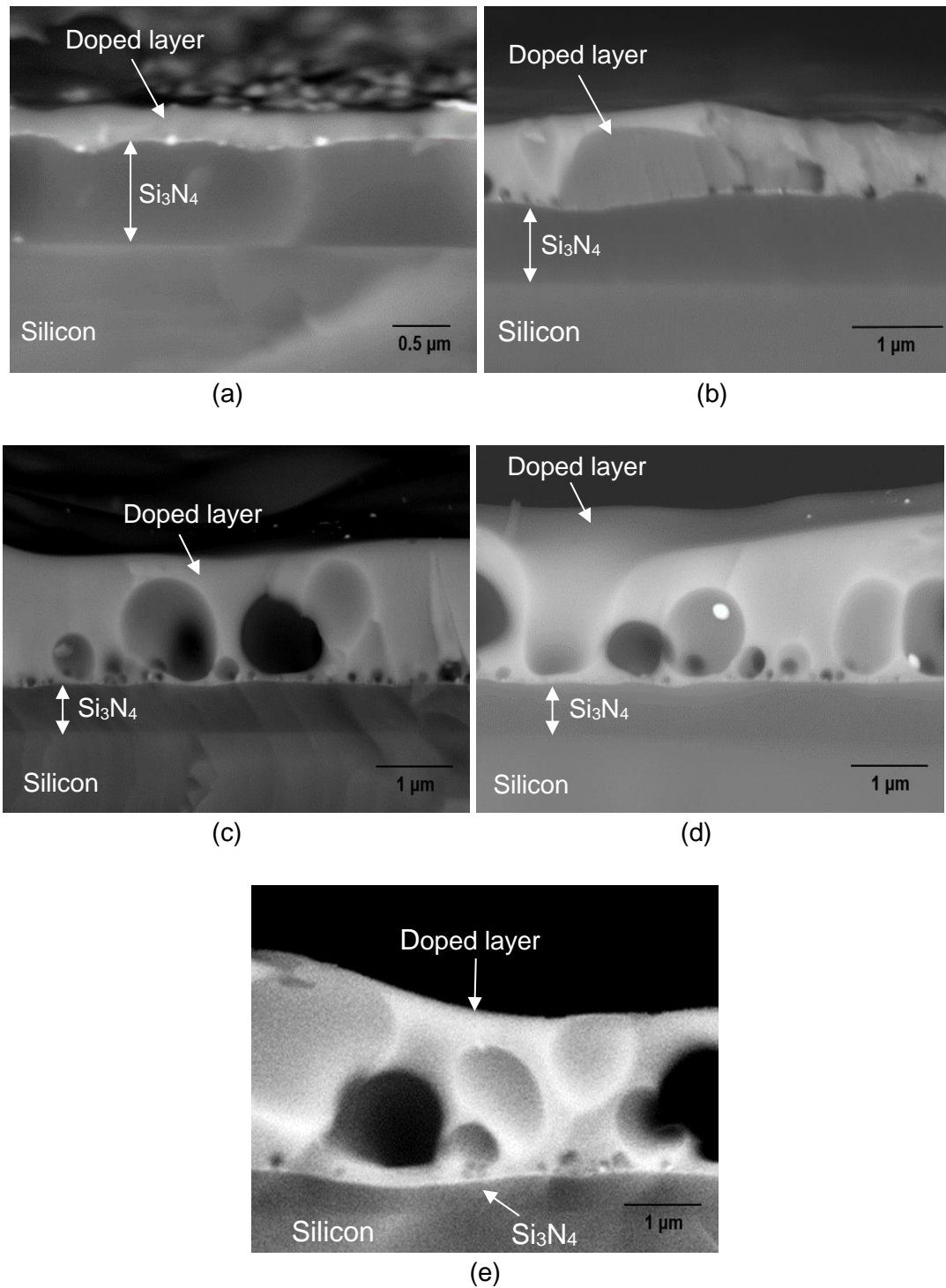
Figure 6.18: Backscattered cross-section SEM image of samples doped with Er-TZN using fs-laser energy of (a) 30 µJ (N30) (b) 40 µJ (N40), (c) 50 µJ (N50), (d) 60 µJ (N60) and (e) 80 µJ (N80).

Table 6.10: Thickness of upper layer and Si_3N_4 underneath it measured by SEM for samples N30, N40, N50, N60 and N80.

Sample	Thickness (µm)	
	Doped layer	Si_3N_4 under doped layer
N30	0.3 ± 0.1	0.81 ± 0.05
N40	0.9 ± 0.2	0.75 ± 0.09
N50	1.6 ± 0.3	0.60 ± 0.09
N60	2.0 ± 0.3	0.55 ± 0.03
N80	2.3 ± 0.9	0.47 ± 0.07

Figure 6.19 (a)–(c) shows three different positions in the N30, N40 and N60 samples measured by EDX-SEM to obtain the elemental concentrations at those particular positions, which are given in Table 6.11. In Table 6.11, for sample N30, it is found that very few Er-TZN elements managed to penetrate into the Si_3N_4. The upper layer still has plenty of nitrogen species, and this proves that at an fs-laser energy of 30 µJ, species in the Er-TZN are unable to interact efficiently with the Si_3N_4 network due to species in the plasma plume having low kinetic energy and velocity. This causes the reaction between Er-TZN and Si_3N_4 to be very low for this sample. On the other hand, at position 3, concentrations of Na, Zn and Te are higher than at positions 1 and 2, and this might be the reason that position 3 appears brighter. Although the element concentrations present in the doped layer are uneven, decreasing levels of N could still be seen for samples prepared using higher fs-laser energy. This shows that the reaction between Er-TZN and Si_3N_4 increases when a higher fs-laser energy is used.

Figure 6.20 displays the XRD patterns for samples that were fabricated with different fs-laser energies. The absence or almost invisible halo around 30° indicates that the doped layer for samples N30 and N40 is not really an amorphous silicate layer due to the scarcity of species from Er-TZN in it. The increase of Er-TZN in the doped layer (N50, N60 and N80) caused the crystalline phase SiO_2 (21.34°) (ICCD reference code: 00-039-1425) to be destroyed, making it more likely to consist of amorphous SiO_2. In addition, the increased intensity for the peak of Te when higher laser energy was used indicated that the level of Te clustering increased with laser energy. Furthermore, the Si_2N_2O peak at *2θ* of 26.32° [293] appeared in the N30 sample, and this clearly showed that there is still a high nitrogen content in this layer.

Figure 6.21 shows the Raman spectra for samples N30, N40, N50, N60 and N80. Peaks of Te-Te at 121 and 142 cm^{-1} are lower for the N30 sample compared to the other samples, which are similar to the levels of Te recorded via EDX-SEM.

Furthermore, peaks in the high wavenumber regime appeared to be unclear due to the very small concentration of Er in the N30 sample. In addition, the very thin doped layer of sample N30 caused the signal from crystalline Si (521 cm^{-1}) to be prominent compared to the other samples. A broad peak around 900-1050 cm^{-1} also appeared, which is believed to be associated with Si-O bond, as reported in the literature [259,261,262]. This peak was generally overshadowed by the prominent Er PL like other samples reported in this thesis.
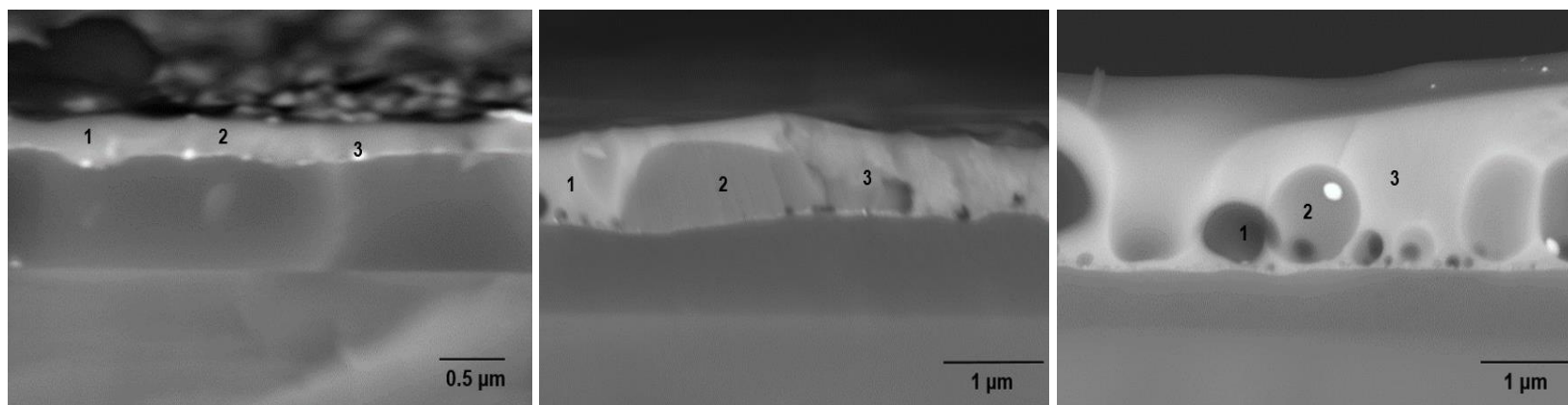
(a) (b) (c)

Figure 6.19: EDX-SEM measurement at three different locations for samples (a) N30, (b) N40 and (c) N60.

Table 6.11: Elemental concentration at three different positions in Figure 6.19 for samples N30, N40 and N60.

Element	Concentration (at. %)								
	Sample N30			Sample N40			Sample N60		
	Position 1	Position 2	Position 3	Position 1	Position 2	Position 3	Position 1	Position 2	Position 3
O	12.84	12.35	6.59	59.04	51.15	58.93	30.35	33.59	52.71
Si	30.96	31.22	34.24	14.82	24.04	19.84	18.97	29.8	22.02
Te	0.19	0.16	3.15	2.37	0.45	0.21	33.63	13.57	3.35
Zn	1.61	1.46	1.98	6.67	5.3	4.07	6.97	10.14	8.95
Na	2.61	2.53	3.04	10.81	8.48	8.13	8.45	10.23	9.36
Er	0.07	0.10	0.12	0.34	0.25	0.25	1.17	1.51	2.03
N	51.72	52.18	50.88	5.95	10.33	8.57	0.46	1.16	1.58

162
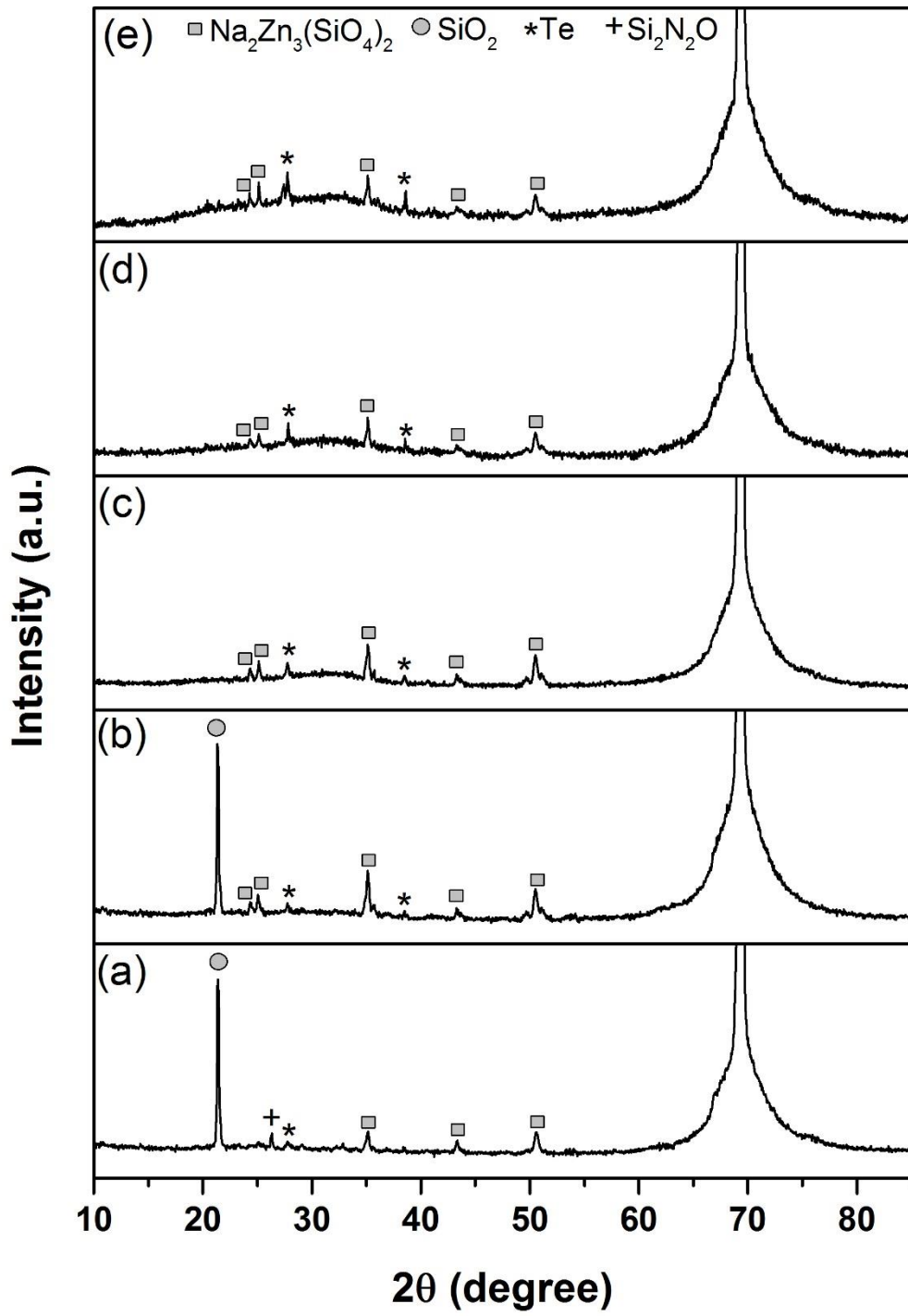
Figure 6.20: XRD patterns of doped layer on Si_3N_4-on-silicon fabricated using an fs-laser energy of (a) 30 µJ (N30), (b) 40 µJ (N40), (c) 50 µJ (N50), (d) 60 µJ (N60) and (e) 80 µJ (N80).
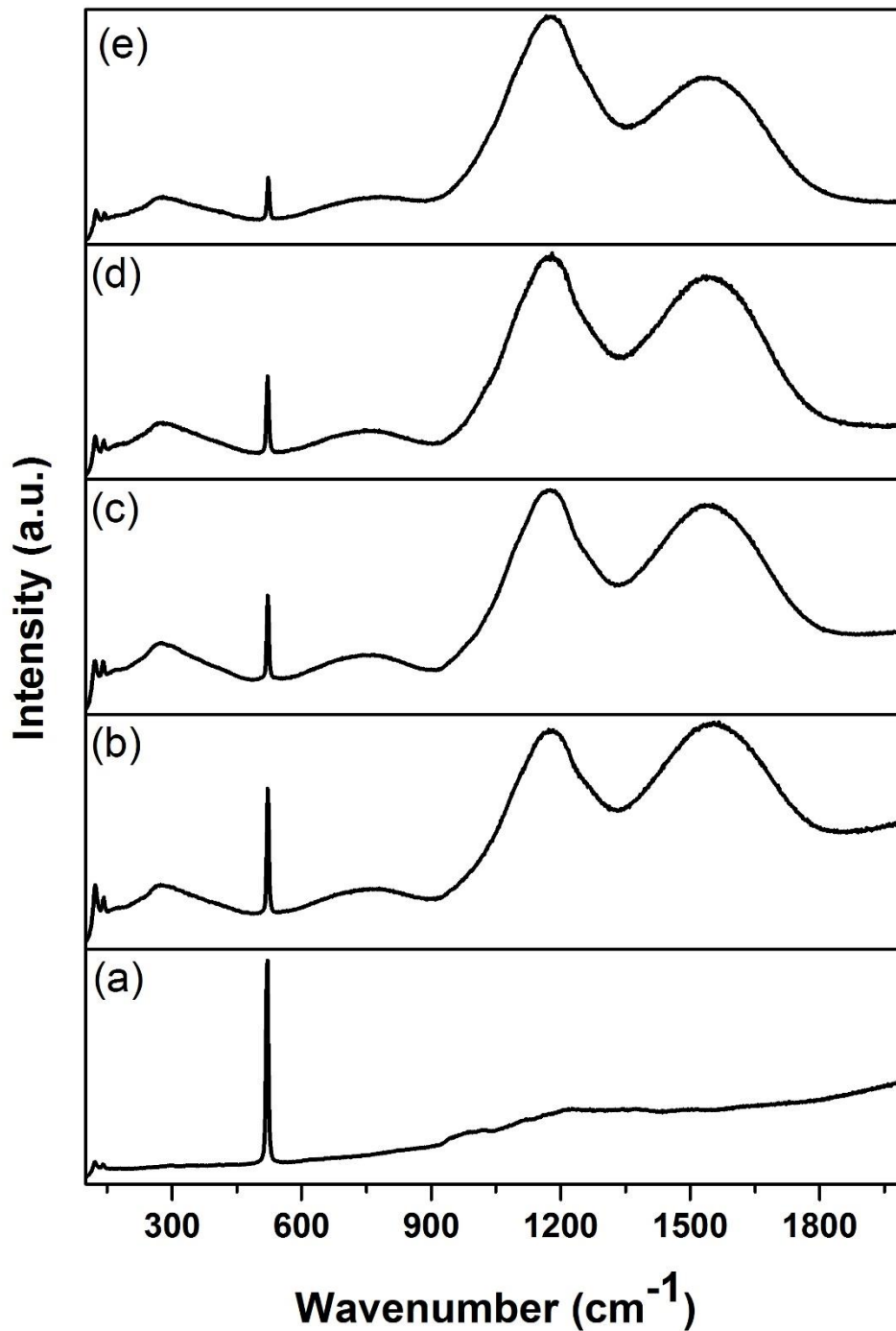
Figure 6.21: Raman spectra for sample fabricated using an fs-laser energy of (a) 30 μJ (N30), (b) 40 μJ (N40), (c) 50 μJ (N50), (d) 60 μJ (N60) and (e) 80 μJ (N80).

Figure 6.22 illustrates the PL spectra for samples N30, N40, N50, N60 and N80. The PL intensity becomes higher for samples that were prepared with higher laser energy except the N80 sample. The phenomenon of decreasing PL intensity that was observed for the N80 sample is known as photoluminescence quenching, and is due

to the very high concentration of erbium in the sample [294,295]. The short distance between Er^{3+}-Er^{3+} triggered this concentration quenching effect, which could have induced energy transfers between them. Otherwise, the very low erbium concentration in the N30 sample caused Er emission to appear very weak. PL lifetime and FWHM for every sample are shown in Table 6.12. Based on the obtained FWHM, all samples, except for N30 and N40, showed PL characteristics like the EDTS. The broader FWHM for sample N30 and N40 might have been due to its environment host that differed from the other samples. Samples N30 and N40 had a very low lifetime of 3.95 s and 5.12 s, respectively, and this low lifetime was probably due to erbium in the silicon oxynitride environment, which is often reported to have a PL lifetime in the range of 0.5-7 ms [247,296,297]. For the N80 sample, the main network was still silicate based on its FWHM which had a value of 20 nm. However, the drastic decrease of PL lifetime for this sample was due to concentration quenching [295,298].
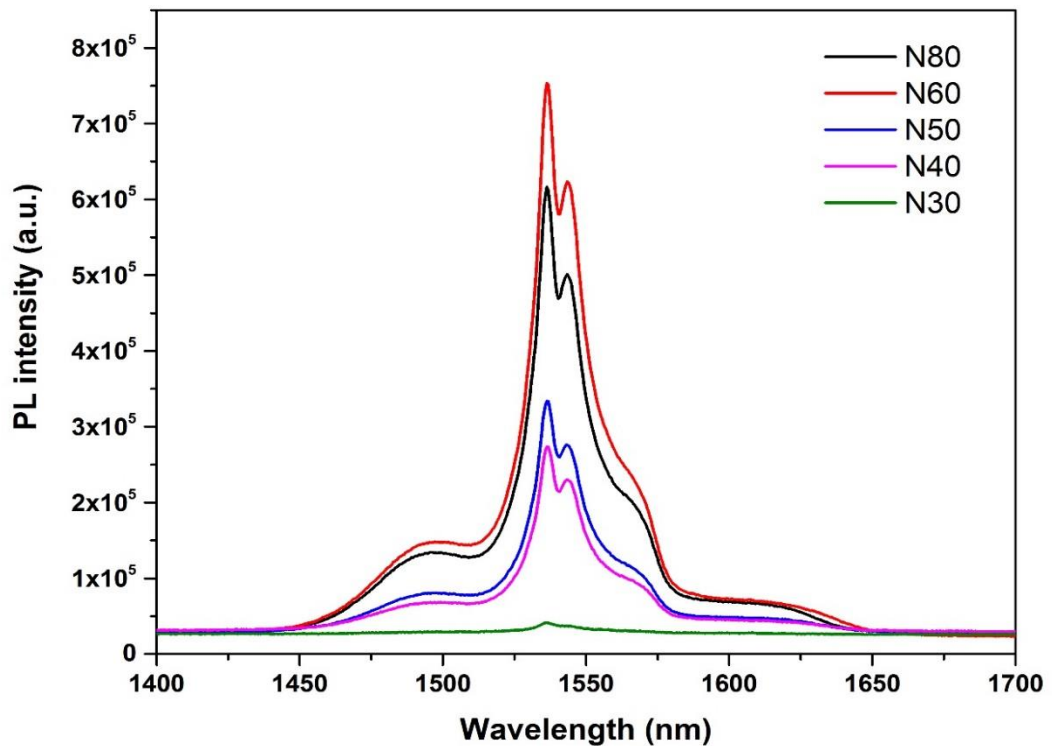
Figure 6.22: Room temperature PL spectra for the $^4I_{13/2} \rightarrow {}^4I_{15/2}$ transition of erbium ions for samples N30, N40, N50, N60 and N80.

Table 6.12: PL lifetime and FWHM for doped layer prepared using different laser energies.

Samples	PL lifetime (ms)	FWHM (nm)
N30	3.95	25
N40	5.14	23
N50	9.59	20
N60	9.02	20
N80	6.33	20

6.4 Fs-laser repetition rate

The process used to obtain the homogeneously doped layer is continued in this section by varying fs-laser repetition rate. Two repetition rates were used during sample fabrication, 0.5 Hz and 1.0 kHz, which are labelled R0.5 and R1. The process parameters that were used to fabricate each sample are listed in Table 6.13.

Table 6.13: The parameters used to dope Er-TZN into Si_3N_4-on-silicon substrate by using two different fs-laser repetition rates.

Process parameter	Operating conditions
Substrate	Si_3N_4 (t=1 µm)-on-silicon
Target material	$79.5TeO_2$-$10ZnO$-$10Na_2O$-$0.5Er_2O_3$ (Er-TZN)
Fs-laser energy	50 µJ
Fs-laser repetition rate (sample name)	0.5 kHz (R0.5), 1.0 kHz (R1)
Substrate temperature	650 °C
Ablation period	4 hours
Background gas pressure	70 mTorr O_2

Figure 6.23 shows the cross-section BSE SEM image for samples R0.5 and R1 while Table 6.14 gives the thickness of the doped layer and the Si_3N_4 underneath the doped layer. From both the micrographs and thickness measurements, it is clear that the sample prepared with the lower repetition rate (R0.5) is thinner. Nevertheless, this sample was more homogeneous. It is speculated that this is due to a smaller particle size when a lower repetition rate is used. The relationship between particle size and repetition rate, however, is still not well understood. However, one possible reason for this is the heating effect generated during the ablation process [299]. The increase in the repetition rate resulted in a higher heat accumulation which raised the plume temperature and subsequently led to an enlargement of the crystallite particles as well as enhanced crystallisation [300–303]. The higher error for the thickness of

sample R1 compared to that of R0.5 indicated that it had a rougher surface, which is contributed to by a larger particle size. The different surface topologies for the two samples were imaged with an optical microscope, and these images are shown in Figure 6.24. These two images proved that surface sample R1 is rougher.

(a)   (b)
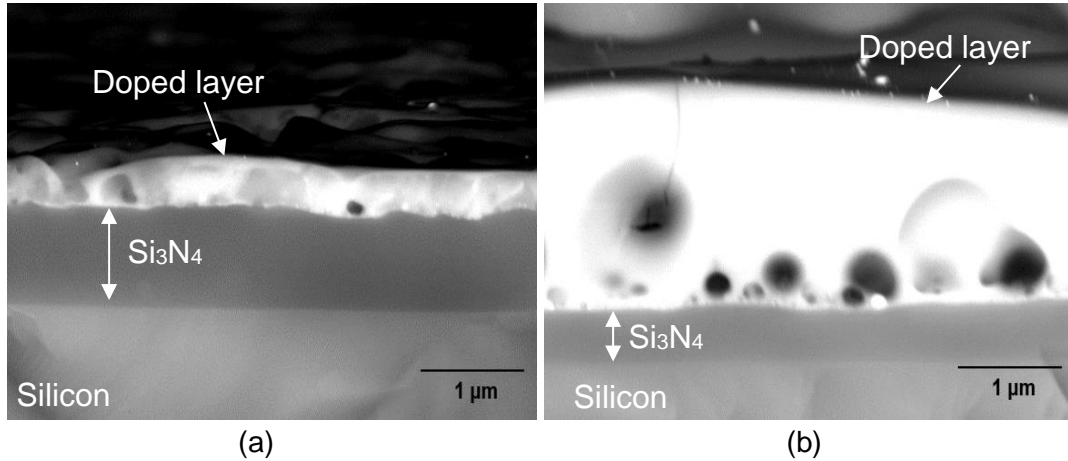
Figure 6.23: Cross-sectional BSE SEM micrograph of doped layer on Si_3N_4-on-silicon prepared using an fs-laser repetition rate of (a) 0.5 kHz (R1) and (b) 1.0 kHz (R2).

Table 6.14: Thickness of doped layer and Si_3N_4 underneath obtained from SEM.

Sample	Thickness (µm)	
	Upper layer	Si_3N_4 under upper layer
R0.5 (0.5 kHz)	0.5 ± 0.1	0.83 ± 0.04
R1 (1.0 kHz)	1.7 ± 0.3	0.57 ± 0.06

(a)   (b)
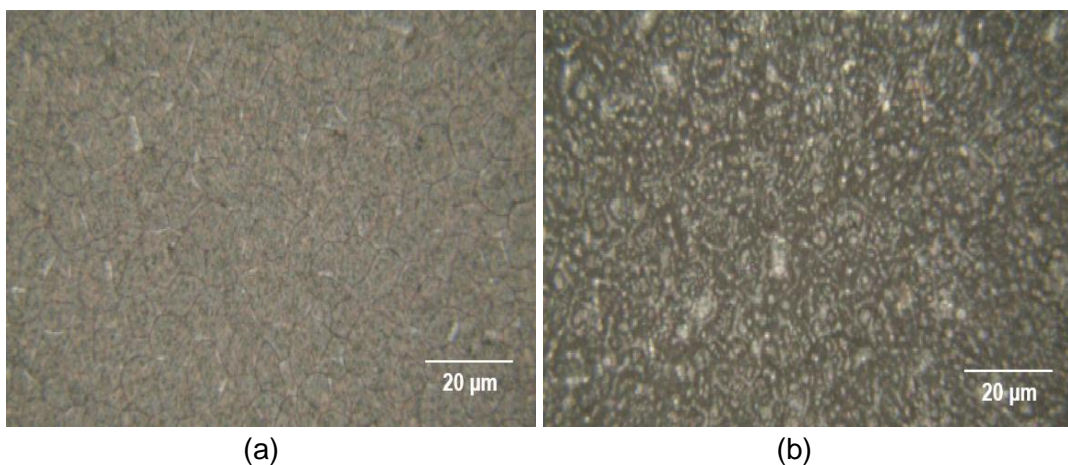
Figure 6.24: Surface topology obtained by optical microscope for samples (a) R1 and (b) R2.

Figure 6.25 displays the XRD patterns for samples fabricated at fs-laser repetition rates of 0.5 kHz and 1.0 kHz. Both patterns demonstrate the mixed amorphous-

crystalline phase with the crystalline peaks for Te being higher for sample R1. A higher XRD intensity also indicated that the crystallite particle content and size are greater [304]. As mentioned earlier, the low content of Er-TZN in sample R0.5 caused SiO_2 to likely be in the crystalline form as observed at angle 21-22°.
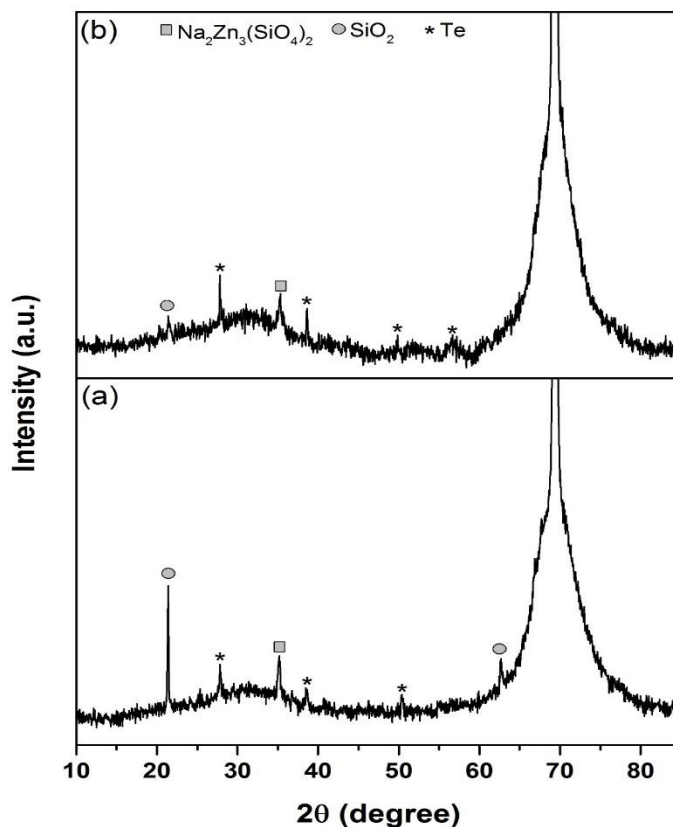
Figure 6.25: XRD patterns for samples (a) R0.5 and (b) R1.

Raman spectra for samples R0.5 and R1 are shown in Figure 6.26. From this figure, a low-intensity effect from erbium fluorescence at high wavenumbers clearly showed that the erbium concentration was lower in sample R0.5. This also caused the peak of the Si-O bond (900-1000 cm^{-1}) to appear.

Figure 6.27 shows PL spectra of samples R0.5 and R1. The PL intensity for sample R1 is higher, which means that the erbium concentration is much higher. As sample R1 had a higher erbium concentration, the PL lifetime for the sample was shorter (9.94 ms) compared to sample R0.5 which had a PL lifetime of 11.02 ms. To demonstrate this, the erbium concentration was determined using EDX-SEM, and the results are shown in Figure 6.28 (a)-(b). Clearly, the figure shows that the R0.5 sample had a lower content of erbium and other elements from the target. Higher

nitrogen concentration in R0.5 also indicated that the reaction between the plasma plume and Si_3N_4 was lower when a lower fs-laser repetition was used.
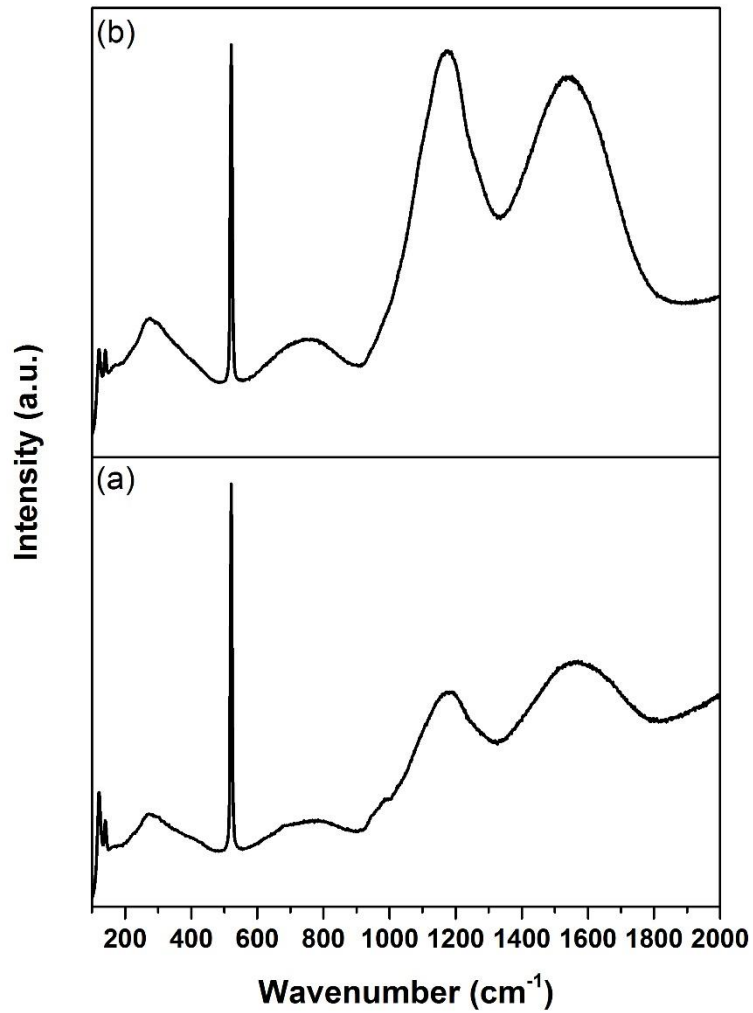
Figure 6.26: Raman spectra for samples (a) R0.5 (0.5 kHz) and (b) R1 (1.0 kHz).
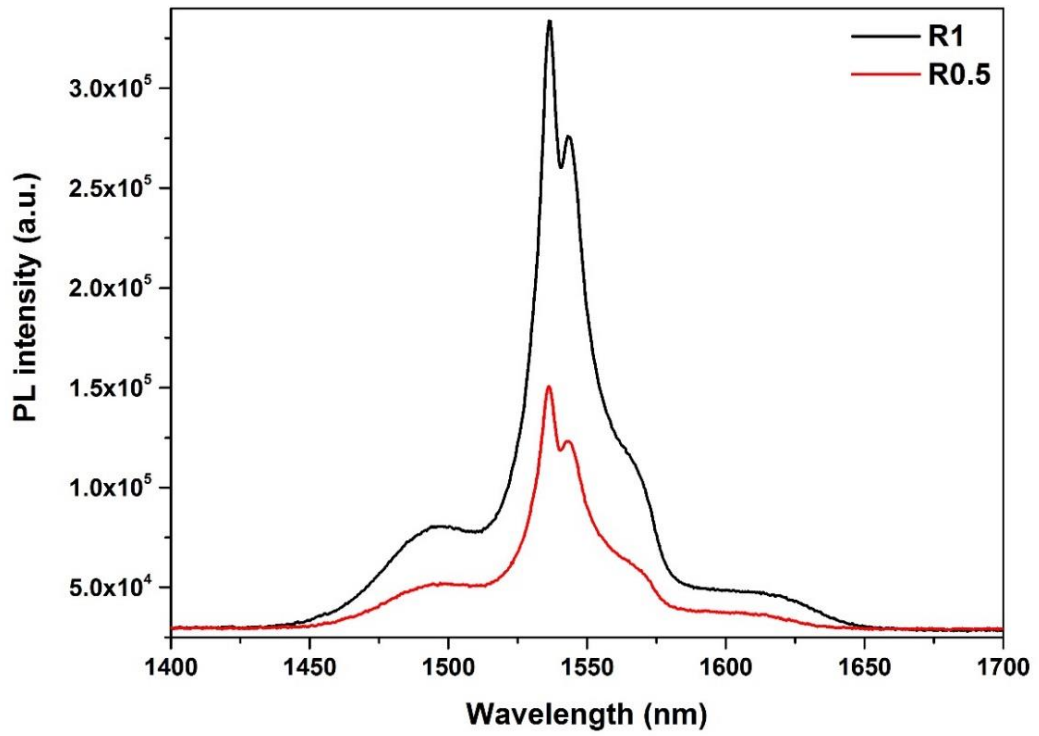
Figure 6.27: PL spectra for the sample prepared using different repetition rates.
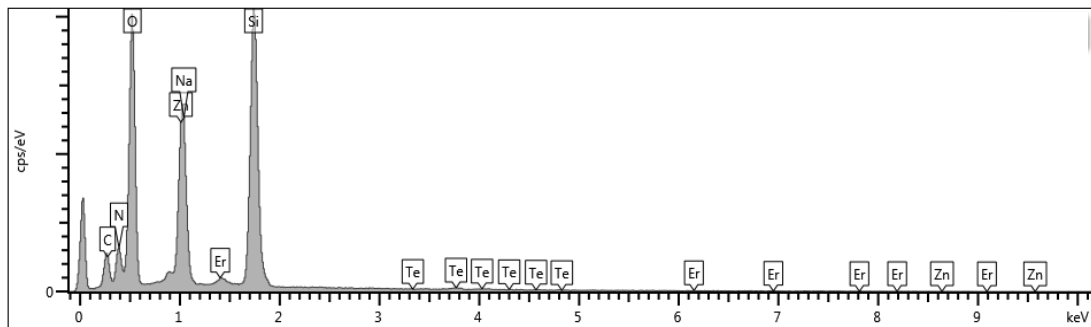
(a)
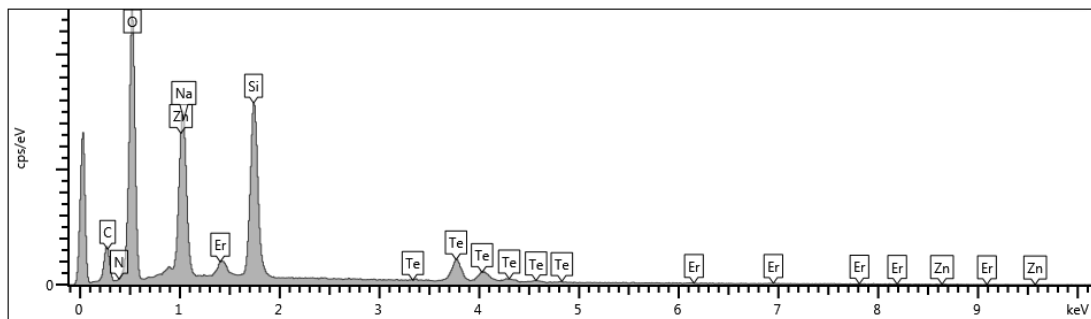
(b)

Figure 6.28: EDX-SEM pattern of the doped layer on Si_3N_4-on-silicon for samples (a) R0.5 (b) R1.

6.5 Other parameters

The other parameters investigated to dope Er-TZN into Si_3N_4-on-silicon were different oxygen pressures (30, 50, 70 and 90 mTorr) and ablation periods (1, 2, 3 and 4 hours). All of the parameters used were still unable to yield a uniformly doped layer. In terms of layer properties, they were similar to what has been reported so far in this chapter. To avoid repetition, they are, therefore, not discussed further. Some important results for these two sets of experiments are in Appendices 1 and 2. As expected, both parameters exhibit similar trends as observed when doping into SOS with regard to thickness. The thicknesses of the doped layers decrease with increasing oxygen gas pressure while the relationship between doped layer thickness and ablation period is linear.

6.6 Conclusion

The doping of Er-TZN into Si_3N_4-on-silicon substrate was not as successful as doping into silica-on-silicon. There were six different process parameters involved for this chapter in order to produce a homogeneous doped layer. For different substrate temperatures, a higher temperature resulted in a thicker layer. Nevertheless, at a temperature of 470 °C, deposition of Er-TZN onto the substrate has occurred. This shows that a temperature of 470 °C was not high enough to break the Si-N bond. On the other hand, the atmosphere in the chamber during the ablation process is important as different background gases used or in vacuum environment affect the thickness and roughness of the doped layer. The doped layer appeared to be the thickest for the sample fabricated under the oxygen environment and this is probably due to the fact that an oxygen atom is a light atom and this makes the plume have less collision effect. Besides that, O_2 is more reactive and chemical reactions between O_2 with the ablated particles may form single monoxide or multioxide molecules. These heavier monoxide or multioxide molecules experience less scattering to the flank side compared to lighter elements, and this also causes the doped layer to become thicker. The samples prepared under the argon environment exhibit the roughest surface that is suggested due to higher collision with a particle in the plasma plume. For other process parameters such as different fs-laser energies, different fs-laser repetition rates, different background gas pressures and different ablation periods, the relationship between these process parameters with the doped layer is almost similar to the EDTS except a homogeneous layer is still failed to be achieved. Interestingly, the interaction of Er-TZN with Si_3N_4 involved the released of nitrogen, and this made the resulting doped layer a silicate-based layer. However, none of the process parameters used were able to obtain a homogeneous doped layer. In the

doped layer, some parts appeared to be porous, or there was an accumulation of certain elements. It is strongly believed that higher temperatures might be required to allow the dissolution of Er-TZN into Si_3N_4 with homogeneous layer formation.

CHAPTER 7

**DESIGN, FABRICATION AND CHARACTERISATION OF AN EDTS
CHANNEL WAVEGUIDE**

The EDTS on SOS reported in Chapter 4 can be considered as a planar slab
waveguide. Light guided through a channel waveguide experiences less diffraction
compared to a slab waveguide. Channel waveguides are required for integrated
optical device fabrication and applications such as amplification, switching, and
modulation. Before fabricating a channel waveguide on SOS for amplifier
applications, a simple simulation using commercially available COMSOL software
was performed to determine the required thickness of the lower cladding. This is
important as the silica has a lower refractive index compared to silicon and any
waveguide closer to silicon will be leaky due to the difference in this refractive index.
After designing low loss waveguide structures, some early attempts on fabrication
were carried out and reported in this chapter.

7.1 Design of the channel waveguide

The design of the channel waveguide for this work was performed using commercially
available COMSOL software. The main purpose of this modelling was to identify the
suitable thickness of the lower cladding and hence the thickness of the starting silica
layer on the silicon before ULPD. Fabrication of two types of channel waveguide was
planned based on the current fs-PLD availability and capability. The two waveguide
structures, diffused and ridge waveguides, are as shown in the schematic diagram in
Figure 7.1 (a) and (b).
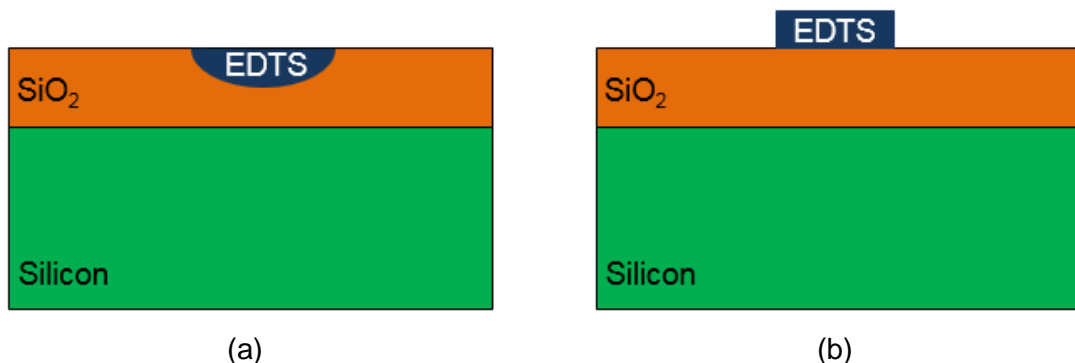
(a)   (b)

Figure 7.1: The two types of channel waveguide proposed for this work are
(a) diffused and (b) ridge channel waveguide.
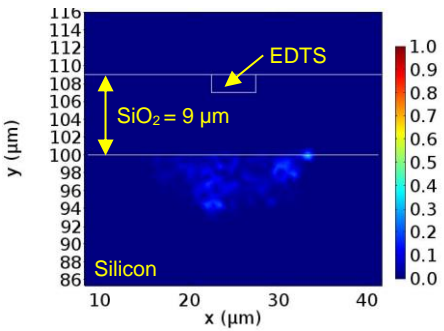
Table 7.1 shows the parameters used in the simulation for the diffused waveguide.
All parameters are maintained except for the thickness of the lower cladding layer,

which varies from 9 to 14 µm. Table 7.2 tabulates the simulation of a 2D cross-section of propagated mode radiation in an EDTS on SOS substrate with a varying thickness of SiO_2. SiO_2 should be thick enough in order to prevent leakage loss into the silicon substrate. From Table 7.2, it can be observed that the light stops leaking into the silicon when the thickness of SiO_2 is 12 µm. The leakage appears to decrease when the SiO_2 thickness increases. For a silicate-based channel waveguide, it is reported experimentally that the SiO_2 layer that acts as a lower cladding is in the range of 8–20 µm depending on the refractive index of the core [92,305–307].

Table 7.1: The parameters used in COMSOL software for different thicknesses of lower cladding layer for the diffused channel waveguide.

Description	Value
Core (EDTS) thickness	2 µm
Core (EDTS) width	5 µm
Core (EDTS) real refractive index	1.62
Core (EDTS) imaginary refractive index	$2x10^{-6}$
Lower cladding (SiO_2) thickness	9-14 µm
Lower cladding (SiO_2) refractive index	1.45
Substrate refractive index	3.45
Light wavelength	1535 nm

Table 7.2: Simulation of a 2D cross-section of propagated mode radiation in an EDTS on SOS substrate with a varying thickness of SiO_2 for the diffused channel waveguide.

SiO_2 thickness	2D cross-section of propagated mode radiation
9 µm	

10 μm	Power flow, z component (W/m²) (normalised)
11 μm	Power flow, z component (W/m²) (normalised)
12 μm	Power flow, z component (W/m²) (normalised)
13 μm	Power flow, z component (W/m²) (normalised)

14 µm	Power flow, z component (W/m²) ((normalised)
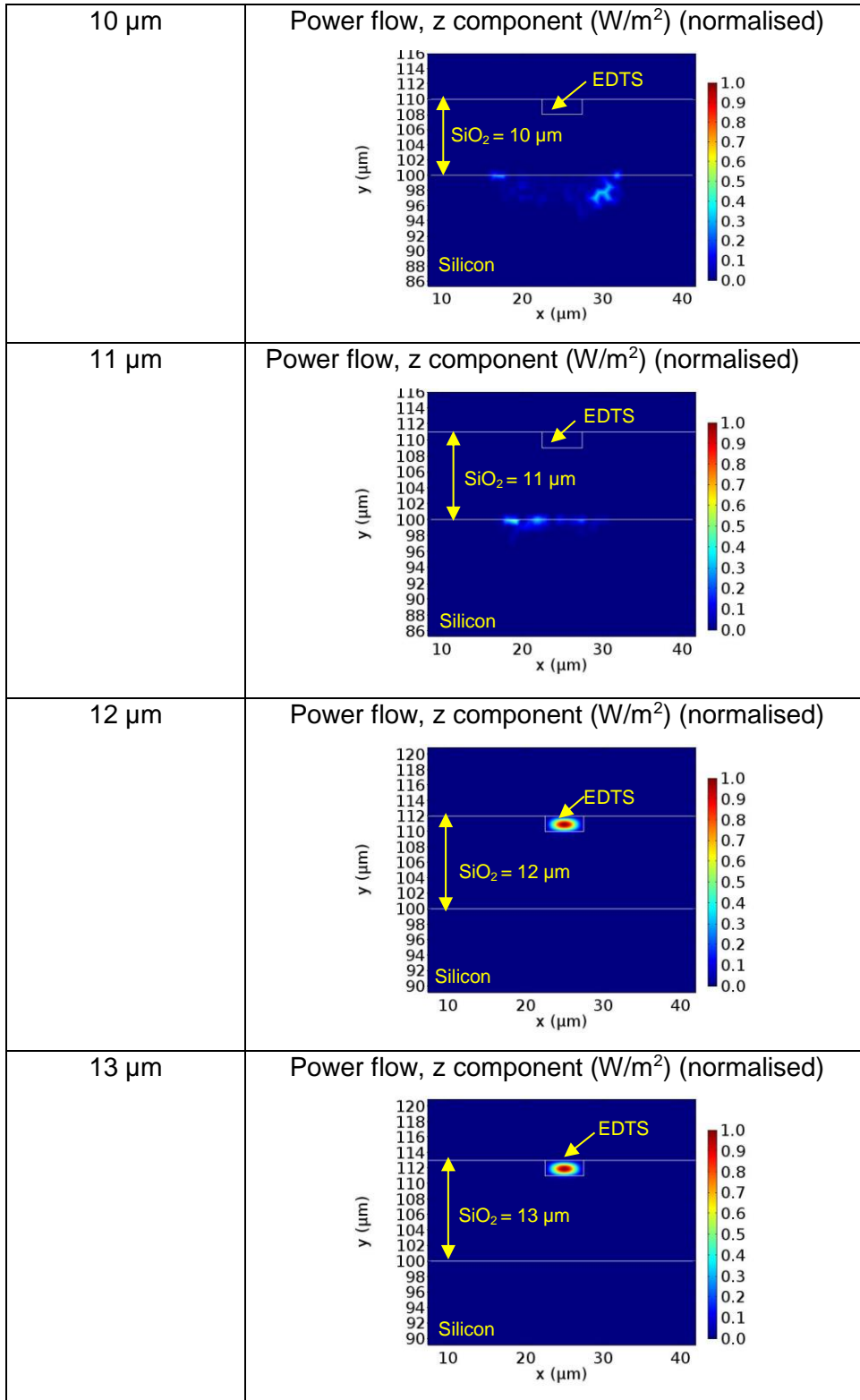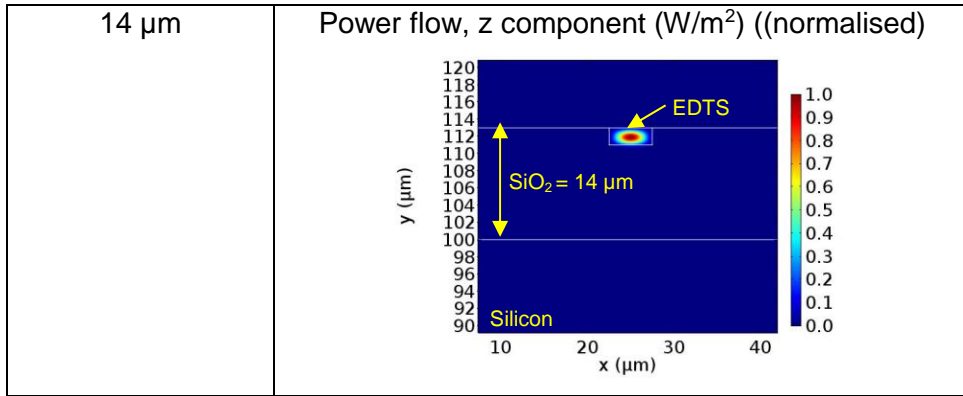
For a ridge waveguide, the same simulation parameters were applied as in Table 7.1, except that the lower cladding thickness varied from 5–10 µm. The output of this simulation is exhibited in Table 7.3. The results for varying SiO_2 thickness appear to be slightly different from those for the diffused waveguide. The minimum thickness of SiO_2 needed to avoid leakage loss is 8 µm. The lower SiO_2 thickness of the ridge waveguide was probably due to air instead of SiO_2 that acts as cladding on the other three sides. Air, which has a lower refractive index than SiO_2, assumedly assists in minimising the leakage loss.

Table 7.3: Simulation of a 2D cross-section of propagated mode radiation in an EDTS on SOS substrate with a varying thickness of SiO_2 for the ridge channel waveguide.

SiO_2 Thickness	2D cross-section of propagated mode radiation
5 µm	Power flow, z component (W/m²) (normalised)
6 µm	Power flow, z component (W/m²) (normalised)

7 µm	Power flow, z component (W/m²) (normalised)
8 µm	Power flow, z component (W/m²) (normalised)
9 µm	Power flow, z component (W/m²) (normalised)
10 µm	Power flow, z component (W/m²) (normalised)
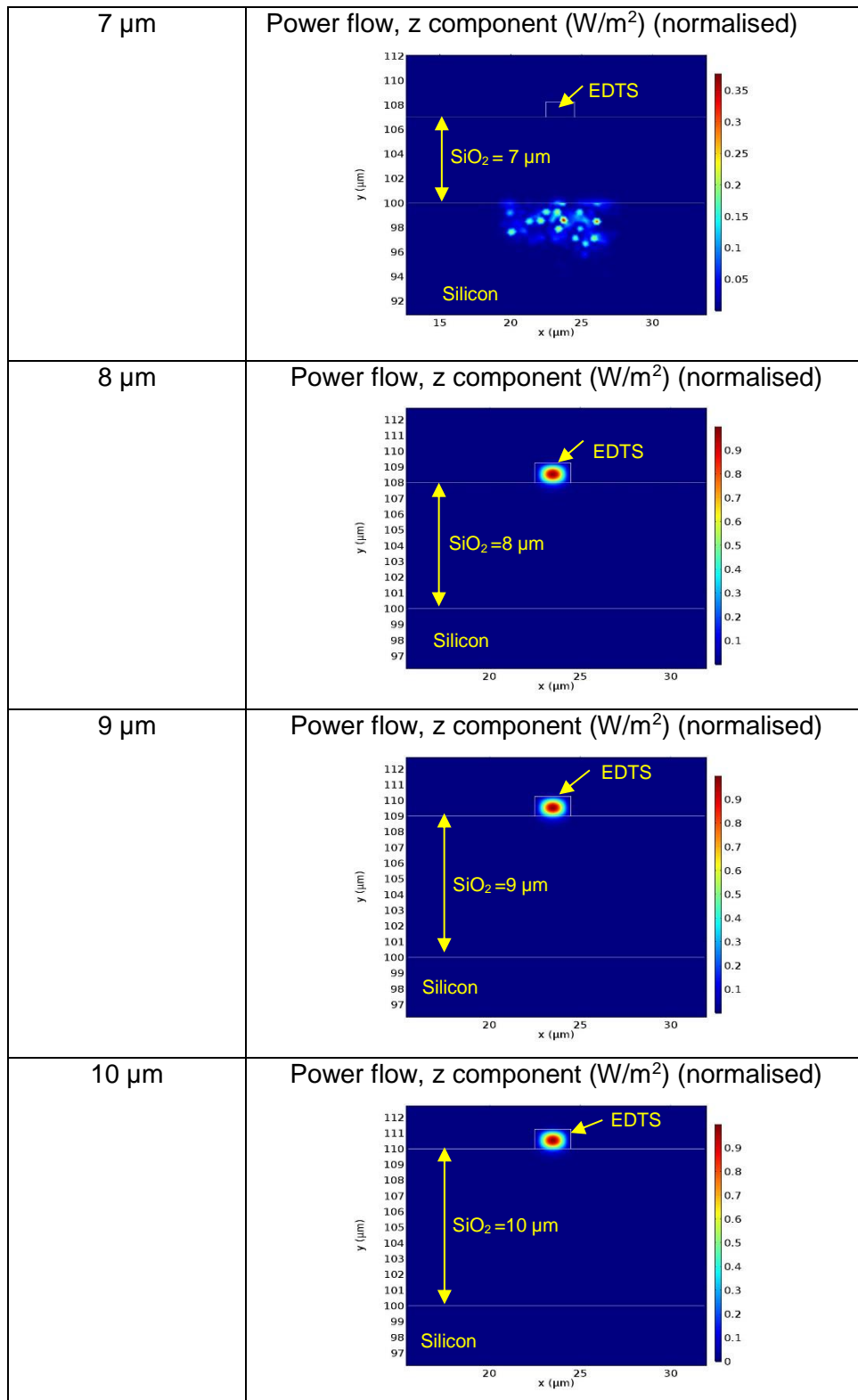
7.2 Fabrication and characterisation of the channel waveguide

The method selection is based on the type of channel waveguide that needs to be fabricated.

7.2.1 Diffused channel waveguide

The list of process parameters used to fabricate this sample for diffused waveguide purpose is displayed in Table 7.4.

Table 7.4: List of process parameters used to fabricate sample for diffused waveguide purpose.

Process parameters	Operating conditions
Substrate	Silica (t=2 µm)-on-silicon (SOS)
Target material	$79.5TeO_2$-$10ZnO$-$10Na_2O$-$0.5Er_2O_3$ (Er-TZN)
Fs-laser energy	50 µJ
Fs-laser repetition rate	1.0 kHz
Substrate temperature	570 °C
Ablation period	6 hours
Background gas pressure	70 mTorr O_2

A metal shadow mask, as illustrated in Figure 7.2 (a), is used when diffused channel waveguide fabrication is performed. The specific dimensions of the metal shadow mask are shown in Figure 7.2 (b). All three holes had a width of 15 µm. A core width of 15 µm was chosen due to the limitation of the laser micromachining process that was used to fabricate them. The metal shadow mask was placed under the substrate in close contact with it to allow Er-TZN to penetrate through the mask openings.

(a)   (b)
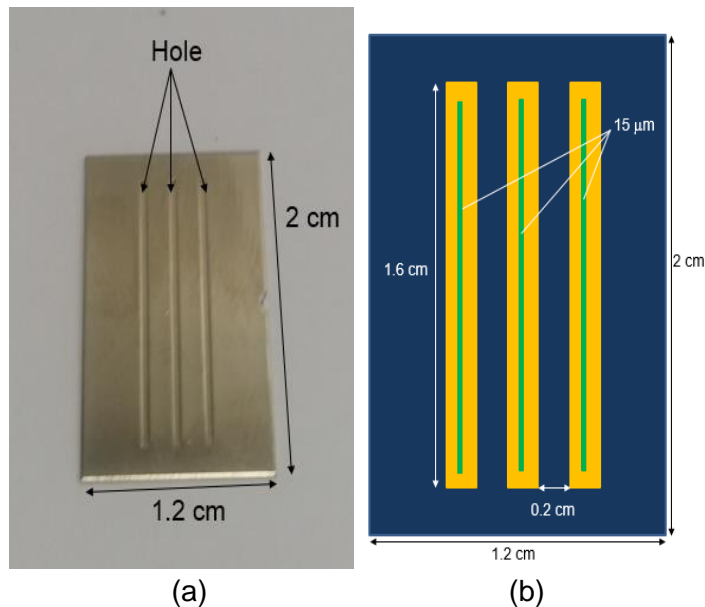
Figure 7.2 : (a) Metal mask used to fabricate diffused channel waveguide and (b) Dimensions of the metal mask.

The surface and cross-sectional images of samples obtained with this metal shadow mask are shown in Figures 7.3 and 7.4. From Figure 7.3, the channels obtained are clearly not as expected because the mask shifted position during the process. To avoid, this the whole substrate holder and mask alignment need to be redesigned which was beyond scope of this work. Nevertheless, formation of a waveguiding layer in the mask openings are observed (Figure 7.4) as expected but with lower and varying thicknesses depending on the mask position variations.

(a)   (b)

(c)
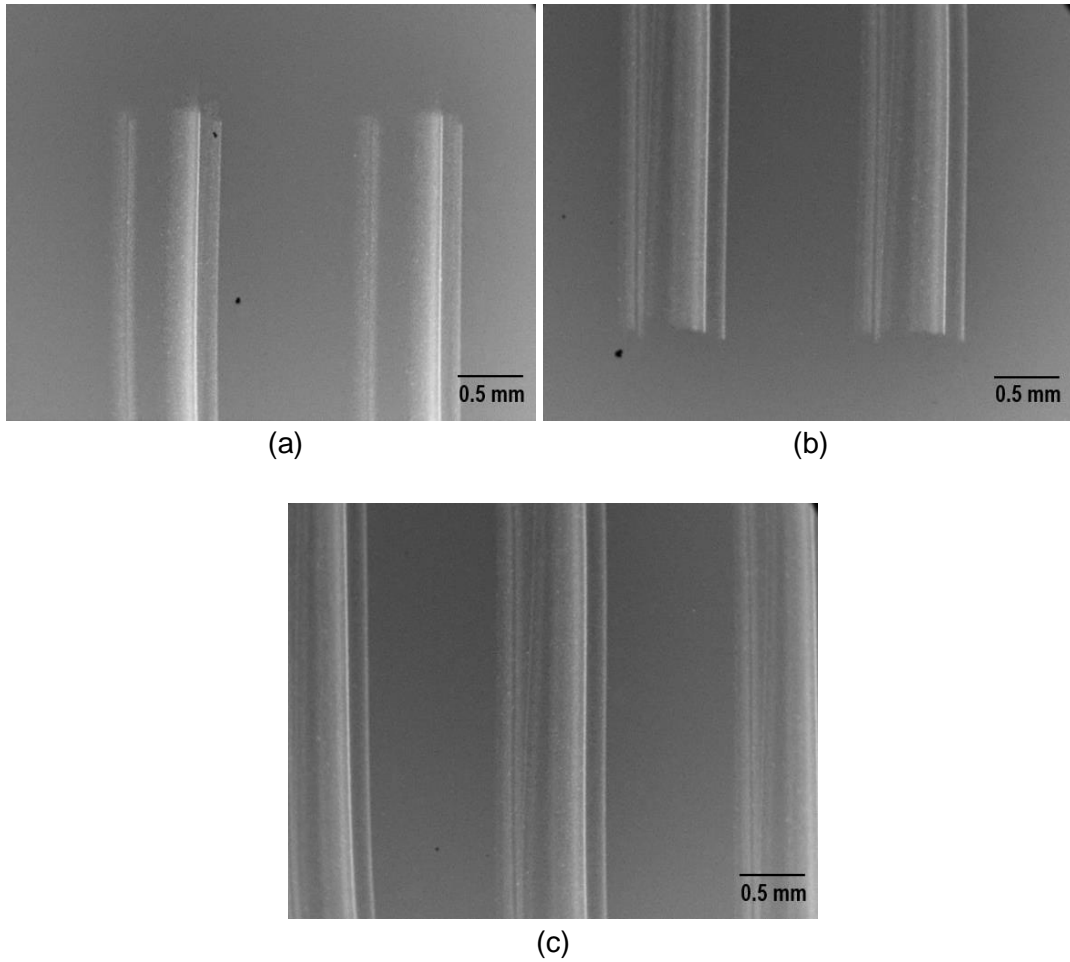
Figure 7.3: Backscattered SEM microscopic surface image of (a) top, (b) bottom and (c) middle of the fabricated diffused channel waveguide.

(a)   (b)
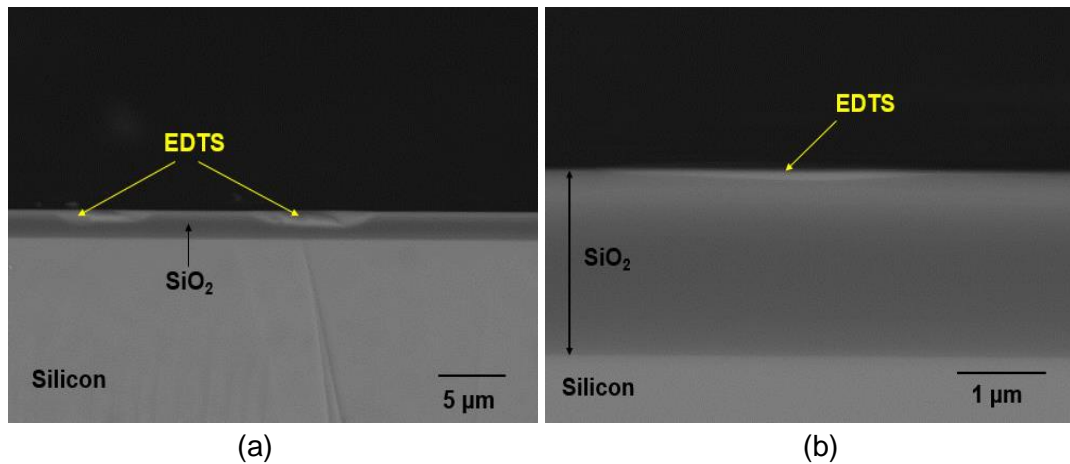
Figure 7.4: Backscattered SEM cross-section image of (a) low and (b) high magnification at a different region of the fabricated diffused channel waveguide. The obtained diffused waveguide has a varied thickness and width.

7.2.2 Ridge channel waveguide

Three samples labelled C1, C2 and C3 were fabricated using the same process parameters in Table 7.4 except the silica thickness on the silicon. A silica thickness of 10 µm on silicon was chosen mainly due to the simulation output from COMSOL software, which required at least 8 µm of lower cladding thickness in order to prevent light leakage to the silicon. The cross-section BSE SEM for sample C1 is shown in Figure 7.5. The EDTS layer and SiO_2 thicknesses are 1.034 µm and 9.474 µm, respectively. These three samples were sent to the University of Glasgow for fabricating ridge waveguides, which was carried out by Dr Nasser Babazadeh. In this trial, the channel form should have five different sizes which are 5 µm, 7 µm, 9 µm, 11 µm and 13 µm and the EDTS should be etched until it reaches the SiO_2 layer underneath (Figure 7.6).
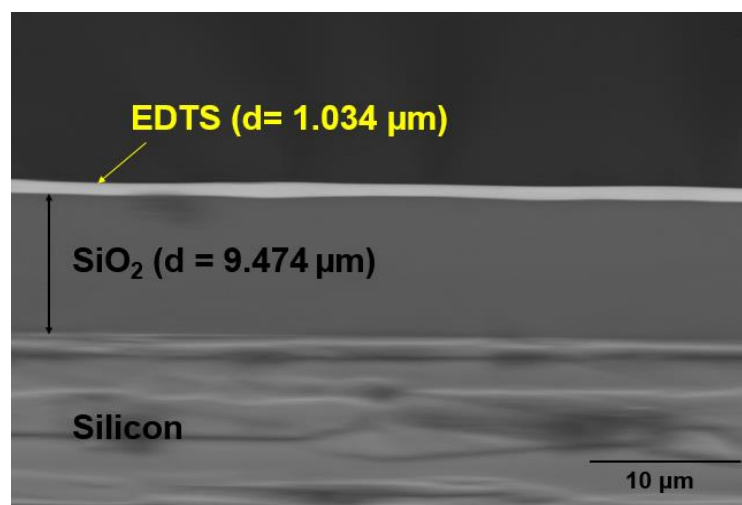
Figure 7.5: Cross-section BSE SEM of sample C1.
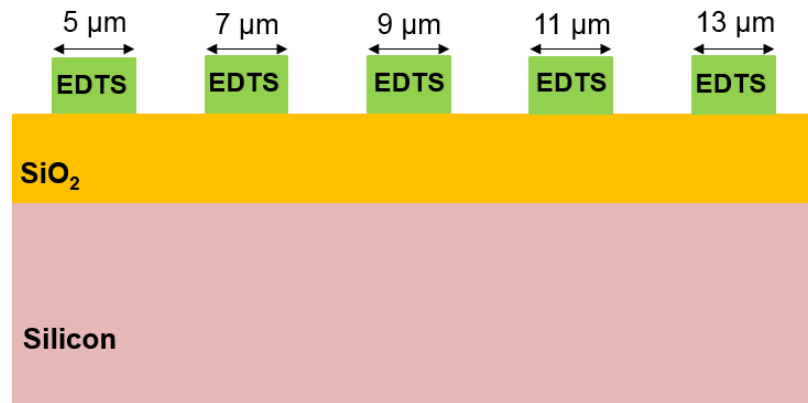
Figure 7.6: Illustration of the expected ridge waveguide that should be obtained.

The fabrication of the ridge waveguide involved photolithography, etching and a cleaning process as depicted in Figure 7.7. All three samples underwent the same process parameters. The process started with the deposition of a positive photoresist (PR) (AZ4562 photoresist) by a spin-coating method with a spin speed of 4,000 rpm. Then, the samples were baked at 90 °C for 50 minutes. After that, the process continued with multiple exposures (3 x 80 seconds) (Figure 7.7 (a)). The parts which are not covered by a mask become softened, and when the samples are immersed in the developer solution, the areas that are exposed to the light dissolve away (Figure 7.7 (b)). Later, the mask was manually moved and the processes of exposure (Figure 7.7 (c)) and development were repeated (Figure 7.7 (d)). The samples were baked again at 90 °C for 60 minutes. After that, the areas (EDTS) not covered by the photoresist were etched using a dry etching (Inductively coupled plasma reactive ion etching) process (Figure 7.7 (e)). The etchant gases used were C4F8 (15 sccm) and CF4 (5 sccm). The process continued with the removal of the photoresist and cleaning (Figure 7.7 (f)).

(a)

Develop

Photoresist

EDTS

SiO₂

Silicon

(b)

Photoresist

EDTS

SiO₂

Silicon

(c)

Develop

PR

EDTS

SiO₂

Silicon

(d)

Etch

PR

EDTS

SiO₂

Silicon
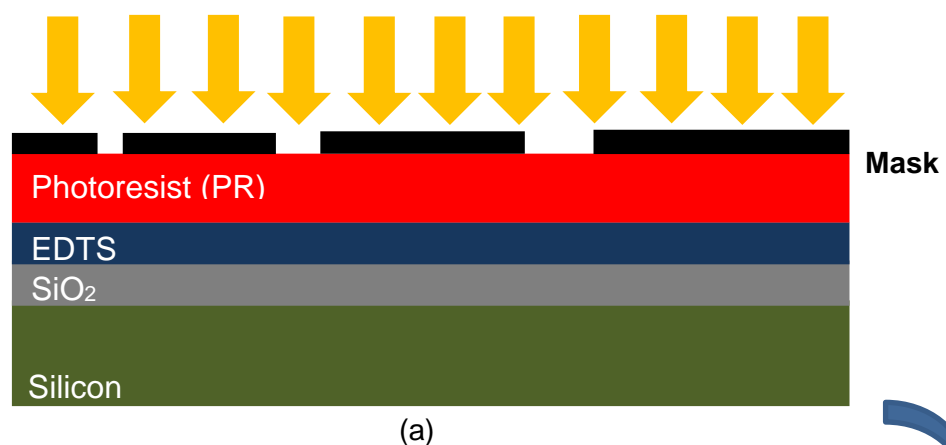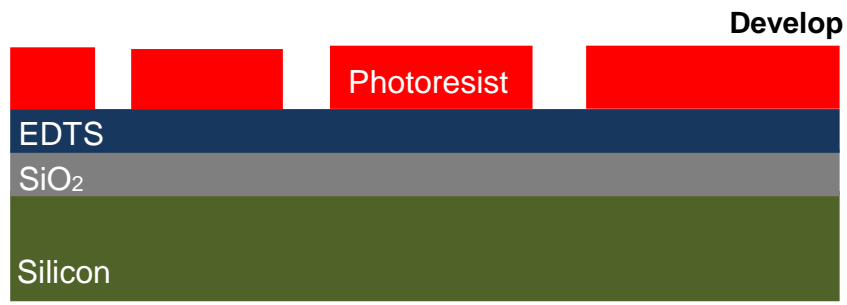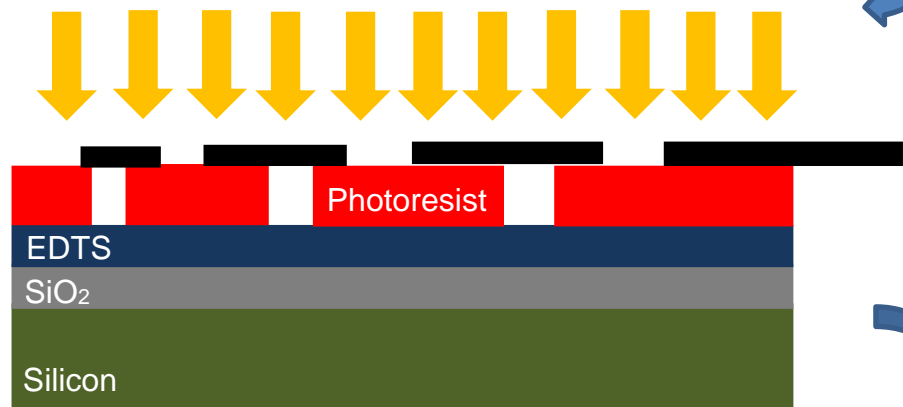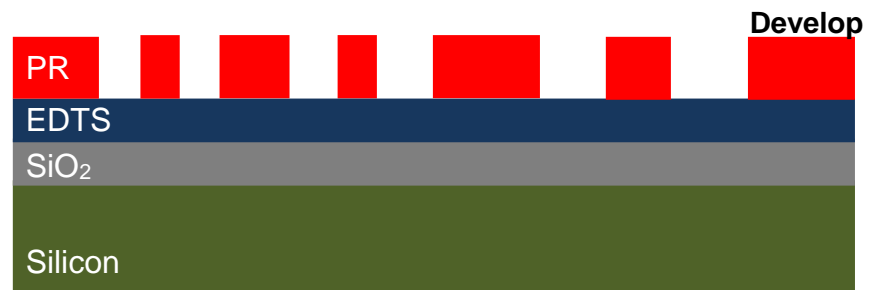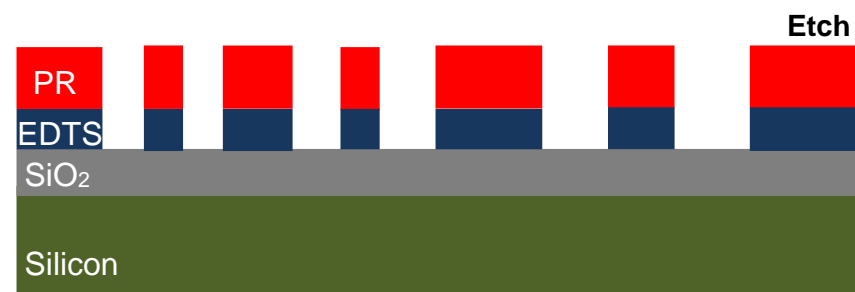
(e)

(f)

Figure 7.7: Processes involved in fabricating the ridge waveguide: (a) the first photolithography, (b) first development, (c) second photolithography, (d) second development, (e) etching (RIE) and (f) cleaning.

However, the output of the etching for a ridge waveguide formation was unsatisfactory. For sample C1, the channel width was very large compared to the expected width (Figure 7.8). The widths of the channels obtained for C1 were in the range of 24–30 µm with the distance between the channels at around 271 µm. The typical cross-section SEM to observe the trench could not be performed. This is probably because the trenches were too shallow to be detected by this method. Because of this, the sample was tilted to 30° to see the interface between the surface and the side of the sample (Figure 7.9). In these images, a trench at the side of the sample still cannot be seen, which also indicates perhaps that it is very shallow.

(a)

(b)
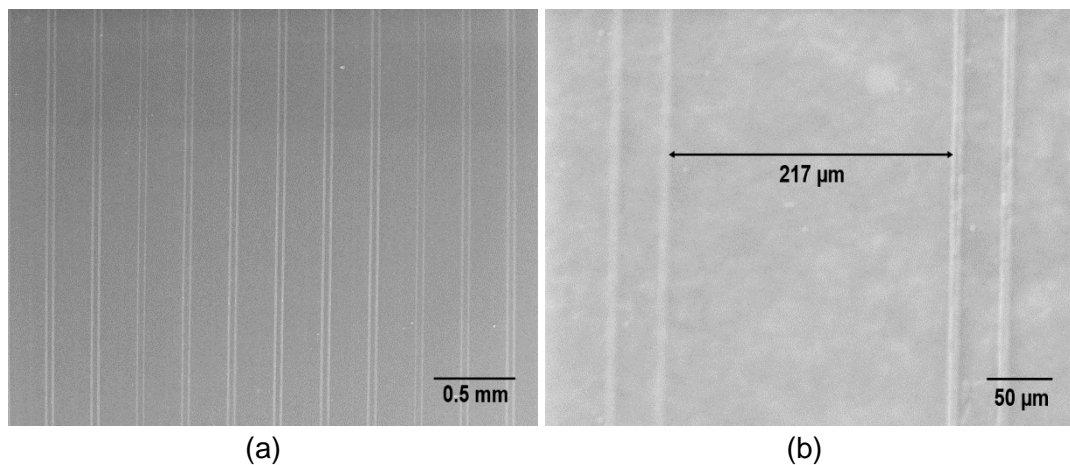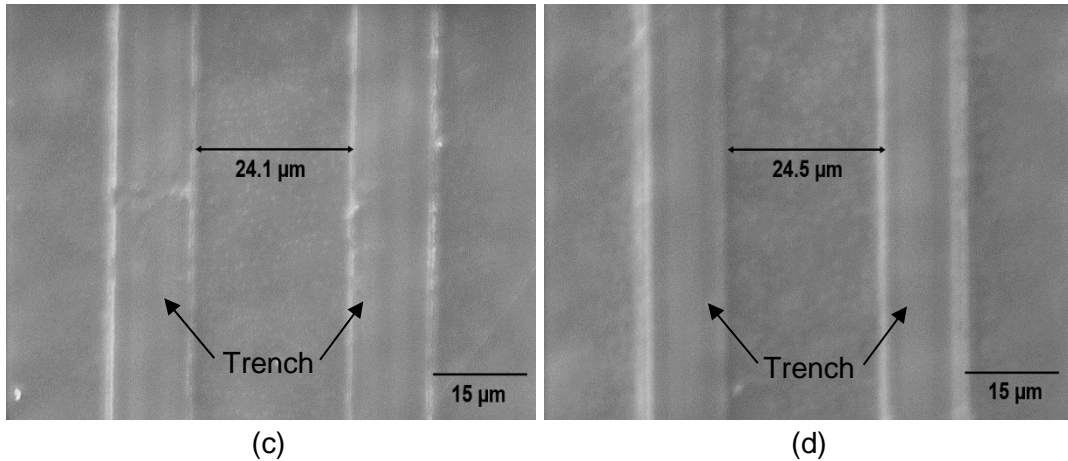
Figure 7.8: Surface SEM microscopic measurement for sample C1. (a) A few channels and trenches are formed, (b) the distance between the channels is around 217 µm and (c) and (d) shows that the channel widths are very large compared to the expected core width.
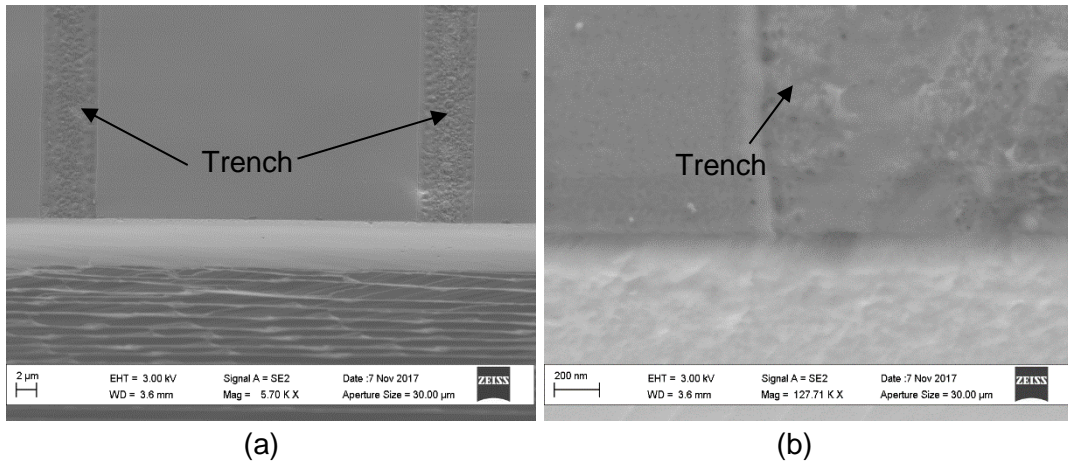
Figure 7.9: Sample C1 was tilted to 30⁰ in order to see the interface between the surface and the side of the sample. For (a), the image was taken under low magnification and shows that there is a channel in between the two trenches, and (b) high magnification for one trench. The scale is not accurate due to the position of the sample.

For sample C2, the surface SEM microscopic images are shown in Figure 7.10. From all the micrographs, it can be observed that some channels did not form and for those that did, the channel widths were very small (0.3-2 µm). The distance between the trenches was around 236-238 μm. For sample C3, the surface SEM microscope images are shown in Figure 7.11. This sample was much better than samples C1 and C2. The five cores with different widths were almost the same as the expected width core.
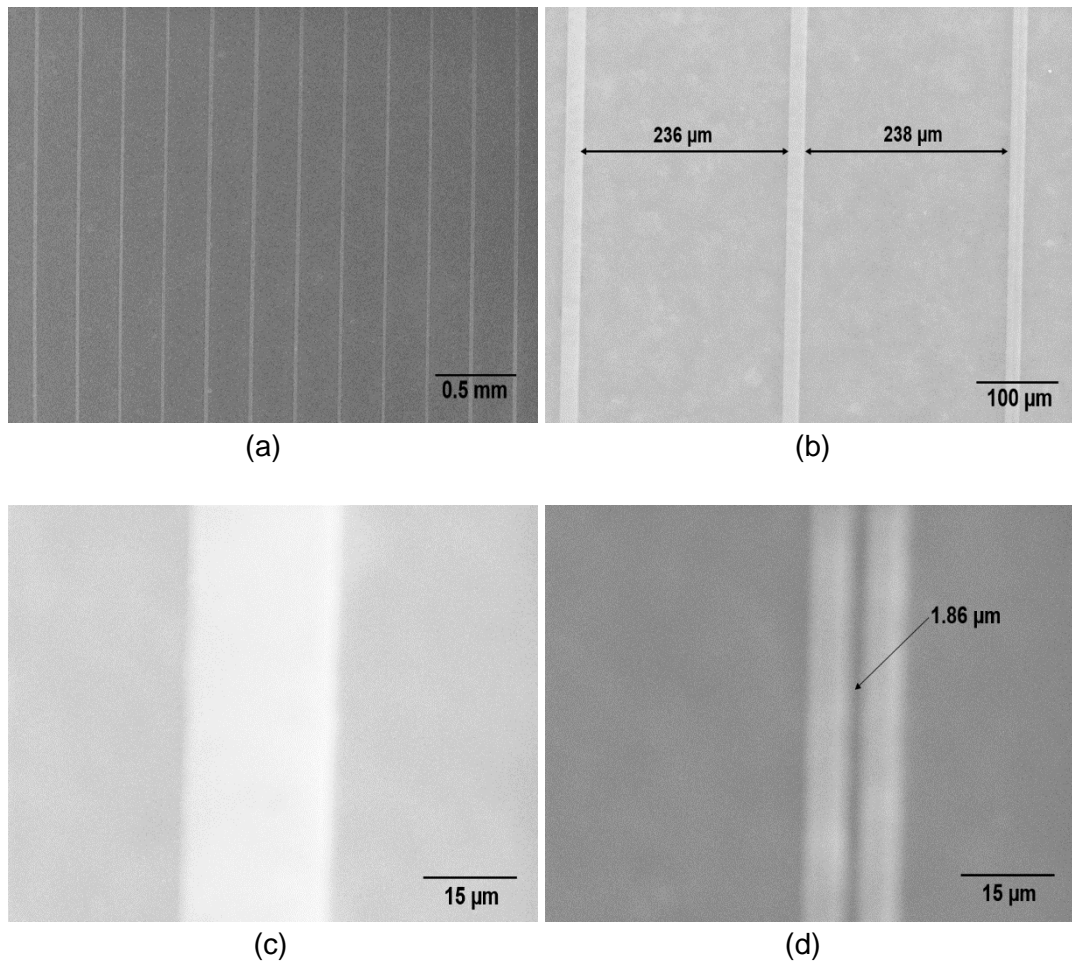
Figure 7.10: Surface SEM microscopic measurement for sample C2. (a) Some of the channels are formed between the two trenches, and some are not, (b) distance between the trench is around 236-238 μm, (c) channel is not formed and (d) channel width is very small.

(c)

(d)

(e)

(f)

(g)
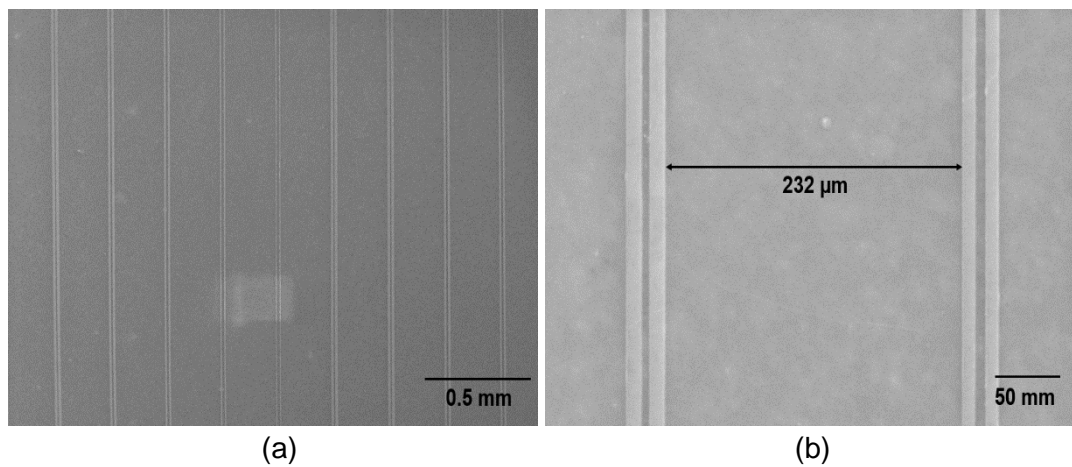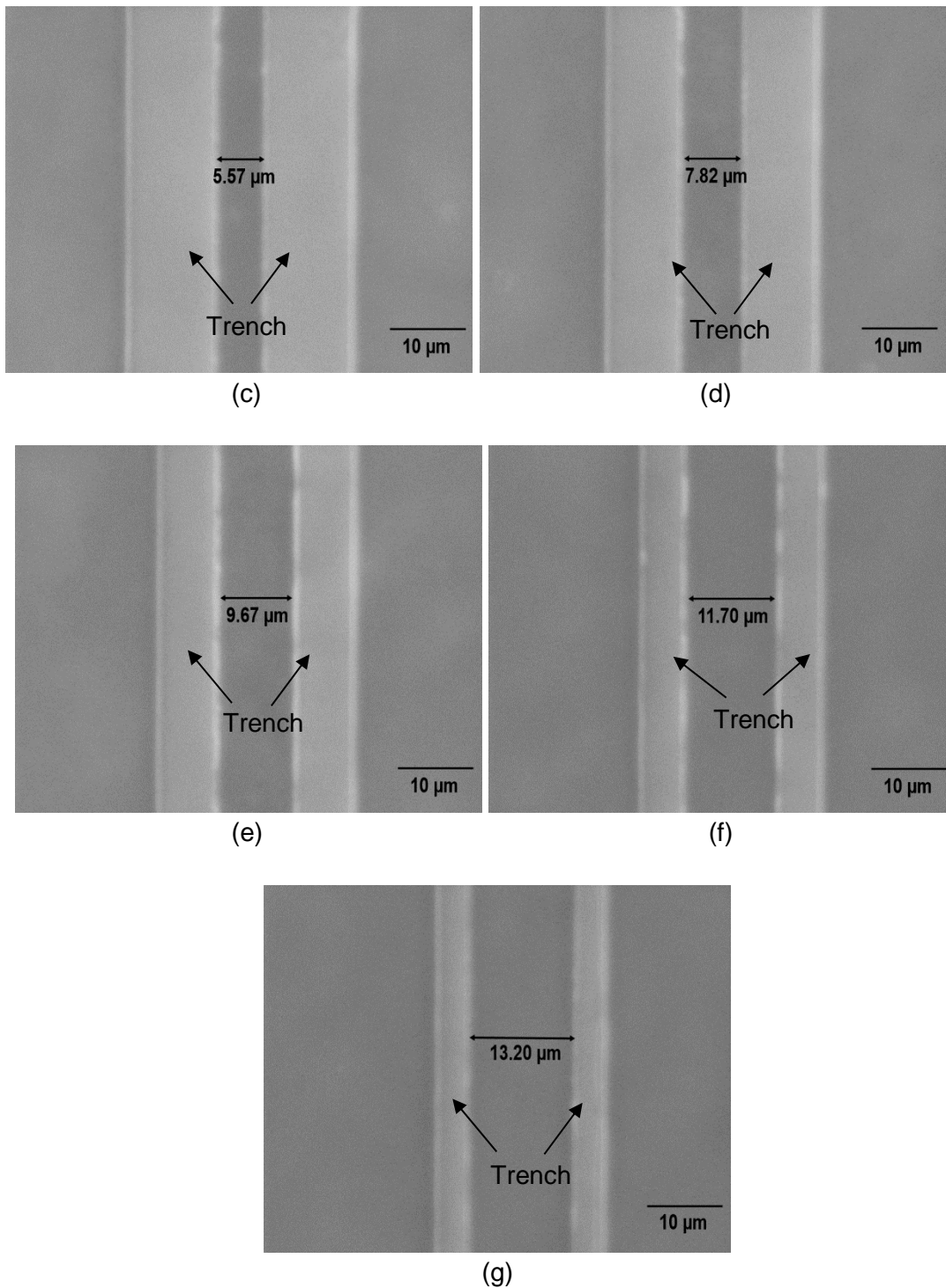
Figure 7.11: Surface SEM microscopic measurement for sample C3. (a) Channel form shows various core widths, (b) gap between the channel, and (c), (d), (e), (f), and (g), shows the core width close to the expected values (i.e. 5, 7, 9, 11 and 13 µm, respectively).

7.3 Conclusion

The fabrication of a channel waveguide failed to produce satisfactory results. For the diffused waveguide, the metal shadow mask used shifted during the ablation process, which led to the conclusion that this method requires further improvement to be

successful with a ULPD technique. On the other hand, for the ridge waveguide, three samples which underwent photolithography, etching and cleaning with the same process parameters were unable to give satisfactory output especially for samples C1 and C2. The trenches obtained were also very shallow. Obviously, further optimisation needs to be performed to obtain optical quality channel waveguides.

CHAPTER 8
CONCLUSION AND FUTURE WORK

8.1 Conclusion

This chapter consists of a conclusion on the major findings throughout this work. The main aim of this work was to explore a new EDWA host material on a silicon platform. The ULPD technique was employed to integrate the two immiscible materials (Er-TZN and silica) that resulted in a homogeneous layer of the mixture, referred to as the EDTS. The fs-laser generated plasma which modified the original silica structure, and produced a high index contrast layer suitable for on-chip PIC production. This modified layer has the potential to be used as an EDWA, due to the highest erbium concentration obtained being 4.92×10^{20} cm^{-3} with a PL lifetime of 9.39 ms. The EDTS is a silicate-based glass and is amorphous in nature. Based on the XPS analysis, bridging oxygen (BO) appeared to be more dominant compared to non-bridging oxygen (NBO) in the EDTS network. Besides that, according to the analysis of high-resolution Te $3d_{5/2}$ and Er $4p_{3/2}$ spectra, Te and Er metals were found to exist in the glass network, and it is suggested that they are located in the interstitial site. The XPS depth profiling performed proved that the EDTS consisted of a homogeneous mixture of elements from the target material and silica from the substrate.

Two types of channel waveguide (diffused and ridge) based on an EDTS were fabricated on SOS substrate. For the former waveguide, the attempt to fabricate it failed because the metal shadow mask used shifted during the ablation process, which led to the conclusion that this method requires further improvement to be successful with a ULPD technique. On the other hand, for the ridge waveguide, the exact core width and etch depth have yet to be obtained, and further optimisation needs to be performed.

The success of the Er-TZN doped into silica inspired this work to be extended onto a Si$_3$N$_4$-on-silicon substrate. Si$_3$N$_4$ is a very attractive material because it has a high refractive index (1.99) and similarly to SiO$_2$, it is a Si-based material. Nevertheless, the outcome differs from doping into SOS. The resulting layer failed to show homogenous mixing between Er-TZN and Si$_3$N$_4$. Some parts were seen to be porous or accumulate certain elements. However, surprisingly, the concentration of N in the doped layer was significantly low when compared to its concentration in Si$_3$N$_4$. It is suggested that nitrogen was released when the tellurite glass reacted with Si$_3$N$_4$. The failure to obtain a homogenous layer was probably due to the limitation of the current

instrument, which was not able to reach a high temperature, because Si_3N_4 has a high melting temperature, and also due to its rigid structure.

8.2 Suggestions for future works

The main aim of this thesis was to dope Er-TZN into SOS and Si_3N_4-on-silicon substrate and also to fabricate a channel waveguide. There is more room for improvement that can and needs to be performed for this work. There are also some suggestions in order to expand the scope of the study. Some of these suggestions are addressed below:

Explore different target compositions

As has been reported in many studies, Al_2O_3 [11,308] and P_2O_5 [14,15] can reduce the clustering effect of Er^{3+} ions. Perhaps the integration of this oxide material in the tellurite glass would enhance the solubility of Er^{3+} ions in silica. Furthermore, besides tellurite glass, other host materials which have a higher solubility of Er^{3+} ions such as Ta_2O_5 and Al_2O_3 are also interesting for use as a target material. Also, different rare-earth ions doped or co-doped would also be attractive because they can be applied to different applications or increase the optical gain.

Other characterisation techniques

Further characterisation techniques could be employed for a deeper understanding of the obtained doped layer and could be used to compare the existing data. Among the recommended tools are x-ray absorption spectroscopy (XAS), x-ray fluorescence spectroscopy (XRF), Rutherford backscattering spectrometry (RBS) and plasma profiling time of flight mass spectrometry (PP-TOFMS). XAS can be utilised to further understand the local structure in glass and amorphous materials. Even at the range of sub-nanometer, XAS is able to trace cluster formation and composition [309]. It is very useful to track Er and Te clusters if they are present in the doped layer. With respect to XRF, it is known as a fast, versatile and non-destructive technique to measure the thickness of single or multi-layers of a thin film. It can also be used for elemental or composition analysis and to estimate the density of a thin film [310]. Apart from that, RBS is competent to provide an elemental concentration for the surface of the film and also for depth profile measurement [234]. PP-TOFMS, on the other hand, can also be applied to investigate the relative element density in the doped layer [86].

Wider range of process parameters

The failure to obtain a homogeneous mixture of Er-TZN and Si_3N_4 means that a wider range of process parameters is required, particularly for higher temperatures. The new system of fs-PLD (currently not yet fully operational) offers a wider range of process parameters, which may help to mitigate this issue.

Optimisation of etching process and gain measurement for ridge waveguide

To fabricate a ridge waveguide, further optimisation of the etching process needs to be done. The setup of gain measurement for an EDWA also needs to be made in order to test whether the EDTS layer can guide and amplify the signal.

References:

[1]   J. Liu, M. Beals, J. Michel, and L.C. Kimerling, "Light up the future of silicon microprocessors", *ECS Transactions*, vol. 19, no. 1, pp. 17–28, 2009.

[2]   V.S. Bagad, *Optical fiber communications*.   Pune: Technical Publications Pune, 2009.

[3]   X.C. Tong, *Advanced materials for integrated optical waveguides*, vol. 46. Switzerland: Springer, 2014.

[4]   I.T. Monroy and E. Tangdiongga, *Crosstalk in WDM communication networks*. New York: Springer, 2012.

[5]   T.S. El-Bawab, *Optical switching.* New York: Springer, 2006.

[6]   A.J. Kenyon, "Recent developments in rare-earth doped materials for optoelectronics", *Progress in Quantum Electronics*, vol 26, pp. 225–284, 2002.

[7]   F. Auzel and P. Goldner, "Towards rare-earth clustering control in doped glasses", *Optical Materials*, vol. 16, pp. 93–103, 2001.

[8]   N.D. Afify, G. Dalba, and F. Rocca, "XRD and EXAFS studies on the structure of Er^{3+}-doped SiO_2–HfO_2 glass-ceramic waveguides: Er^{3+}-activated HfO_2 nanocrystals", *Journal of Physics D: Appllied Physics*, vol. 42, pp. 115416 (11), 2009.

[9]   K. Bourhis, J. Massera, L. Petit, H. Ihalainen, A. Fargues, T. Cardinal, L. Hupa, M. Hupa, M. Dussauze, V. Rodriguez, C. Boussard-Pledel, B. Bureau, C. Roiland, and M. Ferraris, "Influence of P_2O_5 and Al_2O_3 content on the structure of erbium-doped borosilicate glasses and on their physical, thermal, optical and luminescence properties", *Materials Research Bulletin*, vol. 63, pp. 41–50, 2015.

[10]   P.G. Kik and A. Polman, "Erbium-doped optical-waveguide amplifiers on silicon", *MRS Bulletin*, vol. 23, no. 4, pp. 48–54, 1998.

[11]   S. Il Seok, M.A. Lim, J.J. Ju, and M.H. Lee, "Optical properties of Er-doped Al_2O_3–SiO_2 films prepared by a modified sol–gel process", *Journal of American Ceramic Society*, vol. 88, no. 9, pp. 2380–2384, 2005.

[12]   L. Armelao, S. Gross, G. Obetti, and E. Tondello, "Er^{3+}-doped SiO_2-Al_2O_3 thin films prepared by the sol-gel route", *Surface and Coatings Technolology*, vol. 109, 218–222, 2005.

[13]   J. Lægsgaard, "Dissolution of rare-earth clusters in SiO_2 by Al codoping: A microscopic model", *Physical Review B*, vol. 65, pp. 174114, 2002.

[14]   K. Hattori, T. Kitagawa, M. Oguma, H. Okazaki, and Y. Ohmori, "Optical amplification in Er^{3+}-doped P_2O_5–SiO_2 planar waveguides", Journal of Appllied Physics, vol. 80, no. 9, pp. 5301–5308, 1996.

[15] A.N. Abramov, M.M. Bubnov, N.N. Vechkanov, a. N. Guryanov, K. V. Zotov, D.S. Lipatov, M.E. Likhachev, and M. V. Yashkov, "Fabrication of heavily Er_2O_3 doped aluminophosphosilicate glass fibers", *Inorganic Materials*, vol. 46, no. 4, pp. 439–444, 2010.

[16] N.D. Afify, G. Dalba, C. Armellini, M. Ferrari, F. Rocca, and A. Kuzmin, "Local structure around Er^{3+} in SiO_2-HfO_2 glassy waveguides using EXAFS", Physical Review B, vol. 76 , p. 24114, 2007.

[17] S. Sakida, T. Nanba, and Y. Miura, "Optical properties of Er^{3+}-doped tungsten tellurite glass waveguides by Ag^+-Na^+ ion-exchange", *Optical Materials*, vol. 30, no. 4, pp. 586–593, 2007.

[18] H. Lin, S. Jiang, J. Wu, F. Song, N. Peyghambarian, and E.Y.. Pun, "Er^{3+} doped Na_2O-Nb_2O_5-TeO_2 glasses for optical waveguide laser and amplifier", *Journal of Physics D: Appllied Physics*, vol. 36, pp. 812–817, 2003.

[19] V.A.G. Rivera, E.F. Chillcce, E. Rodriguez, C.L. Cesar, and L.C. Barbosa, "Planar waveguides by ion exchange in Er^{3+}-doped tellurite glass", *Journal of Non- Crystalline Solids*, vol. 352, pp. 363–367, 2006.

[20] F. Ren, Y. Mei, C. Gao, L. Zhu, and A. Lu, "Thermal stability and Judd-Ofelt analysis of optical properties of Er^{3+}-doped tellurite glasses", *Transactions of Nonferrous Metals Society of China*, vol. 22, pp. 2021–2026, 2012.

[21] E. Kashchieva and Y. Dimitriev, "Some peculiarities of the phase separation in the TeO_2-B_2O_3-SiO_2 system", *Journal of Materials Science Letters*, vol. 14, pp. 732–735, 1995.

[22] A.C.M. Rodrigues, R. Keding, and C. Russel, "Mixed former effect between TeO_2 and SiO_2 in the Li_2O TeO_2 SiO_2 system", *Journal of Non-Crystalline Solids*, vol. 273, pp. 53–58, 2000.

[23] D.H. Cho, Y.G. Choi, and K.H. Kim, Improvement of $^4I_{11/2} \rightarrow {}^4I_{13/2}$ transition rate and thermal stabilities in Er^{3+}-doped TeO_2-B_2O_3 (GeO_2)-ZnO-K_2O glasses, *ETRI Journal*, vol. 23, pp. 151–157, 2001.

[24] J. Chandrappan, M. Murray, T. Kakkar, P. Petrik, E. Agocs, Z. Zolnai, D.P. Steenson, A. Jha, and G. Jose, "Target dependent femtosecond laser plasma implantation dynamics in enabling silica for high density erbium doping", *Scientific Reports*, vol. 5, p. 14037, 2015.

[25] G. Jose, T.T. Fernandez, A. Jha, S. Saha, and D.P. Steenson, "Novel material", 0297958 A9, 2017.

[26] G. Jose, J. Chandrappan, S.A. Kamil, M. Murray, Z. Zolnai, P. Petrik, P. Steenson, and T. Krauss, "Ultrafast laser plasma assisted rare-earth doping for silicon photonics," in: *Conference on Lasers Electro-Optics (CLEO), 5-10*

June 2016, San Jose, California, IEEE.

[27]   M. Paniccia, V. Krutul, and S. Koehl, "Introducing Intel's advances in silicon photonics", *Intel Corporation White Paper*, 2004.

[28]   V.J. Sorger, R.F. Oulton, R.-M. Ma, and X. Zhang, "Toward integrated plasmonic circuits", *MRS Bulletin*, vol. 37, no. 8, pp. 728–738, 2012.

[29]   E. Iannone, *Labs on chip: principles, design and technology*, Boca Raton: CRC Press, 2015.

[30]   J. Liu, *Photonic devices*. Cambridge: Cambridge University Press, 2005.

[31]   A. Polman, "Erbium as a probe of everything?", *Physica B*, vol. 300, no. 1-4, pp. 78–90, 2001.

[32]   S.T. Krishnaswamy, "Erbium doped fiber lasers for long distance communication using network of fiber optics," *American Journal of Optics and Photonics*, vol. 3, no. 3, pp. 34–37, 2015.

[33]   A. Jha, B. Richards, G. Jose, T. Teddy-Fernandez, P. Joshi, X. Jiang, and J. Lousteau, "Rare-earth ion doped TeO_2 and GeO_2 glasses as laser materials," *Progress in Materials Science*, vol. 57, pp. 1426–1491, 2012.

[34]   M.D. Shinn, W. a. Sibley, M.G. Drexhage, and R.N. Brown, "Optical transitions of Er^+ ions in fluorozirconate glass", *Physical Review B*, vol. 27, no. 11, pp. 6635–6648, 1983.

[35]   D. Manzani, J.L. Ferrari, F.C. Polachini, Y. Messaddeq, and S.J.L. Ribeiro, "1.5 μm and visible up-conversion emissions in Er^{3+}/Yb^{3+} co-doped tellurite glasses and optical fibers for photonic applications", *Journal of Materials Chemistry*, vol. 22, p. 16540, 2012.

[36]   L. Thevenaz, ed., "Highly doped fiber technology", in *Advanced fiber optics: concepts and technology*, Lausanne: EPFL Press, 2011.

[37]   E. Sorokin, Solid-state materials for few-cycle pulse generation and amplification", in: *Few-cycle laser pulse generation and its applications*, Franz X. Kärtner, Ed. Heidelberg: Springer, 2004, pp. 3–72.

[38]   W. Lenth, A.J. Silversmith, and R.M. Macfarlane, "Green infrared-pumped erbium upconversion lasers", *Appllied Physics Letters*, vol. 51, no. 24, pp. 1977–1979, 1987.

[39]   P.C. Becker, N.A. Olsson, and J.R. Simpson, *Erbium-doped fiber amplifiers: fundamentals and technology*, San Diego: Academic Press, 1999.

[40]   C. Yeh, *Applied photonics*. San Diego: Academic Press, 1994.

[41]   W.J. Miniscalco, "Erbium-doped glasses for fiber amplifiers at 1500 nm", *Journal of Lightwave Technology*, vol. 9, no. 2, pp. 234–250, 1991.

[42]   T. Pan, E. Demaray, V. Milonopoulou, Q. Zhu, H. Zhang, Y. Chen, R. Pethe,

M. Narasimhan, L. Fan, B. Lee, Y. Xie, H. Xu, K. Wang, D. Li, J. Liu, D. Dawes, R. Mullapudi, K. Zhang, and J. Egermeier, "Gain flattened , high index contrast planar Er³⁺-doped waveguide amplifier with an integrated mode size converter", in: *Optical Fiber Communication Conference 2002 (OFC 2002),* 2002, pp. 3-5.

[43] K. Hattori, T. Kitagawa, M. Oguma, Y. Ohmori, and M. Horiguchi, "Erbium-doped silica-based waveguide amplifier integrated with a 980/1530 nm WDM coupler", *Electronics Letters*, vol. 30, no. 11, pp. 856–857, 1994.

[44] K. Shuto, K. Hattori, T. Kitagawa, Y. Ohmori, and M. Horiguchi, "Erbium-doped phosphosilicate glass waveguide amplifier fabricated by PECVD", *Electronics Letters*, vol. 29, no. 2, pp. 139–141, 1993.

[45] M. Nakazawa, Y. Kimura, "Electron-beam vapour-deposited erbium-doped glass waveguide laser at 1.53 um", *Electronics Letters*, vol. 28, no. 2, pp. 2054–2056, 1992.

[46] R.R. Thomson, H.T. Bookey, N. Psaila, S. Campbell, D.T. Reid, S. Shen, A. Jha, and A.K. Kar, "Internal gain from an erbium-doped oxyfluoride-silicate glass waveguide fabricated using femtosecond waveguide inscription", *IEEE Photonics Technology Letters*, vol. 18, no. 14, pp. 1515–1517, 2006.

[47] S. Shen and A. Jha, "The influence of F--ion doping on the fluorescence (^{4}I$_{13/2}$ → ^{4}I$_{15/2}$) line shape broadening in Er³⁺-doped oxyfluoride silicate glasses", *Optical Materials*, vol. 25, pp. 321–333, 2004.

[48] R.N. Ghosh, J. Shmulovich, C.F. Kane, M.R.X. de Barros, G. Nykolak, A.J. Bruce, and P.C. Becker, "8-mV threshold Er³⁺-doped planar waveguide amplifier", *IEEE Photonics Technology Letters*, vol. 8, no. 4, pp. 518–520, 1996.

[49] A. Bouajaj, R.R. Gonçalves, M. Ferrari, "Sol-gel-derived erbium-activated silica-titania and silica-hafnia planar waveguides for 1.5 µm application in C band of telecommunication", *Spectroscopy Letters*, vol. 47, pp. 381–386, 2014.

[50] R.K. Ramamoorthy, A.K. Bhatnagar, F. Rocca, M. Mattarelli, and M. Montagna, Structural and optical characterization of the local environment of Er³⁺ ions in PbO-ZnO tellurite glasses., *Journal of Physics: Condensed Matt*er, vol. 24, p. 505101, 2012.

[51] S. Zhao, X. Wang, D. Fang, S. Xu, L. Hu, "Spectroscopic properties and thermal stability of Er³⁺-doped tungsten–tellurite glass for waveguide amplifier application", Journal of Alloys and Compound, vol. 424, pp. 243–246, 2006.

[52] S. Marjanovic, J. Toulouse, H. Jain, C. Sandmann, V. Dierolf, a. R. Kortan, N. Kopylov, and R.G. Ahrens, "Characterization of new erbium-doped tellurite

glasses and fibers", *Journal of Non-Crystalline Solids*, vol. 322, no. 1-3, pp. 311–318, 2003.

[53]   K. Vu and S. Madden, Tellurium dioxide erbium doped planar rib waveguide amplifiers with net gain and 2.8 dB/cm internal gain, *Optics Express*, vol. 18, no. 18, pp. 19192–19200, 2010.

[54]   Y.C. Yan, A.J. Faber, H. de Waal, P.G. Kik, and A. Polman, "Erbium-doped phosphate glass waveguide on silicon with 4.1 dB/cm gain at 1.535 μm", *Appllied Physics Letters*, vol. 71, no. 20, pp. 2922–2924, 1997.

[55]   M. Ono, Y. Kondo, J. Kageyama, and N. Sugimoto, "Fabrication of ultra-compact Er-doped waveguide amplifier based on bismuthate glass", Journal of Ceramic Society Japan, vol. 116, no.10, pp. 1134–1138, 2008.

[56]   Y. Kondo, T. Nagashima, S. Takenobu, N. Sugimoto, and S. Ito, "Fabrication of Bi_2O_3-based Er-doped waveguide for integrated optical amplifiers, in: *Optical Fiber Communication Conference 2002 (OFC 2002),* 2002*,* pp. 11-12.

[57]   J.D.B. Bradley, L. Agazzi, D. Geskus, F. Ay, K. Wörhoff, and M. Pollnau, "Gain bandwidth of 80 nm and 2 dB/cm peak gain in $Al_2O_3{:}Er^{3+}$ optical amplifiers on silicon", *Journal of the Optical Society of America B*, vol. 27, no. 2, pp. 187–196, 2010.

[58]   J.D.B. Bradley, R. Stoffer, L. Agazzi, F. Ay, K. Wörhoff, and M. Pollnau, "Integrated $Al_2O_3{:}Er^{3+}$ ring lasers on silicon with wide wavelength selectivity", *Optics Letters*, vol. 35, no.1, pp. 73–75, 2009.

[59]   T.H. Hoekstra, P.V. Lambeck, H. Albers, and T.J.A. Popma, "Sputter-deposited erbium-doped Y_2O_3 active optical waveguides", *Electronics Letters*, vol. 29, no. 7, pp. 581–583, 1993.

[60]   A.Z. Subramanian, G.S. Murugan, M.N. Zervas, and J.S. Wilkinson, "High index contrast $Er{:}Ta_2O_5$ waveguide amplifier on oxidised silicon", Optics Communications, vol. 285, pp. 124–127, 2012.

[61]   A.Z. Subramanian, C.J. Oton, J.S. Wilkinson, and R. Greef, "Waveguiding and photoluminescence in Er^{3+}-doped Ta_2O_5 planar waveguides", Journal of Luminiscence, vol. 129 , pp. 812–816, 2009.

[62]   A.Q. Le Quang, R. Hierle, J. Zyss, I. Ledoux, G. Cusmai, R. Costa, A. Barberis, and S.M. Pietralunga, "Demonstration of net gain at 1540 nm in an erbium-doped polymer single mode rib waveguide", *Appllied Physics Letters*, vol. 89, pp. 1–3, 2006.

[63]   A.Q. Le Quang, V.G. Truong, A.M. Jurdyc, B. Jacquier, J. Zyss, and I. Ledoux, Gain properties of an Er^{3+} complex in a poly(methylmethacrylate) matrix for 1540 nm broadband optical amplification", *Journal of Appllied Physics*, vol.

101, pp. 1–7, 2007.

[64] R. Schermer, W. Berglund, C. Ford, R. Ramberg, and A. Gopinath, "Optical amplification at 1534 nm in erbium-doped zirconia waveguides", *IEEE Journal of Quantum Electronics*, vol. 39, no. 1, pp. 154–159, 2003.

[65] C.C. Baker, J. Heikenfeld, Z. Yu, and A.J. Steckl, "Optical amplification and electroluminescence at 1.54 um in Er-doped zinc silicate germanate on silicon", *Appllied Physics Letters*, vol. 84, pp. 1462–1464, 2004.

[66] K. Seneschal, F. Smektala, B. Bureau, M. Le Floch, S. Jiang, T. Luo, J. Lucas, and N. Peyghambarian, "Properties and structure of high erbium doped phosphate glass for short optical fibers amplifiers", *Materials Research Bulletin*, vol. 40 , pp.1433–1442, 2005.

[67] O.N. Egorova, S.L. Semjonov, V. V Velmiskin, Y.P. Yatsenko, S.E. Sverchkov, B.I. Galagan, B.I. Denker, and E.M. Dianov, "Phosphate-core silica-clad Er/Yb-doped optical fiber and cladding pumped laser, *Optics Express*, vol. 22, no.7, pp. 7625–7630, 2014.

[68] S. Berneschi, G.N. Conti, and G.C. Righini, "Planar waveguide amplifiers, *Glasses for Photonics Technologies*, vol. 10, no. 3, pp. 75–85, 2007.

[69] S.J. Pearce, M.D.B. Charlton, J. Hiltunen, J. Puustinen, J. Lappalainen, and J.S. Wilkinson, "Structural characteristics and optical properties of plasma assisted reactive magnetron sputtered dielectric thin films for planar waveguiding applications", *Surface and Coatings Technologies*, vol. 206, pp. 4930–4939, 2012.

[70] M.J.F. Digonnet, *Rare-Earth-Doped Fiber Lasers and Amplifiers*, Second Ed., New York: Marcel Dekker, 1993.

[71] D. Lowe, R.R.A. Syms, and W. Huang, "Layout optimization for erbium-doped waveguide amplifiers", *Journal of Lightwave Technology*, vol. 20, pp. 454–462, 2002.

[72] H.J. van Weerden, T.H. Hoekstra, P.V. Lambeck, and T. Popma, "Low-threshold amplification at 1.5 um in Er:Y", in: *8th European Conference on Integrated Optics and Techinal Exhibition*, 1997, pp. 169–172.

[73] L. Wang, H. Huang, D. Shen, J. Zhang, H. Chen, Y. Wang, X. Liu, and D. Tang, "Room temperature continuous-wave laser performance of LD pumped Er:Lu$_2$O$_3$ and Er:Y$_2$O$_3$ ceramic at 2.7 μm", *Optics Express*, vol. 22, no. 16, p. 19495, 2014.

[74] Y. Zhao, "Design of higher-k and more stable rare earth oxides as gate dielectrics for advanced CMOS devices", *Materials*, vol. 5, pp. 1413–1438, 2012.

[75] K. Miura, T. Osawa, Y. Yokota, T. Suzuki, and O. Hanaizumi, "Fabrication of Tm-doped Ta_2O_5 thin films using a co-sputtering method," *Results in Physics*, vol. 4, pp. 148–149, 2014.

[76] J.L. Ferrari, K.O. Lima, L.J.Q. Maia, and R.R. Gonçalves, "Sol-gel preparation of near-infrared broadband emitting Er^{3+}-doped SiO_2-Ta_2O_5 nanocomposite films", *Thin Solid Films*, vol. 519, pp. 1319–1324, 2010.

[77] A. Chen, "Introduction to polymer photonics for information technology", in: *Introduction to organic electronic and optoelectronic materials and devices*, S. S. Sun and L.R. Dalton, Eds. Boca Raton, Florida: CRC Press, 2017, pp. 225–250.

[78] L.H. Sloof, M.J.A. de Dood, A. van Blaaderen, and A. Polman, "Effects of heat treatment and concentration on the luminescence properties of erbium-doped silica sol- gel films", Journal of Non-Crystaline Solids, vol. 296, pp. 158–164, 2001.

[79] C.G. Choi, M.Y. Jeong, and T.G. Choy, "Characterization of borophosphosilicate glass soot fabricated by flame hydrolysis deposition for silica-on-silicon device applications", Journal of Materials Science, vol. 34, no. 24, pp. 6035–6040, pp. 1999.

[80] B. Svecova, J. Spirkova, S. Janakova, and M. Mika, "Ion-exchanged optical waveguides fabricated in novel Er^{3+} and Er^{3+}/Yb^{3+}-doped silicate glasses: relations between glass composition, basicity and waveguide properties", Materials Science and Engineering B, vol. 149, pp. 177–180, 2008.

[81] P. Nandi, G. Jose, C. Jayakrishnan, S. Debbarma, K. Chalapathi, K. Alti, A.K. Dharmadhikari, J.A. Dharmadhikari, and D. Mathur, "Femtosecond laser written channel waveguides in tellurite glass", *Optics Express*, vol. 14, pp. 12145–12150, 2006.

[82] H.B. Xiao, C.S. Zhang, X.L. Jia, Y.J. Wang, X.L. Cheng, G.B. Cao, F. Zhang, and S.C. Zou, "Photoluminescence and transmission spectrum characterization of Er-implanted Al_2O_3 films", *Applied Surface Science*, vol. 222, pp. 180–185, 2004.

[83] K. Liu, E.Y.B. Pun, T.C. Sum, A.A. Bettiol, J.A. Van Kan, and F. Watt, "Erbium-doped waveguide amplifiers fabricated using focused proton beam writing", *Applied Physics Letters*, vol. 84, pp. 684–686, 2004.

[84] A.P. Caricato, A. Fazzi, A. Jha, A. Kar, G. Leggieri, A. Luches, M. Martino, F. Romano, S. Shen, M. Taghizadeh, R. Thomson, and T. Tunno, Er-doped oxyfluoride silicate thin films prepared by pulsed laser deposition, *Optical Materials*, vol. 29, pp. 1166–1170, 2007.

[85]   S.A. Kamil, J. Chandrappan, M. Murray, P. Steenson, T.F. Krauss, and G. Jose, "Ultrafast laser plasma doping of Er^{3+} ions in silica-on-silicon for optical waveguiding applications", Optics Letters, vol. 41, no. 20. pp. 4684-4687, 2016.

[86]   J. Chandrappan, M. Murray, P. Petrik, E. Agocs, Z. Zolnai, A. Tempez, S. Legendre, D.P. Steenson, A. Jha, and G. Jose, "Doping silica beyond limits with laser plasma for active photonic materials", *Optical Materials Express*, vol. 5, pp. 2849–2861, 2015.

[87]   C.J. Brinker, and S.W. Scherer, *Sol-gel science: the physics and chemistry of sol-gel processing*, New York: Academic Press, 1990.

[88]   N. Asim, S. Ahmadi, M.A. Alghoul, F.Y. Hammadi, K. Saeedfar, and K. Sopian, "Research and development aspects on chemical preparation techniques of photoanodes for dye sensitized solar cells", *International Journal of Photoenergy*, vol. 2014, pp. 1–21 (518156), 2014.

[89]   H. Kose, A.O. Aydin and H. Akbulut, "Sol-gel synthesis of nanostructured SnO_2 thin film anodes for Li-Ion Batteries", *Acta Physica Polonica A*, vol. 121, no. 1, pp. 227–229, 2011.

[90]   S.M. Zanetti, E.R. Leite, E. Longo, and J.A. Varela, "Cracks developed during $SrTiO_3$ thin-film preparation from polymeric precursors", Applied Organometallic Chemistry, vol. 13, pp. 373–382, 1999.

[91]   G. Giordano, C. Durante, A. Gennaro, and M. Guglielmi, "Multilayer deposition of silica sol-gel films by electrochemical assisted techniques", *The Journal of Physical Chemistry C*, vol. 120, pp. 28820–28824, 2016.

[92]   W. Huang, R.R.A. Syms, E.M. Yeatman, M.M. Ahmad, T. V. Clapp, S.M. Ojha, "Fiber-device-fiber gain from a sol-gel erbium-doped waveguide amplifier", *IEEE Photonics Technology Letters*, vol. 14, no. 7, pp. 959–961, 2002.

[93]   A. Laliotis, E.M. Yeatman, M.M. Ahmad, and W. Huang, "Molecular homogeneity in erbium-doped sol-gel waveguide amplifiers", *IEEE Journal of Quantum Electronics*, vol. 40, pp. 805–814, 2004.

[94]   E.M. Yeatman, M.M. Ahmad, O. McCarthy, A. Vannucci, P. Gastaldo, D. Barbier, D. Mongardien, and C. Moronvalle, "Optical gain in Er-doped SiO_2–TiO_2 waveguides fabricated by the sol–gel technique", *Optics Communications*, vol. 164, pp. 19–25, 1999.

[95]   D.M. Mattox, *Handbook of physical vapor deposition (PVD) processing: film formation, adhesion, surface preparation and contamination control*. New Jersey: Noyes Publications, 1998.

[96]   G. Subramanyam, M.W. Cole, N.X. Sun, T.S. Kalkur, N.M. Sbrockey, G.S.

Tompa, X. Guo, C. Chen, S.P. Alpay, G.A. Rossetti, K. Dayal, L.Q. Chen, and D.G. Schlom, "Challenges and opportunities for multi-functional oxide thin films for voltage tunable radio frequency/microwave components", *Journal of Applied Physics*, vol. 114, no. 19. p. 191301, 2013.

[97] G.C. Righini, S. Pelli, M. Ferrari, C. Armellini, L. Zampedri, C. Tosello, S. Ronchin, R. Rolli, E. Moser, M. Montagna, A. Chiasera, and S.J.L. Ribeiro, Er-doped silica-based waveguides prepared by different techniques: RF-sputtering, sol-gel and ion-exchange", *Optical and Quantum Electronics*, vol. 34, no. 12, pp. 1151–1166, 2002.

[98] A. Chiasera, I. Vasilchenko, D. Dorosz, M. Cotti, S. Varas, E. Iacob, G. Speranza, A. Vaccari, S. Valligatla, L. Zur, A. Lukowiak, and G.C. Righini, "SiO_2-P_2O_5-HfO_2-Al_2O_3-Na_2O glasses activated by Er^{3+} ions: From bulk sample to planar waveguide fabricated by rf-sputtering", *Optical Materials*, vol. 63, pp. 153–157, 2017.

[99] A. Laliotis, and E.M. Yeatman, Consolidation and homogeneity of sol-gel Er-doped waveguide amplifiers, in *Conference on Lasers Electro-Optics/ International Quantum Electronics Conference and Photonics Applications System Technologies*, 2004, pp. 1–2.

[100] Y.P. Li and C.H. Henry, "Silicon optical bench waveguide technology", in *Optica fiber telecommunications IIIB*, I.P. Kaminow and T.L. Koch , Eds. San Diego: Academic Press, 1997, pp. 319–376.

[101] D. Shin, "Photoluminescence of erbium-doped silica-based waveguide film via flame hydrolysis deposition and aerosol doping," *Journal of Ceramic Processing Research*, vol. 7, no. 4, pp. 379–383, 2006.

[102] E. Talbot, R. Lardé, P. Pareige, L. Khomenkova, K. Hijazi, and F. Gourbilleau, "Nanoscale evidence of erbium clustering in Er-doped silicon-rich silica", *Nanoscale Research Letters*, vol. 8, no.1, pp. 1–8, 2013.

[103] M. Celikin, D. Barba, A. Ruediger, M. Chicoine, F. Schiettekatte, and F. Rosei, "Co-mediated nucleation of erbium/silicon nanoclusters in fused silica", Journal of Materials Research, vol. 30, no. 20, pp. 3003–3010, 2017.

[104] S. Abedrabbo, B. Lahlouh, S. Shet, A.T. Fiory, and N.M. Ravindra, "Spin-coated erbium-doped silica sol-gel films on silicon," in Supplemental Proceedings: Materials Processing and Interfaces, 1st ed., New Jersey: John Wiley & Sons, 2012.

[105] P. Tandon, and H. Boek, "Experimental and theoretical studies of flame hydrolysis deposition process for making glasses for optical planar devices", *Journal of Non-Crystalline Solids*, vol. 317, pp. 275-289, 2002.

[106] M. Behringer, "High-Power Diode Laser Technology and Characteristics", in *High power diode lasers: technology and applications*, F. Bachmann, P. Loosen, and R. Poprawe, Eds. New York, Springer, 2007.

[107] C. Regnier, J. Desmaison, P. Tristant, and D. Merle, "Remote Microwave Plasma Enhanced Chemical Vapour Deposition of SiO_2 Films : Oxygen Plasma Diagnostic", *Journal de Physique IV*, vol. 5, pp. 621–628, 1995.

[108] C.E. Chryssou and C.W. Pitt, "Er^{3+}-doped Al_2O_3 thin films by plasma-enhanced chemical vapor deposition (PECVD) exhibiting a 55-nm optical bandwidth, *IEEE Journal of Quantum Electronics*, vol. 34, no. 2, pp. 282–285, 1998.

[109] J. Schmidt, M. Kerr, A. Cuevas, "Surface passivation of silicon solar cells using plasma-enhanced chemical-vapour-deposited SiN films and thin thermal SiO_2/plasma SiN stacks", *Semiconductor Science and Technology*, vol. 16, pp. 164–170, 2001.

[110] S. Guldberg-Kjaer, J. Hubner, M. Kristensen, C. Laurent-Lund, M. Rysholt Poulsen, and M.W. Sckerl, "Planar waveguide laser in Er/Al-doped germanosilicate", *Electronics Letters*, vol. 35, pp. 302–303, 1999.

[111] C. Laurent-Lund, M.R. Poulsen, M. Beukema, and J.E. Pedersen, "PECVD grown multiple core planar waveguides with extremely low interface reflections and losses", *IEEE Photonics Technology Letters*, vol. 10, no. 10, pp. 1431–1433, 1998.

[112] M. Hoffmann, P. Kopka, and E. Voges, "Low-loss fiber-matched low-temperature PECVD waveguides with small-core dimensions for optical communication systems", *IEEE Photonics Technology Letters*, vol. 9, no. 9, pp. 1238–1240, 1997.

[113] M.W. Sckerl, S.A. Guldberg-Kjær, C. Laurent-Lund, and M.R. Poulsen, Loss-less planar waveguide 1:4 power splitter at 1550 nm, in *25th European Conference on Optical Communication*, 1999, pp. 48–49.

[114] G.C. Schwartz, K. V. Srikrishnan, Interlevel dielectrics, in: *Handbook of semiconductor interconnection technology*, 2nd ed., G.C. Schwartz and K. V. Srikrishnan, Eds., Massachusetts: Taylor & Francis, 2006.

[115] C. He and N. Zhao, "Production of carbon onions," in: *Handbook of nanophysics: clusters and fullerenes*, K.D. Sattler, Ed., CRC Press, 2010.

[116] D.K. Avasthi and G.K. Mehta, *Swift heavy ions for materials engineering and nanostructuring*, New Delhi: Springer, 2011.

[117] R. Hellborg, and H.J. Whitlow, "Direct current accelerators for industrial applications, in *Reviews of accelerator science and technology*, Volume 4, A.W. Chao and W. Chou, Eds. Singapore: World Scientific Publishing, 2011,

pp. 183–212.

[118] W. Gao, and N.M. Sammes, *An introduction to electronic and ionic materials*, Singapore: World Scientific Publishing, 2000.

[119] P.D. Townsend, P.J. Chandler, and L. Zhang, *Optical effects of ion implantation.* Cambridge: Cambridge University Press, 1994.

[120] C. Constantinescu, E. Morintale, N. Scarisoreanu, A. Moldovan, and M. Dinescu, "Nanometric-sized Fe/Pt thin films with perpendicular anisotropy developed by layer-by-layer pulsed lased deposition", *Physics AUC*, vol. 20, no.1, pp. 73–82, 2010.

[121] P. Balling and J. Schou, "Femtosecond-laser ablation dynamics of dielectrics: basics and applications for thin films," *Reports on Progress in Physics*, vol. 76, no. 3, p. 36502, 2013.

[122] M.N.R. Ashfold, F. Claeyssens, G.M. Fuge, and S.J. Henley, "Pulsed laser ablation and deposition of thin films", *Chemical Society Review*, vol. 33, pp. 23–31, 2004.

[123] E.G. Gamaly, A. V. Rode, B. Luther-Davies, and V.T. Tikhonchuk, "Ablation of solids by femtosecond lasers: Ablation mechanism and ablation thresholds for metals and dielectrics", *Physics of Plasmas*, vol. 9, no. 3, pp. 949–957, 2002.

[124] S. Han, Y. Kim, Y.-J. Kim, S. Kim, S. Park, J. Park, and S.-W. Kim, "Axiomatic system design for non-thermal dicing of quartz wafer," in *International Conference on Auditory Displays (ICAD)*, 2011, pp. 185–189.

[125] S.M. Eaton, G. Cerullo, and R. Osellame, "Fundamentals of femtosecond laser modification of bulk dielectrics," in *Femtosecond laser micromachining: photonic microfluid. devices transparent materials*, R. Osellame, G. Cerullo, and R. Ramponi, Eds. Femtosecond Laser Micromach. Photonic Microfluid. Devices Transparent Mater., Heidelberg, Springer-Verlag Berlin Heidelberg, 2012, pp. 3–26.

[126] D. Zhang and L. Guan, "Laser ablation", in *Comprensive materials processing*, S. Hashmi, Ed. Amsterdam: Elsevier, 2014.

[127] A. Kaiser, B. Rethfeld, M. Vicanek, and G. Simon, "Microscopic processes in dielectrics under irradiation by subpicosecond laser pulses", *Physical Review B*, vol. 61, no. 17, pp. 11437–11450, 2000. doi:10.

[128] S.S. Harilal, J.R. Freeman, P.K. Diwakar, and A. Hassanein, "Femtosecond laser ablation: fundamentals and applications", in *Laser-induced breakdown spectroscopy: theory and applications*, S. Musazzi and U. Perini, Eds. Heidelberg: Springer-Verlag Berlin Heidelberg, 2014, pp. 143–168.

[129] P. Lorazo, L.J. Lewis, and M. Meunier, "Short-pulse laser ablation of solids:

from phase explosion to fragmentation", *Physical Review Letters*, vol. 91, no. 22, p. 225502, 2003.

[130] E. Lafontaine and M. Comet, *Nanothermites*, New Jersey: Wiley, 2016.

[131] A. Barchanski, "Laser-generated functional nanoparticle bioconjugates: design for applications in biomedical science and reproductive biology," University of Duisburg-Essen, 2015.

[132] J. Schou, "Physical aspects of the pulsed laser deposition technique: The stoichiometric transfer of material from target to film, *Applied Surface Science*, vol. 255, pp. 5191–5198, 2009.

[133] M. Yamane, and Y. Asahara, *Glasses for Photonics*, Cambridge: Cambridge University Press, 2004.

[134] M. Epifani, E. Carlino, C. Blasi, C. Giannini, L. Tapfer, and L. Vasanelli, "Sol-gel processing of Au nanoparticles in bulk 10% B_2O_3-90% SiO_2 glass", *Chemistry of Materials*, vol. 13, no. 5, pp. 1533–1539, 2001.

[135] S.K.R.S. Sankaranarayanan, E. Kaxiras, and S. Ramanathan, "Electric field tuning of oxygen stoichiometry at oxide surfaces: molecular dynamics simulations studies of zirconia", *Energy and Environmental Science*, vol. 2, pp. 1196–1204, 2009.

[136] A. Khomchenko, *Waveguide spectroscopy of thin films*, 1st ed., vol. 33, Cambridge, Massachusetts: Academic Press, 2005.

[137] M. Haniff Ibrahim, N. Mohd Kassim, A. Bakar Mohammad, and M. K. Chin, "Prism coupling measurement of benzocyclobutene (BCB 4024 - 40) polymer for optical devices application, *Elektrika*, vol. 8, no. 2, pp. 13–16, 2006.

[138] T*hin film thickness/refractive index measurement system*, Metricon Corporation, 2003.

[139] R.T. Kersten, *Electromagnetic principles of optics*, New York: John Wiley & Sons, 1986.

[140] R.T. Kersten, "Numerical solution of the mode-equation of planar dielectric waveguides to determine their refractive index and thickness by means of a prism-film coupler", Optical Communication, vol. 9, no. 4, pp. 427–431, 1973.

[141] G.C. Righini and M. Ferrari, "Photoluminescence of rare-earth-doped glasses", *Rivista del Nuovo Cimento*, vol. 28, no.12, pp. 1–53, 2005.

[142] R. Sharma, D.P. Bisen, U. Shukla, and B.G. Sharma, "X-ray diffraction: a powerful method of characterizing nanomaterials," *Recent Research in Science and Technology*, vol. 4, no. 8, pp. 77–79, 2012.

[143] C. Gorecki, "Optical waveguides and silicon based micromachined architecture", in *MEMS and MOEMS technology and applications*, P. Rai-

Choudhury, Ed. Washington: SPIE Press, 2000.

[144] M.A. Moram and M.E. Vickers, "X-ray diffraction of III-nitrides", *Reports on Progress in Physics*, vol. 72, no. 3, p. 36502, 2009.

[145] V. Manoj, M. Karthika, V.S.R. Praveen Kumar, S. Boomadevi, K. Jeyadheepan, R.K. Karn, R.J.B. Balaguru, and S.K. Pandiyan, "Synthesis of ZnO Nanoparticles using Carboxymethyl cellulose Hydrogel", *Asian Journal of Applied Sciences*, vol. 7, no. 8, pp. 798–803, 2014.

[146] A.R. West, *Basic solid state chemistry*, 2nd ed. New York: John Wiley & Sons, 1999.

[147] S.P. Singh, R.P.S. Chakradhar, J.L. Rao, and B. Karmakar, "EPR, FTIR, optical absorption and photoluminescence studies of Fe_2O_3 and CeO_2 doped $ZnO-Bi_2O_3$ glasses", *Journal of Alloys and Compounds*, vol. 493, pp. 256–262, 2010.

[148] C.G. Pantano, "X-ray Photoelectron Spectroscopy of Glass", in *Experimental techniques of glass science*, C.J. Simmons and O.H. El-Bayoumi, Eds. Westerville: American Ceramic Society, 1993, pp. 129–160.

[149] E. Mazzotta, S. Rella, A. Turco, and C. Malitesta, "XPS in development of chemical sensors", *RSC Advances*, vol. 5, pp. 83164–83186, 2015.

[150] D. Sykes, "Surface Chemical Analysis", in *Springer handbook of electronic and photonic materials*, S. Kasap and P. Capper, Eds. New York: Springer, 2006.

[151] J. Meichsner, M. Schmidt, R. Schneider, and H. E. Wagner, *Nonthermal plasma chemistry and physics*, Boca Raton: CRC Press, 2013.

[152] U. Ilyas, R.S. Rawat, T.L. Tan, P. Lee, R. Chen, H.D. Sun, L. Fengji, and S. Zhang, "Oxygen rich p-type ZnO thin films using wet chemical route with enhanced carrier concentration by temperature-dependent tuning of acceptor defects", Journal of Applied Physics, vol. 110, no. 93522-7, pp. 1–7, 2011.

[153] N. Fairley, *CasaXPS Manual 2.3.15: Introduction to XPS and AES*, Casa Software Ltd, 2009.

[154] N. Winograd and S.W. Gaarenstroom, "X-ray photoelectron spectroscopy, in: *Physical methods in modern chemical analysis*, vol. 2, T. Kuwana, Ed. London: Academic Press, 1980, pp. 115–169.

[155] A. Sharma, H. Jain, A.C. Miller, "Surface modification of a silicate glass during XPS experiments", Surface and Interface Analysis, vol. 31, pp. 369–374, 2001.

[156] J. Serra and P. Gonz, FTIR and XPS studies of bioactive silica based glasses, *Journal of Non-Crystalline Solids*, vol. 332, pp. 20–27, 2003.

[157] B. Schreder and W. Kiefer, "Raman spectroscopy on II-VI-semiconductor nanostructures", in *Handbook of Raman Spectroscopy: from the research*

laboratory to the process line, I.R. Lewis and H.G.M. Edwards, Eds. New York: Marcel Dekker, 2001.

[158] P. Larkin, *Infrared and raman spectroscopy: principles and spectral interpretation*, Massachusetts: Elsevier, 2011.

[159] M.J. Baker, C.S. Hughes, and K.A. Hollywood, *Biophotonics: vibrational spectroscopic diagnostics*, Morgan & Claypool Publishers, 2016.

[160] D.W. Oxtoby, H.P. Gills, and L.J. Butler, *Principles of modern chemistry*, 8th ed. Massachusetts: Cengage Learning, 2016.

[161] M.A. Linne, S*pectroscopic measurement: an introduction to the fundamentals*. Cornwall: Academic Press, 2002.

[162] M.R. Kagan and R.L. McCreery, "Reduction of fluorescence interference in Raman spectroscopy via analyte adsorption on graphitic carbon", *Analytical Chemistry*, vol. 66, pp. 4159–4165, 1994.

[163] Y. Leng, *Materials characterization: Introduction to microscopic and spectroscopic methods*, 2nd ed. Weimheim: Wiley, 2013.

[164] K.D. Vernon-Parry, "Scanning electron microscopy: an introduction," *III-Vs Review*, vol. 13, no. 4, pp. 40–44, 2000.

[165] H. Jaksch and J.P. Martin, "High-resolution, low-voltage SEM for true surface imaging and analysis", *Fresenius' Journal of Analytical Chemistry*, vol. 353, pp. 378–382, 1995.

[166] D.H. Krinsley, K. Pye, S.J. Broggs, and N.K. Tovey, *Backscattered scanning electron microscopy and image analysis of sediments and sedimentary rocks*, Cambridge: Cambridge University Press, 1998.

[167] W. Zhou, R. Apkarian, Z.L. Wang, and D. Joy, "Fundamentals of scanning electron microscopy, in Scanning microscopy for nanotechnology-technique and applications, W. Zhou and Z.L. Wang, Eds. New York: Springer, 2007, pp. 1-40.

[168] B. Min, C. Dachen, and P. Fabian, "Resist charging and heating", in *Handbook photomask manufacturing technology*, S. Rizvi, Ed. Fluorida: CRC Press, 2005.

[169] J. Goldstein, D. Newbury, D. Joy, C. Lyman, P. Echlin, E. Lifshin, L. Sawyer, and J. Michael, *Scanning electron microscopy and X-ray microanalysis*, 3rd ed. New York: Kluwer Academic/Plenum Publishers, 2003.

[170] C. Soong, P. Woo, and D. Hoyle, "Contamination Cleaning of TEM/SEM Samples with the ZONE Cleaner", *Microscopy Today*, pp. 6–9, 2012.

[171] A. Hernandez, J.I. Calvo, P. Pradanos, and L. Palacio, "A multidisciplinary approach towards pore size distributions of microporous and mesoporous

surfaces, in *Surface chemistry and electrochemistry of membranes*, T.S. Sorensen, Ed. New York: Marcel Dekker, 1999.

[172] D.B. Williams and C.B. Carter, *Transmission electron microscopy: a textbook for materials science*, 2nd ed. New York: Springer, 2009.

[173] W. Walkosz, "Atomic Scale Characterization and First-Principles Studies of Si_3N_4 Interfaces", University of Illinois-Chicago, 2011.

[174] R.F. Egerton, P. Li, and M. Malac, "Radiation damage in the TEM and SEM", *Micron*, vol. 35, pp. 399–409, 2004.

[175] D. Schaumlöffel, R. Hutchinson, J. Malherbe, E.G. Philippe Le Coustumer, and M. P. Isaure, "Novel Methods for bioimaging including LA-ICP-MS, nanoSIMS, TEM/X-EDS, and SXRF 83, in *Metallomics: analytical techniques and speciation methods*, B. Michalke, Ed. Weinheim: Wiley-VCH Verlag GmbH & Co, 2016, p. 95.

[176] J. Ayache, L. Beaunier, J. Boumendil, G. Ehret, and D. Laub, Sample preparation handbook for transmission electron microscopy methodology. New York: Springer-Verlag, 2010.

[177] Y. Leng, *Material characterization: Introduction to microscopic and spectroscopic methods*, Singapore: Wiley, 2008.

[178] S. Zhang, *Electric-Field Control of Magnetization and Electronic Transport in Ferromagnetic/ Ferroelectric Heterostructures*, Heidelberg: Springer, 2014.

[179] H.W. Shim, "Fabrication and Properties of Silicon Carbide Nanowires", Rensselear Polytechnic Institute, 2008.

[180] J. Xu, X. Liu, S. Wang, Y. Ma, C. Pei, X. Duan, "A novel 3D network nanostructure constructed by single-crystal nanosheets of B4C", *Ceramics International*, vol. 43, pp. 16787–16791, 2017.

[181] G. Kaur, A. Mitra and K.L. Yadav, "Pulsed laser deposited Al-doped ZnO thin films for optical applications", *Progress in Natural Science: Materials International*, vol. 25, pp. 12–21, 2015.

[182] J.M. Titchmarsh, "Transmission electron microscopy, in: *Handbook of surface and interface analysis methods for problem-solving*, J.C. Rivière and S. Myhra, Eds. Boca Raton: CRC Press, 2009.

[183] P.D. Nellist, "The principles of STEM imaging", in *Scanning transmission electron microscopy: imaging and analysis*, S.J. Pennycook and P.D. Nellist, Eds. New York: Springer, 2011.

[184] R. Brydson, A. Brown, L.G. Benning, and K. Livi, "Analytical transmission electron microscopy", *Reviews in Mineralogy and Geochemistry*, vol. 78, pp. 219–269, 2014.

[185] H. Cha, M. Kang, K. Shin, and C. Yang, "Transmission electron microscopy specimen preparation of delicate materials using tripod polisher", *Applied Microscopy*, vol. 46, no. 2, pp. 110–115, 2016.

[186] S. Kasap and P. Capper, *Springer handbook of electronic and photonic materials*, New York: Springer, 2006.

[187] V. Raffa, P. Castrataro, A. Menciassi, and P. Dario, "Focused ion beam as a scanning probe: methods and applications, in *Applied scanning probe methods II: scanning probe microscopy techniques*, B. Bhushan and H. Fuchs, Eds. Heidelberg: Springer, 2006.

[188] V.B.Ö. Özdöl, V. Srot, and P.A. Aken, "Sample preparation techniques for transmission electron microscopy, in *Handbook of Nanoscopy*, G. Van Tendeloo, D. V. Dyck and S.J. Pennycook, Eds. Weinheim: Wiley-VCH Verlag GmbH & Co, 2012.

[189] L.A. Giannuzzi and F.A. Stevie, "A review of focused ion beam milling techniques for TEM specimen preparation", *Micron*, vol. 30, no. 3, pp. 197–204, 1999.

[190] M.S. Beckwith, K.S. Beckwith, P. Sikorski, N.T. Skogaker, T.H. Flo, Ø. Halaas, "Seeing a mycobacterium-infected cell in nanoscale 3D: correlative imaging by light microscopy and FIB/SEM tomography", *PLoS One*, vol. 134644, pp. 1–19, 2015.

[191] E.B. Gutoff, and E.D. Cohen, *Coating and drying defects - troubleshooting operating problems*, 2nd ed. New Jersey: John Wiley & Sons, 2006.

[192] P.D. Nellist, "Scanning Transmission Electron Microscopy", in Science of Microscopy, 1st ed., P. Hawkes and J.C.H. Spence, Eds. New York, Springer, 2007, pp. 65–132.

[193] B.J. Inkson, "Scanning electron microscopy (SEM) and transmission electron microscopy (TEM) for material characterization", in Materials characterization using nondestructive evaluation (NDE) methods, G. Huebschen, I. Altpeter, R. Tschuncky, H.G. Herrmann, Eds. Duxford: Woodhead Publishing, 2016, pp. 17–44.

[194] S. Molatta, S. Haindl, S. Trommler, M. Schulze, S. Wurmehl, and R. Hühne, "Interface control by homoepitaxial growth in pulsed laser deposited iron chalcogenide thin films", *Scientific Reports*, vol. 5, p. 16334, 2015.

[195] H.J. Goldsmid, "Bismuth telluride and its alloys as materials for thermoelectric generation", *Materials, vol.* 7, pp. 2577–2592, 2014.

[196] H. Palme and H.S.C. O'neill, "Comsochemical estimates of mantle composition", in *The mantle core: treatise on geochemistry*, 2nd ed., R.W.

Carlson, Ed. Oxford: Elsevier, 2005, pp. 1–38.

[197] F.J. Himpsel, F.R. McFeely, A. Taleb-Ibrahimi, J.A. Yarmoff and G. Hollinger, "Microscopic structure of the SiO_2/Si interface", *Physical Review B*, vol. 38, no. 9, pp. 6084–6096, 1988.

[198] M.M. Banaszak Holl, and F.R. McFeely, "Si/SiO_2 interface: new structures and well-defined model systems", *Physical Review Letters*, vol. 71, no. 15, pp. 2441–2444, 1993.

[199] G. Kovačević and B. Pivac, "Structure, defects, and strain in silicon-silicon oxide interfaces", *Journal of Applied Physics*, vol. 115, pp. 0–11 (043531), 2014.

[200] H. Zhang, J.-H. Zhou, Q.-L. Zhang, and H. Yang, "Mechanical and optical properties of ion-exchange strengthened glass coated with sol-gel derived ZrO_2-SiO_2 film", *Journal of Inorganic Materials*, vol. 28, no. 7, pp. 785–789, 2013.

[201] X. Kang, S. Huang, P. Yang, P. Ma, D. Yang and J. Lin, "Preparation of luminescent and mesoporous Eu^{3+}/Tb^{3+} doped calcium silicate microspheres as drug carriers via a template route", *Dalton Transactions*, vol. 40, pp. 1873–1879, 2011.

[202] M. Fuchs, E. Gentleman, S. Shahid, R.G. Hill, and D.S. Brauer, "Therapeutic ion-releasing bioactive glass ionomer cements with improved mechanical strength and radiopacity", *Frontiers in Materials*, vol. 2, October, pp. 1–11, 2015.

[203] A. Polman,"Erbium implanted thin film photonic materials", *Applied Physics Review*, vol. 82, no. 1, pp. 1–39, 1997.

[204] E. Snoeks, P.G. Kik and A. Polman, "Concentration quenching in erbium implanted alkali silicate glasses", *Optical Materials*, vol. 5, pp. 159–167, 1996.

[205] F. Patel, S. DiCarolis, P. Lum, S. Venkatesh, and J. Miller, "A compact high-performance optical waveguide amplifier", *IEEE Photonics Technology Letters*, vol. 16, no.12, pp. 2607–2609, 2004.

[206] M. Irannejad, G. Jose, P. Steenson, and A. Jha, "Enhancement in optical and microstructure properties of Er^{3+}-doped phospho-tellurite glass thin film", *Optical Materials*, vol. 34, pp. 1272–1276, 2012.

[207] N.G. Boetti, J. Lousteau, A. Chiasera, M. Ferrari, E. Mura, G.C. Scarpignato, S. Abrate, and D. Milanese, "Thermal stability and spectroscopic properties of erbium-doped niobic-tungstentellurite glasses for laser and amplifier devices", Journal of Lumininescence, vol. 132, pp. 1265–1269, 2012.

[208] L. Zhang, G. Dong, M. Peng, and J. Qiu, "Comparative investigation on the

spectroscopic properties of Pr^{3+}-doped boro-phosphate, boro-germo-silicate and tellurite glasses", *Spectrochimica Acta Part A: Molecular and Biomelecular Spectroscopy*, vol. 93, pp. 223–227, 2012.

[209] J. Morel, A. Woodtli, and R. Dandliker, "Characterization of the fluorescent lifetime of doped fibers by measuring the frequency transfer function", *Journal of Lightwave Technology*, vol. 14, no. 5, pp. 739–742, 1996.

[210] Jianhu Yang, Shixun Dai, N. Dai, S. Xu, L. Wen, L. Hu, and Z. Jiang, "Effect of Bi_2O_3 on the spectroscopic properties of erbium-doped bismuth silicate glasses", *Journal of Optical Society of America B*, vol. 20, no. 5, pp. 810–815, 2003.

[211] M. Jiménez De Castro and J.M. Fernández Navarro, "Infrared luminescence of erbium-doped sodium lead germanate glass", *Applied Physics B: Lasers and Optics,* vol. 106, no. 3, pp. 669–675, 2012.

[212] W. Luo, J. Liao, R. Li, X. Chen, "Determination of Judd–Ofelt intensity parameters from the excitation spectra for rare-earth doped luminescent materials", *Physical Chemistry Chemical Physics*, vol. 12, pp. 3276–3282, 2010.

[213] G. Jose, T.T. Fernandez, P. Steenson and A. Jha, "Multi-ion diffusion in silica glass using femtosecond pulsed laser deposition", in *Conference on Lasers Electro-Optics: Science and Innovations*, 2012.

[214] N. Sharma, M. Hooda, and S.K. Sharma, "Synthesis and characterization of LPCVD polysilicon and silicon nitride thin films for MEMS Applications, *Journal of Materials*, vol. 2014, pp. 1–8, 2014.

[215] A.Y. Suh, N. Yu, K.M. Lee, A.A. Polycarpou, and H.T. Johnson, "Crystallite coalescence during film growth based on improved contact mechanics adhesion models", *Journal of Applied Physics*, vol. 96, no. 3, pp. 1348–1359, 2004.

[216] R.W. Eason, S.J. Barrington, C. Grivas, T.C. Mary-Smith, and D.P. Shepherd, "Optical waveguide growth and applications", in *Pulsed laser deposition thin films: applications-led growth of functional materials*, R. Eason, Ed. New Jersey: John Wiley & Sons, 2007, pp. 385–420.

[217] R. Eason, *Pulsed laser deposition of thin films: applications-led growth of functional materials*, New Jersey: John Wiley & Sons, 2007.

[218] Y.R. Ryu, S. Zhu, J.D. Budai, H.R. Chandrasekhar, P.F. Miceli, and H.W. White, "Optical and structural properties of ZnO films deposited on GaAs by pulsed laser deposition", *Journal of Applied Physics*, vol. 88, no. 1, pp. 201–204, 2000.

[219] D.B. Geohegan, *Laser ablation: mechanism and application*, Heidelberg: Springer, 1991.

[220] M. Okoshi, H. Kumagai, and K. Toyoda, "Pulsed laser deposition of carbon nitride thin films in nitrogen gas ambient", *Journal of Materials Research*, vol. 12, no. 12, pp. 3376–3379, 1997.

[221] J. Gottmann, T. Klotzbiicher, and E.W. Kreutz, "Pulsed laser deposition of ceramic thin films using different laser sources", *Surface and Coatings Technology*, vol. 100–101, pp. 411–414, 1998.

[222] A. Pillonnet, C. Garapon, C. Champeaux, C. Bovier, R. Brenier, H. Jaffrezic, and J. Mugnier, "Influence of oxygen pressure on structural and optical properties of Al_2O_3 optical waveguides prepared by pulsed laser deposition", *Applied Physics A: Materials Science & Processing*, vol. 69, pp. S735–S738, 1999.

[223] A. Suárez-García, J. Gonzalo, C.N. Afonso, "Low-loss Al_2O_3 waveguides produced by pulsed laser deposition at room temperature, *Applied Physics A: Materials Science and Processing*, vol. 77, pp. 779–783, 2003.

[224] P. Tian, J. Cheng, and G. Zhang, "X-ray photoelectron spectroscopy of Sm^{3+}-doped CaO–MgO–Al_2O_3–SiO_2 glasses and glass ceramics", *Applied Surface Science*, vol. 257, pp. 4896–4900, 2011.

[225] A. Mekki, "X-ray photoelectron spectroscopy of CeO_2-Na_2O-SiO_2 glasses", *Journal of Electron Spectroscopy and Related Phenomena*, vol. 142, pp. 75–81, 2005.

[226] E.C. Onyiriuka, "Zinc phosphate glass surfaces studied by XPS", *Journal of Non-Crystaline Solids*, vol. 163, pp. 268–273, 1993.

[227] A. Mekki, "XPS study of lead vanadate glasses", *The Arabian Journal for Science and Engineering,* vol. 28, no. 1A, pp. 73–85, 2003.

[228] H.W. Nesbitt, G.M. Bancroft, G.S. Henderson, R. Ho, K.N. Dalby, Y. Huang, and Z. Yan, "Bridging, non-bridging and free (O^{2-}) oxygen in Na_2O-SiO_2 glasses: An X-ray Photoelectron Spectroscopic (XPS) and Nuclear Magnetic Resonance (NMR) study", *Journal of Non-Crystalline Solids*, vol. 357, pp. 170–180, 2011.

[229] A. Mekki, D. Holland, C.F. McConville, and M. Salim, "An XPS study of iron sodium silicate glass surfaces", *Journal of Non-Crystalline Solids*, vol. 208, pp. 267–276, 1996.

[230] O. Catalina, M. Popa, E. Ionela, and M. Zaharescu, "Correlation of structural units and chemical stability in SiO_2–PbO–Na_2O ternary glasses : spectroscopic methods", *Journal of Non-Crystalline Solids*, vol. 361, pp. 130–141, 2013.

[231] G.C. Smith, "Evaluation of a simple correction for the hydrocarbon contamination layer in quantitative surface analysis by XPS", *Journal of Electron Spectroscopy and Related Phenomena*, vol. 148, pp. 21–28, 2005.

[232] D.R. Baer, D.J. Gaspar, M.H. Engelhard, and A.S. Lea, "Beam effects during AES and XPS analysis, in *Surface Analysis by Auger X-Ray Photoelectron Spectroscopy*, D. Briggsa and J.T. Grant, Eds. Chichester: IM Publications and Surface Spectra Limited, 2003.

[233] D.E. Newbury and N.W.M. Ritchie, "Performing elemental microanalysis with high accuracy and high precision by scanning electron microscopy/silicon drift detector energy-dispersive X-ray spectrometry (SEM/SDD-EDS)", *Journal of Materials Science*, vol. 50, pp. 493–518, 2015.

[234] A.S. Gorzalski, C. Donley, and O. Coronell, "Elemental composition of membrane foulant layers using EDS, XPS, and RBS", *Journal of Membrane Science*, vol. 522, pp. 31–44, 2017.

[235] D. Ferrah, O. Renault, C. Petit-Etienne, H. Okuno, C. Berne, V. Bouchiat, and G. Cunge, "XPS investigations of graphene surface cleaning using H_2- and Cl_2-based inductively coupled plasma", *Surface and Interface Analysis*, vol. 48, pp. 451–455, 2016.

[236] B.W. Veal, D.J. Lam, and A.P. Paulikas, XPS study of CaO in sodium silicate glass, *Journal of Non-Crystalline Solids*, vol. 49, pp. 309–320, 1982.

[237] L.F. Edge, D.G. Schlom, S. Stemmer, G. Lucovsky, and J. Luning, "Detection of nanocrystallinity by X-ray absorption spectroscopy in thin film transition metal/rare-earth atom, elemental and complex oxides", *Radiation Physics and Chemistry*, vol. 75, pp. 1608–1612, 2006.

[238] R. Wojcieszak, M.J. Genet, P. Eloy, P. Ruiz, and E.M. Gaigneaux, "Determination of the size of supported Pd nanoparticles by X-ray photoelectron spectroscopy. Comparison with X-ray diffraction, transmission electron microscopy, and H_2 chemisorption methods, *Journal of Physical Chemistry C*, vol. 114, no. 39, pp. 16677–16684, 2010.

[239] L. C. Chen, "Particulates generated by pulsed laser ablation", in *Pulsed laser deposition of thin films*, D.B. Chrisey and G.K. Hubler, Eds. New York: John Wiley & Sons, 1994, pp. 167–198.

[240] V.I. Bukhtiyarov, I.P. Prosvirin, R.I. Kvon, S.N. Goncharova, and B.S. Bal'zhinimaev, "XPS study of the size effect in ethene epoxidation on supported silver catalysts", *Journal of Chemical Society, Faraday Transactions*, vol. 93, pp. 2323–2329, 1997.

[241] Y. Lykhach, S.M. Kozlov, T. Skála, A. Tovt, V. Stetsovych, N. Tsud, F. Dvořák,

V. Johánek, A. Neitzel, J. Mysliveček, S. Fabris, V. Matolín, K.M. Neyman, and J. Libuda, "Counting electrons on supported nanoparticles", *Nature Materials*, vol. 15, pp. 284–289, 2016.

[242] A.B. Andrade, N.S. Ferreira, and M.E.G. Valerio, "Particle size effects on structural and optical properties of BaF$_2$ nanoparticles", *RSC Advances*, vol. 7, pp. 26839–26848, 2017.

[243] R.L. Park, "Core-level spectroscopies", in *Solid state physics: surfaces*, R.L. Park and M.G. Lagally, Eds. London: Academic Press, 1985, pp. 187–236.

[244] G. Gantefor, "Photoelectron spectroscopy", in *Quantum phenomena in clusters and nanostructures*, S.N. Khanna and A.W. Castleman, Eds. Heidelberg: Springer-Verlag Berlin Heidelberg, 2003, pp. 29–54.

[245] D. Sebilleau, "X-ray and electron spectrocopies: an introduction", in *Magnetism: a synchrotron radiation approach*, E. Beaurepaire, H. Bulou, F. Scheurer, and J.P. Kappler, Eds. Heidelberg: pringer-Verlag Berlin Heidelberg, 2006, pp. 15–58.

[246] A.M.A. Bennett, T. Douglas, K.M. Unruh, S.I. Shah, and K.H. Theopold, "Synthesis of III-V semiconductor particles from organometallic precursors", in N*anophase materials synthesis-properties-applications,* G.C. Hadjipanayis and R.W. Siegel, Eds. Dordrecht: Springer, 1994, pp. 29–36.

[247] A. Pal, P. Saini, and S. Sapra, "Conjugated-polymer/quantum-confined nanomaterials-based hybrids for optoelectronics applications", in *Fundamentals of conjugated polymer blends, copolymers and composites: synthesis, properties and applications*, P. Saini, Ed. New Jersey: John Wiley & Sons, 2015, pp. 163–228.

[248] V. Ponec, G.C. Bond, *Catalysis by metals and alloys*, Amsterdam: Elsevier, 1995.

[249] T. Seuthe, M. Grehn, A. Mermillod-Blondin, H.J. Eichler, J. Bonse, and M. Eberstein, "Structural modifications of binary lithium silicate glasses upon femtosecond laser pulse irradiation probed by micro-Raman spectroscopy", *Optical Materias Express*, vol. 3, no. 6, pp. 755–764, 2013.

[250] W. Qiu, C. Cheng, Y. Zhao, and Q. Li, "Residual Stress Measurement in Si-based Multilayer Structure by Micro-Raman Spectroscopy", *Optics*, vol. 4, no. 3-1, pp. 33–38, 2015.

[251] W.D. Bonificio, and D.R. Clarke, "Bacterial recovery and recycling of tellurium from tellurium-containing compounds by Pseudoalteromonas sp. EPR3", *Journal of Applied Microbiology*, vol. 117, pp. 1293–1304, 2014.

[252] Y.C. Her and S.L. Huang, "Growth mechanism of Te nanotubes by a direct

vapor phase process and their room-temperature CO and NO$_2$ sensing properties", *Nanotechnology*, vol. 24, p. 215603, 2013.

[253] J. Cui and G.A. Hope, Raman and fluorescence spectroscopy of CeO$_2$, Er$_2$O$_3$, Nd$_2$O$_3$, Tm$_2$O$_3$, Yb$_2$O$_3$, La$_2$O$_3$, and Tb$_4$O$_7$, *Journal of Spectroscopy*, vol. 2015, p. 940172, 2015.

[254] V.N. Sigaev, S. V. Lotarev, E. V. Orlova, N. V. Golubev, V. V. Koltashev, V.G. Plotnichenko, and G. a. Komandin, "Structure of lanthanum-borogermanate glass with stillwellite composition according to vibrational spectroscopy data", *Glass and Ceramics*, vol. 67, no. 3-4, pp. 105–108, 2010.

[255] D.R. Neuville, D. de Ligny and G.S. Henderson, "Advances in raman spectroscopy applied to earth and materials science", in *Spectroscopic methods in mineralogy and material science*, G.S. Henderson and D.R. Neuville, Eds. Virgina: The Mineralogical Society of America, 2015.

[256] S.K. Ghoshal, A. Awang, M.R. Sahar and R. Arifin, "Gold nanoparticles assisted surface enhanced Raman scattering and luminescence of Er^{3+} doped zinc–sodium tellurite glass", *Journal of Luminescence*, vol. 159, pp. 265–273, 2015.

[257] M.R. Dousti, M.R. Sahar, R.J. Amjad, S.K. Ghoshal, and A. Awang, "Surface enhanced Raman scattering and up-conversion emission by silver nanoparticles in erbium–zinc–tellurite glass", *Journal of Luminescence*, vol. 143, pp. 368–373, 2013,

[258] T. Sekiya, N. Mochida, and A. Soejima, "Raman spectra of binary tellurite glasses containing tri- or tetra-valent cations", *Journal of Non-Crystalline Solids*, vol. 191, pp. 115–123, 1995.

[259] L. Robinet, C. Coupry, K. Eremin, and C. Hall, "The use of Raman spectrometry to predict the stability of historic glasses", *Journal of Raman Spectroscopy*, vol. 37, pp. 789–797, 2006.

[260] B. Suresh, Y. Zhydachevskii, M.G. Brik, A. Suchocki, and M.S. Reddy, "Amplification of green emission of Ho^{3+} ions in lead silicate glasses by sensitizing with Bi^{3+} ions", *Journal of Alloys and Compounds*, vol. 683, pp. 114–122, 2016.

[261] K. Bourhis, Y. Shpotyuk, J. Massera, V. Aallos, T. Jouan, C. Boussard-plédel, B. Bureau, L. Petit, J. Koponen, L. Hupa, M. Hupa, and M. Ferraris, "Thermal and structural characterization of erbium-doped borosilicate fibers with low silica content containing various amounts of P$_2$O$_5$ and Al$_2$O$_3$", *Optical Materials*, vol. 37, pp. 87–92, 2014.

[262] C. Calahoo, J.W. Zwanziger, and I.S. Butler, "Mechanical−structural

investigation of ion-exchanged lithium silicate glass using micro-raman spectroscopy", *Journal of Physical Chemistry C*, vol. 120, pp. 7213–7232, 2016.

[263] P. McMillan, "Structural studies of silicate glasses and melts-applications and limitations of Raman spectroscopy", *American Mineralogist*, vol. 69, pp. 622–644, 1984.

[264] X. Bai, W. Jie, G. Zha, W. Zhang, P. Li, H. Hua, and L. Fu, XPS and SRUPS study of oxygen adsorption on $Cd_{0.9}Zn_{0.1}Te$ (111)A surface, *Applied Surface Science*, vol. 255, pp. 7966–7969, 2009.

[265] O. Ogbuu, Q. Du, H. Lin, L. Li, Y. Zou, E. Koontz, C. Smith, S. Danto, K. Richardson, and J. Hu, "Impact of stoichiometry on structural and optical properties of sputter deposited multicomponent tellurite glass films", *Journal of American Ceramic Society*, vol. 98, no. 6, pp. 1731–1738, 2015.

[266] P. Cheng, Y. Zhou, M. Zhou, X. Su, Z. Zhou, and G. Yang, "Enhanced broadband near-infrared luminescence from Pr^{3+}-doped tellurite glass with silver nanoparticles," *Optical Materials*, vol. 73, pp. 102–110, 2017.

[267] Z. Zhou, Y. Zhou, M. Zhou, X. Su, and P. Cheng, "The enhanced near-infrared fluorescence of Nd^{3+}-doped tellurite glass", *Journal of Non-Crystalline Solids*, vol. 470, pp. 122–131, 2017.

[268] S. Watanabe, T. Kodera, and T. Ogihara, "Influence of tellurite glass on reaction between Si3N4 anti-reflection coating film and Ag paste for electrodes in Si solar cells", *Journal of Ceramic Society of Japan*, vol. 124, no. 3, p. 218, 2016.

[269] D.M. Dobkin and M.K. Zuraw, *Principles of chemical vapor deposition: What's going on inside the reactor*, Dordrecht: Springer, 2003.

[270] W. Zhang, S. Wu and X. Chen, "Effects of substrate temperature and ambient oxygen pressure on growth of $Ba(Fe_{1/2}Nb_{1/2})O_3$ thin films by pulsed laser deposition", *Chinese Science Bulletin*, vol. 58, no. 27, pp. 3398–3402, 2013.

[271] V. Gupta and K. Sreenivas, "Pulsed laser deposition of zinc oxide (ZnO)", in *Zinc oxide bulk, thin film and nanostructures*, C. Jagadish and S. Pearton, Eds. Chennai: Elsevier, 2006, pp. 85–174.

[272] Z. Cun, Z. Qin-Yuan, P. Yue-Xiao, and J. Zhong-Hong, "Effects of Nb_2O_5 on thermal stability and optical properties of Er^{3+}-doped tellurite glasses", C*hinese Physics*, vol. 15, no. 9, pp. 2158–2164, 2006.

[273] A. Polman, D.C. Jacobson, D.J. Eaglesham, R.C. Kistler, and J.M. Poate, "Optical doping of waveguide materials by MeV Er implantation", *Journal of Applied Physics*, vol. 70, no. 7, pp. 3778–3784, 1991.

[274] Y. Gong, S. Yerci, R. Li, L.D. Negro, and J. Vuckovic, "Enhanced light emission from erbium doped silicon nitride in plasmonic metal-insulator-metal structures", *Optics Express*, vol. 17, no. 23, pp. 20642–20650, 2009.

[275] D. Olaosebikan, S. Yerci, A. Gondarenko, K. Preston, R. Li, L. Dal Negro, and M. Lipson, "Absorption bleaching by stimulated emission in erbium-doped silicon-rich silicon nitride waveguides", *Optics Letters*, vol. 36, no. 1, pp. 4–6, 2011.

[276] E.Ã. Coetsee, J.J. Terblans, and H.C.Ã. Swart, "Characteristic properties of Y_2SiO_5:Ce thin films grown with PLD", *Physica B: Physics of Condensed Matter*, vol. 404, pp. 4431–4435, 2009.

[277] M. Miyabe, M. Oba, H. Iimura, K. Akaoka, A. Khumaeni, M. Kato, and I. Wakaida, "Ablation plume structure and dynamics in ambient gas observed by laser-induced fluorescence imaging spectroscopy", *Spectrochimica Acta Part B.* vol. 110, pp. 101–117, 2015.

[278] M.S. Dawood, A. Hamdan, and J. Margot, "Influence of surrounding gas, composition and pressure on plasma plume dynamics of nanosecond pulsed laser-induced aluminum plasmas, *AIP Advances*, vol. 5, no. 10, p. 107143, 2015.

[279] K. Wissenbach, A. Weisheit, E. Willenborg, A. Temmler, A. Weisheit, G. Backes, A. Gasser, and J. Gottmann, "Surface treatment", in *Tailored Light 2: laser application technology*, R. Poprawe, Ed. Berlin: Springer, 2011, pp. 173–240.

[280] S.T.S. Dlamini, H.C. Swart, J.J. Terblans, and O.M. Ntwaeaborwa, "The effect of different gas atmospheres on the structure, morphology and photoluminescence properties of pulsed laser deposited $Y_3(Al,Ga)_5O_{12}$:Ce^{3+} nano thin films", *Solid State Science*, vol. 23, pp. 65–71, 2015.

[281] I. Marozau, A. shkabko, M. Döbeli, T. Lippert, D. logvinovich, M. Mallepell, C.W. Schneider, A. weidenkaff, and A. Wokaun, "Optical properties of nitrogen-substituted strontium titanate thin films prepared by pulsed laser deposition", *Materials*, vol. 2, no. 3, pp. 1388–1401, 2009.

[282] K.L. Saenger, "Angular distribution of ablated material", in *Pulsed laser deposition of thin films*, D.B. Chrisey and G.K. Hubler, Eds. New York: John Wiley & Sons, 1994, pp. 199–228.

[283] M.O. Boffoué, B. Lenoir, H. Scherrer, and A. Dauscher, "Pulsed laser deposition of bismuth in the presence of different ambient atmospheres," *Thin Solid Films*, vol. 322, pp. 132–137, 1998.

[284] E. Hasabeldaim, O.M. Ntwaeaborwa, R.E. Kroon, D.E. Motaung, E. Coetsee,

and H.C. Swart, "Effect of PLD growth atmosphere on the physical properties of ZnO:Zn thin films", *Optical Materials*, pp. 1–10.

[285] A. Ojeda-G-P, C.W. Schneider, M. Döbeli, T. Lippert, and A. Wokaun, "Plasma plume dynamics, rebound, and recoating of the ablation target in pulsed laser deposition", *Journal of Applied Physics*, vol. 121, p. 135306, 2017.

[286] X. Chen, S.. Xiong, Z.. Sha, and Z.. Liu, "The interaction of ambient background gas with a plume formed in pulsed laser deposition", *Applied Surface Science*, vol. 115, pp. 279–284, 1997.

[287] J.K. Park, "Electrochemical and material property analysis", in *Principle and applications of lithium secondary batteries*, Weinheim: Wiley-VCH, 2012.

[288] T. Chen, X.M. Li, S. Zhang, and H.R. Zeng, "Oxygen-pressure dependence of the crystallinity of MgO films grown on Si(100) by PLD", *Journal of Crystal Growth*, vol. 270, pp. 553–559, 2004.

[289] J.T. Pikturna, "Particle size prediction in reactive precipitation processes", Iowa State University, 2004.

[290] J. Martín-Sánchez, A. Chahboun, S.R.C. Pinto, A.G. Rolo, L. Marques, R. Serna, E.M.F. Vieira, M.M.D. Ramos, and M.J.M. Gomes, "A shadowed off-axis production of Ge nanoparticles in Ar gas atmosphere by pulsed laser deposition", *Applied Physics A: Materials Science and Processing*, vol. 110, pp. 585–590, 2013.

[291] A. Nath and A. Khare, "Laser-induced breakdown at solid-liquid interface", in *Laser ablation in liquids: principles and applications in the preparation of nanomaterials*, G. Yang, Ed. Temasek Boulevard: Pan Stanford Publishing, 2012, pp. 947–1012.

[292] S. Bar, "Crystalline rare earth doped sesquioxide PLD-films on A-alumina: preparation and characterization", University of Hamburg, 2004.

[293] S. Wu and X. Li, "Preparation of pure nano-grained Si_2N_2O ceramic", *International Journal of Refractory Metals and Hard Materials*, vol. 36, pp. 97–100, 2013.

[294] Y.L. Lu, Y.Q. Lu, and N.B. Ming, "Fluorescence and attenuation properties of Er^{3+}-doped phosphate-glass fibers and efficient infrared-to-visible up-conversion", *Applied Physics B*, vol. 62, pp. 287–291, 1996.

[295] S. Dai, C. Yu, G. Zhou, J. Zhang, G. Wang and L. Hu, "Concentration quenching in erbium-doped tellurite glasses", *Journal of Luminescence*, vol. 117, pp. 39–45, 2006.

[296] S.Saini, "Gain efficient waveguide optical amplifiers for gain efficient waveguide optical amplifiers for Si Microphotonics", Massachusetts Institute of

Technology, 2004.

[297] J.G. Sandland, "Sputtered silicon oxynitride for microphotonics: a materials study", Massachusetts Institute of Technology, 1999.

[298] W.J. Miniscalco, "Optical and electronic properties of rare earth ions in glasses", in *Rare-earth-doped fiber lasers and amplifiers*, M.J.F. Digonnet, Ed. New York: Marcel Dekker, 2001, pp. 18–130.

[299] H. Nishikawa and S. Umatani, "Effect of ablation laser pulse repetition rate on the surface protrusion density of hydroxyapatite thin films deposited using pulsed laser deposition", *Materials Letters*, vol. 209, pp. 330–333, 2017.

[300] S. Eaton, H. Zhang, P.R. Herman, F. Yoshino, L. Shah, J. Bovatsek, and A.Y. Arai, "Heat accumulation effects in femtosecond laser-written waveguides with variable repetition rate", *Optics Express*, vol. 13, no. 12, pp. 4708–4716, 2005.

[301] S. Biswas, A. Karthikeyan, and A. M. Kietzig, "Effect of repetition rate on femtosecond laser-induced homogenous microstructures", *Materials* , vol. 9 , p. 1023, 2016.

[302] A. V. Moholkar, S.S. Shinde, A.R. Babar, K.U. Sim, Y. bin Kwon, K.Y. Rajpure, P.S. Patil, C.H. Bhosale, and J.H. Kim, "Development of CZTS thin films solar cells by pulsed laser deposition: Influence of pulse repetition rate", *Solar Energy*, vol. 85, pp. 1354–1363, 2011.

[303] M. Sivayoganathan, B. Tan, and K. Venkatakrishnan, "Effect of mega-hertz repetition rate on the agglomerated particle size of femtosecond synthesized nanostructures", *Optical Material Express*, vol. 2, no. 8, pp. 987–995, 2012.

[304] P. Pichat, "Design and devolepment of active titania and related photocatalysts", in *Photocatalysis and water purification: from fundamentals to recent applications*, Weinheim: Wiley-VCH Verlag GmbH & Co., 2013.

[305] R.R.A. Sym, V. Schneider, H. W, and A.S. Holmes, "Low loss achieved in sol-gel based silica-on-silicon integrated optics using borophosphosilicate glass", *Electronics Letters*, vol. 31, no. 21,pp. 1833–1834, 1995.

[306] F.A. Sigoli, R.R. Gonçalves, Y. Messaddeq, and S.J.L. Ribeiro, "Erbium- and ytterbium-doped sol-gel SiO_2-HfO_2 crack-free thick films onto silica on silicon substrate", *Journal of Non-Crystalline Solids*, vol. 352, pp. 3463–3468, 2006.

[307] R.R.A. Syms, Silica-on-silicon integrated optics, in *Advances in integrated optics*, S. Martellucci, A.N. Chester, and M. Bertolotti, Eds. Boston: Springer, 1994.

[308] F. Rocca, M. Ferrari, A. Kuzmin, N. Daldosso, C. Duverger, and F. Monti, "EXAFS studies of the local structure of Er^{3+} ions in silica xerogels co-doped with aluminium", *Journal of Non-Crystalline Solids*, vol. 295, pp. 112–117,

2001.

[309] C. Maurizio, G. Mattei, and P. Mazzoldi, "X-ray absorption spectroscopy for metal-implanted silica", *Radiation Effects and Defects in Solids*, vol. 167, no. 7, pp. 478–486, 2012.

[310] J.A.M. Vrielink, R.M. Tiggelaar, J.G.E. Gardeniers, and L. Lefferts, "Applicability of X-ray fluorescence spectroscopy as method to determine thickness and composition of stacks of metal thin films: A comparison with imaging and profilometry", *Thin Solid Films*. vol. 520, pp. 1740–1744, 2012.

Appendix 1

The effect of oxygen pressure on properties of doped layer on Si_3N_4-on-silicon
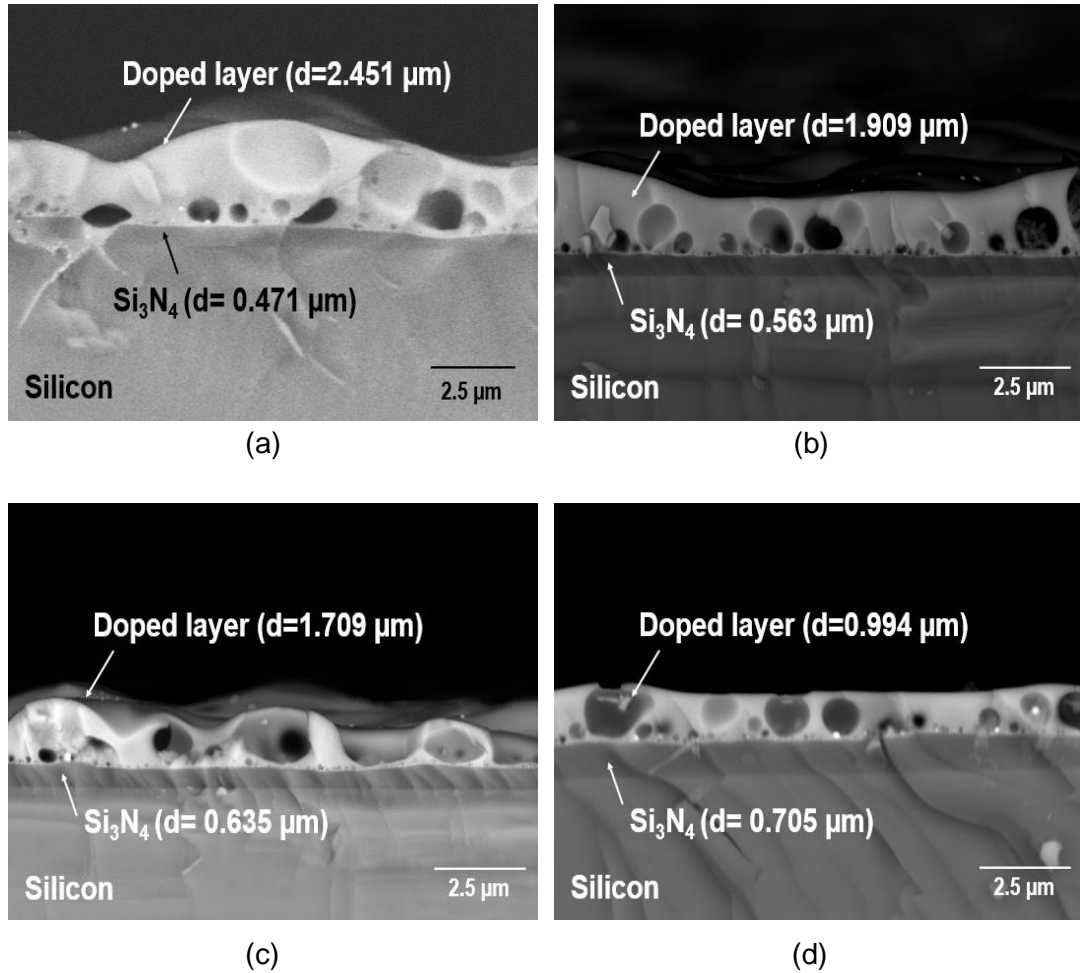

Figure 1: Backscattered cross-section SEM image of samples doped with Er-TZN using oxygen pressure of (a) 30 mTorr, (b) 50 mTorr, (c) 70 mTorr, and (d) 100 mTorr
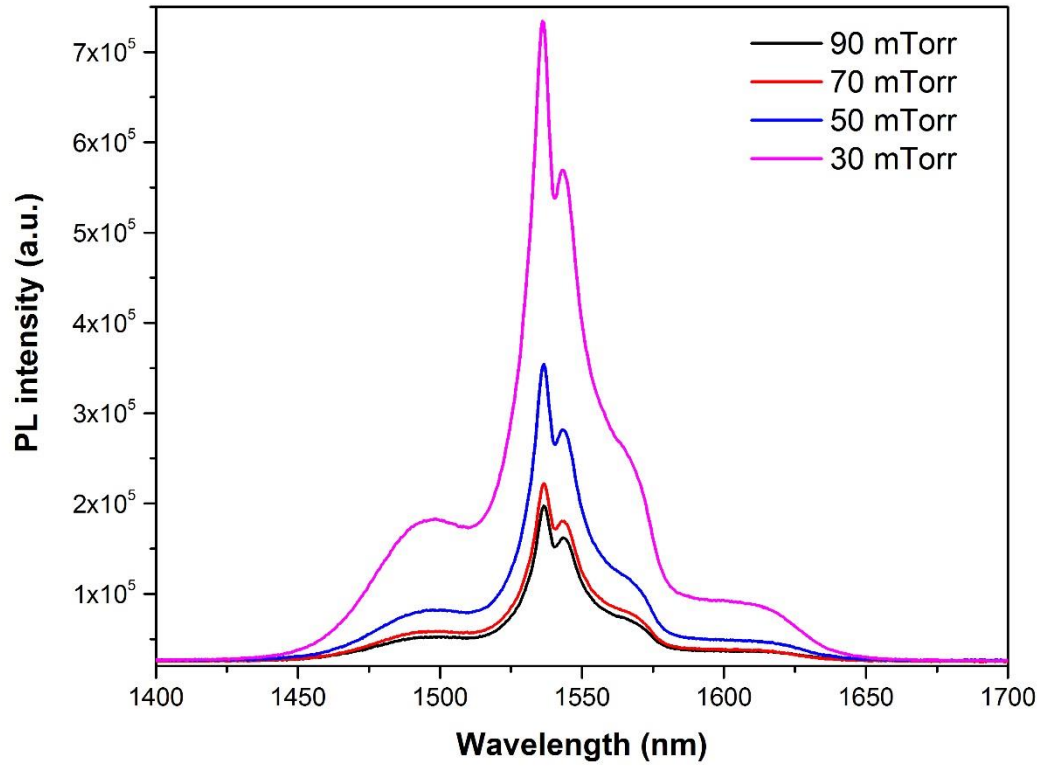
Figure 2: PL pattern of the $^4I_{13/2}$-$^4I_{15/2}$ transition of erbium ions with varying oxygen pressure.

Appendix 2

The effect of ablation period on properties of doped layer on Si_3N_4-on-silicon
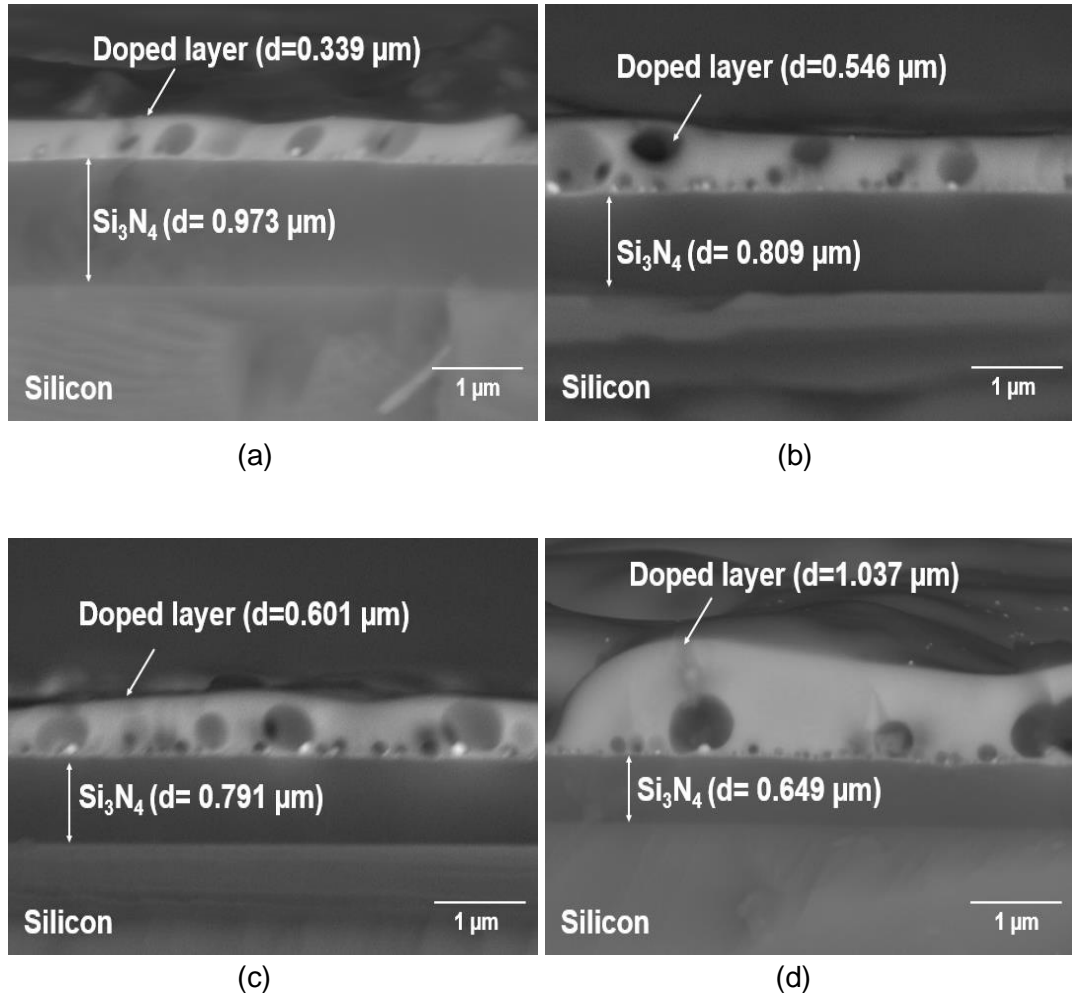

(a) (b)

(c) (d)

Figure 1: Backscattered cross-sectional SEM images of samples doped with Er-TZN into Si_3N_4-on-silicon when when target been ablated for (b) 1 hour (b) 2 hours (c) 3 hours, and (d) 4 hours.
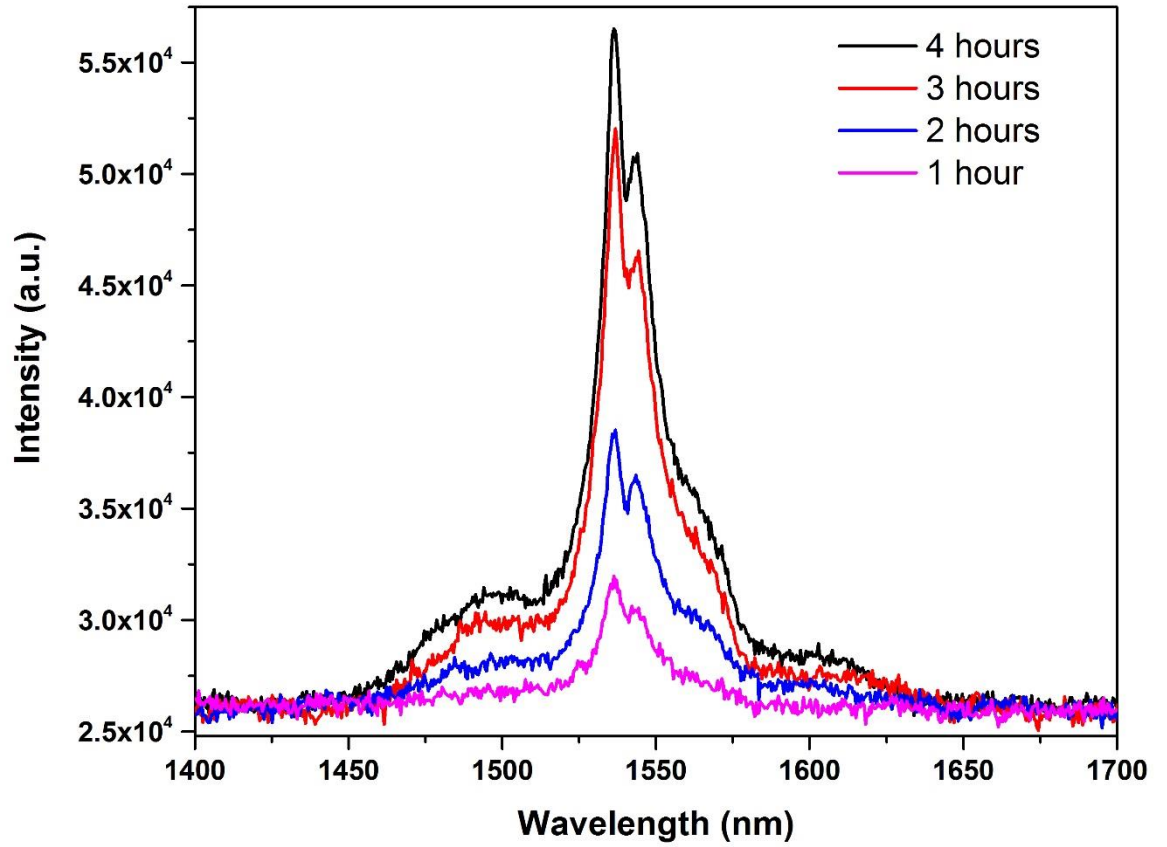
Figure 2: PL pattern of the $^4I_{13/2}$-$^4I_{15/2}$ transition of erbium ions with varying ablation period.